Luminescent nanohybrids based on silica and d-f heterobimetallic silylated complexes

Rafael Miguel Sábio

THÈSE

En vue de l'obtention du

DOCTORAT DE L'UNIVERSITE DE TOULOUSE

Délivré par :
Université Toulouse 3 Paul Sabatier (UT3 Paul Sabatier)
Cotutelle internationale avec « Universidade Estadual Paulista Júlio Mesquita Filho »

Présentée et soutenue par **Rafael MIGUEL SÁBIO**

Le **13 octobre 2016**

NANOHYBRIDES LUMINESCENTS A BASE DE SILICE ET DE COMPLEXES HETEROBIMETALLIQUES *d-f* SILYLES

ED SDM : Sciences et Génie des Matériaux – CO034

Unité de recherche :

Centre Interuniversitaire de Recherche et d'Ingénierie des Matériaux – UMR 5085

Directeurs de thèse :

Pr. Marie-Joëlle MENU	CIRIMAT, Université de Toulouse 3, France
Pr. Sidney José Lima RIBEIRO	Universidade Estadual Paulista, IQ Araraquara, Brésil

Autres membres du jury :

Dr. Michel WONG CHI MAN	Institut C. Gerhardt, ENSCM Montpellier2, France	Rapporteur
Pr. Lauro JUNE QUEIROZ MAIA	Instituto de Física, U. F. de Goiás, Goiânia, GO, BR	Rapporteur
Pr. Isabelle GAUTIER LUNEAU	Institut NEEL UPR 2940, Grenoble, France	Examinateur
Pr. Marc VERELST	CEMES, Université Toulouse3, France	Examinateur
Dr. J. Maurício ALMEIDA CAIUT	Universidade de São Paulo, Ribeirão Preto, SP, BR	Examinateur
Dr. Lucas ALONSO ROCHA	Universidade de Franca, Franca, SP, BR	Examinateur

UNESP - UNIVERSIDADE ESTADUAL PAULISTA
CAMPUS DE ARARAQUARA
PROGRAMA DE PÓS-GRADUAÇÃO EM QUÍMICA

Luminescent nanohybrids based on silica and *d-f* heterobimetallic silylated complexes: new tools for biological media analysis

RAFAEL MIGUEL SÁBIO

Doctoral Thesis
2016

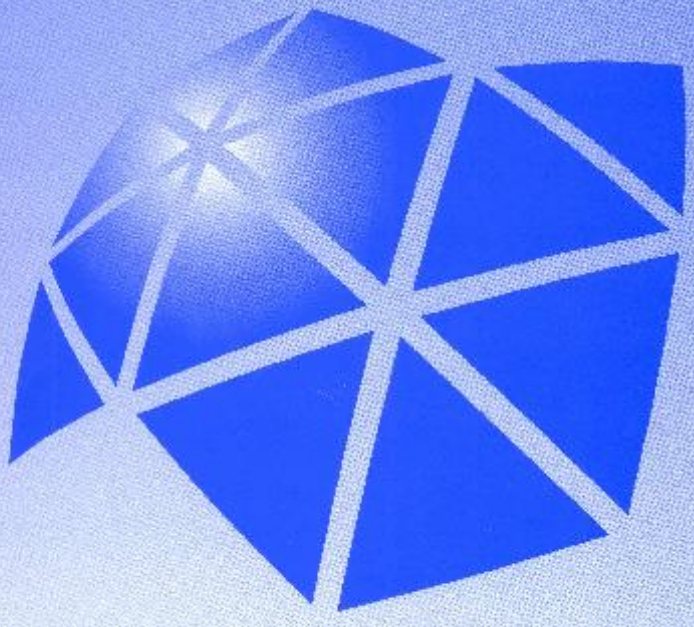

Instituto de Química

RAFAEL MIGUEL SÁBIO

Luminescent nanohybrids based on silica and *d-f* heterobimetallic silylated complexes: new tools for biological media analysis

Nanohybrides luminescents à base de silice et de complexe hétérobimétalliques d-f silylés: de nouveaux outils d'analyse des milieux biologiques

Thesis in Co-title with the Université de Toulouse 3 – Paul Sabatier – France presented to the Intitut of Chemistry, Universidade Estadual Paulista, to obtain the degree of Doctor in Chemistry.

Brazilian Advisor: Prof. Dr. Sidney José Lima Ribeiro (UNESP-BR)
French Advisor: Profa. Dra. Marie-Joëlle Menu (UPS-FR)
Co advisor: Prof. Dr. José Maurício Almeida Caiut (USP-BR)

Araraquara
2016

FICHA CATALOGRÁFICA

Sábio, Rafael Miguel
S116n Luminescent nanohybrids based on silica and *d-f* heterobimetallic silylated complexes: new tools for biological media analysis / Rafael Miguel Sábio. – Araraquara: [s.n.], 2016
244 p.: il.

Thesis (doctor) – Universidade Estadual Paulista, Instituto de Química
Advisor: Sidney José Lima Ribeiro
Advisor: Marie-Joëlle Menu
Co-advisor: José Maurício Almeida Caiut

1. Metallic complexes. 2. Rare earth metals. 3. Mesoporous materials. 4. Silica. 5. Luminescence. I. Title.

Elaboração: Seção Técnica de Aquisição e Tratamento da Informação
Biblioteca do Instituto de Química, Unesp, câmpus de Araraquara

RAFAEL MIGUEL SÁBIO

Tese em Co-tutela com a Université Toulouse III Paul Sabatier apresentada ao Instituto de Química, Universidade Estadual Paulista, como parte dos requisitos para obtenção do título de Doutor em Química.

Araraquara, 13 de Outubro de 2016.

BANCA EXAMINADORA

Prof. Dr. Sidney José Lima Ribeiro (Orientador)
Instituto de Química, UNESP – Araraquara/SP

Profª Drª Marie-Joëlle Menu
Materials Chemistry, Université Toulouse III Paul Sabatier – Toulouse/França

Prof. Dr. Lucas Alonso Rocha
Laboratório de Pesquisa em Química, UNIFRAN – Franca/SP

Prof. Dr. Lauro June Queiroz Maia
Instituto de Física, UFG – Goiânia/GO

Prof. Dr. Michel Wong Chi Man
Institut Charles Gerhardt, Université Montpellier II – Montpellier/França

Prof. Dr. Marc Verelst
Centre d'élaboration de Matériaux et d'études Structurales, Université Toulouse III Paul Sabatier – Toulouse/França.

Drª Isabelle Gautier-Luneau
Centre National de la Recherche Scientifique, Néel Institut – Grenoble/França

CURRICULUM VITAE

PERSONAL DETAILS

Name: Rafael Miguel Sábio
Name in citations: SÁBIO, RAFAEL MIGUEL; SÁBIO, R. M.

PROFESSIONAL ADDRESS

1) Universidade Estadual Paulista "Júlio de Mesquita Filho" - UNESP, Instituto de Química, Departamento de Química Geral e Inorgânica, Laboratório de Materiais Fotônicos (Lamf)
Rua Prof. Francisco Degni, 55. Jd. Quitandinha, CEP: 14800-900 – Araraquara – SP
Telefone: 16 3301-9765

E-mail: rafaelmsabio@gmail.com

ACADEMIC GRADUATION/TITLES

Undergraduate

Bachelor degree

Institution: Universidade Estadual Paulista "Júlio de Mesquita Filho" - UNESP, Instituto de Química, Campus Araraquara
Location: Araraquara – SP
Degree: Bachelor in Chemistry
Period: 2006-2009
Trabalho Orientado em Química – Departamento de Química Analítica: Monografia intitulada - "Avaliação de Preparo Alternativo de Amostra de Óleo Lubrificante na Determinação de Zn por Espectrometria de Absorção Atômica", sob orientação do Prof. Dr. José Anchieta Gomes Neto.

Graduate

Master Degree

Institution: Universidade Estadual Paulista "Júlio de Mesquita Filho" - UNESP, Instituto de Química, Departamento de Química Analítica, Campus Araraquara
Location: Araraquara – SP
Period: 2010-2012
Scholarship: CNPq
Dissertation Title: Ancoragem de complexos de rutênio com ligantes sililados em sílica mesoporosa obtida via pirólise de spray.
Advisor: Sidney José Lima Ribeiro
Co advisor: José Maurício Almeida Caiut

Internship Abroad:

Institution: Institut Carnot/CIRIMAT – Université de Toulouse 3 - Paul Sabatier
Location: Toulouse, França
Period: Fevereiro/2011 – Maio/2011

Ph.D. Degree (co-title thesis)

Institution: Universidade Estadual Paulista "Júlio de Mesquita Filho" - UNESP, Instituto de Química e Institut Carnot/CIRIMAT – Université de Toulouse 3 - Paul Sabatier. Universidade Estadual Paulista "Júlio de Mesquita Filho" - UNESP, Instituto de Química, Departamento de Química Geral e Inorgânica, Campus Araraquara
Location: Araraquara – SP e Toulouse – FR
Period: 2012-2016
Scholarship: CAPES/COFECUB
Thesis title: Luminescent nanohybrids based on silica and *d-f* heterobimetallic silylated complexes: new tools for biological media analysis.
French advisor: Prof.ª Dr.ª Marie-Joëlle Menu
Brazilian advisor: Prof. Dr. Sidney José Lima Ribeiro
Brazilian co advisor: Prof. Dr. José Maurício Almeida Caiut

BIBLIOGRAPHIC PRODUCTION

Papers published

1. SÁBIO, R. M.; GRESSIER, M.; CAIUT, J. M. A.; MENU, M.-J.; RIBEIRO, S. J. L. Luminescent multifunctional hybrids obtained by grafting of ruthenium complexes on mesoporous silica. **Materials Letters**, v. 174, p. 1-5, 2016.

2. SÁBIO, R. M.; OLIVEIRA, S. R.; TOGNOLLI, J. O.; GOMES NETO, J. A. Determination of zinc in lubricating oil by flame AAS employing ultrasonic extraction. **Atomic Spectroscopy**, v. 32, p. 240-245, 2011.

Papers accepted for publication

1. R. SILVA, R. R.; DUARTE, A. P.; SÁBIO, R. M.; CAIUT, J. M. A.; GRESSIER, M.; MENU, M.-J.; FRANCO JR, A.; RIBEIRO, S. J. L. Bifunctional magnetic luminescent particles based on iron oxide nanoparticles grafted with europium silylated bypiridine tris(β-diketonate) complex. **ChemistrySelect**, 2016.

CONFERENCE/CONGRESS

Conference proceedings (full paper)

1. SÁBIO, R. M.; DUARTE, A. P.; MESSADDEQ, Y.; GRESSIER, M.; MENU, M. J.; CAIUT, J. M. A.; RIBEIRO, S. J. L. Luminescence SiO_2 Mesoporous Based in d-Block Chromophores as Antenna Groups for System Ru(III)Nd(III) Binuclear Complex In: MRS SPRING MEETING, 2012, San Francisco. **MRS SPRING MEETING**, 2012.

2. STAIN, S. N.; SÁBIO, R. M.; ROCHA, L. A.; SARMENTO, V. H. V.; RIBEIRO, S. J. L.; CAIUT, J. M. A. Structural and Luminescence Properties of the SiO2/TiO2 Mesoporous System Doped with Europium Complex In: MRS SPRING MEETING, 2012, San Francisco. **MRS SPRING MEETING**, 2012.

Conference proceedings (abstract)

1. SÁBIO, R. M.; GRESSIER, M.; MENU, M. J.; CAIUT, J. M. A.; RIBEIRO, S. J. L. New near-infrared luminescent nanohybrids obtained by grafting of Ru, Ln complexes on mesoporous silica nanoparticles. In: GFL 2015 - Rénion du Groupe Français des Luminophores, 2015, Clermont-Ferrrand. **GFL 2015 - Réunion du Groupe Français des Luminophores**, 2015.

2. SÁBIO, R. M.; GRESSIER, M.; CAIUT, J. M. A.; RIBEIRO, S. J. L.; MENU, M. J. Preparação de complexos binucleares Ru^{2+}-Nd^{3+}: processos de sensibilização e transferência de energia d-f. In: 6° Encontro Nacional sobre Terras Raras, 2014, Recife. **6° Encontro Nacional sobre Terras Raras**, 2014.

3. SÁBIO, R. M.; DUARTE, A. P.; GRESSIER, M.; CAIUT, J. M. A.; RIBEIRO, S. J. L.; MENU, M. J. Study of d-f energy transfer in heteronuclear M-Ln dyads incorporated in silica nanoparticles obtained by sol-gel method In: XVII International Sol-Gel Conference, 2013, Madrid. **XVII International Sol-Gel Conference**, 2013.

4. SÁBIO, R. M.; OLIVEIRA, S. R.; TOGNOLLI, J. O.; GOMES NETO, J. A. Avaliação da Extração Ultrassônica para Determinação de Zinco em Óleo Lubrificante por Espectrometria de Absorção Atômica em Chama In: 2° Congresso Analitica Latin America, 2011, São Paulo. **2° Congresso Analitica Latin America**, 2011.

5. SÁBIO, R. M.; CAIUT, J. M. A.; Rocha, L. A.; DUARTE, A. P.; RIBEIRO, S. J. L.; MENU, M. J. Luminescents Mesoporous Materials Obtained by Aerosols Pyrolysis - Supramolecular Arrays and Energy Transfers. In: X Encontro Anual da Sociedade Brasileira de Pesquisa em Materiais (SBPMat), 2011, Gramado. **X Encontro Anual da Sociedade Brasileira de Pesquisa em Materiais (SBPMat)**, 2011.

6. SÁBIO, R. M.; CAIUT, J. M. A.; Rocha, L. A.; RIBEIRO, S. J. L.; MENU, M. J. Materiais Mesoporosos Luminescentes Obtidos Via Pirólise de Aerossóis In: 34ª Sociedade Brasileira de Quimica (SBQ Nacional), 2011, Florianópolis. **34ª Sociedade Brasileira de Química (SBQ Nacional)**, 2011.

7. SÁBIO, R. M.; CAIUT, J. M. A.; Rocha, L. A.; RIBEIRO, S. J. L.; MENU, M. J. Materiais Mesoporosos Luminescentes Obtidos via Pirólise de Aerossol In: 18 Encontro da Sociedade Brasileira de Química (SBQ Regional), 2011, São José do Rio Preto. **18° Encontro da Sociedade Brasileira de Química (SBQ Regional)**, 2011.

8. ROCHA, L. A.; CAIUT, J. M. A.; RIBEIRO, S. J. L.; MESSADDEQ, Y.; SÁBIO, R. M.; DUARTE, A. P.; DEXPERT-GHYS, J. Advanced Functional Materials Obtained By Spray Pirolysis Process In: IX Encontro Anual da Sociedade Brasileira de Pesquisa em Materiais (SBPMat), 2010, Ouro Preto. **IX Encontro Anual da Sociedade Brasileira de Pesquisa em Materiais (SBPMat)**, 2010.

Conference proceedings (expanded abstract)

1. SÁBIO, R. M.; CAIUT, J. M. A.; GRESSIER, M.; RIBEIRO, S. J. L.; MENU, M. J. Nouveaux complexes binucléaires d-f à fonction alkoxysilane pour l'obtention de nanomarqueurs luminescents dans l'IR In: Materiaux 2014, 2014, Montpellier. **Materiaux 2014**, 2014.

2. LAHOUD, M. G.; MUNIZ, E. C.; SÁBIO, R. M.; JAVIER, E.; DAVOLOS, M. R.; FREM, R. C. G. Investigation of the relationship between thermal treatment and emission intensity of thulium(III) complexes In: Third International Conference on Multifunctional, Hybrid and Nanomaterials, 2013, Sorrento. **Third International Conference on Multifunctional, Hybrid and Nanomaterials**, 2013.

3. SÁBIO, R. M.; LAHOUD, M. G.; CAIUT, J. M. A.; RIBEIRO, S. J. L.; DAVOLOS, M. R.; FREM, R. C. G. Luminescent Hybrids obtained by mesoporous silica doped with new terbium complex. In: III International Conference on Multifunctional Hybrid and Nanomaterials In: Third International Conference on Multifunctional, Hybrid and Nanomaterials, 2013, Sorrento. **Third International Conference on Multifunctional, Hybrid and Nanomaterials**, 2013.

4. LAHOUD, M. G.; MATURI, F. E.; SÁBIO, R. M.; RIBEIRO, S. J. L.; DAVOLOS, M. R.; FREM, R. C. G. PMMA-[$Tb_2(dcpz)_2(suc)$] organic inorganic hybrids In: Third International Conference on Multifunctional, Hybrid and Nanomaterials, 2013, Sorrento. **Third International Conference on Multifunctional, Hybrid and Nanomaterials**, 2013.

Events
Oral presentations / events

1. Apresentação oral no **GFL 2015 - Réunion du Groupe Français des Luminophores**, 2015. (Encontro). New near-infrared luminescent nanohybrids obtained by grafting of Ru, Ln complexes on mesoporous silica nanoparticles.

2. **Workshop: Ano Internacional da Luz - IYL 2015**, 2015.

3. Apresentação oral no **Materiaux 2014,** 2014. (Conferência) Nouveaux complexes binucléaires d-f à fonction alkoxysilane pour l'obtention de nanomarqueurs luminescents dans l'IR.

4. **1st SAMPA - Advanced School on Materials for Photonic Applications**, 2012.

OTHER EXPERIENCE ACADEMIC

- **Teaching:**
Química Inorgânica Estrutura e Propriedades Teórico e Experimental – 120 horas**:** Universidade Estadual Paulista "Júlio de Mesquita Filho" (UNESP) - Araraquara, Brasil. Supervisor: Prof. Dr. Sidney José Lima Ribeiro.

Responsável pela disciplina de Química para o curso de Técnico em Automação Industrial ministrada no CETEC (Centro Educacional Técnico) período de 08/2014 a 02/2015 - Catanduva-SP

DEDICO esta Tese aos meus amados pais José e Marlei,

pelo carinho, apoio e confiança em todos os momentos!

E principalmente por me proporcionarem uma das coisas mais importantes na vida: a educação!

Para todos que contribuíram para eu chegar onde estou hoje!

REMERCIEMENTS

Les travaux de recherche présentés dans ce mémoire ont été réalisés au Laboratório de Materiais Fotônicos de l'Universidade Estadual Paulista (UNESP) à Araraquara et au Centre Interuniversitaire de Recherche et d'Ingénierie des Matériaux de l'Université Paul Sabatier à Toulouse. Je remercie Monsieur Philippe Tailhades, Directeur de recherche CNRS, pour m'avoir permis de mener à bien ce travail.

Je remercie Monsieur Michel Wong Chi Man, Directeur de Recherche au CNRS, Institut Charles Gerhardt à ENSCM de Montpellier et Monsieur Lauro June Queiroz Maia, Professeur à l'Universidade Federal de Goias du Brésil pour avoir accepté de juger ce mémoire en qualité de rapporteur et pour participer à ce jury. Je tiens également à remercier Madame Isabelle Gautier Luneau Professeur à l'Université de Grenoble, Monsieur Marc Vereslt Professeur à l'Université de Toulouse 3 – Paul Sabatier et Monsieur Lucas Alonso Rocha Professeur de l'Universidade de Franca, Brésil, pour avoir accepté de siéger à ce jury.

Je remercie mes directeurs de thèse **Prof. Dr. Sidney J. L. Ribeiro** et **Prof Dra. Marie-Joëlle Menu**. Je leur témoigne toute ma reconnaissance pour la disponibilité, les conseils et l'aide dont ils ont su me faire part et pour la confiance qu'ils ont su m'accorder.

Je tiens à remercier mes co-encadrants de thèse **José Mauricio A. Caiut** et **Dr. Marie Gressier**, pour une participation effective dans cette thèse, la discussion des résultats, corrections des rapports, enfin, pour leur énorme disponibilité et attention.

Je tiens à remercier les enseignants, étudiants et employés du Département de Chimie Générale et Inorganique de l'Institut de Chimie à Araraquara qui ont, de quelques façons que ce soit, contribué à ma formation et à l'exécution de cette thèse.

Je tiens à remercier tout les membres du Laboratório de Materiais Fotônicos, **Karina**, **Gustavo**, **Robson**, **Fernando**, **Hernane**, **Laís**, **Silvia**, **Juliane**, **Marcelo**, entre autres pour l'amitié et aussi les moments à Araraquara.

Je tiens à remercier tout particulièrement tous les membres du RMN **Nivaldo** e **Silvia** pour les mesures realisés et aussi les discussions.

Je tiens à remercier tout particulièrement tous les membres du CIRIMAT pour l'accueil qu'ils m'ont réservé lors de mon arrivée au laboratoire. Je tiens à remercier **Lucien Datas**, **Marie**

Claire Barthelemy, **Stephane Le Blond du Plouy** et **Jean Jacques Demay** pour leurs contributions dans les diverses analyses (Microscopie et surface spécifique).

Je tiens à remercier le programme de coopération entre le Brésil et la France - CAPES-COFECUB, par l'échange de formation et de soutien en France.

Je tiens à remercier mes parents pour l'amour, particulièrement **José** et **Marlei**, **Natalie**, **Vanessa**, **Wilma**, **João** e **João Victor** pour leur soutien inconditionnel. Vous êtes mon exemple de vie. Sans oublier toute ma famille qui sera toujours mon refuge.

Je remercie mes amies de colocation **Coti** et **Noé**, pour les moments de détente, de soutien, et les nombreux souvenirs qui seront toujours inscrits dans ma mémoire.

Enfin je tiens à remercier tous mes amis : **André**, **Carol**, **Adriana**, **Léo**, **Luiza**, **Lucianna**, **Fabio**, **Alex**, **Wan-Yu**, **Laurent**, **Leila, Cédric**, entre autres. Merci à vous pour tous les moments en France.

Je remercie mes amis de Catanduva et Araraquara, **Guilherme**, **Fernanda**, **Jaque**, **Daiane**, **Leandro**, **Izabela**, **Fred**, **Rodrigo**, **Marlon**, **Paulo**, **Jefferson** et **Harry**. Merci à vous pour tous les moments au Brésil et les nombreux souvenirs qui seront toujours présents dans ma mémoire.

“Nossas dúvidas são traidoras e nos fazem perder o que, com frequência, poderíamos ganhar, por simples medo de arriscar.”

William Shakespeare

ABSTRACT

The design of heterobimetallic luminescent complexes has gained growing interest in recent years due to their unique photophysical properties. More specifically, the development of heterobimetallic complexes using *d*-block chromophores to sensitize the near-infrared (NIR) emission of lanthanide complexes (such as Nd(III) and Yb(III)) has received significant attention taking into account their longer emission wavelengths and the interest of the NIR emission which penetrates human tissue more effectively than UV light. These properties give them potential applications in medical diagnostics or biomedical assays. Transitions to excited state levels of transition metal complexes occurring in the visible and characterized by large absorption coefficients, could efficiently sensitize *f-f* levels of Ln(III) ions. In this work new *d-f* heterobimetallic complexes containing silylated ligands were prepared supported on silica materials. $[Ru(bpy)_2(bpmd)]Cl_2$ (labeled **Ru**), $[Ru(bpy)(bpy\text{-}Si)(bpmd)]Cl_2$ (labeled **RuL**) and $[Ln(TTA\text{-}Si)_3]$ (labeled **LnL3**) and *d-f* heterobimetallic complexes, **Ru—LnL3** and **Ln—RuL** (Ln = Nd^{3+}, Yb^{3+}) were prepared. Structural characterization was carried out by Raman Scattering, ^{1}H and ^{13}C NMR spectroscopies. Results obtained from ^{1}H-^{13}C HMBC and HSQC correlation NMR spectra confirm the formation of proposed complexes. Photophysical properties studies highlight the efficiency of **Ru—Ln** energy transfer processes in NIR-emitting lanthanide complexes mediated by conjugated bridging ligand (2,2'-bipyrimidine). Lifetime measurements were carried out and values of quantum yield for energy transfer (Φ_{ET}) between 30 and 84 % could be evaluated. Φ_{ET} of 73.4 % obtained for the **Yb—RuL** complex is the largest value reported for Ru(II)—Yb(III) heterobimetallic complexes so far. Grafting on different silica matrix was also demonstrated. **SiO_2-Ru**, **SiO_2-NdL3** and **SiO_2-YbL3** nanohybrids were obtained with grafting efficiencies from 0.08 to 0.18 mmol g^{-1} of silica. **SiO_2-RuNd** and **SiO_2-RuYb** were performed from simultaneous grafting of ruthenium and lanthanides silylated complexes. Grafting efficiencies from 0.10 to 0.16 were obtained. Φ_{ET} of 40 and 27.5 % were obtained from **SiO_2-RuNd** and **SiO_2-RuYb**, respectively. The higher values observed for the Nd(III) nanohybrid is well explained by the matching of donor and acceptor energy levels. **SiO_2-RuYbL3**, **SiO_2-YbRuL**, **SiO_2 d-YbRuL** and **SiO_2-NdRuL** were carried out from grafting of *d-f* heterobimetallic silylated complexes. Grafting efficiencies from 0.03 to 0.17 were obtained. Luminescent properties from these nanohybrids were similar to the free complexes. However, the **SiO_2-YbRuL** and **SiO_2 d-YbRuL** showed distinct luminescent profiles compared with the free **Yb—RuL**. The grafting inside the mesoporous channels may prevent luminescent desactivation processes comparing to the dense silica matrix. The photophysical properties associated with the morphology and stability of the mesoporous silica matrix allow suggesting these new NIR luminescent nanohybrids as nanoprobes or nanomarkers in biomedicine.

RÉSUMÉ

Le design de complexes luminescents hétérobimétalliques a suscité ces dernières années un intérêt croissant en raison de leurs propriétés photophysiques uniques. Dans ces complexes de lanthanide (Nd (III) et Yb (III)) associé à des chromophores du bloc *d,* la forte émission des métaux de transition dans le visible est utilisée pour sensibiliser de façon efficace les niveaux *f-f* des lanthanides(III) qui émettent à leur tour dans le visible ou l'IR selon les terres rares. Plus spécifiquement l'attention s'est focalisée sur le développement de complexes hétérobimétalliques *d-f* pour l'émission dans le proche infrarouge (NIR). En effet le proche infrarouge, comparé à l'UV, pénètre plus facilement les tissus biologiques humains notamment la peau. Bien que de telles propriétés confèrent à ces complexes bimétalliques un fort potentiel pour le diagnostic médical, aucun complexe hétérobimétallique *d-f* greffé de façon covalente à une matrice de silice n'a été décrit.

Dans ce travail de nouveaux complexes hétérobimétalliques *d-f* contenant des ligands silylés ont été préparés et greffés sur la silice. Les complexes monomères $[Ru(bpy)_2(bpmd)]Cl_2$ (noté **Ru**), $[Ru(bpy)(bpy\text{-}Si)(bpmd)]Cl_2$ (noté **RuL**) et $[Ln(TTA\text{-}Si)_3]$ (noté **LnL3**) et les complexes hétérobimétalliques *d-f* **Ru-LnL3** et **Ln-RuL** (Ln = Nd^{3+}, Yb^{3+}) ont été préparés. La caractérisation des complexes a été effectuée par spectroscopie Raman, RMN ^1H et ^{13}C RMN. Les spectres RMN 1D ^1H et ^{13}C NMR ainsi que 2D de corrélation HSQC confirment les structures proposées. L'étude des propriétés photophysiques met en évidence l'émission de l'élément lanthanide dans le proche infrarouge ainsi que l'efficacité du processus de transfert d'énergie Ru-Ln qui est facilité par le ligand (2,2'-bipyrimidine). Les mesures de durée de vie et de rendement quantique (Φ_{ET}) pour le transfert d'énergie indiquent des valeurs remarquables comprises entre 30 et 84 %. La valeur du rendement quantique (Φ_{ET}) du complexe d'**Yb-RuL**, 73,4 %, est à ce jour la plus grande valeur rapportée pour un complexe hétérobimétallique Ru (II)-Yb (III). Le greffage sur différentes matrices de silice, mésoporeuse **SiO_2** ou dense **SiO_2 d**, a été réalisé. Les nanohybrides **SiO_2-RuL**, **SiO_2-NdL3** et **SiO_2-YbL3** ont été obtenus avec des taux de greffage allant de 0,08 à 0,18 mmol de complexe par gramme de silice. **SiO_2-RuNd** et **SiO_2-RuYb** ont été obtenus par greffage simultané des complexes silylés monomères de ruthénium et de lanthanide, des taux de greffage de 0,10 à 0,16 $mmol.g^{-1}$ ont été obtenus, respectivement. Les rendements quantiques Φ_{ET} de transfert d'énergie des nanohybrides **SiO_2-RuNd** et **SiO_2-RuYb** sont respectivement de 40 and 27,5 %. La valeur remarquable obtenue pour le nanohybride impliquant le néodyme, **SiO_2-RuNd**, s'explique par bonne adéquation entre les niveaux d'énergie du donneur et de l'accepteur. Les nanohybrides **SiO_2-RuYbL3**, **SiO_2-YbRuL**, **SiO_2d-YbRuL** et **SiO_2-NdRuL** ont été obtenus par greffage des complexes silylés hétérobimétallic *d-f* élaborés dans ce travail, les taux de greffage, de 0,03 à 0,17 $mmol.g^{-1}$ permettent d'envisager une fonctionnalisation chimique ultérieure de ces nanoobjets.

Les propriétés de luminescence de ces nanohybrides sont similaires à celles des complexes non greffés hormis pour **SiO_2-YbRuL** and **SiO_2d-YbRuL** qui présentent des profils de luminescence différents comparés au complexe libre **Yb—RuL**. Le greffage à l'intérieur des pores de la silice pourrait éviter le processus de désactivation de la luminescent contrairement au greffage sur la matrice de silice dense. Les propriétés photophysiques associées à la

morphologie et à la stabilité de la matrice de silice mésoporeuse permettent d'envisager l'utilisation de ces nouveaux nanohybrides luminescents dans le proche infrarouge comme nanosondes ou nanomarqueurs de systèmes biologiques.

LIST OF FIGURES

LIST OF TABLES

LIST OF ABBREVIATIONS AND ACRONYMS

OLEDs: Organic Light Emitting Diodes

A: Absorption

F: Fluorescence

P: Phosphorescence

IC: Internal Conversion

ISC: Intersystem crossing

ET: Energy Transfer

S_0 or S_1: singlet

T_1 or T_2: triplet

ϕ: quantum yield

ϕ': relative quantum yield

Abs: Absorbance

Em: Emission

R: Reference

S: Unknown

ANMTTA: [4'-(4-amino-3-nitrophenoxy)methylene-2,2':6',2''-terpyridine-6,6''-diyl] bis(methylenenitrilo) tetrakis(acetic acid)

HOCl: hypochlorous acid

HTTA: (4'-hydroxymethyl-2,2':6',2''-terpyridine-6,6''-diyl) bis(methylenenitrilo) tetrakis(acetic acid)

TTA: 2-thenoyltrifluoroacetonate

DBSO: dibenzyl sulfoxide

TFAC: trifluoroacetylacetonate

DBM: 1,3-diphenylpropane-1,3-dione

PTSO: p-tolylsulfoxide

NIR: Near-Infrared

hfaa = anion of hexafluoroacetylacetone

pz = pyrazole

BT: Back Transfer

1P: one photon

2P: two photons

H_2pdo: 5,6-dihydroxyphenanthroline

dppz: 2,3-bis(2-pyridyl)pyrazine

dik: 1,3-diketonate

bppz: 2,3-bis(2-pyridyl)pyrazine

MLCT: metal-to-ligand charge transfer

LC: ligand centered

H_2L: 2-(1H-benzo[d]imidazol-2-yl)-6-methoxyohenol

ppy: 2-phenylpyridine

dcbpy: 2,2'-bipyridine-4,4'-dicarboxylate

bpmc: 5-bromopyrimidine-2-carboxylic acid

pdt: 1,3-dimethyl-5-phenyl-1H-[1,2,4]triazole

PLIM: Phosphorescence Lifetime Imaging Microscopy

TPA: two-photons absorption

OPA: one-photon absorption

NA = nicotinamide (pyridine-3-carboxamide)

tpphz: tetrapyrido[3,2-a:2',3'- c:3'',2''-h:3''',4'''-j] phenazine

Φ_{EnT}: quantum yield of energy transfer

k_{EnT}: energy transfer rate constant

AFP: alpha-fetal protein

$BibzImH_2$: Bibenzimidazole

bpmd: 2,2'-bipyrimidine

bpy: 2,2'-bipyridine

LUMO: Lowest Unoccupied Molecular Orbital

fod: 6,6,7,7,8,8,8-heptafluoro-2,2-dimethyl-3,5-octanedionato

LED: Light Emitting Diode

MSNs: mesoporous silica nanoparticles

DSNs: dense silica nanoparticles

APTES: 3-aminotriethoxysilane

DBM: dibenzoylmethane

HMDSA: hexamethyldisilazane

phen-Si: 5-(N,N-bis-3-(triethoxysilyl)-propyl)ureyl-1,10-phenanthroline

bpy-Si: 4-methyl-4'-(n-triethoxysilylpropyl)amine- methyl- 2,2'-bipyridine

TTA-Si: 4,4,4-Trifluoro-2-(3-(trimethoxysilyl)-propyl)-1-(2-thienyl)-1,3-butanedione

Ru: $[Ru(bpy)_2(bpmd)]Cl_2$

RuL: $[Ru(bpy)(bpy\text{-}Si)(bpmd)]Cl_2$

RuL1: $[Ru(bpy)_2(bpy\text{-}Si)]Cl_2$

Nd: $Nd(TTA)_3\ 2H_2O$

Yb: $Yb(TTA)_3\ 2H_2O$

NdL3: $[Nd(TTA\text{-}Si)_3]$

YbL3: $[Yb(TTA\text{-}Si)_3]$

Ru—NdL3: $[Ru(bpy)_2(bpmd)Nd(TTA\text{-}Si)_3]Cl_2$

Ru—YbL3: $[Ru(bpy)_2(bpmd)Yb(TTA\text{-}Si)_3]Cl_2$

Nd—RuL: $[Ru(bpy)(bpy\text{-}Si)(bpmd)Nd(TTA)_3]Cl_2$

Yb—RuL: $[Ru(bpy)(bpy\text{-}Si)(bpmd)Yb(TTA)_3]Cl_2$

TEOS: tetraethylorthosilicate

CTAB: cetyltrimethylammonium bromide

AIBA: 2,2'-Azobis (2-methylpropionamide) dihydrochloride

EA: Elemental Analysis

FTIR: Fourier Transformed Infra-Red Spectroscopy

DRIFT: Diffuse Reflectance Infra-Red Fourier Transformed Spectroscopy

FT-Raman: Fourier Transformed Raman Spectroscopy

UV-Vis: Ultraviolet-Visible Spectroscopy

NMR: Nuclear Magnetic Resonance

MAS NMR: Magic Angle Spinning Nuclear Magnetic Resonance

CP-MAS NMR: Cross-Polarization and Magic Angle Spinning Nuclear Magnetic Resonance

TOCSY: Total Correlation Spectroscopy

HSQC: Heteronuclear Single Quantum Coherence

HMBC: Heteronuclear Multiple Bond Correlation

TMS: Tetramethylsilane

MS: Mass Spectrometry

ESI: Electrospray

DCI: Desorption Chemical Ionization

FAB: Fast Atom Bombardment

FWHM: Full Width at Half Maximum

FEG-SEM: Field Emission Gun - Scanning Electron Microscopy

STEM: Transmission and Scanning Transmission Electron Microscopy

TEM: Transmission Electron Microscopy

EDX or EDS: Energy Dispersive X-ray spectroscopy

TGA: Thermogravimetric Analysis

DTA: Differetial Thermal Analysis

J: coupling constant

λ: wavelength

MeOH: methanol

EtOH: ethanol

THF: tetrahydrofuran

CH_2Cl_2: dichloromethane

DMF: dimethylformamide

MeOD: deuterated methanol

$CDCl_3$: deuterated cloroform

CONTENTS

1 – INTRODUCTION

1. INTRODUCTION

The group of elements known as "Rare Earths" includes lanthanide metals (elements with atomic number between Z = 57, the lanthanum, and Z = 71, lutetium), and scandium (Z = 21) and yttrium (Z = 39). Lanthanides share similar chemical and physical properties, existing mainly in their trivalent state LnIII ([Xe]$4f^n$, n = 0-14).[1–3] Shielding of the 4f orbitals by the outer 5s and 5p sub-shells results in weak ligand field effects and consequently, characteristic narrow-line emission and long lifetimes of the excited states are observed from the visible to the near-infrared region.[1–3] Lanthanide based materials have been widely employed as analytical sensors, imunoassays, bioimaging device, OLEDs, optical communication devices and in solar energy conversion, among others.[3–7] For example, Eu^{3+} ions provide suitable red luminescence for biological detection and organic electroluminescence.[8, 9] Nd^{3+} ions and Yb^{3+}, emiting in the range of 900 to 1400 nm, are good candidates for biological luminescence imaging, laser systems and luminescent nanothermometers.[7, 10] Pr^{3+} ions (emission at 1300 nm) and Er^{3+} ions (emission at 1500 nm) have been mainly used in optical amplifiers for fiber-optic networks.[7, 11–13]

Although there are a number of energy levels available for the f-f transitions of lanthanide ions the very low molar absorption coefficients for UV-visible light (< 10 M) is a serious drawback.[4, 14] This problem has been circumvented by using organic chromophores. These ligands exhibit strong absorption in the UV region (~10^6 M) and subsequent ligand to Lanthanide energy transfer can take place in the so-called “antenna effect”.[4, 14] The figure 1 shows the schematic representation of the energy transfer mechanism between organic ligands and lanthanide ion.

Figure 1. Schematic representation of the antenna effect from the organic ligand to the lanthanide(III) ion. Abbreviations: A = absorption; F = fluorescence; P = phosphorescence; ISC = intersystem crossing; ET = energy transfer; S = singlet; T = triplet. Full vertical lines indicate radiative transitions; dashed vertical lines indicate nonradiative transitions.[4, 13, 15, 16]

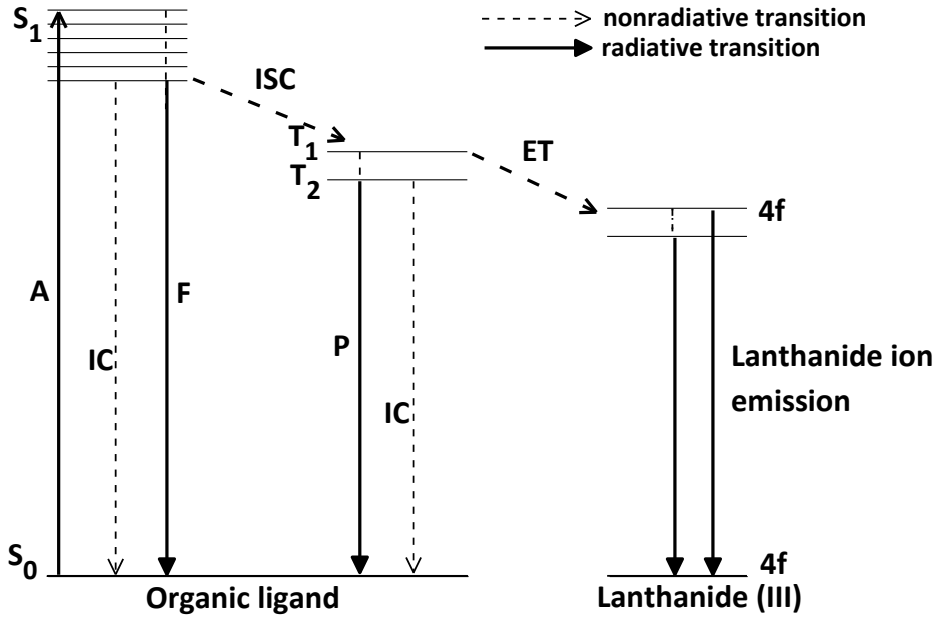

Upon irradiation in UV the organic ligands are excited to a vibrational level of the first excited singlet state ($S_0 \rightarrow S_1$). The molecule undergoes fast internal conversion (IC) to lower vibrational levels of the S_1 state, for instance, through interaction with solvent molecules. The excited singlet state can be deactived radiatively to the ground state (fluorescence, $S_1 \rightarrow S_0$) or can undergo nonradiative intersystem crossing (ISC) from the singlet state (S_1) to the triplet state (T_1 and T_2). The triplet state (T_1 and T_2) can be deactivated radiatively to the ground state (molecular phosphorescence (P)). Alternatively, the energy transfer (ET, nonradiative transition) takes place from the triplet state of the ligand to the central lanthanide ions (excited 4f state) in the so-called "antenna effect".[4, 13, 15, 16] After this indirect excitation (ET), the lanthanide ion may undergo a radiative transition to a lower 4f state by characteristic line-like photoluminescence or may be deactivated by nonradiative processes.[4, 13, 15, 16]

In this way, the luminescent quantum yield (ϕ) is an important parameter for evaluation of the efficiency of the emission process in luminescent compounds, for instance,

luminescent complexes. The quantum yield is defined as the ratio of the number of emitted to absorbed photons according to the equation 1.[16, 17]

$$\Phi = \frac{number\ of\ emitted\ photons}{number\ of\ absorbed\ photons} \quad (1)$$

One method to determine the luminescent quantum yield consists on determine the relative quantum yield (ϕ'). In this case, the quantum yield of unknown sample is compared with that of the reference sample, in solution, according to the equation 2.[16, 17]

$$\Phi' = \left(\frac{Abs_R}{Abs_S}\right)\left(\frac{Em_S}{Em_R}\right)\left(\frac{n_S}{n_R}\right)^2 \Phi_R \quad (2)$$

Where, Abs is the absorbance at the excitation wavelength, Em is emission intensity, and n is the refractive index of the solvent used. Subscripts R and S refer to the reference and the unknown, respectively.[16, 17]

The energy gap between the excited state of the ligand and that of the lanthanide ion determines whether or not effective energy transfer takes place. For efficient energy transfer, the lowest energy triplet state of the sensitiser must be higher than (1000-2000 cm^{-1}) the lowest excited state (emitting state) of the lanthanide ions.[13, 18] Botelho and co-workers reported the synthesis, characterization and study of photophysical properties of a nine-coordinate Eu^{3+} complex based on the tridentate 4-(4'-tert-butylbiphenyl-4-yl)-2,2'-bipyridine-6-carboxylic acid ligand. This complex contains three tridentate ligands acting as an efficient sensitizer avoiding the coordinated water and solvents in the first coordination sphere. Besides that, it exhibits one of the highest quantum yield values in solution (ϕ = 85 %) and a long excited-state lifetime (τ = 1.8 ms).[19] Xiao and co-workers described the design, synthesis and applications of two new lanthanide complexes, ANMTTA-Eu^{3+} and ANMTTA-Tb^{3+} {ANMTTA, [4'-(4-amino-3-nitrophenoxy)methylene-2,2':6',2''-terpyridine-6,6''-diyl] bis(methylenenitrilo) tetrakis(acetic acid)} for the highly sensitive and selective luminescence detection of hypochlorous acid (HOCl) in aqueous media. These probes are almost nonluminescent due photoinduced electron transfer process (due the 4-amino-3-nitrophenyl moiety) but upon reaction with HOCl, the quencher moiety is rapidly cleaved from the probe

complexes, which affords strongly luminescent lanthanide complexes HTTA-Eu^{3+} and HTTA-Tb^{3+} {HTTA, (4'-hydroxymethyl-2,2':6',2''-terpyridine-6,6''-diyl) bis(methylenenitrilo) tetrakis(acetic acid)}, accompanied by the remarkable luminescence enhancements.[20]

In this way, several organic ligands have been used to design efficient luminescent lanthanide complexes.[5, 16, 21] Among the several organic ligands that have been used β-diketone ligands display high molar absorption coefficients (~10^6 M^{-1} cm^{-1}) and stability constants. Besides that, the synthesis of lanthanide complexes using these chromophores is relatively easy, leading to the complexes with excellent luminescent properties.[16] Malta and co-workers described the synthesis, characterization and spectroscopic properties of the $[Eu(TTA)_3.2(DBSO)]$, (TTA = 2-thenoyltrifluoroacetonate and DBSO = dibenzyl sulfoxide), a complex highly luminescent under ultraviolet excitation.[15]

Andreiadis and co-workers[22] reported the synthesis of new octacoordinated ternary beta-diketonates of europium and terbium using an anionic tetradentate terpyridine-carboxylate ligand (2,2':6',2''-terpyridine-6-car- boxylate, L) as a sensitizer of lanthanide luminescence with two beta-diketonates ligands TTA^- for Eu^{3+} and trifluoroacetylacetonate ($TFAC^-$) for Tb^{3+}. These complexes showed high stability in solution and high luminescence quantum yield (66 % for Eu^{3+} complex). Furthermore, these complexes were incorporated in polymer matrixes leading to highly luminescent flexible layers with luminescence quantum yield up to 62 %. Recently, Lima et al.[23] showed a new and fast way to synthesize beta-Diketonate ternary europium complexes without $Eu(\beta\text{-diketonate})_3(H_2O)_2$ as an intermediate. The strategy consisted on adding non-ionic ligand (DBSO, DBM = 1,3-diphenylpropane-1,3-dione or PTSO = p-tolylsulfoxide, as L ligand) to the original salt, $EuCl_3(H_2O)_6$, to obtain the intermediates $EuCl_3(L)_4(H_2O)_n$, which were soluble in methanol or ethanol. Subsequently, the β-diketonate ligands are carefully added to the intermediate to obtain the final product $Eu(beta\text{-diketonate})_3(L)_2$. The usual synthetic route that takes a few weeks, can be carried out in days. Besides that, average overall yield up to 69 % obtained from this faster synthesis was significantly larger than the usual synthesis.

Despite the large number of visible emitting β-diketonates lanthanide complexes[15, 16, 24], fewer NIR-emitting lanthanides have been reported. This can be explained by the fact that the NIR emitting lanthanides exhibit lower excited state than the visible emitting lanthanides, requiring organic ligands with lowest excited state low enough to sensitize them ($^4F_{3/2}$ for Nd^{3+},

11257 cm^{-1}; $^2I_{13/2}$ for Er^{3+}, 6536 cm^{-1} and $^2F_{5/2}$ for Yb^{3+}, 10400 cm^{-1}), according to the representation of the diagram of the f–f energy levels in the figure 2.[13, 25]

Figure 2. Representation of the diagram of the f–f energy levels of Nd(III), Er(III) and Yb(III) up to ca. 20,000cm^{-1}. The energy levels from which NIR luminescence originates are marked in bold, and the main NIR emissions showed as descending arrows. Adapted from[25].

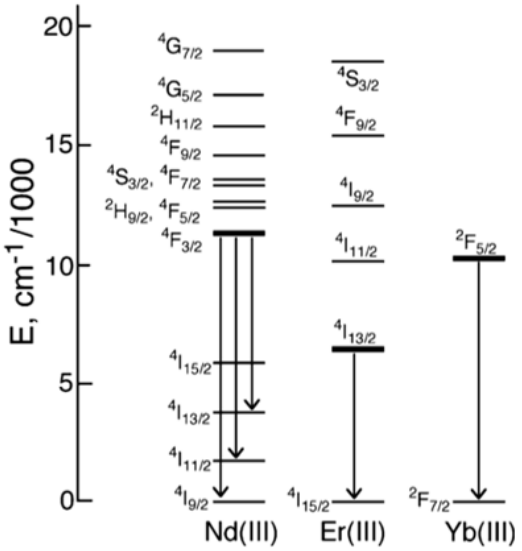

In this sense, some authors have described a series of lanthanide complexes of the type $[Ln(hfaa)_3(pz)_2]$ (Ln = La, Pr, Nd, Eu, Gd, Tb, Dy, Ho, Er, Tm and Yb; hfaa = anion of hexafluoroacetylacetone and L = pyrazole).[26] These complexes are volatile, which is advantageous for their use as precursors for high-performance lanthanide-based materials through chemical vapor deposition. Futhermore, the authors related that the environment around these metal ions was asymmetric, leading to increased radiative rates and luminescence efficiencies. Both ligands (hfaa and pyrazole) were good sensitizers for all the visible and NIR emitters except for Tb(III), Dy(III), and Tm(III), where pyrazole gave a negative effect (energy back transfer (BT)), due to poor intramolecular energy transfer match. Thus, the good luminescent properties make these NIR-luminescent complexes to have potential application in optical communication, telecommunications, and fluoroimmunoassays.[26] For instance, Woodward and co-workers[27] showed the synthesis of a fluorine-based donor-acceptor beta-diketone ligand to obtain a series of luminescent lanthanides complexes from visible- to NIR-emitting region. The preferred form (cis-enol) binds strongly to the lanthanide(III) ions (Ln = Eu, Sm, Dy, Tb, Yb, Nd, Er, and Gd) in the presence of phenanthroline,

which resulted in ternary tris(diketonates) complexes with 1,10-phenanthroline. The successfully sensitization by two photons (2P) excitation to access these complexes through the biological window (~800 nm), along with the delay of these long lifetime lanthanide luminescence emissions (from visible to NIR), displayed significant potential for applications in biomedical analysis (imaging and sensing) as luminescent probes.[27]

Nevertheless, NIR emitting Nd^{3+} and Yb^{3+} are rarely used in analytical detection or imunoassays. The visible emitting lanthanide complexes (as Eu^{3+} and Tb^{3+}) are widely used in this field due to their strong emission. However, most of these lanthanide complexes require excitation in the UV region, which is harmful for the biological systems. The aromatic residues of proteins and DNA absorbs in competition with the chromophores. In addition, the UV excitation cause damages in these biological systems. Moreover, biological tissues are opaque throughout most of the visible region.[13, 14] Three biological windows are described.[13, 14] The first one from 0.65 to 1.0 μm, the second one from 1.0 to 1.3 μm and the third one from 1.5 to 1.8 μm. Figure 3 shows the absorption spectrum of human skin (gray line) with light scattering contribution (dotted blue line) together with the three biological windows (BW) and the emission wavelengths of some lanthanide(III) ions.

Figure 3. Absorption spectrum of human skin (gray line) with light scattering contribution (dotted blue line), definition of biological windows, and emission wavelengths of some lanthanide(III) ions.[14]

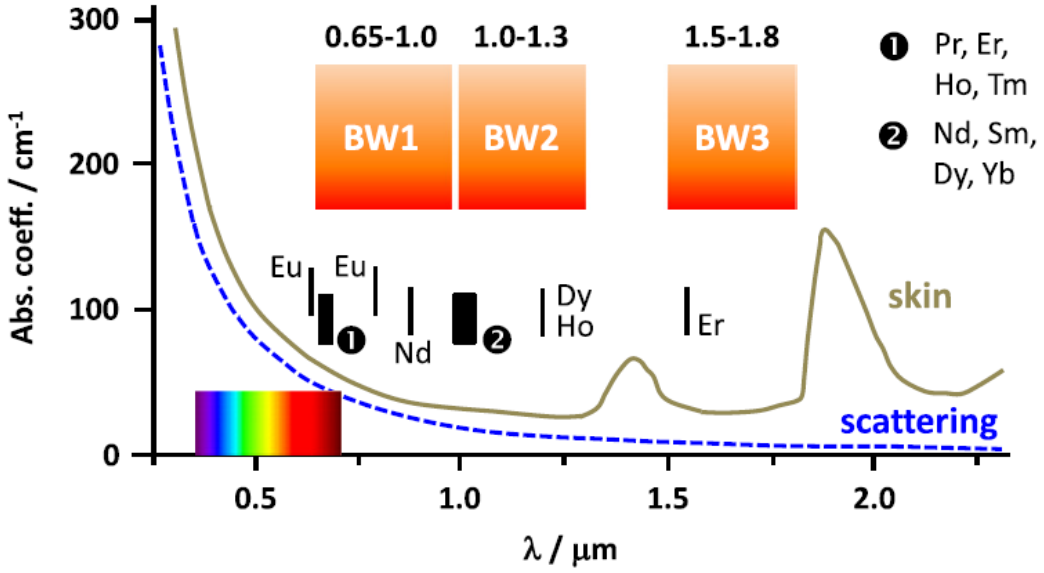

One of the strategies to overcome the limitations of UV absorbing by organelles, low transparency in the visible region and light scattering in order to achieve luminescent probes consists on using d-block chromophores as antenna groups to generate sensitized luminescence from Ln^{3+} ions with low energy f-f excited states.[13, 28, 29] Several transition metals such as Ru(II), Os(II), Fe(II), Pt(II), Au(I), Pd(II), Re(I), Cr(III), Co(III), Zn(II) and Ir(III) have been used to synthesize heterometallic complexes with lanthanide ions.[13, 25] The Ward group have extensively worked on synthesis and study of photophysical properties from d-chromophores as sensitisers in d-f heterobimetalic complexes. For instance, Shavaleev and co-workers[30] described a series of dinuclear platinum(II)—lanthanide(III) complexes, starting from a square-planar Pt(II) units. The $[(PPh_3)_2Pt(pdo)]$ (H_2pdo = 5,6-dihydroxyphenanthroline) or $[Cl_2Pt(dppz)]$ (dppz = 2,3-bis(2-pyridyl)pyrazine) units were connected to a $\{Ln(dik)_3\}$ unit ("dik" = 1,3-diketonate ligand and Ln = Nd, Yb, Er) through a diamine-type binding sites present in the Pt(II) units. All complexes displayed excitation bands from 440 to 520 nm (characteristic of Pt—centred absorption band), which resulted in a NIR luminescence from the Nd, Yb and Er centres (in solid state and CH_2Cl_2 solution). These results demonstrated that Pt antenna chromophores can be used as sensitisers, via energy transfer processes and using bridging ligands, to achieve NIR luminescence from the lanthanide units. Kennedy and co-workers synthesized luminescent transition metal complexes based on Re(I) and Pt(II) units. The $[Re(CO)_3Cl(bppz)]$ and $[Pt(CC–C_6H_4CF_3)_2(bppz)]$ [bppz = 2,3-bis(2-pyridyl)pyrazine] centres possesses a diimine binding sites available to coordinate $\{Ln(dik)_3\}$ (Ln = Pr, Nd, Er, or Yb) fragment and then, to obtain heterodinuclear d-f complexes. The photophysical properties were evaluated and the sensitization of the lanthanide(III)-based luminescence in the NIR region was achieved according to the quenching of the ^{3}MLCT (MLCT = metal-to-ligand charge transfer) luminescence, ascribed to the Pt(II) or Re(I) units emission. The degree of quenching of the ^{3}MLCT luminescence was achieved from luminescent and UV/Visible measurements, according to the nature of the Ln(III) unit. For all complexes, the Nd(III) unit was found to be the most effective at quenching the ^{3}MLCT luminescence of the d-block components. This can be explained by the high density of f–f excited states of suitable energy that make it an effective energy-acceptor. Shi, Zou and co-workers[31, 32] have shown the synthesis of four heterobinuclear Zn(II)—Ln(III) complexes using benzimidazole-based ligand (H_2L: 2-(1H-benzo[d]imidazol-2-yl)-6-methoxyohenol) and $Ln(NO_3)_3{\cdot}6H_2O$ to obtain $[ZnLn(HL)_2(Py)(NO_3)_3]$

(Ln = Nd, Yb, Er and Gd). Their photophysical properties displayed strong and characteristic NIR luminescence of Nd^{3+} or Yb^{3+} ion with emissive lifetimes in microsecond range, which were sensitized from the excited state (^{1}LC and ^{3}LC) of the benzimidazole-based ligand.

Typically, Ru(II), Os(II), Re(I) and Ir(III) are used to sensitize NIR emitting lanthanide ions through a strong absorption of light in the visible region by ^{3}MLCT excited state. These d-block chromophores act as a good energy donors due to the relatively low lying ^{3}MLCT states and efficient energy transfer to NIR emitting Ln^{3+} (Pr^{3+}, Nd^{3+}, Er^{3+} and Yb^{3+}). Therefore, the design and assembly of heterobimetallic complexes based on d-block metalloligands with NIR lanthanide luminescence have become a hot topic in the recent years according to the possibility of application in non-invasive bio-analysis and bio-imaging.[13] Li and co-workers[33] have introduced the synthesis of four novel Ir(III)–Ln(III) heteronuclear coordination polymers $\{Ln[Ir(ppy)_2(dcbpy)]_2(OH)\}.H_2O$ (Ln = Gd, Yb, Er, Nd, ppy = 2-phenylpyridine, dcbpy = 2,2'-bipyridine-4,4'-dicarboxylate) obtained by hydrothermal reactions. In these systems, the Ir unit acts as a good light-harvesting antenna showing high visible light absorption via ^{3}MLCT, and effectively sensitizes Ln(III)-based NIR luminescence (d→f energy transfer from the Ir unit to the Ln^{3+} ions). These coordination polymers displayed characteristic NIR emission of Ln(III) ions when excited by 500 nm visible light, while the characteristic ^{3}MLCT luminescence of the Ir unit was almost quenched. The Ir(III)–Nd(III) polymer exhibited the maximum quenching of the ^{3}MLCT luminescence. The Nd(III) ion was the most effective energy-acceptor due to the high density of low-lying f–f states. Besides that, the coordination polymer structures of Ir–Ln reduced the effect of high-energy oscillators (O–H, C–H) and further increased the Ln(III)-based emission lifetimes and quantum yields. These results suggested that the Ir unit is an attractive candidate for visible light harvesting antenna to effectively sensitize Ln(III)-based NIR luminescence. Chen and co-workers[34] have reported the synthesis of d-f bimetallic complexes using the (N^O)(N^O) bridging ligand (5-bromopyrimidine-2-carboxylic acid; bpmc) to connect the Ir(III) and Ln(III) centers. So, a series of d−f bimetallic complexes $Ir(pdt)_2(\mu\text{-}bpmc)Ln(TTA)_3$ (pdt = 1,3-dimethyl-5-phenyl-1H-[1,2,4]triazole and Ln = Nd, Yb, Er, Gd) were achieved. From Crystallographic analyses, very short spatial distances between the d−f centers (about 6 Å) were obtained and photophysical studies demonstrated that the energy level of the Ir(III) chromophore was suitable to sensitize the NIR lanthanide ions. Energy transfer rates

values from IrIII-NdIII, IrIII-YbIII, and IrIII-ErIII were 3.6 x 10^9, 2.8 x 10^8, and 4.0 x 10^8 s^{-1}, respectively.

Recently, the Ward group have introduced the heteronuclear d-f complexes as molecular probe in biological media.[35–37] Firstly, a new rigid and conjugated ligand structure connecting phenanthroline and poly(amino-carboxylate) binding sites have provided d–f complexes based on a strongly phosphorescent Ir(III) unit connected to a water-stable Gd(III) unit. This complex displayed a long-lived luminescence which can be used in PLIM imaging under one-photon or two-photon excitation, and a long relaxivity from a single Gd(III) centre as a consequence of the rigid design. So, for the first time, the combination of both Ir(III) and Gd(III) centres showed high potential for use in dual (luminescence + magnetic resonance) imaging. The optimization of d-f energy transfer processes in the isostructural have been discussed and, in this case, the dual- luminescent was of interest for applications as imaging and white-light emission.[35] In this way, the utilization of the above mentioned binuclear Ir(III)—Eu(III) complex for cell imaging using two independent emission components was reported. The Ir(III)—Eu(III) complex was observed to be water-stable and permeable to the cells. Besides that, the binuclear complex in the cell media underwent partial Ir→Eu energy transfer following two-photon excitation of the Ir unit (at 780 nm). The excitation in the NIR region generated simultaneously green Ir-based emission and red Eu-based emission from the same probe with lifetime values in different orders of magnitude (Ir(II) = μs; Eu = 0.5 ms) that allowed them to be identified by time-gated detection. Phosphorescence lifetime imaging microscopy (PLIM) measurements allowed the lifetime of the Ir-based emission to be measured and, simultaneously, the cells were imaged by using Eu-based emission component at longer timescales. This new approach allowed autofluorescence-free, time-resolved imaging and lifetime mapping in cell media under two-photon excitation, with submicron spatial resolution, on a timescale orders of magnitude longer than fluorescence.[36] Sequentially, heterotrimetallic Ir_2(III)—Ln(III) complexes (Ln = Gd and Eu) have been described and their luminescence cell imaging have been compared to the heterobimetallic Ir(III)—Ln(III) complexes previously described. The binuclear (Ir(III)—Ln(III)) complexes performed best in cellular studies, exhibiting good solubility in aqueous solutions, low toxicity after 4 and 18 h, respectively, and punctate lysosomal staining. Variations in luminescence lifetime (in Ir(III)—Gd(III) complex) allowed it to be used as a sensor toward molecular oxygen, an important

biological analyte, in solution and *in vitro*. To do this, the emission lifetime of Ir(III)—Gd(III) complex was investigated under increasing concentrations of O_2 in aqueous solution, in full cell media, using single-photon PLIM, and in fixed HeLa cells, using two-photon PLIM. So the lifetime of the Ir(III)-based luminescence was successfully used as a probe for the oxygen concentration in cells under *in vitro* conditions. Thus, this complex provided an excellent platform to optimize a dual-imaging oxygen- sensitive probe.[38]

1.1. Ru(II) complexes as sensitizer for NIR lanthanide luminescence

Ru(II) polypyridyl complexes have been studied due to the unique photochemistry and photophysics.[39] $[Ru(bpy)_3]^{2+}$ possesses a wide and strong absorption in the visible region (up to 500 nm) and a low triplet state (E_T = 17400 cm^{-1}) that can allow NIR lanthanide ions to be efficiently excited. Besides that, the metal-to-ligand charge transfer (MLCT) excited states (absorption bands in the visible) can be achieved through two-photons absorption (TPA).[39, 40] Figure 4 shows some examples of Ru(II) and dinuclear Ru(II)—Ru(II) complexes that can be excited by TPA.

Figure 4. Chemical structures of some Ru(II) and dinuclear Ru(II)—Ru(II) complexes with Two-Photon Absorption (TPA).[40–42]

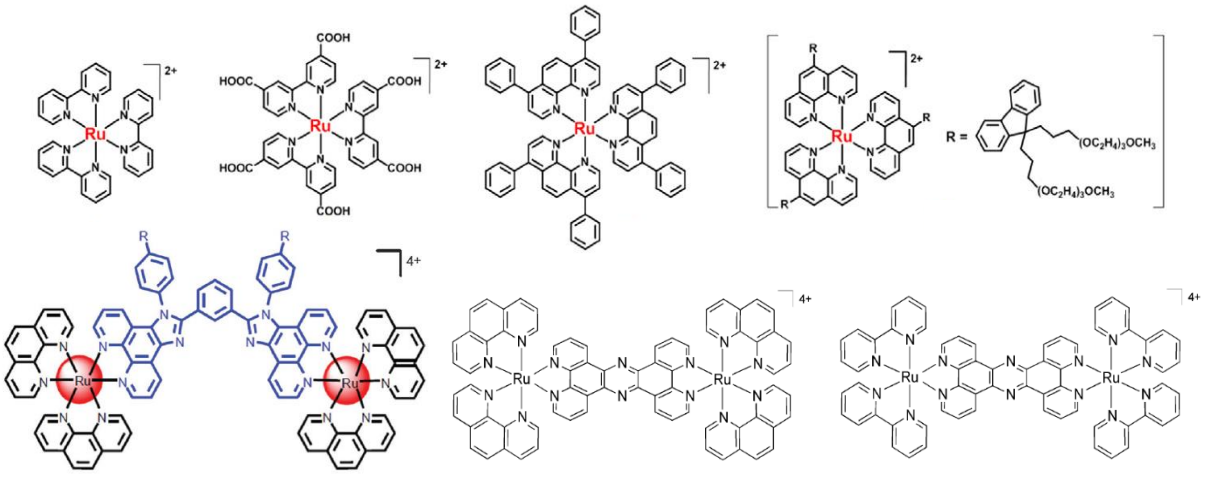

Greenough and co-workers[43] have investigated the photodynamics of a ruthenium(II) polypyridyl complex, a cis-$[Ru(bpy)_2(NA)_2]^{2+}$ (NA = nicotinamide, pyridine-3-carboxamide) activated through two-photon absorption (TPA) or one-photon absorption (OPA). Using the

TPA (620-1000 nm) or OPA (465 nm) the authors described that the dynamics processes were identical, showing that TPA prodrug design may use knowledge gathered from the more numerous and easily conducted OPA studies. In this way, luminescent emission of a great number of Ru(II) polypyridyl complexes can be achieved by one- or two-photons absorption.

Alternatively, great effort have been carried out to modify the 2-2'-bipyridine (bpy) ligands towards more efficient coordination with lanthanide ions. In this way, bridging ligands have been used to obtain Ru(II)—Ln(III) bimetallic species and promoting efficient electron and energy transfer processes. Some *d-f* heterobimetallic (Ru—Ln) complexes connected by some types of bridging ligands have been described according to the figure 5.

Figure 5. Some examples of Ru(II)—Ln(III) heterobimetallic complexes displayed in the literature.[13, 28, 44, 45]

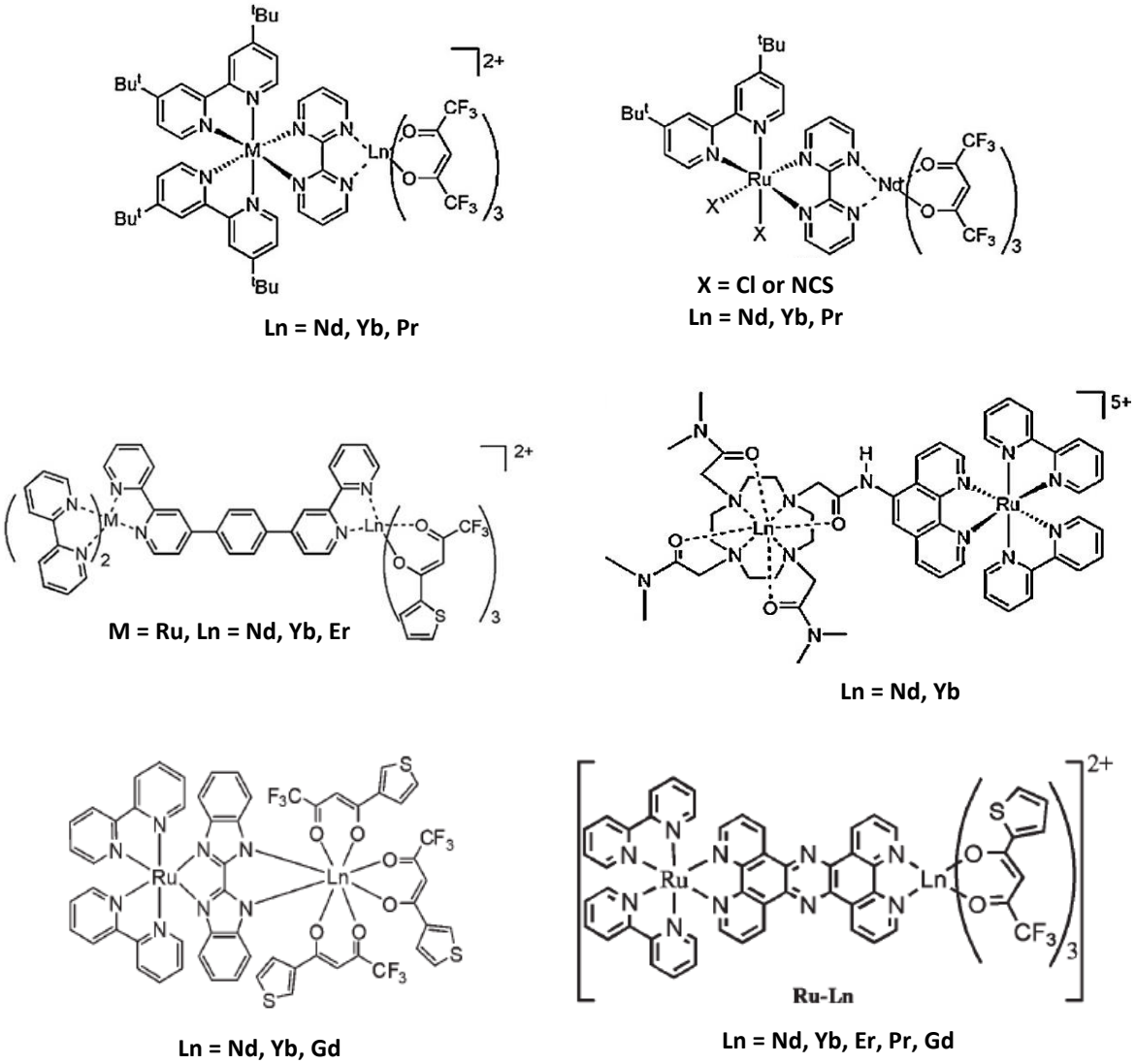

Lazarides and co-workers[28, 29] have studied energy transfer (ET) processes from $[M(bpy)_3]^{2+}$ (M = Ru, Os) chromophores to Ln III ions with low energy f-f states (Ln = Yb, Nd, Er) in *d-f* bimetallic complexes using saturated $–CH_2CH_2–$ spacer, a *p*-C_6H_4 spacer and a *p*-$(C_6H_4)_2$ spacer. The d-f ET is much faster across a conjugated *p*-C_6H_4 spacer than across a shorter CH_2CH_2 spacer. The dominant mechanism was a Dexter-type ET involving electronic coupling mediated by the bridging ligand orbitals. The distance dependence also was evaluated for Ru→Nd ET across different conjugated spacers (*p*-C_6H_4 spacer and a *p*-$(C_6H_4)_2$ groups). In the more extended unsaturated complex [Ru(*p*-$C_6H_4)_2$—Nd)] the ET is less effective because of the great distance involved and the consequent attenuation of other EnT mechanism (electronic coupling).[28] Complexes contain $[M(bipy)^3]^{2+}$ (M = Ru(II), Os(II))chromophores with a pendant aza-18-crown-6 macrocycle (labeled RuL and OsL) for binding of lanthanide(III) ions have been synthesized and described according their photophysical properties. The RuL—Ln and OsL—Ln heterobimetallic complexes were prepared by addition of excess $Ln(NO_3)_3$ (Ln = Nd, Yb) to the solutions of RuL and OsL (in MeCN) and then, the photophysical properties were evaluated using time-resolved and steady-state luminescence methods. The RuL chromophore acted as an energy-donor Nd(III) with a energy-transfer rate constant (k_{ET}) of 6.8 x 10^6 s^{-1}. However, the energy transfer from RuL→Yb(III) can not be observed. In contrast, OsL complex acted as a good sensitizer for both Yb(III) and Nd(III) units, but with faster EnT rate to Yb(III), with k_{ET} of 2.6 x 10^7 s^{-1} than to Nd(III), which showed k_{ET} of 1.4 x 10^7 s^{-1}. The d→f energy transfer in both cases was faster for OsL than for RuL. These difference was ascribed to contributions from the Förster and Dexter mechanisms for energy-transfer in RuL—Nd and OsL—Nd, using calculated spectroscopic overlap integrals coupled with molecular modelling to estimate inter-chromophore separations. The high energy transfer rater in OsL—Yb was explained in terms of the redox mechanism involving an initial *Os(II)→Yb(III) photoinduced electron transfer step generating an Os(III)/Yb(II) state. This redox mechanism was favourable for OsL—Yb but not for complex. The RuL in the RuL—Yb complex acted as a poor excited-state electron-donor by about 0.1 eV.[29]

A series of heterobimetallic complexes of $[Ru(bpy)_2(tpphz)Ln(TTA)_3](PF_6)_2$ (tpphz = tetrapyrido[3,2-a:2’,3’- c:3’’,2’’-h:3’’’,4’’’-j] phenazine; Ln = Er(III), Nd(III), Yb(III) and Gd(III)) have been synthesized by attachment of a $[Ln(TTA)_3]$ units at the vacant diimine site in $[Ru(bpy)_2(tpphz)](PF_6)_2$ complex. The photophysical properties of the *d-f* complexes were

evaluated in solid state and in solutions (CH_2Cl_2 and Tris-HCl buffer solutions). According to Wei and co-workers[44], sensitized NIR luminescence was obtained from Nd and Yb centres following excitation of the d-block Ru(II) unit. Effective Ru→Ln energy transfer was achieved by Nd(III) and Yb(III) but not for Er(III) units. The greater values of energy transfer rate constant and quantum yield of energy transfer (Φ_{ET}) were reached by Ru—Nd complex, in solid state (k_{ET} = 6.18 x 10^6 s^{-1}, Φ_{ET} = 63 %) and in solution (CH_2Cl_2 solution: k_{ET} = 5.35 x 10^6 s^{-1}, Φ_{ET} = 65 %; Tris HCl buffer solution: k_{ET} = 4.26 x 10^6 s^{-1}, Φ_{ET} = 57 %). Interestingly, the NIR luminescence intensity of the Ru—Nd complex decreased in the presence of alpha-fetal protein (AFP), in Tris-HCl buffer solution. A novel NIR luminescent method for the determination of AFP was developed with several advantages as good selectivity, stability and rapidity. Additionally, the present method of detection can prevent the interference of the luminescence of the biological background and reduce the damage in biological samples, thus the proposed NIR luminescent method based on Ru—Nd complex, providing a potential sensor for AFP detection in clinical diagnosis and biomedical applications.

Singaravadivel and co-workers[46] have described the synthesis of new luminescent ruthenium(II) complex using the bibenzimidazole ($BibzImH_2$) group as ligand. The $[(bpy)_2Ru(BibzImH_2)]^{2+}$ possesses a vacant diimine site that was used to prepare three new heterobimetallic Ru—Ln complexes by attaching a $\{Ln(TTA)_3\}$ unit (Ln = Nd, Yb, or Er) at the vacant site. The $BibzImH_2$ is a short bridging ligand that favoring the efficient and faster energy transfer from Ru(II) to Ln(III) units. Photophysical properties were evaluated and from lifetime and luminescent measurements, it was possible to achieved Ru(II)→Ln(III) energy transfer rates of 2.4 x 10^8 s^{-1} (to Nd, Φ_{ET} = 97%), 1.2 x 10^7 s^{-1} (to Er, Φ_{ET} = 63%) and 7.1 x 10^6 s^{-1} (to Yb, Φ_{ET} = 49%). The donor-acceptor overlap decreases (from Nd > Er > Yb) due to the reduced availability of f-f states on the Ln(III) ions. Recently, Zhang and co-workers[45] have designed four Ru(II)/Ir(III) metalloligands from polypyridine and bibenzimidazole (BiBzIm) organic ligands, which showed strong visible light absorption via MLCT transitions. Nd(III), Yb(III) and Gd(III) complexes were coordinated on these Ru(II)/Ir(III) metalloligands and twelve Ru(II)—Ln(III) bimetallic complexes were obtained. The ^{3}MLCT states of the metalloligands (Ru(II)/Ir(III)) in the visible-light region can sensitize the Ln(III)-centered NIR emissions. The energy transfer rate for the Ru(II)/Ir(III)—Nd/Yb(III) complexes was estimated to be within 0.2-20 × 10^7 s^{-1}. As already discussed, Nd(III) complexes have a faster energy transfer rate (in the

most of complexes) due to the fact that Nd(III) has a higher density of f-f excited states between 10 000 and 15 000 cm^{-1} compared with Yb(III), and can be a better energy acceptor from d-block Ru(II)/Ir(III) units. Long lifetimes on a μs scale and high quantum yields up to 1% were obtained in these complexes (by monitoring the lanthanide emission), suggesting that the Ru(II)/Ir(III) metalloligands can be used as a good visible light harvesting antenna to efficiently sensitize the NIR-emitting lanthanide.

The 2,2'-bipyrimidine (bpmd) is one of the classical bridging ligands used to synthesize heterobimetallic complexes. This planar heterocycle easily coordinate two metal centers through four nitrogen sites in order to keep the metal-metal in short distance acting as an efficient channel for electrons and energy transfer from d-block chromophores in the visible region to the NIR lanthanide luminescence.[47–51] Heteronuclear bipyrimidine-bridged Ru—Ln compounds have been developed by Lazarides and co-workers.[52] $[Ru(^tBu_2bpy)(bpmd)X_2]$ (X = Cl, NCS) and $[M(^tBu_2bpy)_2(bpmd)][PF_6]_2$ (M = Ru, Os) polypyridine-type chromophores were successfully synthesized and then connected to a {Ln(diketonate)$_3$} (Ln = Pr, Nd, Yb or Gd) via 2,2'-bipyrimidine (bpmd) as bridging ligand. The d-blocks chromophores showed a low-energy LUMO (Lowest Unoccupied Molecular Orbital) arising from the presence of a bpmd ligand, and consequently have lower energy ^{1}MLCT and ^{3}MLCT states than analogous complexes of bpy. For the $[Ru(^tBu_2bpy)_2(\mu\text{-bpmd})Ln(diketonate)_3][PF_6]_2$ heterobimetallic complexes, the ^{3}MLCT energy of 13 500 cm^{-1} allowed EnT to Yb(III) and Nd(III) resulting in sensitised NIR luminescence.

Energy transfer from organic ligands is well discussed in[4]. In the case of bimetallic compounds where both donor and acceptor components are connected by conjugated bridging ligands, long-range donor-acceptor electronic coupling can occur through an indirect super-exchange process mediated by the orbitals of the bridging ligand which can occur over substantial distances.[28, 53]

To confirm the energy transfer processes in *d-f* heterobimetallic complexes, the luminescent lifetime of the ^{3}MLCT emission was determined and then, used to quantify the energy transfer rate according to the equation 3.[28, 53]

$$k_{ET} = 1/\tau_q - 1/\tau_u \quad (3)$$

where k_{ET} is the energy transfer rate constant and τ_q and τ_u are the lifetime in the presence of a "quencher" (Ru(II) chromophore after coordination with Ln^{3+}) and the "unquenched" lifetime (Ru(II) chromophore beforer coordination with Ln^{3+}). The quantum yield of energy transfer (Φ_{ET}) can be calculated according to the equation 4.

$$\Phi_{ET} = 1 - \tau_q/\tau_u \quad (4)$$

Energy transfer rates constant have been used to establish the energy transfer mechanism in solution in rigid systems where the chromophore lanthanide separation (r) is well defined.[53] The quantum yield of energy transfer (Φ_{ET}) have been calculated to determine the efficacy of energy transfer from Ru(II) chromophore to NIR emitting Ln(III).

1.2. Luminescent silylated complexes and silica-based nanohybrids

Despite some examples of d-f (Ru-Ln) heterobimetallic complexes being reported, their use as biosensors or biomarkers is seldom discussed. Low water solubility and stability and relatively weak luminescence may be the main reasons.[44] Rocha and co-workers[54, 55] have proposed a way to overcome these drawbacks by using mesoporous silica spherical particles to encapsulate metallic complexes as $Eu(fod)_3$ (fod = 6,6,7,7,8,8,8-heptafluoro-2,2-dimethyl-3,5-octanedionato) into mesoporous channels. The excellent luminescent properties of the silica-based hybrids and the successfully encapsulating processes offering the possibility of applications as red emitters in the LED (Light Emitting Diode) field. Botelho and co-workers[56] have described luminescent materials based on the incorporation of the highly emissive Eu^{3+} bypiridine-carboxyl complex $Eu[4\text{-}(4'\text{-tert-butyl-biphenyl-4-yl})\text{-}2,2'\text{-bipyridine-6-carboxyl}]_3$ in the pores of MCM-41 and xerogel (SGIL) matrices, as well as in their phenyl-modified hybrid derivatives (MCM-Ph and SGIL-Ph, respectively). Incorporation of important quantities of the complex were achieved for both hybrids with phenyl groups that suggesting efficient immobilization of the complex by π–π interactions. Long excited state lifetimes (up to 1.7 ms) and high quantum yields (up to 65 %) relating to the complex were obtained for the hybrids, suggesting the potential use of thin films for lighting and bioanalytical applications.

In this way, mesoporous silica matrix have been extensively investigated due to the versatile physicochemical properties such as wide availability, rich functionality and good biocompatibility.[57–59] In particular, mesoporous silica nanoparticles (MSNs) have several attractive features for application as nanosensors or nanomarkers in biological systems, such as high surface area, tailorable pore sizes, controllable particle sizes and shapes, and dual-functional surfaces (exterior and interior).[54, 58, 59] In general, the loading of pharmaceutical drugs, dyads and luminescent phosphors inside the pores of MSNs can prevent their premature release, degradation and desactivation effects before reaching their designated target.[54, 58, 59] Thus, MSNs could be used as drug-delivery vehicles, luminescent sensors, cell markers, photocatalysts, carriers of molecules, for photodynamic therapy, among others.[54, 57–61]

As an alternative to explore the potential of the heterobimetallic complexes and the advantages of the silica matrix, in biological applications, silylated organic ligands have been proposed. Nakahara and co-workers[62] have designed a silylated Terbium(III) complex using the 3-aminotriethoxysilane (APTES) as anchoring group to prepare a novel fluorescent nanohybrids (Tb-SNPs) obtained by reverse micelle method (Water/Oil reverse microemulsion). The luminescent properties of covalently linked terbium complexes in silica nanoparticles were evaluated and showed remarkable photochemical and pH stability. Besides that, high dispersion under physiological conditions and relatively high fluorescence lifetime were also achieved. This nanohybrids were used in cells imaging as a green fluorescent label. Zhang and co-workers[63] have described the synthesis of silylated $[Ru(Phen)_3(Phen\text{-}Si)]^{2+}$ complex and the subsequently grafting onto the sol–gel derived ormosil network (Ru-ORMOSIL). Luminescence oxygen sensing and luminescence temperature sensing properties of the hybrids were investigated. The hybrids obtained by covalent grafting onto the matrix showed oxygen sensing properties superior to the properties of the conventionally physically-incorporated hybrids. Besides that, great luminescence temperature sensing was achieved by the Ru-ORMOSIL hybrid.

De Oliveira and co-workers[64] have introduced a route to obtain highly luminescent silica-based nanomaterials. First, the dibenzoylmethane (DBM) ligand was modified by ethoxysilyl groups to achieved DBM-Si ligands. This silylated ligand was grafted onto mesoporous silica. After that, the Eu^{3+} ions were added and coordinated to the DBM-Si

modified-silica. Two equivalent of DBM ligand was added to obtain the SiDBM-Eu$(DBM)_2$ complex grafted onto mesoporous silica. Luminescent properties were evaluated and confirmed that the method leaded to highly red luminescent nanomaterials. A similar route have been described by Sun and co-workers.[65] NIR-luminescent hybrids were synthesized by grafting of phen-Si (phen-Si = 5-(N,N-bis-3-(triethoxysilyl)-propyl)ureyl-1,10-phenanthroline) onto ordered mesoporous materials MCM-41 and SBA-15. Afterwards $Ln(DBM)_3.2H_2O$ complexes (Ln = Er, Nd, Yb) were added. The influence of the varying the host matrix was discussed according to the luminescent properties. Both hybrids labeled $Ln(DBM)_3$phen-MCM-41 and $Ln(DBM)_3$phen-SBA-15 displayed excellent NIR-luminescent properties. The Readdy group[66, 67] has shown the synthesis of silylated β-diketones ligands (using 3-(triethoxysilyl)propylisocyanate groups), and then the grafting onto mesoporous silica (MCM-41). Eu^{3+} ions were added to coordinate at the site in the mesoporous silica modified, and after that, phenanthroline-type ligand was added leading to Eu(β-diketone-Si)$_3$phen/MCM-41 red emitting hybrids with longer lifetimes and better thermal stability than the precursor complexes.

Ilibi and co-workers[68] have introduced the synthesis of luminescent hybrid material by grafting of a Eu^{3+} bipyridine carboxylate complex inside the pores of the mesoporous silica matrix (MCM-41). The strategy consisted on first grafting of the mesoporous silica using the alkoxisilyl groups 3-aminopropyltriethoxysilane (APTES) and after the hexamethyldisilazane (HMDSA), and further processed to covalently attach a bipyridyl di-carboxylic acid ligand. Exposure of this material to Eu^{3+} solution and subsequent addition of a monocarboxylic acid ligand was performed to immobilize the 9-coordinated Eu^{3+} complex in the pore walls of MCM-41. The authors showed that the completion of the coordination sphere by subsequent addition of a monocarboxyl ligand was probably not fully accomplished in a homogeneous manner. In this way, the use of silylated ligands to synthesize silylated metallic complexes allows a clever strategy in order to graft silica particles surface. This strategy allows preventing the nonhomogeneous embedding and leaching of the luminescent complex in the host matrix.

Thus, Lechevallier and co-workers[69] have described the synthesis of two silylated ligands, the Phen-Si (Phen = 5-amino-1,10-phenanthroline and Si = 3-(triethoxysilyl)propyl isocyanate) and DBM-Si (DBM = dibenzoylmethane and Si = 3-chloropropyltrimethoxysilane). These silylated ligands were used to obtain silylated [Eu$(TTA)_3$(Phen-Si)] complex and

subsequently, two different ways of achieve new silica-based nanoplatforms for luminescent biolabeling. The first strategy consisted on grafting of the silylated Eu^{3+} complexes onto mesoporous silica nanoparticles and the second, the impregnation of the mesoporous silica nanoparticles with the Eu^{3+} complexes. The luminescent properties were evaluated and the best results were achieved for the nanohybrids obtained by grafting of $[Eu(TTA)_3(Phen\text{-}Si)]$ complexes. The best nanoplatform showed emission lifetime suitable for microsecond time gated detection of luminescence. The synthesis of some types of silylated bidentate ligands[70, 71] and the preparation of silylated Ruthenium(II)[72–74] and Europium(III)[71, 75, 76] complexes are presented in figure 6.

Figure 6. Silylated Bidentade Ligands (Bpy-Si, TTA-Si) and Ru(II) and Eu(III) Complexes.[70–76]

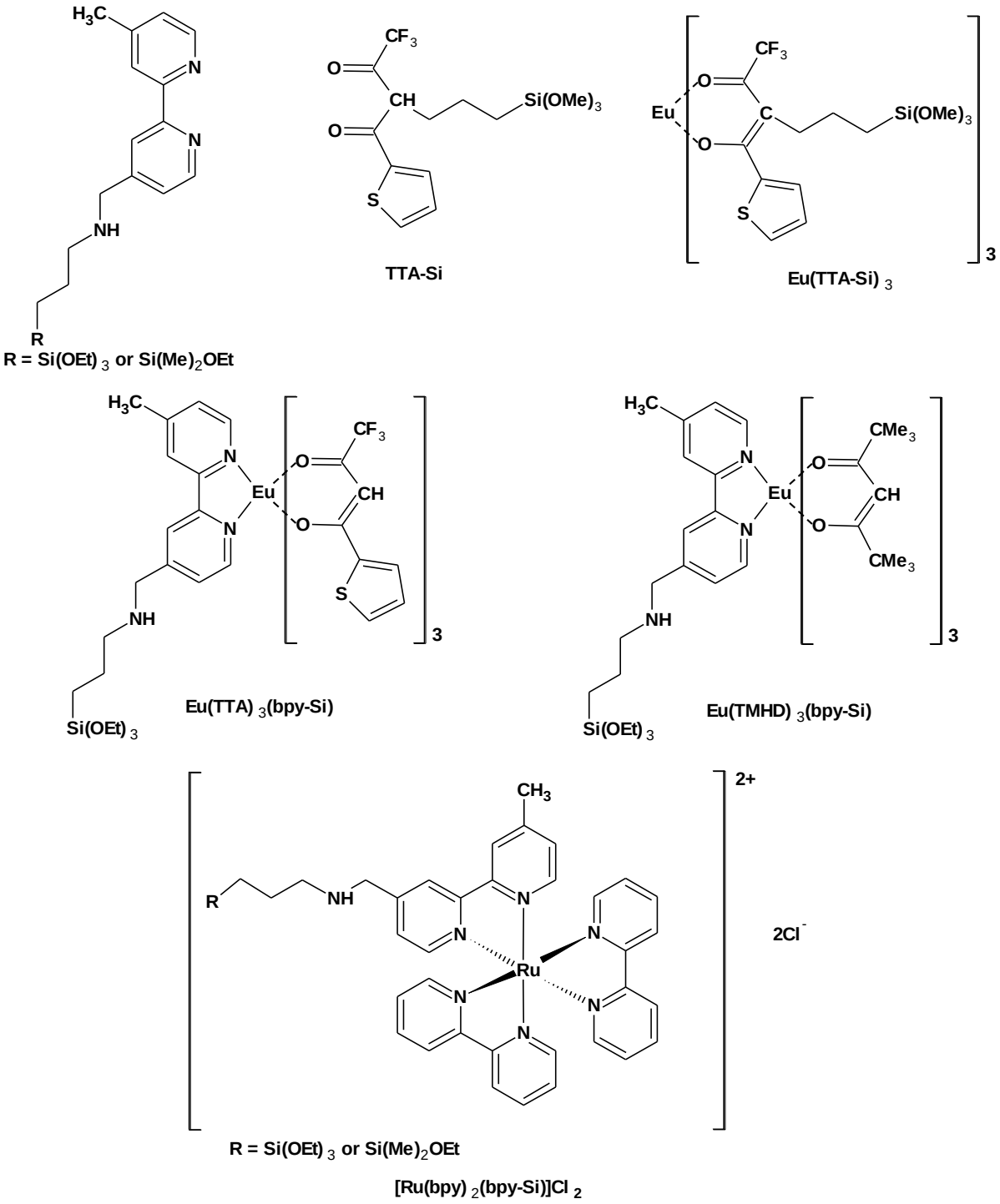

Duarte and co-workers[71, 76] have described the synthesis of beta-diketonate ligand displaying a trimethoxysilyl group (TTA-Si) as grafting function and, subsequently, a highly luminescent silylated Eu(III) complex [Eu(TTA-Si)$_3$] was obtained. The [Eu(TTA-Si)$_3$] was grafted on some types of matrix and high grafting ratios were obtained via this methodology. Furthermore, [Eu(TTA)$_3$(bpy-Si)] luminescent complex have been also synthesized, with organosilyldipyridine ligand modified by ethoxysilyl group (bpy-Si). The silylated complex was grafted inside the silica nanoparticles via covalent bonding. Thus, a new luminescent nanohybrid was developed with high surface area available. This nanocomposite was employed as selective imaging of *Escherichia coli* bacteria.[76]

This general methodology have been used to synthesize some types of Silylated Ru(II) complex. Mauline and co-workers[72, 73] have synthesized [Ru(bpy)$_2$(bpy-Si)]Cl$_2$ complexes and incorporating them via water/oil microemulsion in silica nanoparticles and grafting onto commercial silica nanoparticles. The bifunctional silica nanoparticles (obtained via water/oil microemulsion) were described as a new efficient tool for investigating complex biological systems such as *Pseudomonas aeruginosa* biofilms.[73]

In this way, we have proposed for the first time, the synthesis of *d-f* heterobimetallic complexes with the organic ligands modified by alkoxysilyl groups. Initially, we have synthesized a new [Ru(bpy)$_2$(bpmd)]Cl$_2$ (labeled **Ru**), [Ru(bpy)(bpy-Si)(bpmd)]Cl$_2$ (labeled **RuL**) and [Ln(TTA-Si)$_3$] (labeled **LnL3**) complexes. After that, we have obtained d-f complexes with Ln(III) complexes (Ln = Nd^{3+}, Yb^{3+}) modified by methoxysilyl groups (**Ru—LnL3**), and also d-f complexes with Ru(II) complexes modified by ethoxysilyl groups (**Ln—RuL**). Successful structural characterization of the silylated *d-f* heterobimetallic complexes are described and discussed in this thesis. Furthermore, luminescent and photophysical properties are examined and discussed with respect to the efficiency of energy transfer processes from Ru(II) complexes to the luminescent NIR-emitting lanthanide complexes aiming the grafting on host matrix (dense and mesoporous silica nanoparticles) as an eventual application in bioimaging detection systems.

2 – OBJECTIVES

2.1. General Objective

The aim of this research is to obtain new NIR luminescent system based on *d-f* energy transfer process for nanoprobes or nanomarkers applications. To achieve this objective, the work is divided into five sub-sections as follows:

2.2. Specific Objectives

1. Synthesis, characterization and study of luminescent properties of ruthenium(II), neodymium(III) and ytterbium(III) silylated complexes.

2. Synthesis, characterization and study of luminescence properties of four *d-f* heterobimetallic (Ru(II)—Nd/Yb(III)) silylated complexes.

3. Synthesis and characterization of mesoporous silica nanoparticles by direct micro-emulsion method.

4. Synthesis and characterization of silica-based nanohybrids obtained by grafting of silylated mononuclear or *d-f* heterobimetallic complexes on mesoporous silica nanoparticles and commercial dense silica (Ludox AS-40).

5. Study of the luminescence properties of the nanohybrids.

3 – EXPERIMENTAL SECTION

3.1 Synthesis

3.1.1. Ligands modified by alkoxysilyl groups

*3.1.1.1. Synthesis of 4-methyl-4'-(n-triethoxysilylpropyl)amine- methyl- 2,2'-bipyridine ligand (**bpy-Si**).*

The synthesis of the **bpy-Si** ligand was performed according to the methodology described by Menu and co-workers[70, 72], which consist in three steps:

4'-Formyl-4-ethyldipyridyl synthesis. 13.8 mmol (2.54 g) of 4,4'-dimethyl-2,2'-bipyridine was dissolved in dioxane (100 mL) and then, was added 13.8 mmol (1.53 g) of selenium dioxide. The solution was stirred and refluxing for 24h at 90 °C under N_2 atmosphere. The hot solution was filtrate and cooled at room temperature for 1h. After that, the mixture was filtered again and the solvent evaporated. The obtained powder was dissolved in ethyl acetate (300 mL) and added to a separation funnel. Extraction step was performed with sodium carbonate solution (0.1 mol.L^{-1}, 50 mL), and then three times with sodium bisulfite solution (0.2 mol.L^{-1}) at pH = 5. The resulting aqueous solution was basified to pH = 9, and the aldehyde extracted with dichloromethane (100 ml). The solvent was evaporated to obtain a white powder. Yield: 50 %.

4-Methyl-4'-(iminopropylethoxysilyl)-2,2'-dipyridine synthesis. 4.24 mmol of 4'-Formyl-4-ethyldipyridyl (0.840 g) was reacted with 4.24 mmol of 3-aminopropyltriethoxysilane (APTES, 0.999 mL) in 30 mL of anhydrous chloroform with constant stirring for 3h at room temperature (under N_2 atmosphere). The solvent was evaporated at low pressure, and the obtained colorless oil was washed three times with chloroform. Yield: 95 %.

*4-Methyl-4'-(methylaminopropylethoxysilyl)-2,2'-dipyridine (**bpy-Si**).* 1mmol (0.401 g) of 4-Methyl-4'-(iminopropylethoxysilyl)-2,2'-dipyridine was diluted in 50 mL of anhydrous ethanol and reacted with 3 mmol (0.114 g) of sodium borohydride at room temperature for 24h. A grey powder was obtained after the evaporation of solvent. Excess borohydride was then hydrolyzed with water (30 mL); and the product was obtained by three extractions with dichloromethane (50 mL). The organic phase was allowed to dry on sodium sulfate for 1h and

then was filtrated, and solvent was removed under low pressure. The **bpy-Si** ligand was obtained as a yellow oil ($C_{21}H_{33}N_3O_3Si$, MW: 403.59). Yield: 90 %.

Figure 7. Synthetic route of the 4-methyl-4'-(n-triethoxysilylpropyl)amine-methyl-2,2'-bipyridine ligand (**bpy-Si**).

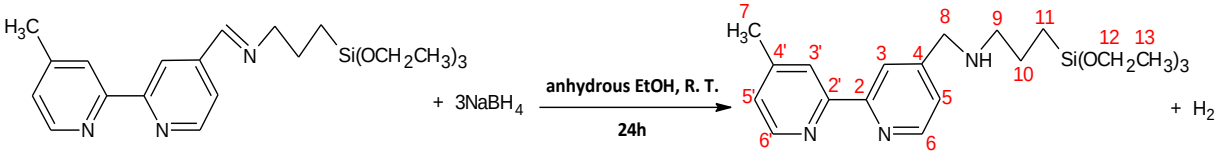

^{1}H NMR (δ ppm, $CDCl_3$): 0.65 (m, 2H, CH_2 (11)); 1.21 (t, 9H, CH_3 (14) , J = 7 Hz); 1.64 (m, 2H, CH_2 (10)); 2.41 (s, 3H, CH_3 (7)); 2.65 (m, 2H, CH_2 (9)); 3.79 (q, 6H, CH_2 (13) , J = 7 Hz); 3.89 (s, 2H, CH_2 (8)); 7.14 (d, 1H, CH (5'), J = 6 Hz); 7.33 (d, 1H, CH (5), J = 6 Hz); 8.24 (s, 1H, CH (3')); 8.33 (s, 1H, CH (3)); 8.54 (d, 1H, CH (6'), J = 6 Hz); 8.62 (s, 1H, CH (6), J = 6 Hz). Mass Spectrum: (DCI, NH_3): m/z 404 $[M]^+$.

*3.1.1.2. Synthesis of 4,4,4-Trifluoro-2-(3-(trimethoxysilyl)-propyl)-1-(2-thienyl)-1,3-butanedione ligand (**TTA-Si**).*

Figure 8. Synthetic route of the 4,4,4-Trifluoro-2-(3-(trimethoxysilyl)-propyl)-1-(2-thienyl)-1,3-butanedione ligand (**TTA-Si**).

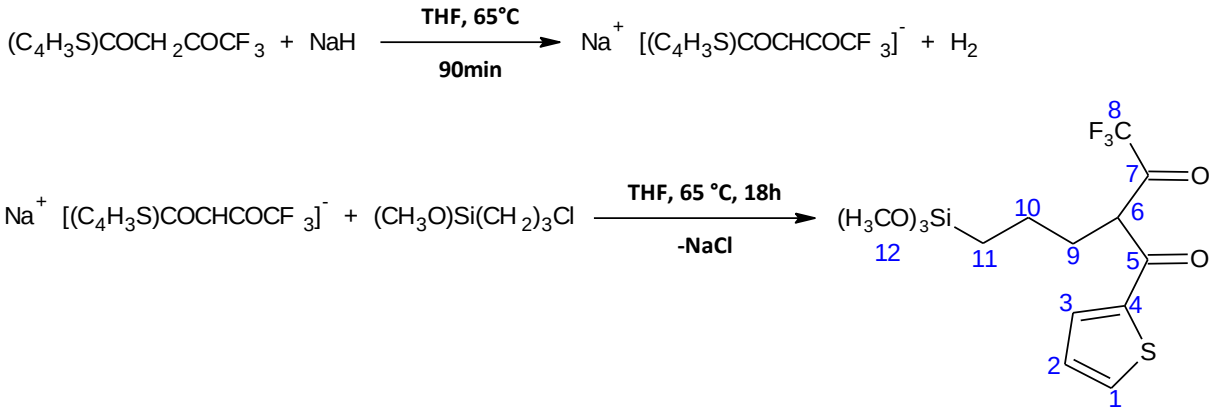

The silylated ligand (**TTA-Si**) was synthesized as described by Duarte and co-workers.[71, 77] Two mmol (444.36 mg) of 2-thenoyltrifluoroacetone (TTA) was added to 20 mL of anhydrous tetrahydrofuran under stirring, 2 mmol (48 mg) of sodium hydride was added and the mixture

was refluxed (65 °C) for 90 min, and then 2 mmol (371 µL) of 3-chloropropyltrimethoxysilane was added dropwise under stirring and reflux (65 °C) was maintained under nitrogen atmosphere for 18h. The solvent was evaporated; the product was dissolved in diethyl ether and filtered. The resulting solution was evaporated, leading to the solid yellow powder ($C_{14}H_{19}F_3O_5SSi$, MW: 384.44). Yield: 80%.

Elemental analysis for $C_{14}H_{19}O_5F_3SSi$, %, found (calcd): C 37.1 (43.7), H 3.5 (4.9). FTIR (KBr, cm^{-1}): 3108 $\nu_{as}(CH)$; 2945 $\nu_{as}(CH_2, CH_3)$; 2843 $\nu_s(CH_2, CH_3)$; 1620 ν(C—O); 1535 and 1515 ν(C—O, C—C); 1501, 1484, 1414, and 1353 ν(C=C, C=S thienyl); 1285 $\nu(CF_3)$; 1244 ν(CSi); 1190 and 1175 $\nu(SiOCH_3)$; 1148 ν(Si—O); 1090 $\delta(O—CH_3)$; 931 δ(Si—O—C); 861 $\delta(CH_3)$; 785 δ(CH thienyl); 713 $\delta(CF_3)$. ^{1}HNMR (δ ppm, $CDCl_3$): 0.79 (m, 2H, CH_2 (11)); 1.90 (m, 2H, CH_2 (10)); 3.54 (m, 2H, CH_2 (9)); 3.59 (s, 9H, CH_3 (12)); 6.20 (t, 1H, CH (6)); 7.06 (d, 1H, CH (2)); 7.52 (d, 1H, CH (1)); 7.66 (d, 1H, CH (3)). Mass Spectrum (FAB) m/z = 385 [M^+]; UV (ethanol): 265 nm (ε= 16 352 L $mol^{-1}cm^{-1}$), 330 nm (ε= 50 112 L $mol^{-1}cm^{-1}$).

3.1.2. Synthesis of Ruthenium(II) complexes

***$RuCl_2DMSO_4$*:** 1.38 mmol (0.810 g) of the $RuCl_3.nH_2O$ was added to 10 mL of degassed DMSO. The reaction mixture was kept under nitrogen atmosphere and refluxing at 210 °C for 5 min. Degassed acetone (50 mL) was added to the mixture and then put on freezer overnight. The obtained powder was filtered and then dried under vacuum. The $RuCl_2DMSO_4$ complex ($RuC_8H_{24}S_4O_4Cl_2$, MW 484.51) was obtained as a yellow powder. Yield: 95 %. Elemental analysis for $RuC_8H_{24}S_4O_4Cl_2$, found (calcd): C 19.8 (19.8), H 5.0 (4.95), S 26.85 (26.4), Ru 17.0 (20.9). FTIR (KBr, cm^{-1}): 3420 $\nu_{as}(NH)$; 1606, 1580, 1542 ν(C=N); 1410, 1301 ν(C=C) and $\delta(CH_2)$; 1192, 1134, 1060, 931 ν(SO); 788, 713 $\nu_{as}(CS)$; 641, 581 $\nu_s(CS)$. Mass spectrum (FAB): m/z 449 [M - Cl]$^+$.

Synthesis of ***[$RuCl_2DMSO_2$(bpy-Si)]*** which representation is given figure 9

Figure 9. Structural representation of **$RuCl_2DMSO_2$(bpy-Si)** silylated complex.

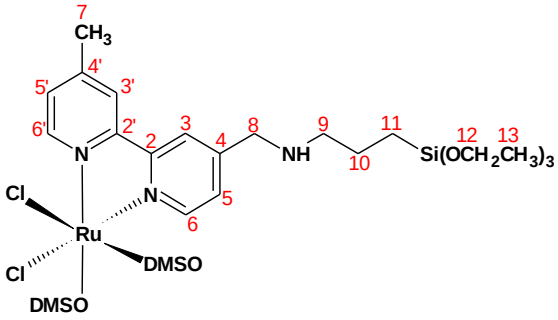

***$RuCl_2DMSO_2$(bpy-Si)*:** 0.208 g (0.52 mmol) of **bpy-Si** was dissolved in 50 ml of degassed ethanol. This solution was added to 0.250 g (0.52 mmol) of $RuCl_2(DMSO)_4$. The mixture was stirred for 3 hours under reflux and then the solvent was evaporated. The residue is taken up in 50 mL of acetone and then filtered. The solution was concentrated at half and 50 mL of degassed diethyl ether was added to precipitated the powders. The obtained powder was kept on cold for 10 min and then filtered and dried under vacuum. The $RuCl_2DMSO_2$(bpy-Si) complex ($RuC_{25}H_{45}N_3O_5S_2SiCl_2$, MW 731.83) was obtained as an orange brown powder. Yield: 89 %. Elemental analysis for $RuC_{25}H_{45}N_3O_5S_2SiCl_2$, found (calcd): C 40.5 (41.0), H 5.7 (6.2), N 6.0 (5.7). FTIR (KBr, cm^{-1}): 2922 $\nu_{as}(CH_2, CH_3)$; 1618 ν(C=N); 1485, 1421, 1383 ν(C=C) and $\delta(CH_2)$; 1167 ν(SOS); 1077 ν(Si—O—C); 954 δ(Si—O); 790, 770 $\nu(CH_{ar})$; 676 δ(CH). Mass spectrum (FAB): m/z 337 [M^{2+}/2]. ^{13}C CP MAS NMR (100.5 MHz): δC (ppm) = 10.3 (C11); 18.9, 21.2, 23.9 (C13, 7, 10); 46.4 (DMSO); 52.1 (C9, 8); 58.4 (C12); 126.7 (C5, 5', 3, 3'); 150.8 (C4, 4', 6, 6'); 157.1 (C2, 2').

Synthesis of ***$RuCl_2$(bpy)(bpy-Si)*** which representation is given figure 10

Figure 10. Structural representation of **$RuCl_2$(bpy)(bpy-Si)** silylated complex.

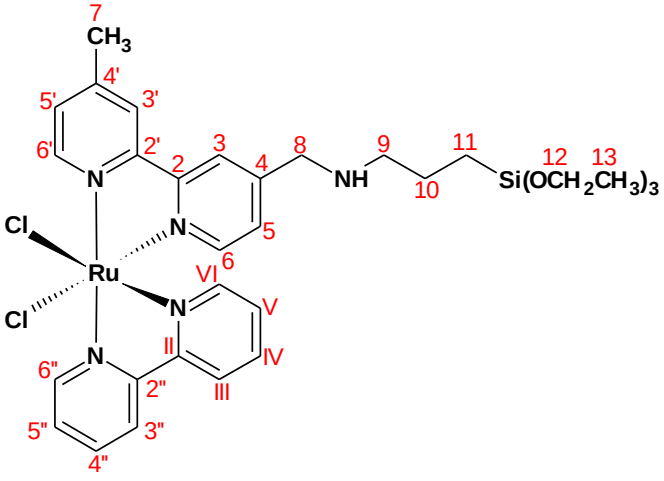

0.126 g of bipyridine (0.81 mmol) was dissolved in 50 ml of degassed ethanol. This solution was added to 0.590 g (0.81 mmol) of $RuCl_2DMSO_2$(bpy-Si). The mixture was stirred for 2 hours at reflux and then concentrated by half. 50 mL of degassed diethyl ether was added on the solution to precipitate the solid. The obtained powder was filtrated and dried under vacuum. The $RuCl_2$(bpy)(bpy-Si) complex ($RuC_{31}H_{41}N_5O_3SiCl_2$, MW 731.75) was obtained as a brown powder. Yield: 62 %.

Elemental analysis for $RuC_{31}H_{41}N_5O_3SiCl_2$, found (calcd): C 48.3 (50.9), H 5.7 (5.65), N 9.7 (9.6). FTIR (KBr, cm^{-1}): 2920 $\nu_{as}(CH_2, CH_3)$; 1617 ν(C=N); 1477, 1445, 1421 ν(C=C); 1070 ν(Si—O—C); 954 δ(Si—O); 769 $\delta(CH_{Ar})$. Mass spectrum (FAB): m/z = 696 $[M+H-HCl]^+$. ^{13}C CP MAS NMR (100.5 MHz): δC (ppm) = 11.1 (C11); 19.0, 21.2, 23.7 (C13, 7, 10); 51.8 (C9, 8); 58.2 (C12); 126.9 (C5; 5'; 3; 3'); 150.4 (C4; 4'; 6; 6'); 156.9 (C2; 2').

Synthesis of ***[Ru(bpy)(bpy-Si)(bpmd)]Cl₂*** , noted **RuL** (Figure 11)

Figure 11. Synthetic route of the **[Ru(bpy)(bpy-Si)(bpmd)]Cl_2** silylated complex (**RuL**).

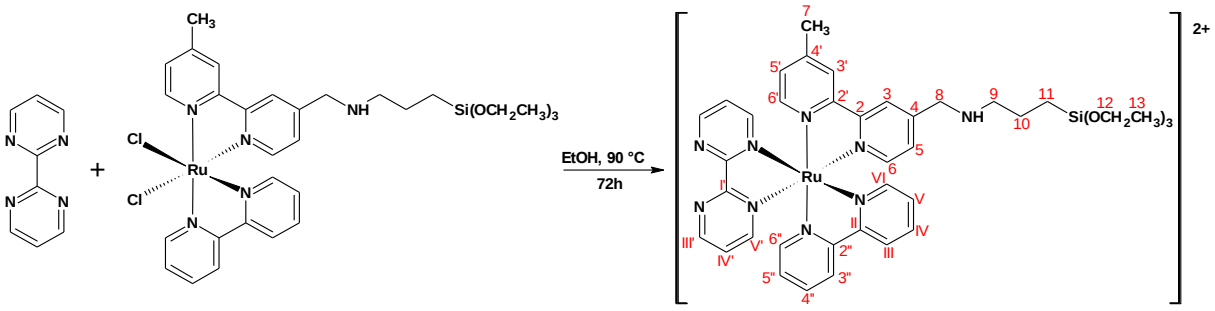

1.38 mmol (0.225 g) of the 2,2'-bipyrimidine and 1.38 mmol (1.01 g) of $RuCl_2$(bpy)(bpy-Si) were added to 40 mL of anhydrous and degassed ethanol. The reaction mixture was kept under nitrogen atmosphere and refluxing at 90 °C for 72 h. The solvent was evaporated, and the obtaining powder was washed with diethyl ether, and dried under vacuum. The [Ru(bpy)(bpy-Si)(bpmd)]Cl_2 complex ($RuC_{39}H_{47}N_9O_3SiCl_2$, MW 889.93) was obtained as a black powder. Yield: 80 %.

Elemental analysis for $RuC_{39}H_{47}N_9O_3SiCl_2$ (MW = 889,93 $g.mol^{-1}$) found (calcd): C 49.7 (52.3), H 3.4 (3.45), N 16.1 (17.4). FTIR (KBr, cm^{-1}): 3432 ν_{as}(NH); 3064 ν_{as}(CH); 2923 $\nu_{as}(CH_2, CH_3)$; 2870 $\nu_s(CH_2, CH_3)$; 1616, 1573, 1547 ν(C=N); 1464, 1444 and 1400 ν(C=C); 1309, 1269;

1240 and 1188 ν(C=C); 1072 ν(Si—O—C); 955 δ(Si—O); 818 δ(CH_3); 771, 751 and 731 δ(CH_{ar}). Mass spectrum (ESI): m/z 409 [M^{2+}/2]; UV (ethanol) 250 nm (ε=19 642 L $mol^{-1}cm^{-1}$), 287 nm (ε= 29 870 L $mol^{-1}cm^{-1}$), 443 nm (ε= 6 842 L $mol^{-1}cm^{-1}$). ^{13}C CP MAS NMR (100.5 MHz): δC (ppm) = 10.6 (C11); 20.0 (C13, 7, 10); 51.2 (C9, 8); 56.3 (C12); 125.2 (C;V';III; 3; 3'); 128.2 (CV; 5; 5'); 138.2 (CIV); 151.1 (C4; 4'; VI; 6; 6'); 156.0 (CII; 2; 2'); 161.2 (CIII', IV').

cis-$RuCl_2(bpy)_2$: The complex was obtained as described in[72], starting by dissolving 1.0 mmol (0.207 g) of $RuCl_3.nH_2O$ in 50 mL of anhydrous dimethylformamide (DMF) and then 2.5 mmol (0.390 g) of 2,2'-bipyridine and 6.5 mmol (0.276 g) of Lithium chloride were added to the solution. The reaction mixture was refluxed (150 °C) for 8h. After that, the solution was cooled at room temperature and then 250 mL of acetone was added. The mixture was filtered and the solid was washed 3 times with water (20 mL) and after 3 times with diethyl ether (20 mL). The obtained powder was recuperate by filtering and dried *in vacuo*. The cis-$RuCl_2(bpy)_2$ complex ($RuC_{20}H_{16}N_4Cl_2$, MW 484.50) was obtained as an black greenish powder. Yield: 77%. Elemental analysis for $RuC_{20}H_{16}N_4Cl_2$, found (calcd): C 44.2 (49.5), H 4.0 (3.3), N 10.6 (11.55). FTIR (KBr, cm^{-1}): 3070 ν_{as}(CH); 1620, 1590 ν(C=N, C=C); 1440 δ(NH); 1017 δ(CH_2); 770, 726 δ(CH_{ar}). Mass spectrum (ESI): m/z 449 [M - Cl]$^+$.

Synthesis of ***[Ru(bpy)$_2$(bpy-Si)]Cl$_2$*** , noted **RuL1** (Figure 12)

Figure 12. Synthetic route of the **[Ru(bpy)$_2$(bpy-Si)]Cl$_2$** silylated complex (**RuL1**).

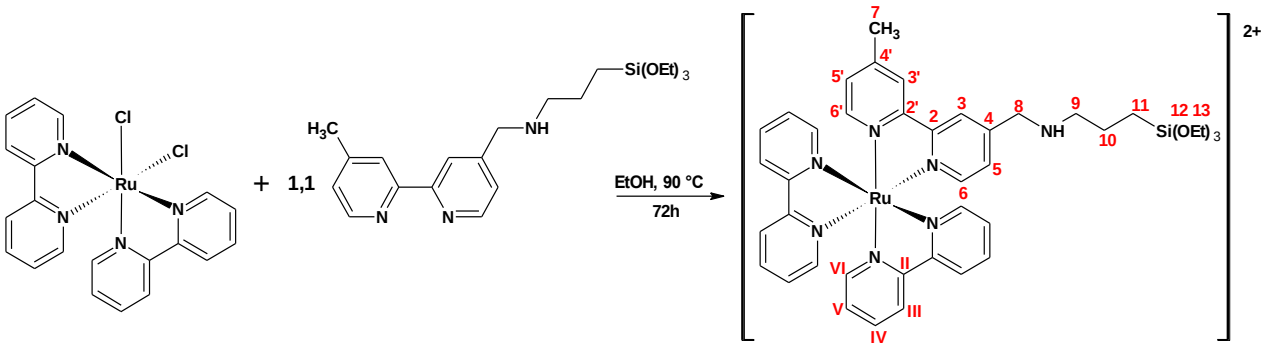

The synthesis was performed as described by Menu et al.[72–74] using 0.38 mmol (0.200 g) of cis-$RuCl_2(bpy)_2.2H_2O$ are dissolved in 50 mL of degassed and anhydrous ethanol and then 0.44 mmol (0.180 g) of **bpy-Si** were added. The mixture was refluxed (90 °C) for 3 days (in N_2

atmosphere) and then the solvent was evaporated. The residue brown-orange was dissolved in 5 mL of anhydrous CH_2Cl_2 and 20 mL anhydrous diethyl ether were added to precipitate the complex. The obtained powder was recuperate by filtering and dried *in vacuo*. The $[Ru(bpy)_2(bpy\text{-}Si)]Cl_2$ complex ($RuC_{41}H_{49}N_7O_3SiCl_2$, MW 887.94) was obtained as an orange-brown powder. Yield: 80%.

Elemental analysis for $RuC_{41}H_{49}N_7O_3SiCl_2$, found (calcd): C 50.0 (55.5), H 5.45 (5.6), N 11.2 (11.0). FTIR (KBr, cm^{-1}): 3066 $\nu(CH_{ar})$; 2966 $\nu as(CH_3)$; 2924 $\nu_{as}(CH_2)$; 2882 $\nu_s(CH_3)$; 1618, 1600 ν(C=N); 1555, 1465, 1445, 1420 ν(C=C); 1375 $\delta(CH_2)$; 1240 ν(Si—C); 1110, 1050 ν(Si—O—C); 911 δ(SiO); 770 $\delta(CH_{ar})$. Mass spectrum (ESI): m/z 409 $[M^{2+}/2]$; UV (ethanol) 246 nm (ε=35 977 L $mol^{-1}cm^{-1}$), 288 nm (ε= 78 564 L $mol^{-1}cm^{-1}$), 455 nm (ε= 14 851 L $mol^{-1}cm^{-1}$). ^{13}C CP MAS NMR (100.5 MHz): δC (ppm) = 10.9 (C11); 21.4 (C13, 7, 10); 51.2 (C9, 8); 56.3 (C12); 125.0 (CIII; 3; 3'); 128.2 (CV; 5; 5'); 138.2 (CIV); 150.8 (C4; 4'; VI; 6; 6'); 156.1 (CII; 2; 2').

Synthesis of ***[Ru(bpy)$_2$(bpmd)]Cl$_2$*** , noted **Ru** (Figure 13)

Figure 13. Synthetic route of the **[Ru(bpy)$_2$(bpmd)]Cl$_2$** complex (**Ru**).

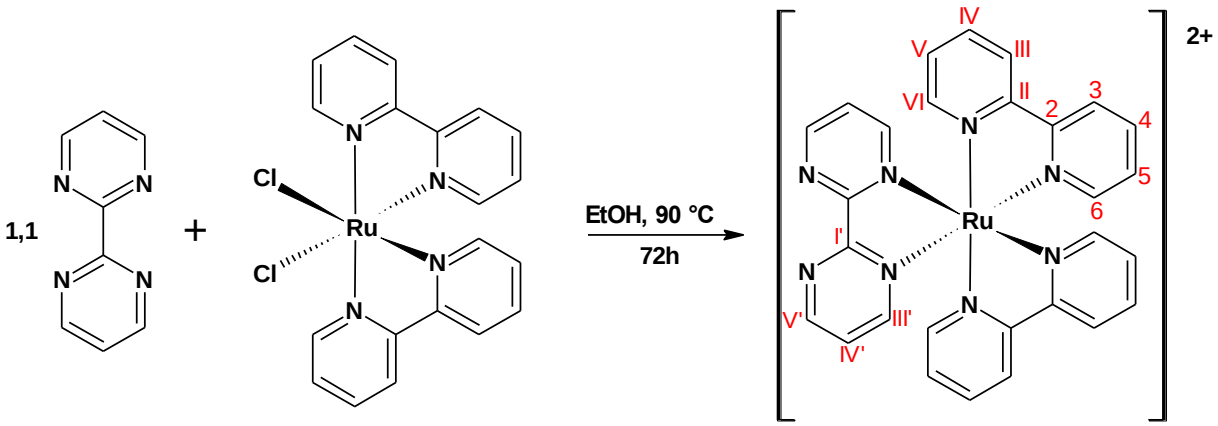

1.88 mmol (0.307 g) of the 2,2'-bipyrimidine and 1.71 mmol (0.830 g) of $RuCl_2(bpy)_2.2H_2O$ were added to 40 mL of anhydrous and degassed ethanol. The reaction mixture was kept under nitrogen atmosphere and refluxing at 90 °C for 72 h. The solvent was evaporated, and the obtaining powder was washed with pentane and diethyl ether, and dried

under vacuum. The $[Ru(bpy)_2(bpmd)]Cl_2$ complex ($RuC_{28}H_{22}N_8Cl_2$, MW 642.52) was obtained as a brown powder. Yield: 85 %.

Elemental analysis for $RuC_{28}H_{22}N_8Cl_2$ (MW =842,52 g.mol^{-1}) found (calcd): C 49.7 (52.3), H 3.4 (3.45), N 16.1 (17.4). FTIR (KBr, cm^{-1}): 3420 ν_{as}(NH); 3069 ν_{as}(CH); 1630, 1602, 1572 and 1542 ν(C=N); 1464, 1444, 1420 and 1400 ν(C=C); 1311, 1270, 1244, 1158 and 1022 ν(C=C); 772, 751, 730 $\delta(CH_{ar})$. Mass spectrum (ESI): m/z 286 [M^{2+}/2]; UV (ethanol) 250 nm (ε=32 270 L mol^{-1}cm^{-1}), 285 nm (ε= 53 516 L mol^{-1}cm^{-1}), 424 nm (ε= 10 121 L mol^{-1}cm^{-1}). ^{13}C CP MAS NMR (100.5 MHz): δC (ppm) = 126.2 (CV; V'; 5; III; 3); 139.6 (CIV); 153.5 (C4; VI; 6); 157.0 (CII; 2;); 160.6 (CIII'; IV').

3.1.3. Synthesis of Lanthanide(III) complexes

Synthesis of ***Ln(TTA)$_3$.2H$_2$O*** , noted **Ln** (Figure 14)

Figure 14. Synthetic route of the **Ln(TTA)$_3$ 2H$_2$O** complex (**Ln**).

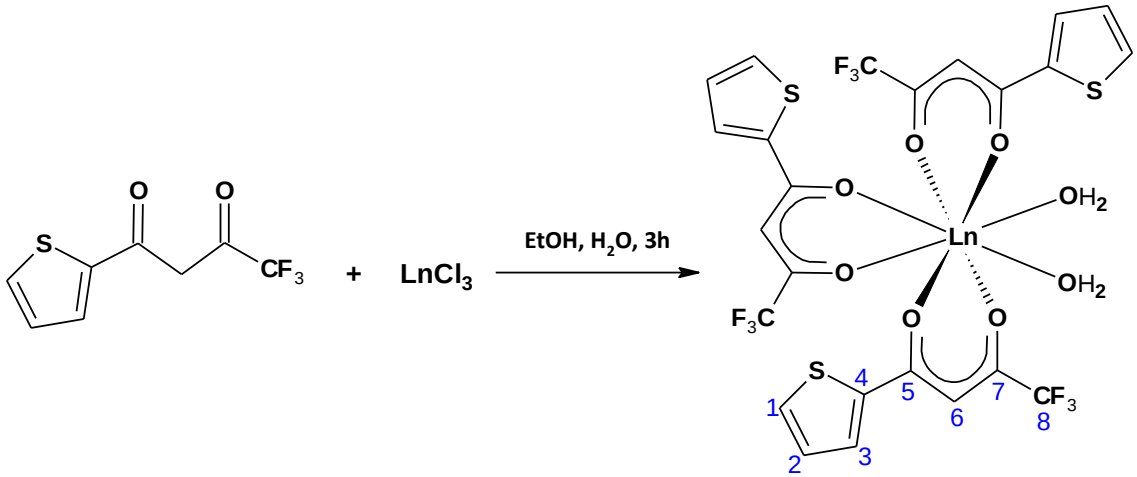

These complexes were obtained according to the procedure described by Duarte et al.[77] using 3 mmol (0.666 g) of the TTA were added to 30 mL of ethanol. After 450 µL were of NH_4OH. 1 mmol (0.279 g) of neodymium (or ytterbium) chloride were dissolved in 30 mL of water and added to the solution. The reaction mixture was kept under stirred for 3 h. The obtained powder was recovered and dissolved in acetone; then it was re-crystalized by precipitation on

cold water and dried under vacuum. The $Nd(TTA)_3.2H_2O$ complex ($NdC_{24}H_{19}O_3F_9S_3$, MW 843.63) was obtained as a yellow powder. Yield: 70%.

Elemental analysis for $NdC_{24}H_{19}O_3F_9S_3$, found (calcd): C 34.1 (34.2), H 1.5 (1.9). FTIR (KBr, cm^{-1}): 3330 ν_{as}(OH); 1606 ν(C--O); 1542 and 1513 ν(C--O, C--C); 1457, 1412 and 1358 ν(C=C, C=S thienyl); 1300 ν(CF_3); 862 δ(CH_3); 793 δ(CH thienyl); 722 δ(CF_3). Mass spectrum (DCI, NH_3): m/z 825 [M^+ - H_2O]; UV (ethanol) 268 nm (ε=17 540 L $mol^{-1}cm^{-1}$), 340 nm (ε= 51 620 L $mol^{-1}cm^{-1}$). The $Yb(TTA)_3.2H_2O$ complex ($YbC_{24}H_{19}O_3F_9S_3$, MW 875.63) was obtained as a yellow powder. Yield: 75%. FTIR (KBr, cm^{-1}): 3426 ν_{as}(OH); 1610 ν(C--O); 1543 and 1509 ν(C--O, C--C); 1452, 1411 and 1355 ν(C=C, C=S thienyl); 1310 ν(CF_3); 860 δ(CH_3); 790 δ(CH thienyl); 722 δ(CF_3). Mass spectrum (DCI, NH_3): m/z 860 [M^+ - H_2O]; UV (ethanol) 269 nm (ε=21 544 L $mol^{-1}cm^{-1}$), 338 nm (ε= 64 216 L $mol^{-1}cm^{-1}$).

Synthesis of ***[Ln(TTA-Si(OCH₃)₃]***, noted **LnL3** (Figure 15)

Figure 15. Synthetic route of the **[Ln(TTA-Si(OCH₃)₃]** silylated complex (**LnL3**).

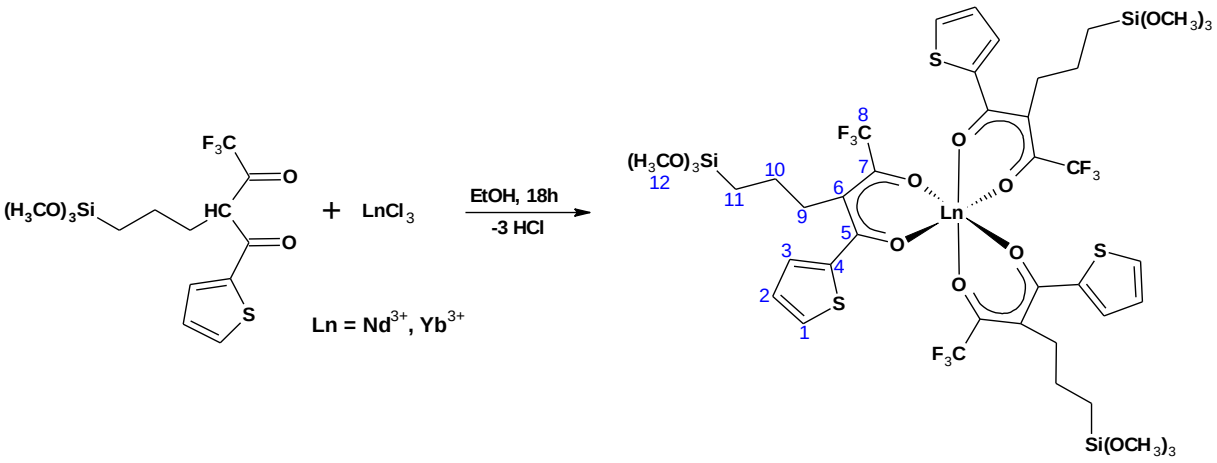

This complex was obtained by the procedure described for Duarte et al.[71, 77] and starting with 6 mmol (2.30 g) of the TTA-Si and 2 mmol (0.501 g) of neodymium (or ytterbium) chloride anhydrous were added to 20 mL of anhydrous ethanol. The reaction mixture was kept under nitrogen atmosphere and stirred for 18 h. The solvent was evaporated, and the obtaining powder was washed with pentane and diethyl ether, and dried under vacuum. The $Nd(TTA\text{-}Si)_3$ complex ($NdC_{42}H_{54}F_9O_{15}S_3Si_3$, MW 1294.57) was obtained as a greenish powder. Yield: 77%. Elemental analysis for $NdC_{42}H_{54}O_{15}F_9S_3Si_3$, found (calcd): C 38.45 (38.9), H 3.5 (4.3).

FTIR (KBr, cm^{-1}): 3106 $\nu_{as}(CH)$; 2977 and 2923 $\nu_{as}(CH_2, CH_3)$; 2851 $\nu_s(CH_2, CH_3)$; 1608 ν(C--O); 1539 and 1509 ν(C--O, C--C); 1454, 1411 and 1353 ν(C=C, C=S thienyl); 1305 $\nu(CF_3)$; 1248 and 1230 ν(C—Si); 1190 ρ(Si—O—CH_3); 1141 ν(Si—O); 1060 δ(O—CH_3); 933 δ(Si—O—C); 860 δ(CH_3); 790 δ(CH thienyl); 721 δ(CF_3). Mass spectrum (ESI): m/z 1216 [M - 6 CH_3]; UV (ethanol) 267 nm (ε=31 632 L $mol^{-1}cm^{-1}$), 340 nm (ε= 86 388 L $mol^{-1}cm^{-1}$). The Yb(TTA-Si)$_3$ complex ($YbC_{42}H_{54}F_9O_{15}S_3Si_3$, MW 1323.37) was obtained as a yellow powder. Yield: 78%.

Elemental analysis for $YbC_{42}H_{54}O_{15}F_9S_3Si_3$, found (calcd): C 38.77 (38.09), H 3.76 (4.19). FTIR (KBr, cm^{-1}): 3109 $\nu_{as}(CH)$; 2977 and 2923 $\nu_{as}(CH_2, CH_3)$; 2875 $\nu_s(CH_2, CH_3)$; 1603 ν(C--O); 1542 and 1510 ν(C--O, C--C); 1457, 1411 and 1356 ν(C=C, C=S thienyl); 1310 $\nu(CF_3)$; 1251 and 1232 ν(C—Si); 1190 ρ(Si—O—CH_3); 1142 ν(Si—O); 1082 δ(O—CH_3); 937 δ(Si—O—C); 861 δ(CH_3); 790, 770, 752 δ(CH thienyl); 722 δ(CF_3). Mass spectrum (ESI): m/z 949 [M -TTA-Si]; UV (ethanol) 267 nm (ε=25 724 L $mol^{-1}cm^{-1}$), 337 nm (ε= 71 968 L $mol^{-1}cm^{-1}$).

3.1.4. Synthesis of *d-f* heterobimetallic (Ru(II)—Ln(III)) silylated complexes

Synthesis of ***[Ru(bpy)$_2$(bpmd)Ln(TTA-Si)$_3$]Cl$_2$*** noted **Ru—LnL3** (Figure 16)

Figure 16. Synthetic route of the **[Ru(bpy)$_2$(bpmd)Ln(TTA-Si)$_3$]Cl$_2$** complex (**Ru—LnL3**).

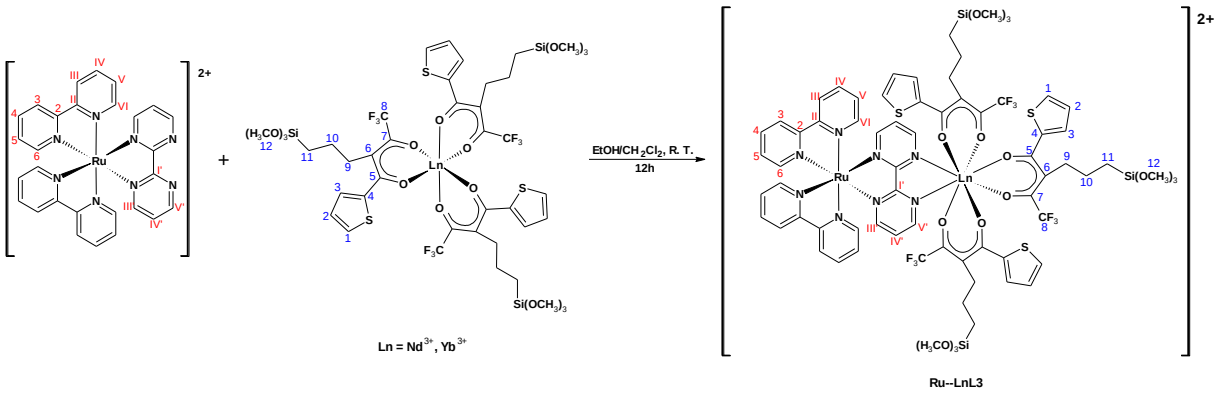

Ru—NdL3: 0.33 mmol (0.208 g) of the $[Ru(bpy)_2(bpmd)]Cl_2$ was added to 10 mL of anhydrous and degassed ethanol and then 0.33 mmol (0.420 g) of Nd(TTA-Si)$_3$ diluted in 10 mL of anhydrous and degassed dichlorometane were added to the ruthenium solution. The reaction mixture was kept under nitrogen atmosphere for 12h at room temperature. The solvent was half evaporated and filtered. The obtained powder was washed with pentane and diethyl

ether, and dried under vacuum. The $[Ru(bpy)_2(bpmd)Nd(TTA\text{-}Si)_3]Cl_2$ complex ($C_{70}H_{79}N_8O_{15}F_9S_3Si_3RuNdCl_2$, MW: 1940.08) was obtained as a brown powder. Yield: 55 %. Elemental analysis for $C_{70}H_{79}N_8O_{15}F_9S_3Si_3RuNdCl_2$, found (calcd): C 41.4 (43.3), H 2.95 (4.1), N 7.8 (5.8), S 5.1 (5.0). FTIR (KBr, cm^{-1}): 3420 ν_{as}(NH); 3074 ν_{as}(CH); 2971 $\nu_{as}(CH_2, CH_3)$; 1605 ν(C--O); 1535 and 1505 ν(C--O, C--C); 1465, 1446, 1411 and 1355 ν(C=C, C=S thienyl); 1302 $\nu(CF_3)$; 1243 and 1229 ν(C—Si); 1184 $\rho(Si—O—CH_3)$; 1140 ν(Si—O); 1060 $\delta(O—CH_3)$; 932 δ(Si—O—C); 858 $\delta(CH_3)$; 784, 767, 750 and 729 $\delta(CH_{ar}$, CH thienyl); 718 and 679 $\delta(CF_3)$. Mass spectrum (ESI): m/z 286 $[Ru(bpy)_2(bpmd)^{2+}/2]$; 1551 [M-TTA-Si]; UV (ethanol) 257 nm (ε=62 079 L $mol^{-1}cm^{-1}$), 270 nm (ε=71 051 L $mol^{-1}cm^{-1}$), 285 nm (ε=96 493 L $mol^{-1}cm^{-1}$), 339 nm (ε=73 297 L $mol^{-1}cm^{-1}$), 423 nm (ε= 15 590 L $mol^{-1}cm^{-1}$).

Ru—YbL3: 0.28 mmol (0.180 g) of the $[Ru(bpy)_2(bpmd)]Cl_2$ was added to 10 mL of anhydrous and degassed ethanol and then 0.28 mmol (0.371 g) of $Yb(TTA\text{-}Si)_3$ diluted in 10 mL of anhydrous and degassed dichlorometane were added to the ruthenium solution. The reaction mixture was kept under nitrogen atmosphere for 12h at room temperature. The solvent was half evaporated and filtered. The obtained powder was washed with pentane and diethyl ether, and dried under vacuum. The $[Ru(bpy)_2(bpmd)Nd(TTA\text{-}Si)_3]Cl_2$ complex ($C_{70}H_{79}N_8O_{15}F_9S_3Si_3RuYbCl_2$, MW: 1968.88) was obtained as a brown powder. Yield: 55 %. Elemental analysis for $C_{70}H_{79}N_8O_{15}F_9S_3Si_3RuYbCl_2$, found (calcd): C 41.9 (42.7), H 2.7 (4.0), N 5.25 (5.7), S 7.2 (4.9). FTIR (KBr, cm^{-1}): 3430 ν_{as}(NH); 3074 ν_{as}(CH); 2971 $\nu_{as}(CH_2, CH_3)$; 1602 ν(C--O); 1537 and 1507 ν(C--O, C--C); 1463, 1444, 1404 and 1355 ν(C=C, C=S thienyl); 1305 $\nu(CF_3)$; 1244 and 1229 ν(C—Si); 1185 $\rho(Si—O—CH_3)$; 1133 ν(Si—O); 1065 $\delta(O—CH_3)$; 931 δ(Si—O—C); 860 $\delta(CH_3)$; 766, 750 and 728 $\delta(CH_{ar}$, CH thienyl); 681 $\delta(CF_3)$. Mass spectrum (ESI): m/z 946 $[M^{2+}/2]$; UV (ethanol) 257 nm (ε=50 251 L $mol^{-1}cm^{-1}$), 270 nm (ε=55 838 L $mol^{-1}cm^{-1}$), 285 nm (ε=70 704 L $mol^{-1}cm^{-1}$), 337 nm (ε=83 728 L $mol^{-1}cm^{-1}$), 424 nm (ε= 10 164 L $mol^{-1}cm^{-1}$).

Synthesis of ***[Ru(bpy)(bpy-Si)(bpmd)Ln(TTA)$_3$]Cl$_2$*** noted **Ln—RuL** (Figure 17)

Figure 17. Synthetic route of the **$[Ru(bpy)(bpy\text{-}Si)(bpmd)Ln(TTA)_3]Cl_2$** complex (**Ln—RuL**).

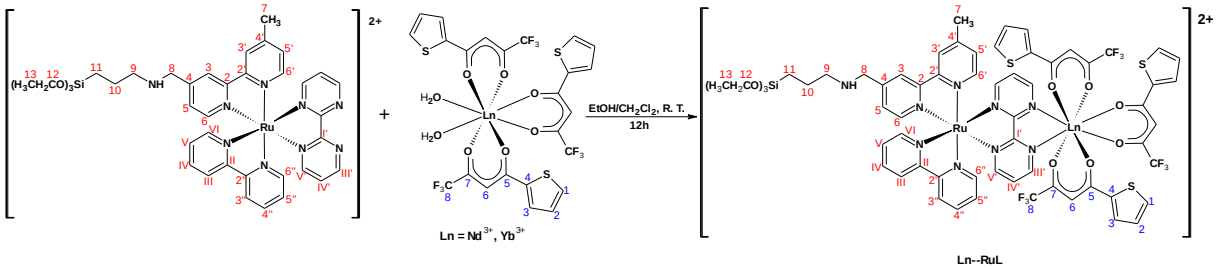

Nd—RuL: 0.28 mmol (0.250 g) of the $[Ru(bpy)(bpy\text{-}Si)(bpmd)]Cl_2$ was added to 10 mL of anhydrous and degassed ethanol and then 0.28 mmol (0.240 g) of $[Nd(TTA)_3(H_2O)_2]$ diluted in 10 mL of anhydrous and degassed dichlorometane were added to the ruthenium solution. The reaction mixture was kept under nitrogen atmosphere for 12h at room temperature. The solvent was half evaporated and filtered. The obtained powder was washed with pentane and diethyl ether, and dried under vacuum. The $[Ru(bpy)(bpy\text{-}Si)(bpmd)Nd(TTA)_3]Cl_2$ complex ($C_{63}H_{62}N_9O_9F_9S_3SiRuNdCl_2$, MW 1697.68) was obtained as a brown powder. Yield: 55 %. Elemental analysis for $C_{63}H_{62}N_9O_9F_9S_3SiRuNdCl_2$, found (calcd): C 44.15 (44.6), H 3.5 (3.5), N 7.6 (7.4). FTIR (KBr, cm^{-1}): 3430 ν_{as}(NH); 3074 ν_{as}(CH); 2921 $\nu_{as}(CH_2, CH_3)$; 1603 ν(C—O); 1576, 1535 and 1503 ν(C—O, C—C); 1466, 1448, 1412 and 1354 ν(C=C, C=S thienyl); 1300 $\nu(CF_3)$; 1243 and 1228 ν(C—Si); 1183 $\rho(Si—O—CH_3)$; 1126 ν(Si—O); 1057 $\delta(O—CH_3)$; 930 δ(Si—O—C); 858 $\delta(CH_3)$; 781, 767 and 748 $\delta(CH_{ar}$, CH thienyl); 725 and 678 $\delta(CF_3)$. Mass spectrum (ESI): m/z 1661 [M - Cl]; UV (ethanol) 252 nm (ε=45 442 L $mol^{-1}cm^{-1}$), 287 nm (ε=71 190 L $mol^{-1}cm^{-1}$), 339 nm (ε=46 514 L $mol^{-1}cm^{-1}$), 437 nm (ε= 15 811 L $mol^{-1}cm^{-1}$).

Yb—RuL: 0.37 mmol (0.330 g) of the $[Ru(bpy)(bpy\text{-}Si)(bpmd)]Cl_2$ was added to 10 mL of anhydrous and degassed ethanol and then 0.37 mmol (0.325 g) of $[Yb(TTA)_3(H_2O)_2]$ diluted in 10 mL of anhydrous and degassed dichlorometane were added to the ruthenium solution. The reaction mixture was kept under nitrogen atmosphere for 12h at room temperature. The solvent was half evaporated and filtered. The obtained powder was washed with pentane and diethyl ether, and dried under vacuum. The $[Ru(bpy)(bpy\text{-}Si)(bpmd)Yb(TTA)_3]Cl_2$ complex ($C_{63}H_{62}N_9O_9F_9S_3SiRuYbCl_2$, MW 1728.40) was obtained as a brown powder. Yield: 55 %. Elemental analysis for $C_{63}H_{62}N_9O_9F_9S_3SiRuYbCl_2$, found (calcd): C 39.9 (43.8), H 3.3 (3.4), N 6.9 (7.3), S 4.8 (5.6). FTIR (KBr, cm^{-1}): 3432 ν_{as}(NH); 3074 ν_{as}(CH); 2921 $\nu_{as}(CH_2, CH_3)$; 1604 ν(C--O); 1580, 1537 and 1506 ν(C--O, C--C); 1469, 1449, 1412 and 1355 ν(C=C, C=S thienyl); 1305 $\nu(CF_3)$;

1244 and 1230 ν(C—Si); 1182 ρ(Si—O—CH_3); 1130 ν(Si—O); 1060 δ(O—CH_3); 933 δ(Si—O—C); 858 δ(CH_3); 782, 769 and 749 δ(CH_{ar}, CH thienyl); 720 and 681 δ(CF_3). Mass spectrum (ESI): m/z 1691 [M - Cl]; UV (ethanol) 260 nm (ε=46 125 L $mol^{-1}cm^{-1}$), 287 nm (ε=64 177 L $mol^{-1}cm^{-1}$), 337 nm (ε=62 069 L $mol^{-1}cm^{-1}$), 442 nm (ε= 11 516 L $mol^{-1}cm^{-1}$).

3.1.5. Mesoporous silica nanoparticles (MSNs)

Spherical mesoporous silica particles with pore size and outer particle diameter in the nanometer range were prepared in a water/oil phase using organic templates method as described by Nandiyanto and co-workers.[78] The mesoporous silica nanoparticles (MSNs) were synthesized using TEOS (99%, Aldrich) as the silica source; L-lysine (lysine, 98%, Aldrich) as the catalyst; styrene monomer as the template; CTAB (98%, Aldrich) as both a template and surfactant; and, 2,2'-Azobis (2-methylpropionamide) dihydrochloride (AIBA, 97%, Aldrich) as the initiator of styrene polymerization. Lysine was used as a catalyst because it can control silica in the nanometer range.[78]

Figure 18. Representation of synthetic route of the mesoporous silica nanoparticles (MSNs).[78] Reference: Adapted from Nandiyanto et al. (2019a) with permission. Copyright 2009 Elsevier n°3898390718024.

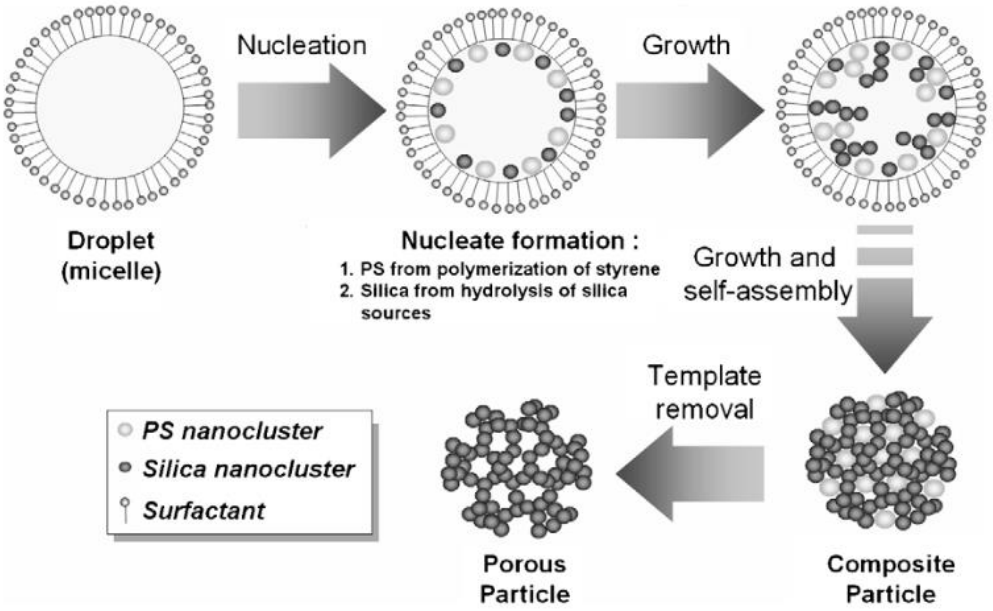

Figure 18 shows a representation of synthetic route of the MSNs. This method involves the simultaneous hydrolytic condensation of tetraethylorthosilicate (TEOS) to form silica and polymerization of styrene into polystyrene. An amino acid catalyst, octane hydrophobic-supporting reaction component, and cetyltrimethylammonium bromide (CTAB) surfactant were used in the preparation process. The final step in the method involved removal of the organic components by calcinations, yielding the MSNs.[78]

MSNs: 0.202 g of CTAB was dissolved in 60 ml of aqueous solution at 60 °C under stirring for 30 min in N_2 atmosphere. After a clear solution was obtained, 18.6 mL of octane was added and stirring for 5 min. Styrene monomer (35 μL), lysine (0.04605 g), TEOS (2.14 mL) and AIBA (0.06725 g) were subsequently added to the solution. The styrene monomer was pre-washed with 2.5 M NaOH (1 mL, three times) to remove the stabilizer prior to use. The reaction was allowed to proceed for 3 h under N_2 atmosphere at 60 °C. Then, the heating was stopped and the suspension was cooled naturally to room temperature. The cooled suspension was decanted for one night (about 12 h) and purified by centrifugation (15000 rpm). The suspension was centrifuged twice to insure that the particle was well purified. The centrifuged particles were washed by ethanol (five times). The obtained particles were dried *in vacuo* and the template was removed by heat treatment at 500 °C under atmospheric conditions. The MSNs were obtained as a white powder. Yield: 50 %. DRIFT: 3430 ν(OH); 1630 δ(OH) 1095 ν_{as}(Si—O—Si); 961 ν(Si—OH); 805 ν_s(Si—O—Si); 465 δ(Si—O—Si). Mean diameter: 47 nm. Specific surface area (S_{BET}): 675 $m^2\ g^{-1}$, pores volume (V_p): 1.55 $cm^3\ g^{-1}$ and average pore size (D_p): 9 nm. ^{29}Si-MAS NMR (δ ppm): Q^2 (-97); Q^3 (-103); Q^4 (-112).

3.1.6. Luminescent silica-based nanohybrids obtained by grafting of ruthenium(II) and lanthanide(II) silylated complexes onto MSNs

Two types of luminescent nanohybrids were obtained: In the first one the mononuclear complex (**RuL1** or **NdL3** or **YbL3**) was grafted on the mesoporous silica nanoparticles (**SiO_2-Ru**, **SiO_2-Nd** and **SiO_2-Yb**). In the second one two mononuclear complexes (**RuL1/NdL3** or **RuL1/YbL3**) were simultaneously grafted on mesoporous silica nanoparticles (**SiO_2-RuNd** and **SiO_2-RuYb)**.

3.1.6.1. SiO_2-Ru, SiO_2-Nd and SiO_2-Yb.

Grafting of **RuL1**, **NdL3** and **YbL3** complexes onto **MSNs**

Figure 19. Representation of **SiO_2-Ru, SiO_2-Nd** and **SiO_2-Yb** nanohybrids.

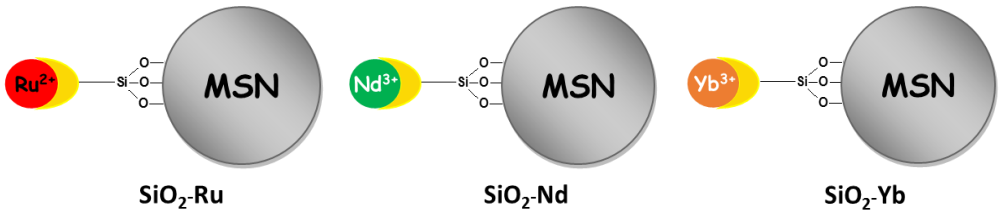

SiO_2-Ru **SiO_2-Nd** **SiO_2-Yb**

For *SiO_2-Ru*, 0.32 mmol (285 mg) of **RuL1** complex was dissolved in ethanol (10 mL) and reacted with (285 mg) of mesoporous silica nanoparticles. For *SiO_2-Nd,* 0.19 mmol (242 mg) of **NdL3** complex was dissolved in ethanol (15 mL) and reacted with (450 mg) of mesoporous silica nanoparticles. For *SiO_2-Yb,* 0.22 mmol (299 mg) of **YbL3** complex was dissolved in ethanol (15 mL) and reacted with (450 mg) of mesoporous silica nanoparticles. The mixtures were stirred for 72 h at 295 K in N_2 atmosphere. The resulting suspensions were dialyzed for 72 h, and the solids were isolated by centrifugation at 15 000 rpm for 15 min. The *SiO_2-Ru* obtained was washed with water, ethanol, and diethyl ether. *SiO_2-Nd* and *SiO_2-Yb* obtained were washed with ethanol, acetone and diethyl ether. All solids obtained were dried under vacuum for 4 h.

SiO_2-Ru: Elemental analysis %, found (calcd): R = 0.18 mmol.g^{-1}: C, 10.5 (9.0); H, 1.3 (0.9); N, 1.05 (1.05).

SiO_2-Nd: Elemental analysis %, found (calcd): R = 0.08 mmol.g^{-1}: C, 3.2 (4.1); H, 2.1 (0.45); S, 0.8 (0.8).

SiO_2-Yb: Elemental analysis %, found (calcd): R = 0.08 mmol.g^{-1}: C, 3.0 (3.9); H, 1.6 (0.4); S, 0.75 (0.75).

3.1.6.2. SiO_2-RuNd and SiO_2-RuYb.

Simultaneous grafting of **RuL1/NdL3** and **RuL1/YbL3** complexes onto **MSNs**

Figure 20. Representation of **SiO_2-RuNd** and **SiO_2-RuYb** nanohybrids.

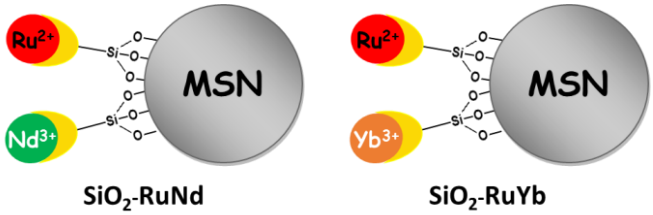

SiO_2-RuNd SiO_2-RuYb

0.20 mmol of **RuL1** complex (178 mg), 0.20 mmol of **NdL3** complex (260 mg) and 0.20 mmol of **YbL3** complex (289 mg) were dissolved in ethanol (20 mL) and reacted with (450 mg) of mesoporous silica nanoparticles. The mixtures were stirred for 72 h at 295 K in an N_2 atmosphere. The resulting suspensions were dialyzed for 72 h, and the solids were isolated by centrifugation at 15 000 rpm for 15 min. The obtained solids were washed with water, ethanol, dichloromethane, and diethyl ether and then dried under vacuum for 4h.

SiO_2-RuNd: Elemental analysis %, found (calcd): R_{Ru} = 0.14 mmol.g^{-1} and R_{Nd} = 0.16 mmol.g^{-1}: C, 15.3 (14.65); H, 1.7 (1.5); N, 1.3 (1.3); S, 1.5 (1.5).

SiO_2-RuYb: Elemental analysis %, found (calcd): R_{Ru} = 0.11 mmol.g^{-1} and R_{Yb} = 0.15 mmol.g^{-1}: C, 15.5 (12.7); H, 1.7 (1.3); N, 1.05 (1.05); S, 1.41 (1.41).

3.1.7. Luminescent silica-based nanohybrids obtained by grafting of *d-f* heterobimetallic silylated complexes onto mesoporous silica nanoparticles (MSNs) and dense silica nanoparticles Ludox AS40 (DSNs)

Four types of luminescent nanohybrids were obtained: (1) silylated binuclear complexes (labeled **RuYbL3**, **NdRuL** and **YbRuL**) were grafted on mesoporous silica nanoparticles (labeled **SiO_2**) and (2) **YbRuL** complex was grafted onto the particle surface (Ludox AS40). The different nanohybrids were noted as **SiO_2-RuYbL3**, **SiO_2-NdRuL**, **SiO_2-YbRuL** and **SiO_2 d-YbRuL** (mesoporous silica nanoparticles and Ludox AS40, respectively). All nanohybrids are chemically stable for months.

3.1.7.1. SiO_2-RuYbL3.

Grafting of **Ru—YbL3** complex onto **MSNs**

Figure 21. Representation of **SiO_2-RuYbL3** nanohybrids.

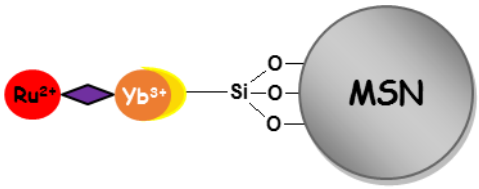

SiO_2-RuYbL3

0.10 mmol (200 mg) of **Ru—YbL3** complex were dissolved in 20 mL of ethanol/dichlorometane (1:1) and reacted with (400 mg) of mesoporous silica nanoparticles. The mixtures were stirred for 72 h at 295 K in N_2 atmosphere. The resulting suspensions were dialyzed for 72 h, and the solids were isolated by centrifugation at 15 000 rpm for 15 min. The solids obtained were washed with water, ethanol, and diethyl ether and then dried under vacuum for 4 h.

SiO_2-RuYbL3: Elemental analysis %, found (calcd): R_{Ru} = 0.06 mmol.g^{-1} and R_{Yb} = 0.03 mmol.g^{-1}: C, 5.6 (5.6); H, 2.0 (0.5); N, 0.75 (0.75); S, 0.25 (0.6).

3.1.7.2. SiO_2-NdRuL.

Grafting of **Nd—RuL** complex onto **MSNs**

Figure 22. Representation of **SiO_2-NdRuL** nanohybrids.

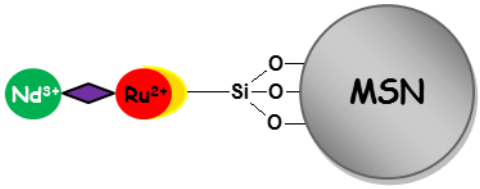

SiO_2-NdRuL

0.12 mmol (204 mg) of **Nd—RuL** complex were dissolved in 20 mL of ethanol/dichlorometane (1:1) and reacted with (490 mg) of mesoporous silica nanoparticles. The mixtures were stirred for 72 h at 295 K in an N_2 atmosphere. The resulting suspensions were dialyzed for 72 h, and the solids were isolated by centrifugation at 15 000 rpm for 15 min. The obtained solids were washed with water, ethanol, dichloromethane, and diethyl ether and then dried under vacuum for 4 h.

SiO_2-NdRuL: Elemental analysis %, found (calcd): R_{Ru} = 0.17 mmol.g^{-1} and R_{Nd} = 0.05 mmol.g^{-1}: C, 10.7 (13.0); H, 1.7 (1.0); N, 2.17 (2.17); S, 0.4 (1.65).

3.1.7.3. SiO_2-YbRuL.

Grafting of **Yb—RuL** complex onto **MSNs**

Figure 23. Representation of **SiO_2-YbRuL** nanohybrids.

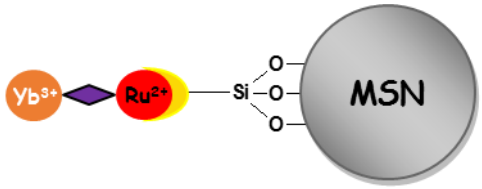

SiO_2-YbRuL

0.14 mmol (240 mg) of **Yb—RuL** complex were dissolved in 20 mL of ethanol/dichlorometane (1:1) and reacted with (415 mg) of mesoporous silica nanoparticles. The mixtures were stirred for 72 h at 295 K in an N_2 atmosphere. The resulting suspensions were dialyzed for 72 h, and the solids were isolated by centrifugation at 15 000 rpm for 15 min. The obtained solids were washed with water, ethanol, dichloromethane, and diethyl ether and then dried under vacuum for 4 h.

SiO_2-YbRuL: Elemental analysis %, found (calcd): R_{Ru} = 0.13 mmol.g^{-1} and R_{Yb} = 0.13 mmol.g^{-1}: C, 13.6 (9.8); H, 1.8 (0.8); N, 1.6 (1.6); S, 1.2 (1.2).

3.1.7.4. SiO_2 d-YbRuL.

Grafting of **Yb—RuL** complex onto **DSNs**

Figure 24. Representation of **SiO_2 d-YbRuL** nanohybrids.

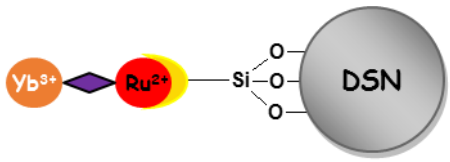

SiO_2 d-YbRuL

0.06 mmol (105 mg) of **Yb—RuL** complex was dissolved in ethanol (10 mL) and reacted with Ludox silica sol 1.40 g that is 0.56 g of SiO_2. The mixtures were stirred for 72 h at 295 K in N_2 atmosphere. The resulting suspensions were dialyzed for 72 h, and the solids were isolated by centrifugation at 15 000 rpm for 15 min. The solids obtained were washed with water, ethanol, and diethyl ether and then dried under vacuum for 4 h.

SiO_2 d-YbRuL: Elemental analysis %, found (calcd): R_{Ru} = 0.05 mmol.g^{-1} and R_{Yb} = 0.04 mmol.g^{-1}: R = 0.055 mmol.g^{-1}: C, 6.2 (4.2); H, 1.0 (0.35); N, 0.7 (0.7); S, 0.4 (0.5).

3.2. Characterization Methods

3.2.1. Elemental Analysis

Elemental analyses of C, H, N and S were performed on a Fisons EA1108 Instrument CHNS/O elemental analyzer. Nitrogen and Sulfur contents allow the determination of the grafting efficiency, *R*, expressed in millimoles of complex per gram of silica, were calculated according to the equation 5.[73, 77]

$$R_N = \frac{\%N}{14\ X\ 100} X \frac{10^3}{n_N} \qquad or \qquad R_S = \frac{\%S}{32\ X\ 100} X \frac{10^3}{n_S} \tag{5}$$

n_N and n_S = Nitrogen and Sulfur numbers present in the each complex, respectively.

3.2.2. Fourier Transformed Infra-Red Spectroscopy

FTIR spectra were obtained in the spectral range from 4000 to 400 cm^{-1} (4 cm^{-1} of resolution) with a Bruker Vector 22 (KBr dispersion). DRIFT spectra were obtained in the spectral range from 4000 to 400 cm^{-1} with a Perkin-Elmer 1760 X (DTGS detector) spectrometer.

3.2.3. Fourier Transformed Raman Spectroscopy

The Raman spectra were collected on a RFS 100 FT-Raman Bruker spectrometer equipped with a Ge detector using liquid nitrogen as the coolant and a Nd:YAG laser emitting at 1064 nm. The laser light, with a power varying from 30 to 150 mW, was introduced and focused on the sample, and the scattered radiation was collected at 180°. For each spectrum,

an average of 1024 scans was performed at a resolution of 4 cm^{-1} over a range from 3500 to 50 cm^{-1}. The OPUS 6.0 (Bruker Optik, Ettlingen, Germany) software was used for Raman data acquisition. For all of the FT-Raman spectra obtained, the samples did not undergo any previous preparation, and all spectra were obtained at least twice to be sure about position and intensity.

3.2.4. Ultraviolet-Visible Spectroscopy

UV-Vis spectra were recorded using a Varian spectrophotometer model Cary 5000 in the region of 800 to 200 nm (resolution of 1 nm) using CarryWin UV software.

3.2.5. Nuclear Magnetic Resonance

Liquid-state NMR: For the silylated ligands, ^{1}H liquid-state NMR spectra were performed on a BRUKER Avance 300 MHz. The central solvent peak ($CDCl_3$) was used as an internal chemical shift reference point (ppm).

For the lanthanide and heterobimetallic complexes, NMR spectra were obtained using a Bruker Avance 600 MHz spectrometer at room temperature in deuterated solvents. TOCSY1D spectra were recorded by exciting in different aromatic ligand protons of the complex with a selective pulse. The spectra were recording after magnetization transfer at 120 ms of mixing time. $^{1}H\{^{13}C\}$-HSQC NMR experiments were recorded using the spectral widths of 12000 and 24000 Hz for the ^{1}H and ^{13}C dimensions, respectively. The number of collected complex points was 1024 for the ^{1}H dimension with a recycle delay of 1.5 s. The number of transients was from 24 to 48 depending of the sample and 128 time increments were recorded in the ^{13}C dimension. The $^{1}J_{HC}$ used was 145 Hz. Prior to Fourier transformation, the data matrices were zero filled to 1024 points in the ^{13}C dimension. $^{1}H\{^{13}C\}$-HMBC NMR experiments were carried out using the spectral widths of 12000 and 24000 Hz for the ^{1}H and ^{13}C dimensions, respectively. The number of collected complex points was 1024 for the ^{1}H dimension with a recycle delay of 2.0 s. The number of transients was from 16 to 32 depending of the sample and 128 time increments were recorded in the ^{13}C dimension. The $^{3}J_{HC}$ used was 8 Hz. Prior to Fourier transformation, the data matrices were zero filled to 1024 points in the ^{13}C dimension. Data processing was performed using standard Bruker Topspin-NMR software. The central solvent peak was used as an internal chemical shift reference point.

Solid-state NMR: For the ruthenium complexes, ^{13}C solid-state NMR spectra were carried out on a Bruker Avance 400WB equipment using dipolar decoupling in combination with cross-polarization (CP) and magic angle spinning (MAS) (100.356 MHz).

High resolution NMR spectroscopy spectra were carried out under condition magic angle spinning (MAS), at room temperature. ^{29}Si-MAS NMR spectra of the MSNs and nanohybrids were recorded on a Varian Unity Inova spectrometer 300MHz, operating at 7.05T, using a 7mm double resonance MAS-NMR probe. All spectra were recorded with a pulse of 90^{o} with spinning speeds of 5kHz.

The $^{29}Si\{^{1}H\}$CP-MAS and $^{13}C\{^{1}H\}$CP-MAS spectra were obtained on a Ascend III 400WB HD spectrometer, operating at 9.4T, using a commercial 4mm double resonance MAS-NMR probe. The frequencies of nuclei are 400.13, 79.49 and 100.6MHz for ^{1}H, ^{29}Si and ^{13}C and spinning speeds of 15 and 10 kHz**,** respectively**.** $^{29}Si\{^{1}H\}$CP-MAS spectra were measured with ^{1}H 90^{o} pulse length of 2.9us, a contact time of 2.5ms, and a relaxation delay of 5s. $^{13}C\{^{1}H\}$CP-MAS spectra were measured with ^{1}H 90^{o} pulse length of 3.1us, a contact time of 3.5ms, and a relaxation delay of 5s. All spectra were acquired with TPPM proton decoupling during the data acquisition applying decoupling pulses of 5.8 μs length (π pulses). Chemical shifts are reported relative to TMS. Signal deconvolutions into Gaussian components were done using the DMFIT software package.[79]

3.2.6. Mass Spectrometry

Mass spectra were recorded by high resolution Q TOF 1er (Waters) spectrometer: electrospray (ESI) source, DSQ Thermo Fisher Scientific spectrometer equipped with chemical ionization source (NH_3) and Fast Atom Bombardment (FAB) using a Nermag R10-10 spectrometer.

3.2.7. Luminescence

Luminescence spectra were measured at room temperature using a Jobin-Yvon Model Fluorolog FL3-22 spectrometer equipped with a H10330-75 Hamamatsu detector, TE: cooled NIR-photomultiplier module and a 450 W Xe excitation lamp. Excitation and emission spectra were recorded under CW excitation and were corrected with respect to the Xe Lamp intensity and spectrometer response. Fluorescence intensity decays for the complexes and nanohybrids were obtained using the time-correlated single-photon counting technique. The excitation

source was a mode-locked Ti:saphire laser (Tsunami 3950 pumped by Millennia X Spectra Physics) producing 5 ps FWHM pulses ranging from 0.5 to 8.0 MHz repetition rate, regulated by the 3980 Spectra Physics pulse picker. The laser was tuned to give output at 892 nm and a second harmonic generator BBO crystal (GWN-23PL Spectra Physics) gave the 448 nm excitation pulses that were directed to an Edinburgh FL900 spectrometer adjusted in L-format configuration. The solid samples were placed in a holder perpendicular to the excitation source. The emission wavelength from 610 to 670 nm were selected by a monochromator and emitted photons were detected by a cooled Hamamatsu R3809U microchannel plate photo-multiplier. The whole instrument response function was typically 100 ps. For the complexes, energy transfer rate constant (k_{ET}) and quantum yield (Φ_{ET}) were obtained using ruthenium ^{3}MLCT decay values from ruthenium precursors and the respectives heterobimetallic complexes. For the nanohybrids, the **SiO_2-Ru** was used as a precursor to obtain values of k_{ET} and Φ_{ET} for **SiO_2-RuNd** and **SiO_2-RuYb.**

3.2.8. Scanning Electron Microscopy

Particle shape and size were examined to the MSNs and nanohybrids via FEG-SEM, using a JEOL JSM 6700 F microscope. A drop of sol was diluted in ethanol. The samples were not metallized. The microscopy measurements were carried out in the Raimond Castaing- UMS 3623 microcharacterization center.

3.2.9. Transmission and Scanning Transmission Electron Microscopy

The shape, size and porous structure of the MSNs were evaluated by TEM using a JEOL JEM 1400 (120 kV). A drop of sol was diluted in ethanol and the carbon-coated grid was dipped in the solution and allowed to air-dry at room temperature. The microscopy measurements were carried out in the Raimond Castaing- UMS 3623 microcharacterization center.

The presence of lanthanides and ruthenium on the mesoporous SiO_2 nanoparticles were evaluated by Scanning and Transmission Electron Microscopy (STEM), using a JEOL JEM-ARM200F Cold FEG - EDS/EELS microscope. A drop of sol was diluted in ethanol. A carbon-coated grid was dipped in the solution and allowed to air-dry at room temperature. The microscopy measurements were carried out in the Raimond Castaing- UMS 3623 microcharacterization center.

3.2.10. N_2 Adsorption and Desorption

Nitrogen adsorption isotherms were measured on a Surface and Porosity Analyser - Tristar 3020 – Micromeritics apparatus, and the experiments were carried out on samples degassed at 90 °C under vacuum for 20 h. Surface areas were determined from the BET method.

3.2.11. Thermogravimetric Analysis

The thermogravimetric curve was obtained in a TA Instruments equipment model SDT Q600 Simultaneous DTA-TGA. The MSNs was heated at 10 °C min^{-1} from 20 °C to 1000 °C in air atmosphere dynamic (flow rate = 100 mL min^{-1}).

4 – LUMINESCENT RUTHENIUM(II), LANTHANIDE(III) AND *d-f* HETEROBIMETALLIC SILYLATED COMPLEXES

4.1. Characterization of the ligands modified by alkoxysilyl groups (bpy-Si and TTA-Si)

Organic ligands as bipyridine (bpy) and 2-thenoyltrifluoroacetone (TTA) were chosen due to act as efficient sensitizers of ruthenium and lanthanide ions. Besides that, according to the methodology developed by Menu and co-workers[70-72], these ligands can be successfully modified by alkoxisilyl groups. In this case, **bpy** ligands were modified by ethoxysilyl groups whereas **TTA** ligands were modified by methoxysilyl groups. The presence of alkoxisilyl groups allows the covalent bound on any hydroxylated matrix, in this case, leading to the covalent bounds on the silica matrix. Figure 25 displays both organic ligands modified by ethoxysilyl and methoxysilyl groups (**bpy-Si** and **TTA-Si**).

Figure 25. Structure of the ligands **bpy-Si** (on the left) and **TTA-Si** (on the right).

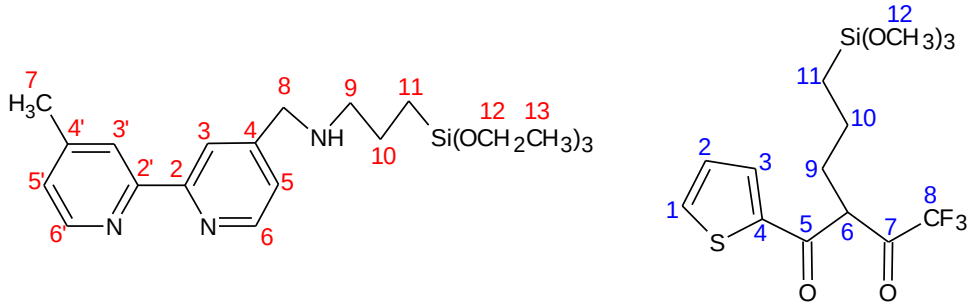

Trialkoxysilyl groups were chosen in order to minimize the hydrolysis and condensation processes of the ligands, and consequently, of the complexes. Moreover, APTES and chloropropyltrimethoxysilane groups give rise to alkylated derivative that are more stable to pH change than amides or imines[70, 77] Both modified ligands were successfully characterized by mass spectrometry, FTIR, elemental analysis and liquid ^{1}H NMR, according to the structure proposed by Cousinié[70] and Duarte[71, 77].

4.2. Synthesis of *d-f* heterobimetallic silylated complexes

The $Ru(bpy)_2(bpy\text{-}Si)Cl_2$ complex (labeled **RuL1**, figure 26) was synthesized and successfully characterized by EA, MS, FTIR, UV-Visible and solid ^{13}C NMR measurements according to the proposed structure obtained by Menu and co-workers.[72–74]

Figure 26. Structure of the **[Ru(bpy)$_2$(bpy-Si)]Cl$_2$** silylated complex (**RuL1**).

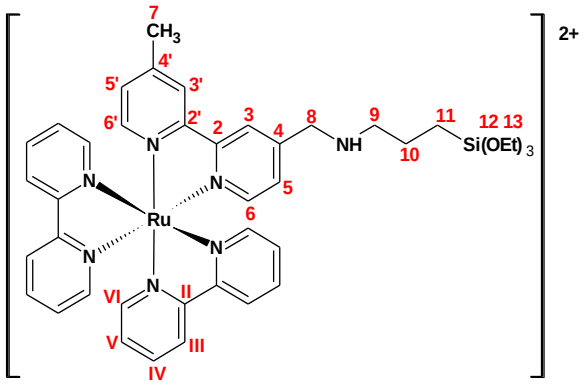

A new ruthenium(II) silylated complex was synthesized and the probable structure showed in the figure 27 (3). The integrity of the ruthenium (II) complexes and the ethoxysilyl groups were evaluated by solid-state NMR measurements (figure 28).

Figure 27. Structure of the **RuCl$_2$DMSO$_2$(bpy-Si)** (**1**), **RuCl$_2$(bpy)(bpy-Si)** (**2**) **[Ru(bpy)(bpy-Si)(bpmd)]Cl$_2$** (**3**) silylated complexes.

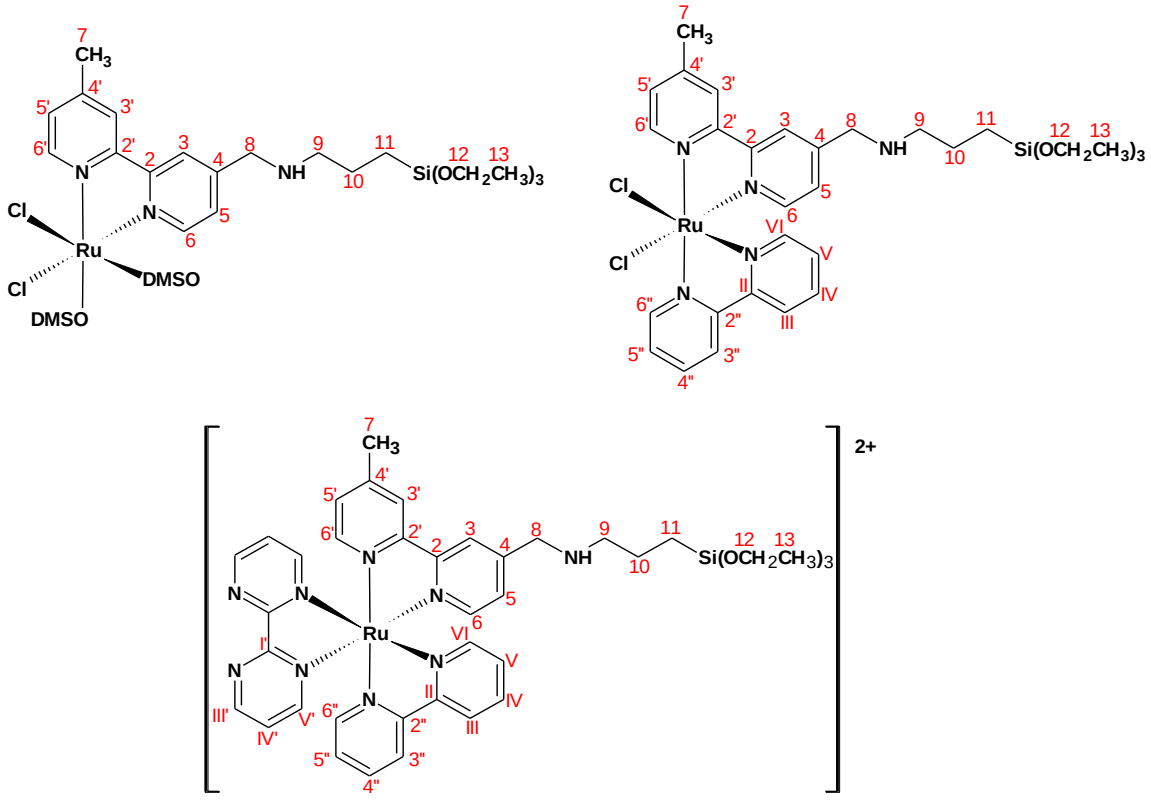

The chemical integrity of the $RuCl_2DMSO_2$(bpy-Si)**,** $RuCl_2$(bpy)(bpy-Si) and [Ru(bpy)(bpy-Si)(bpmd)]Cl_2 complexes were confirmed by solid-state ^{13}C NMR analysis. Peaks are observed at 125.2 (CV'; III; 3; 3'), 128.2 (CV; 5; 5'), 138.2 (CIV), 151.1 (C4; 4'; VI; 6; 6'), 156.0 (CII; 2; 2') and 161.2 (CIII', IV') ppm, assigned to the aromatic C atoms in the **bpy, bpmd** and **bpy-Si** ligands. The presence of **bpmd** can be clearly observed due to the peak at 161.2 ppm and the shoulder at 128.2 ppm. Peaks ascribed to the propyl chain and ethoxysilyl groups are observed at 10.6 (C11), 20.0 (C13, 7, 10), 51.2 (C9, 8) and 56.3 (C12) ppm.

Figure 28. ^{13}C CP MAS solid NMR spectra of **$RuCl_2DMSO_2$(bpy-Si)** (**1**), **$RuCl_2$(bpy)(bpy-Si)** (**2**) and **[Ru(bpy)(bpy-Si)(bpmd)]Cl_2** (**3**) silylated complexes. The numbering of carbon atoms is given on the figure 21.

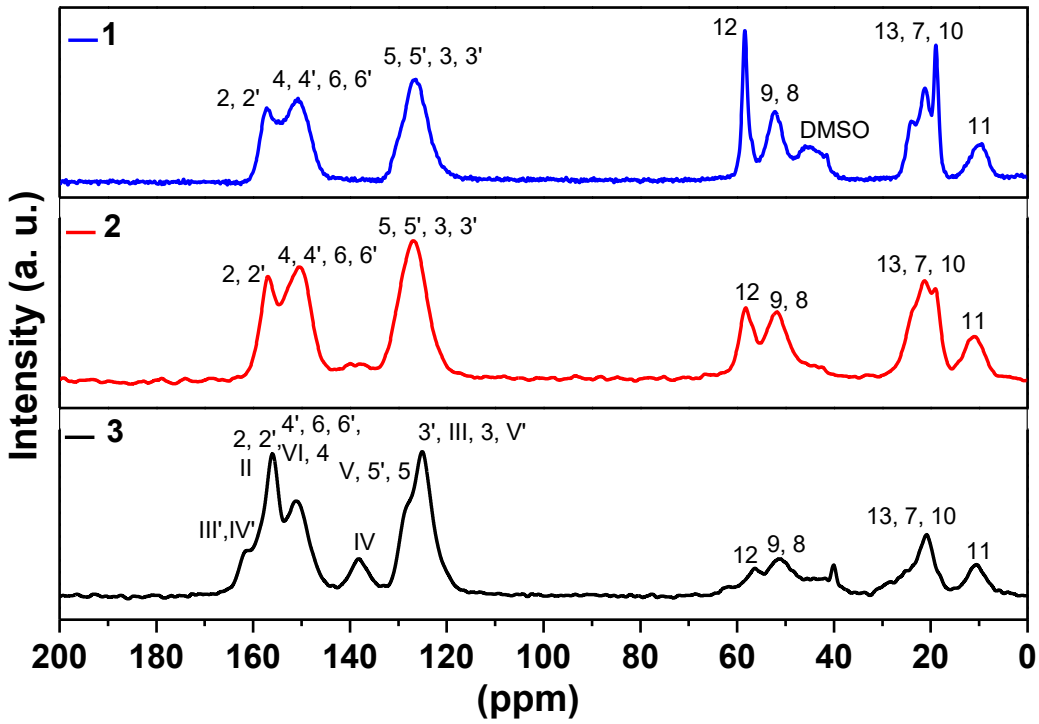

[Ru(bpy)(bpy-Si)(bpmd)]Cl_2 (labeled **RuL**) and three new precursor complexes with (or not) the ligands modified by alkoxysilyl groups were synthesized (figure 29).

Figure 29. Synthesis routes of the **Ru** (i), **RuL** (ii) and **LnL3** (Ln = Nd^{3+}, Yb^{3+}) complexes (iii).

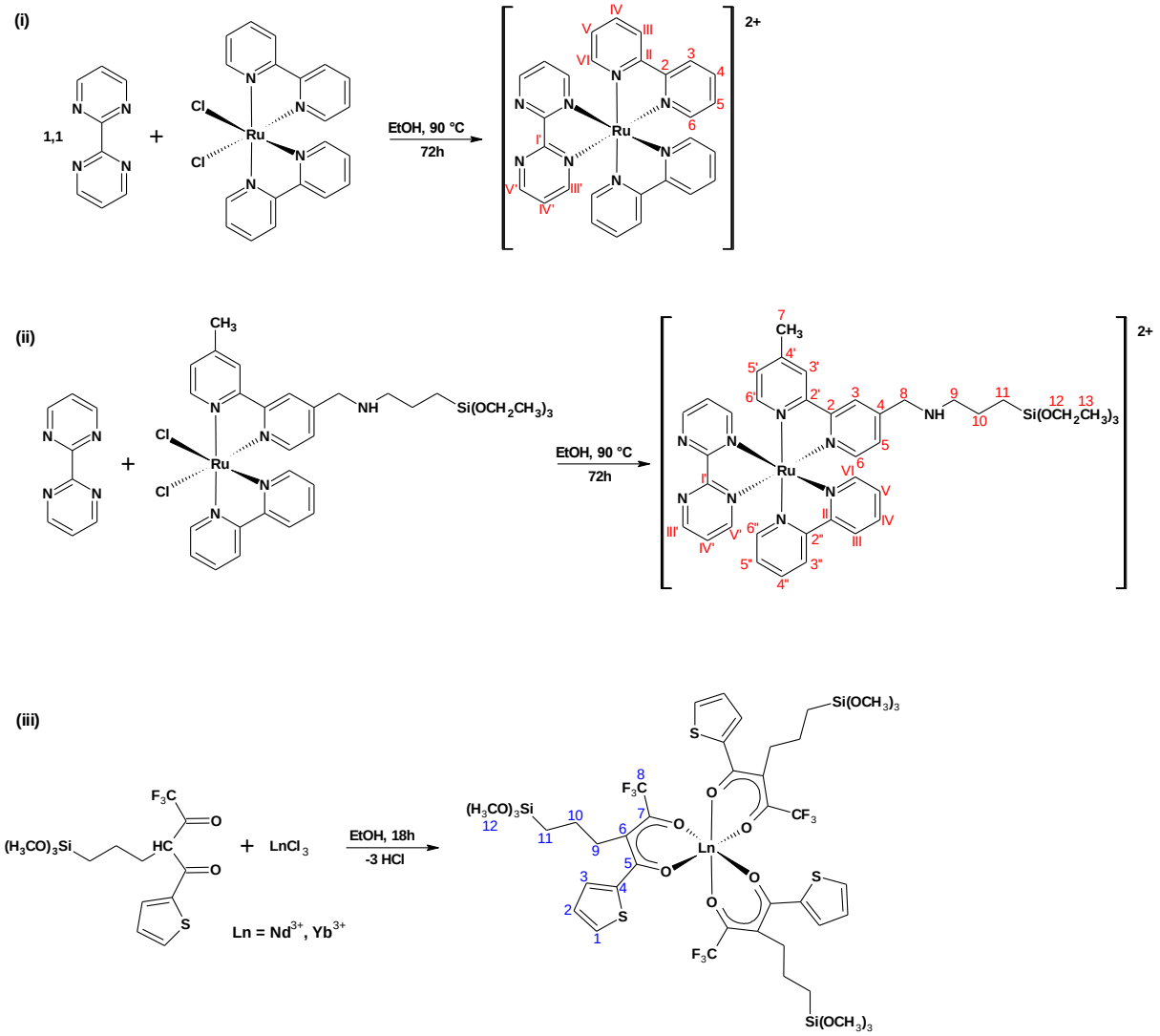

Heterobimetallic silylated complexes (**Ru—LnL3** and **Ln—RuL**) were obtained by the reaction of equal quantities of the precursor complexes. The synthetic routes of the heterobimetallic silylated complexes are displayed in the figure 30.

Figure 30. Synthesis routes of the heterobimetallic **Ru—LnL3** (i) and **Ln—RuL** (ii) silylated complexes (Ln = Nd^{3+}, Yb^{3+}).

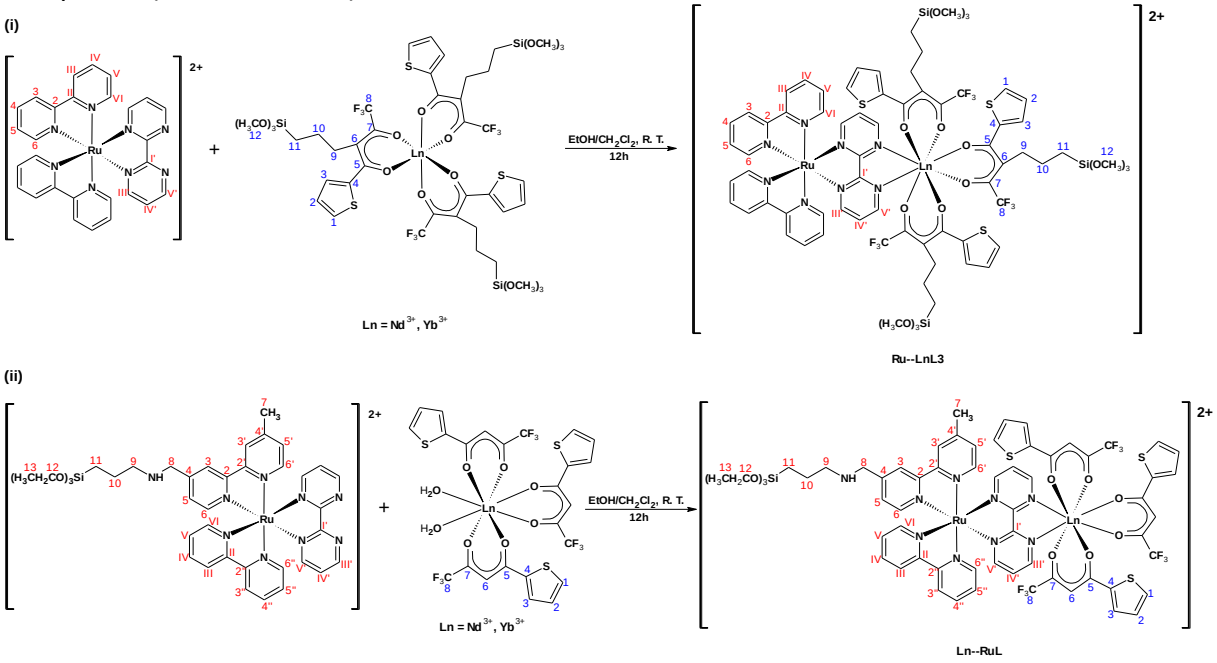

4.3. Spectroscopic characterization of the ruthenium(II), lanthanide(III) and *d-f* heterobimetallic silylated complexes

Figure 31 shows ^{1}H NMR results obtained for the **Ru** complex in MeOD-d_4 (600 MHz). The signals at 9.16 ppm (J = 4.8, 2.0 Hz, 1H), 8.22 ppm (J = 5.7, 2.0 Hz, 1H) and 7.66 ppm (J = 5.7, 4.8 Hz, 1H) are double doublet ascribed to the same system and attributed to the bpmd ligand. Peaks at 8.73 (dd, J = 7.9, 4.7 Hz, 2H), 8.20 – 8.12 (m, 2H), 8.02 (ddd, J = 5.6, 1.4, 0.7 Hz, 1H), 7.79 (ddd, J = 5.7, 1.4, 0.7 Hz, 1H) and 7.53 (dddd, J = 20.6, 7.6, 5.6, 1.3 Hz, 2H) ppm are assigned to the bpy ligands.

It is not possible to assign all signals due to the high symmetry of bpy ligands. In this way, TOCSY1D and $^{1}H\{^{13}C\}$ HSQC NMR experiments were performed.

Figure 31. ^{1}H NMR spectrum of the **Ru** complex (MeOD-d_4, 600 MHz).

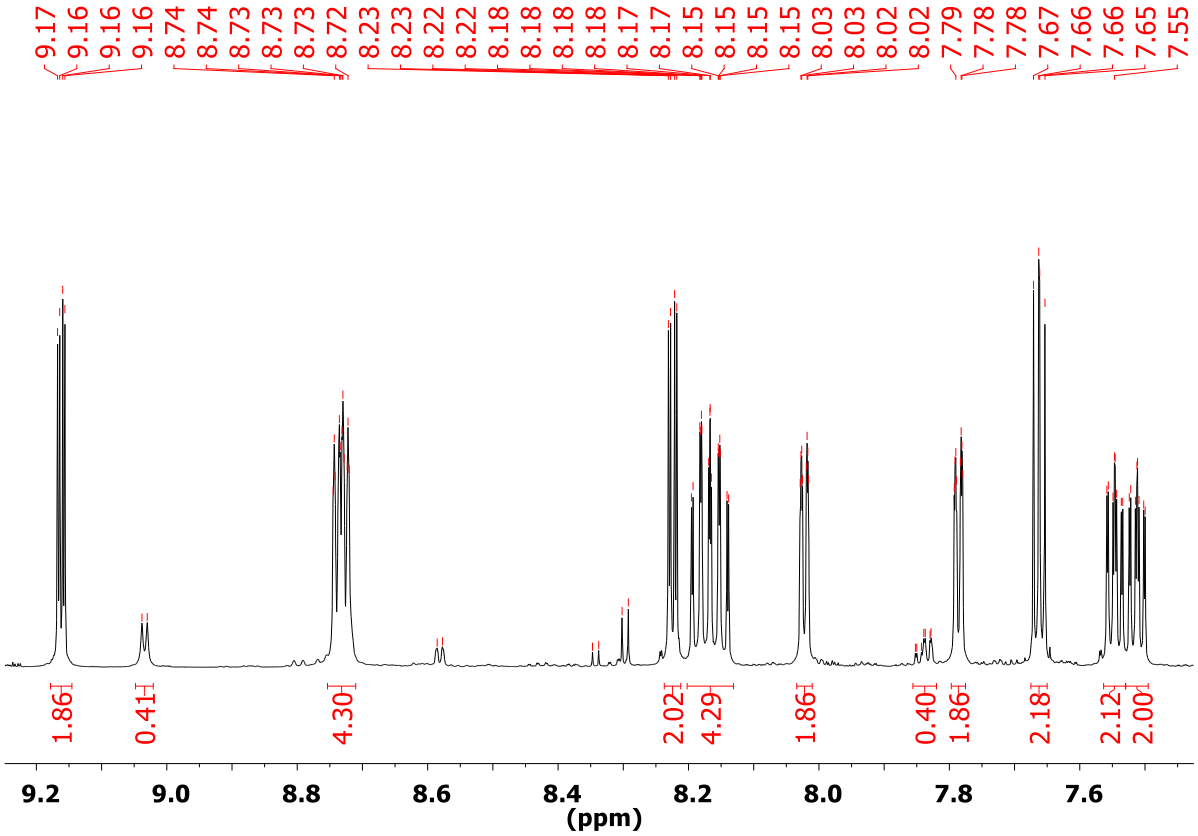

TOCSY1D experiments unravel the connectivity among all the hydrogen atoms in one spin system such as in the bpy rings. The selective TOCSY1D allows the selection of one specific spin systems out of a complex spectrum. TOCSY1D NMR experiments are displayed in figure 32.

Figure 32. TOCSY1D NMR spectra of the **Ru** complex (MeOD-d_4, 600 MHz) irradiated at (a) 9.16 ppm, (b) 8.02 ppm and (c) 7.78 ppm.

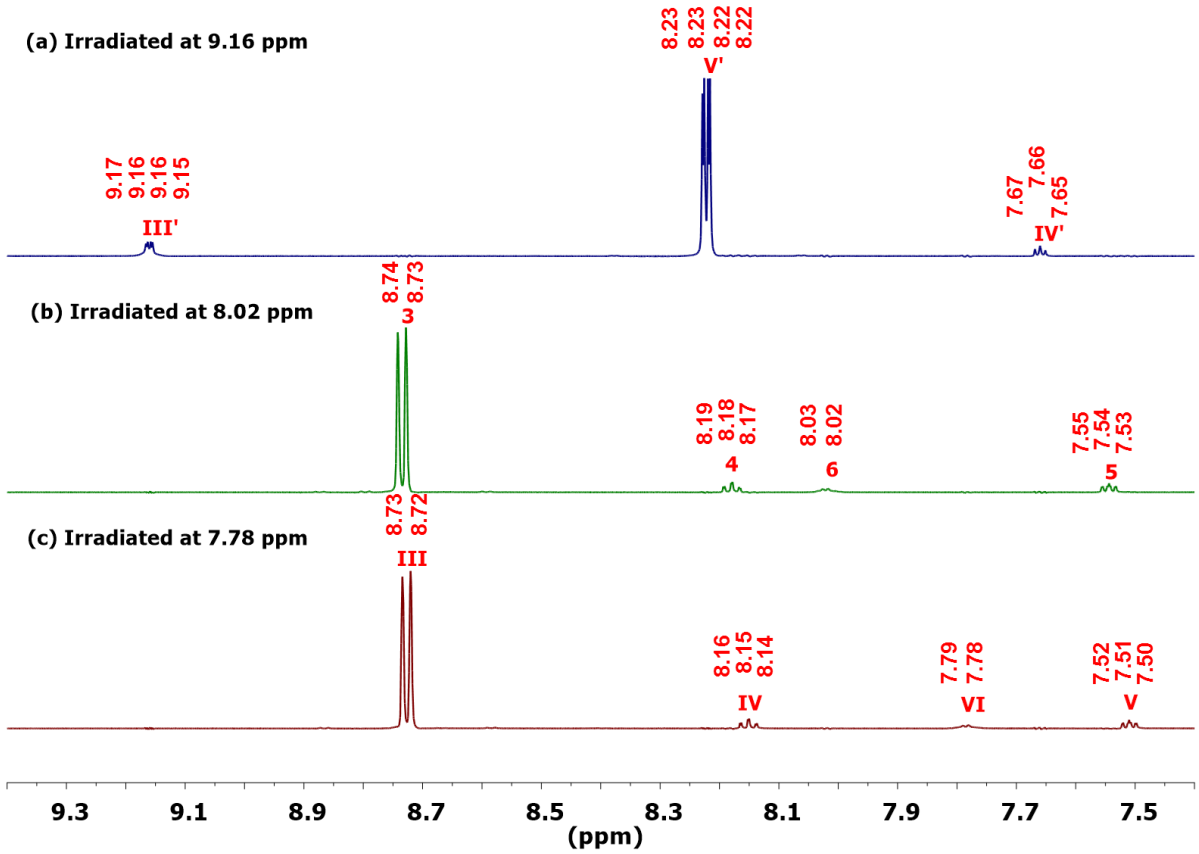

Irradiating selectively at 9.16 ppm (double doublet, J_{H-H}=4.8 and 2.0Hz) three signals were observed in the same spin system. At 8.22 (double doublet, J_{H-H}=5.7 and 2.0Hz) and 7.66 (double doublet, J_{H-H}=5.7 and 4.8Hz) ppm the signals correspond to the hydrogens V' and IV', respectively. Figure 32(a) shows signals corresponding to the hydrogen III'. This spin system containing three hydrogens atoms correspond to the **bpmd** ligand numbering in the figure 29 (i).

Irradiating at 8.02 ppm (figure 32 (b)) assigned to the hydrogen 6, four signals were observed in the same spin system, at 8.73 (doublet), 8.18 (triplet) and 7.54 (triplet) ppm, attributed to the hydrogens 3, 4 and 5 in the ring of bpy, respectively.

Irradiation at 7.78 ppm (doublet, figure 32 (c)) ascribed to the hydrogen VI, it was possible to observe correlations in the same spin system with signals observed at 8.72 (doublet), 8.15 (triplet) and 7.51 (triplet) ppm, assigned to hydrogens III, IV and V in the ring of bpy, respectively.

These results obtained by TOCSY1D experiments show that bpy ligands are present in two distinct conformations in the **Ru** complex.

Figure 33. $^{1}H\{^{13}C\}$ HSQC NMR spectra of the **Ru** complex (MeOD-d_4, 600 MHz) in the aromatic region. The numbering of C and H atoms is given for the complex and present in both spectra.

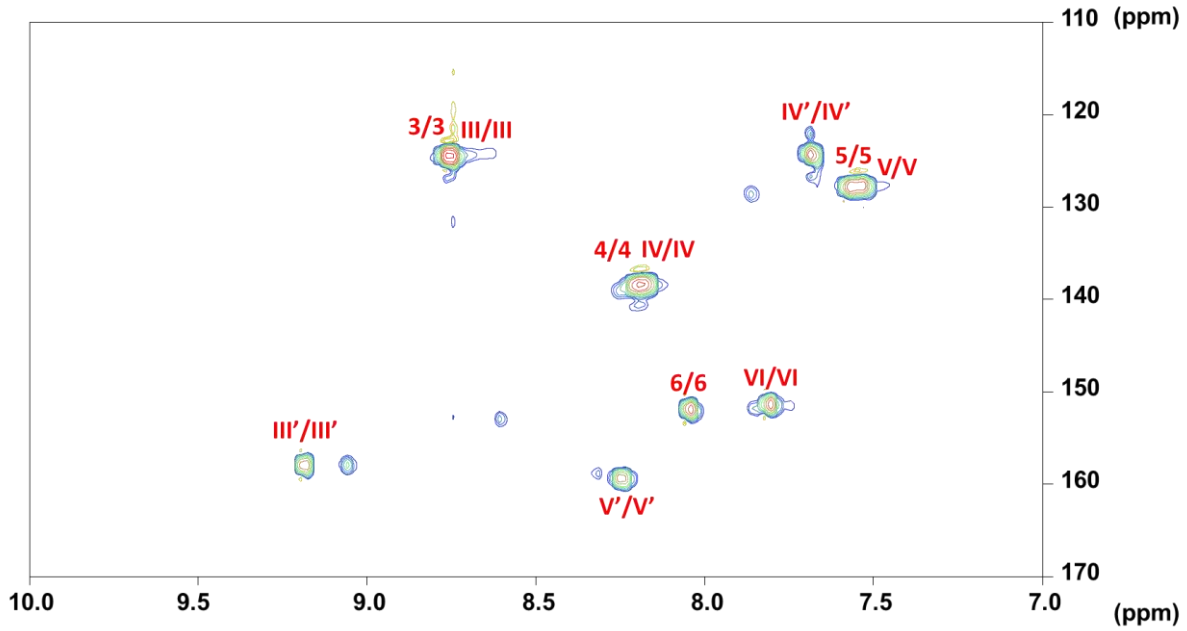

The assignments of the ^{13}C NMR signals of the **Ru** complex were obtained from the $J_{H\text{-}C}$ coupling observed in $^{1}H\{^{13}C\}$ HSQC NMR correlation map. It is worth noting that the correlation map (aromatic region) present the same color due to phase sensitive detection of multiple bond interaction.[80] For CH_3 and CH, correlations are observed in phase, blue color. In this case (figure 33), all correlations present the same phase (CH correlations, blue color) that is in agreement with the aromatic region relating to the bpy and bpmd ligands. Thus the H-C correlations at 8.73/125.65, 8.17/139.64, 8.02/153.15, 7.79/152.60 and 7.53/128.96 ppm can be ascribed to the bpy ligands. The correlations at 7.66/125.50, 8,22/160,58 and 9.16/159.14 are attributed to the bpmd ligand.

2D Heteronuclear Multiple Bond Correlation, $^{1}H\{^{13}C\}$-HMBC NMR experiment was carried out to complete the **Ru** complex structural characterization and identification for quaternary carbon atoms. $^{1}H\{^{13}C\}$ HMBC NMR data provides information about H bonded to C long range, which are 2-3 bonds away ($^{2,3}J_{HC}$).

Figure 34. $^{1}H\{^{13}C\}$-HMBC NMR spectrum of the **Ru** complex in the aromatic region (MeOD-d_4, 600 MHz).

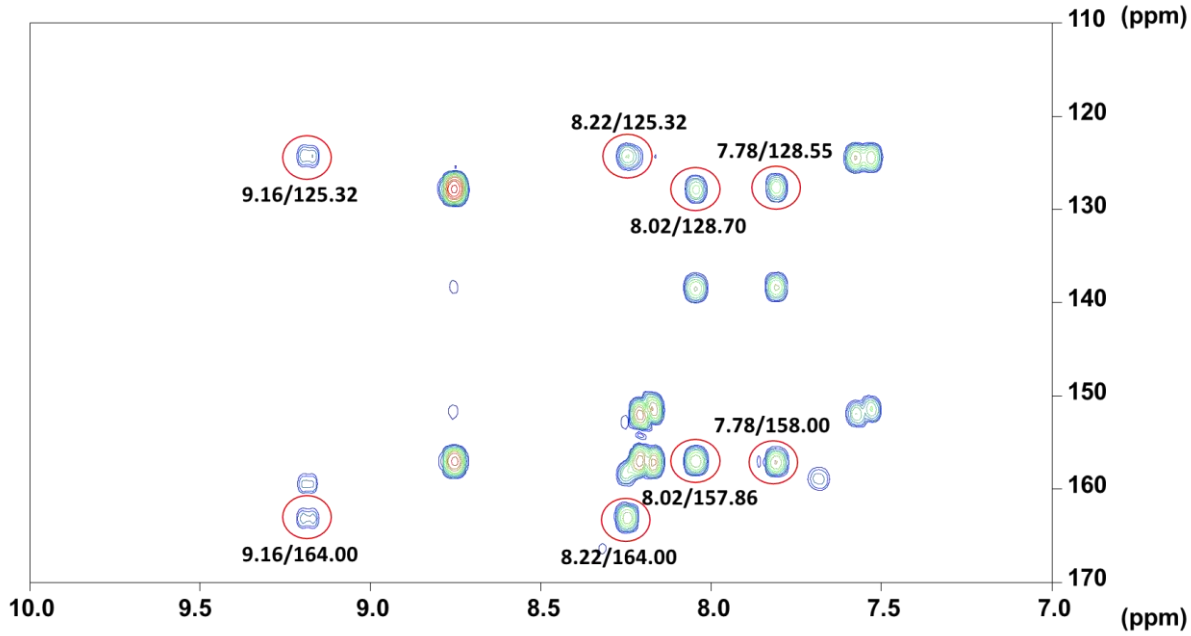

$^{1}H\{^{13}C\}$-HMBC NMR spectrum shows (figure 34) the long range correlations of hydrogen V´ (8.22 ppm) with H-V´/C-IV´ at 8.22/125.32 ppm, and H-V´/C-I´ 8.22/164.00, assigned to the quaternary carbon (I'). In the same way, correlations of hydrogen III´ (9.16 ppm) with H-III´/C-IV´ at 9.16/125.32 ppm, and H-III´/C-I´ 9.16/164.00, assigned to the quaternary carbon (I'). These correlations are in agreement to TOCSY1D and $^{1}H\{^{13}C\}$-HSQC NMR data confirming that at 8.22/160.58 and 9.16/159.14 ppm the signals are ascribed to the V' and III', respectively, present in the bpmd ligand. Besides that the correlations at long range have allowed to characterize the chemical shift for carbon I' at the bpmd ligand. Additionally, correlations of hydrogen 6 (8.02 ppm) with H-6/C-5 at 8.02/128.70 ppm, and H-6/C-2 8.02/157.86, assigned to the quaternary carbon (2). The correlations of hydrogen VI (7.78 ppm) with H-VI/C-V at 7.78/128.55 ppm, and H-VI/C-II 7.78/158.00, assigned to the quaternary carbon (II). Thus $^{1}H\{^{13}C\}$ HMBC NMR experiments confirming TOCSY1D, and $^{1}H\{^{13}C\}$-HSQC NMR data showing the ring of bpy ligand with different conformation due to the slight difference between the long range correlations (H-6/C-5 and H-VI/C-V) and the assignments of two different quaternary carbons (C 2 and II). Therefore, from ^{1}H, TOCSY1D, $^{1}H\{^{13}C\}$-HSQC and $^{1}H\{^{13}C\}$ HMBC NMR HMBC NMR experiments it was possible to determine the most probable structure of the **Ru** complex.

Figure 35 shows the ^{1}H NMR spectrum of the **NdL3** complex. The broadened paramagnetic relaxation enhancement of the lines occurs due to the presence of the Nd^{3+} ion, suggesting a successful synthesis of the **NdL3** complex.

Paramagnetic metal ions not only cause paramagnetic shifts but also enhanced nuclear relaxation, molecular alignment in the magnetic field, and various cross correlation effects. All lanthanide ions except La^{3+} and Lu^{3+} are paramagnetic, resulting in a strong relaxation enhancements and/or significant changes in chemical shift.[81–83]

Figure 35. ^{1}H NMR spectrum of the **NdL3** complex ($CDCl_3$-*d*, 600 MHz).

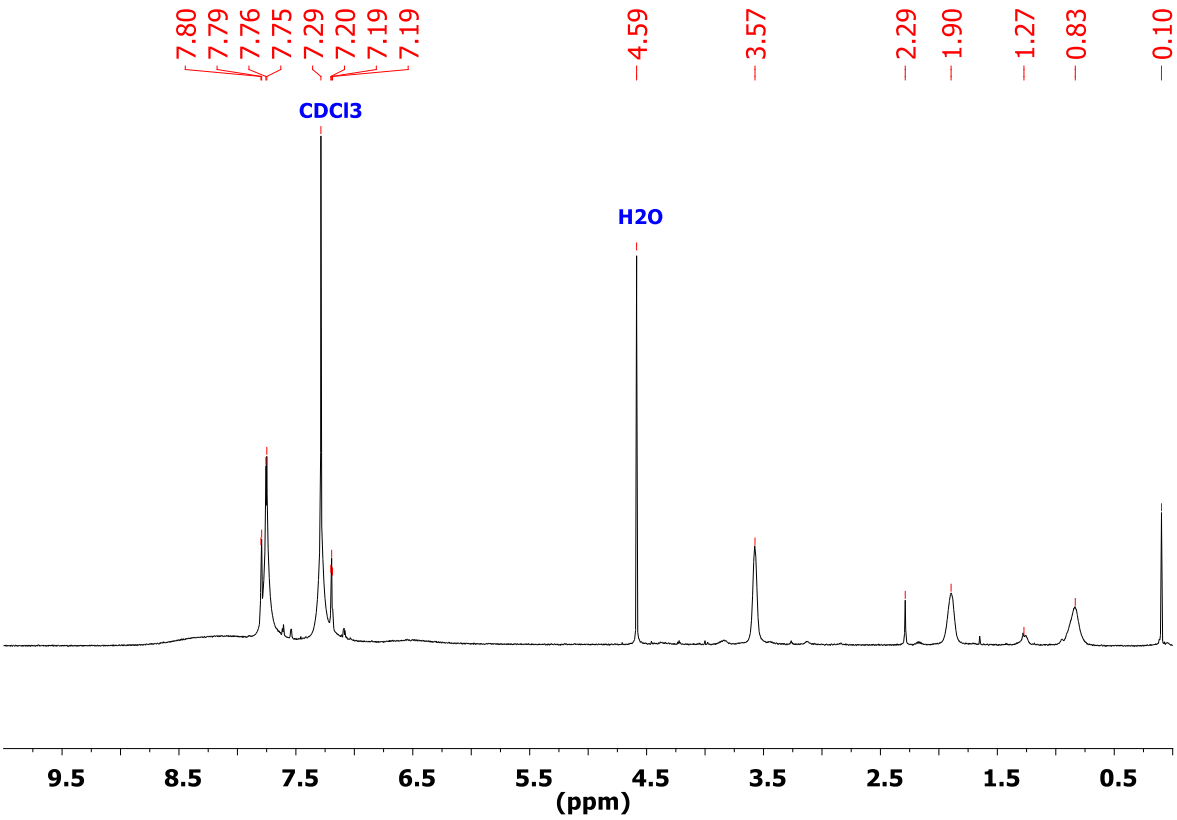

Signals observed at 7.79, 7.75 and 7.19 ppm were attributed to the hydrogen atoms of the thenoyl rings. In addition, for propyl chain the signals were observed at 3.57, 1.90 and 0.83 ppm. The good resolution and the multiplicity signals of three duplet are in agreement with the thenoyl rings; broadened lines was observed for the propyl groups, resulted from different nuclear relaxation enhancements through the complex symmetry.

TOCSY1D experiments unravel the connectivities among all the hydrogen atoms thenoyl rings. The characteristic spin system for the thenoyl rings units was obtained by irradiation of the signal at 7.19 ppm (dd, J_{H-H}=4.5 and 3.4Hz) allowing these hydrogen atoms to be established as belonging to the thenoyl rings units. Figure 36 (a)) shows two signals at 7.74 ppm (d, J_{H-H}=4.9Hz) corresponding to the hidrogen 1 and at 7.79 ppm (d, J_{H-H}=3.4Hz) ascribed to the hidrogen 3 in ortho relationship.

By irradiation at 1.90 ppm (figure 36 (b)), two signals were observed, a broad signal at 0.84 ppm that corresponds to the hydrogen 11 and, at 3.57 ppm, a signal ascribed to the hydrogen 9 (numbering in the figure 29 (iii)).

Thus, that technique corroborated that the signal at 1.90 ppm is assigned correctly to the hydrogen 10 and the hydrogen coupling observed can be attributed to the propyl chain present in the **NdL3** complex.

Figure 36. TOCSY1D NMR spectra of the **NdL3** complex ($CDCl_3$-*d*, 600 MHz) irradiated at (a) 7.19 ppm and (b) 1.90 ppm.

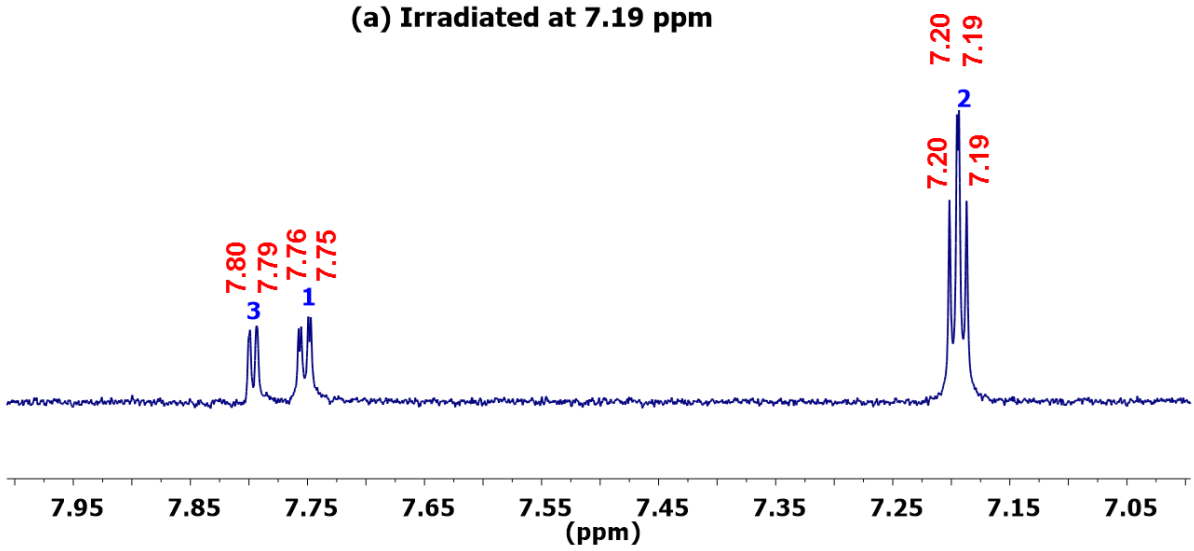

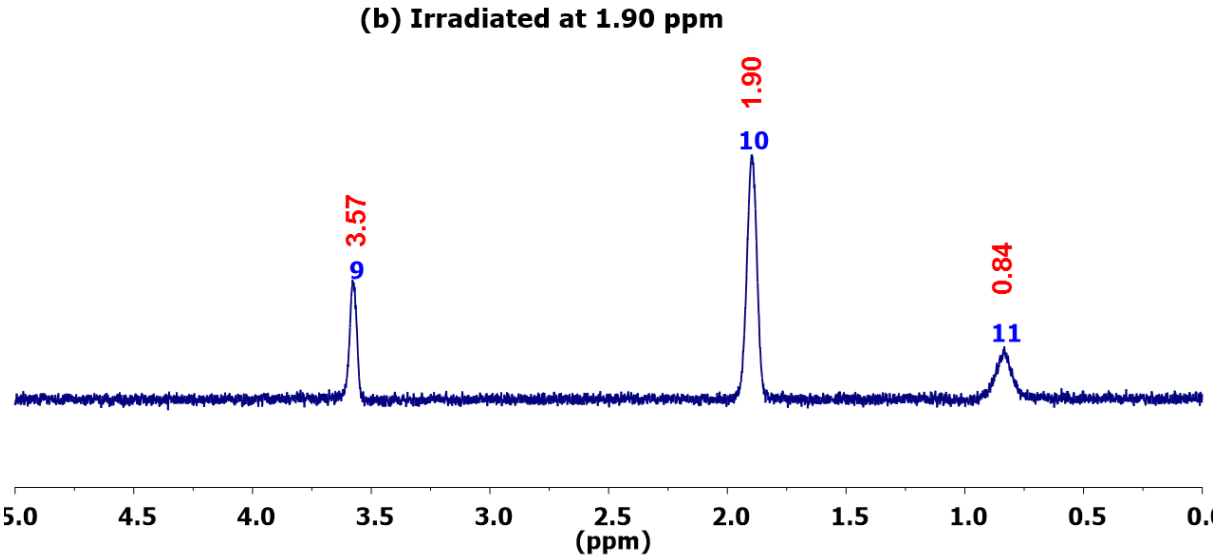

The complete assignments of the ^{13}C NMR signals of the **NdL3** complex were obtained from the J_{H-C} coupling observed in $^{1}H\{^{13}C\}$-HSQC NMR correlation maps. CH_2 correlations are observed in inverse phase, yellow color, for CH_3 and CH correlations are observed in phase, blue color.[80] In figure 37 (a), the correlation H/C for the different nucleus was observed, e.g., the signals at 0.79/10.42, 1.86 / 26.48 and 3.55/47.19 ppm (yellow color) were ascribed to the H/C for the 11, 10 and 9 nucleus, respectively. Additionally, the correlation observed in phase (blue color) at 3.76/57.95 ppm corresponds to the hidrogen 12, ascribed to the methoxysilyl groups, this is required to be available in this complex for further grafting reactions. In the figure 37 (b), it was possible to analyze the correlation map for the betadiketone ligands (aromatic region). The H/C correlations observed at 7.19/128.51, 7.79/133.10 and 7.74/135.11 ppm correspond to the 2, 3 and 1 nucleus respectively present in the thenoyl rings.

Figure 37. $^{1}H\{^{13}C\}$-HSQC NMR spectra of the **NdL3** complex ($CDCl_3$-*d*, 600 MHz): (a) aliphatic region; (b) aromatic region. The numbering of H and C atoms is given for the complex and present in both spectra.

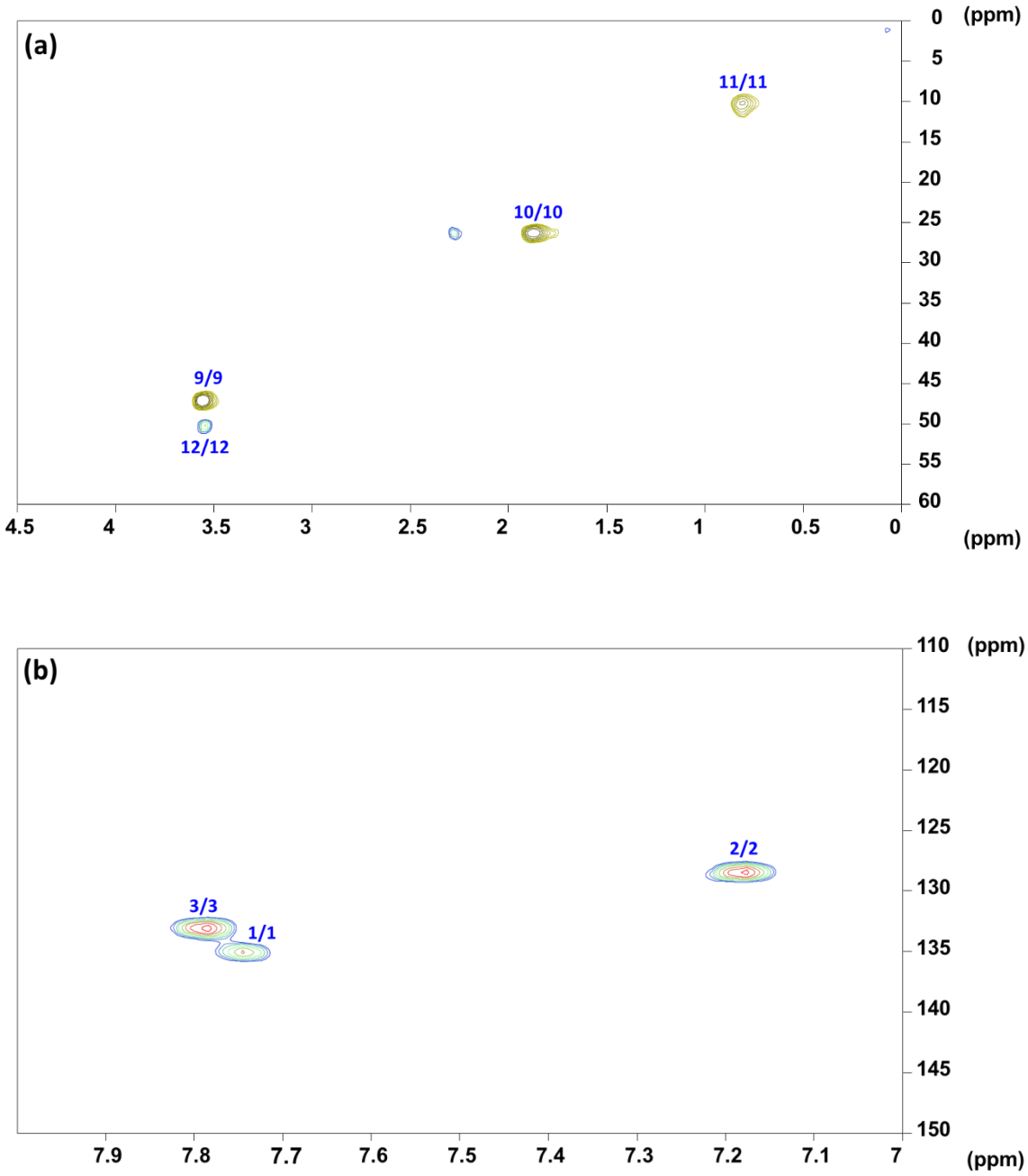

Figure 38 shows a ^{1}H NMR spectrum more detailed than figure 35 by the addition of new signals from the **Ru** portion. The interpretation of that spectrum was supported by TOCSY1D and $^{1}H\{^{13}C\}$ HSQC experiments (figure 39 and 40, respectively). Again, broadly peaks were consequence of the paramagnetic ion (Nd^{3+}) present in the binuclear complex.[83]

Figure 38. ^{1}H NMR spectrum of the **Ru—NdL3** complex (MeOD-d_4, 600 MHz).

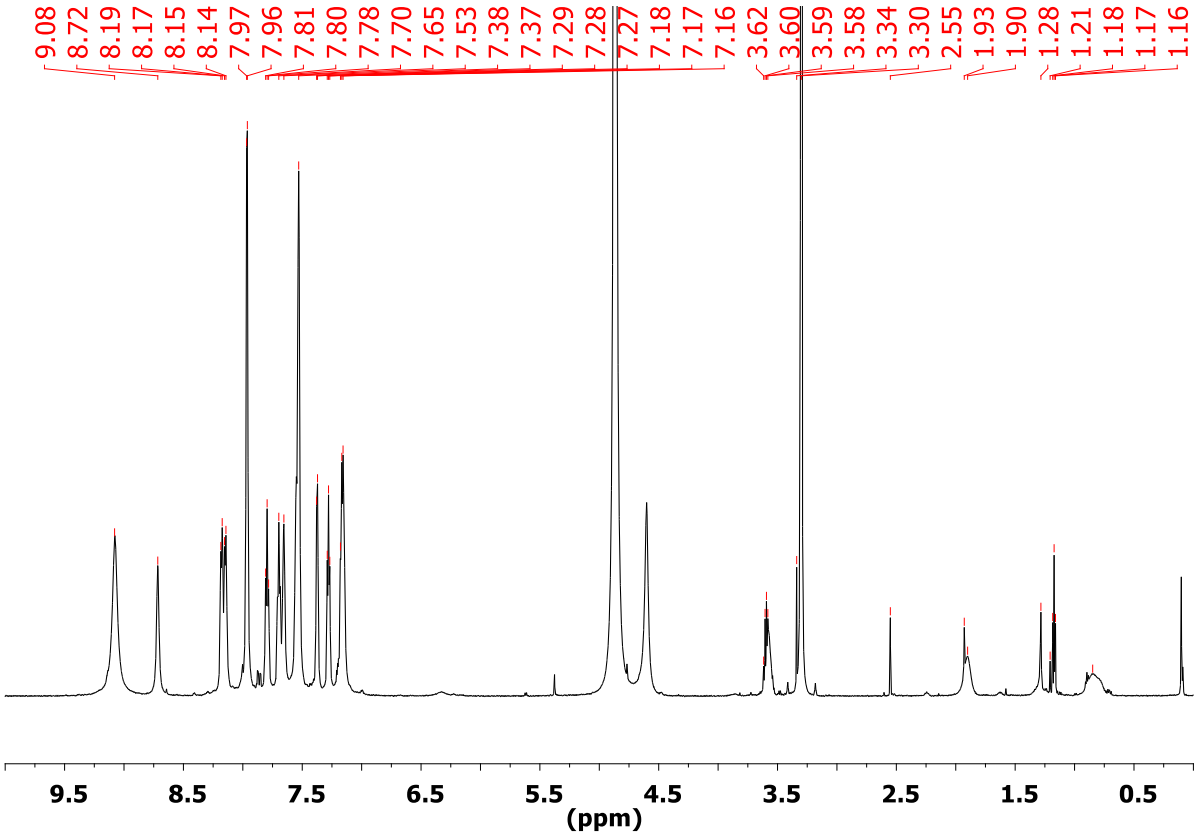

TOCSY1D NMR experiments were carried out and the data shown in figure 31. Initially, by selectively irradiation at 7.97 ppm (d, $J_{H\text{-}H}$=3.8Hz) (figure 39 (a)) the spin correlation was observed with two broadening signals at 9.08 and 7.53 ppm which were assigned to the hydrogen 3 and 2, respectively, present in the thenoyl group at **TTA-Si** ligands. The additional nucleus from TTA-Si ligands were characterized by irradiation at 0.85 ppm (hydrogen 11 at propyl chain, figure 39 (e)), and as consequence, the neighbor hydrogen atoms were detected by two broadening peaks at 1.91 (hydrogen 10) and 3.59 ppm (hydrogen 9). Furthermore, irradiating in the broad signal observed at 7.65 ppm (figure 39 (d) ascribed to hydrogen V´), it was observed correlation in the same spin system with broadened signal at 8.72 and 7.15 ppm attributed to hydrogens III' and IV' in the bipyrimidine ligand, respectively. The ligands **bpmd** and **TTA-Si** were coordinated on lanthanide ion and the TOCSY1D NMR spectra present broad peaks due to the paramagnetic interaction on the nearby atoms. The intensified effect was observed for **Ru—NdL3** complex and it can be attributed to the increase in the size of the complex and consequently decrease in mobility, resulting in a strong relaxation enhancement.[83]

Finally, in order to determine the peaks ascribed to the **bpy** ligands, the noted hydrogen 4 was irradiated (figure 39 (b)) at 7.80 ppm (dd, J_{H-H}=7.7Hz). Four signals were observed in the same spin system, at 8.19 (d, J_{H-H}=7.4 Hz), 7.55 (broadening signal) and 7.29 (dd, J_{H-H}=6.4Hz) ppm, attributed to hydrogen 3, 6 and 5, respectively. After selective irradiation in hydrogen assigned IV at 7.70 ppm (dd, J_{H-H}=6.2Hz, figure 39 (c)), were observed in the same spin system with signals at 8.15 (d, J_{H-H}=5.9Hz), 7.38 (d, J_{H-H}=4.9Hz) and 7.18 (dd, J_{H-H}=6.2Hz) ppm, assigned to hydrogens III, VI and V, respectively.

Figure 39. TOCSY1D NMR spectra of the **Ru—NdL3** complex (MeOD-d_4, 600 MHz) irradiated at (a) 7.97 ppm, (b) 7.80 ppm, (c) 7.70 ppm, (d) 7.65 ppm and (e) 0.85 ppm.

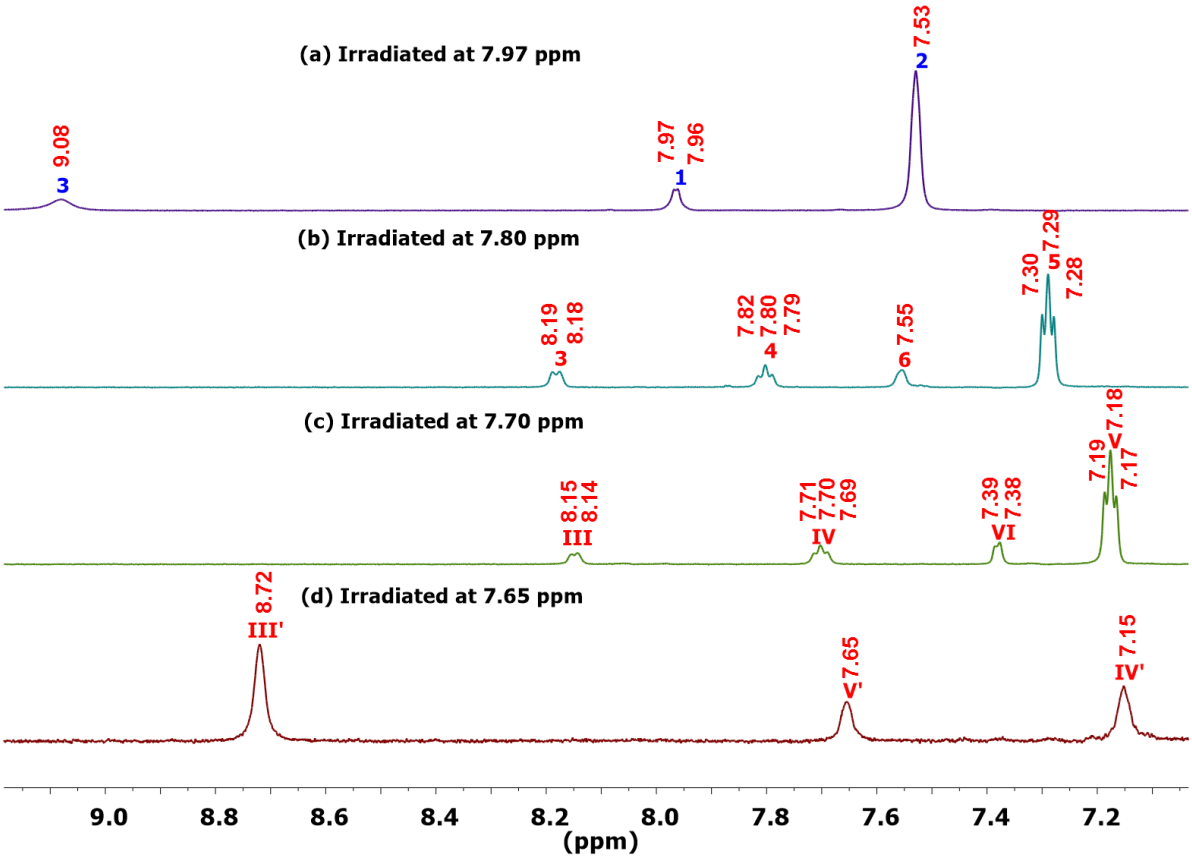

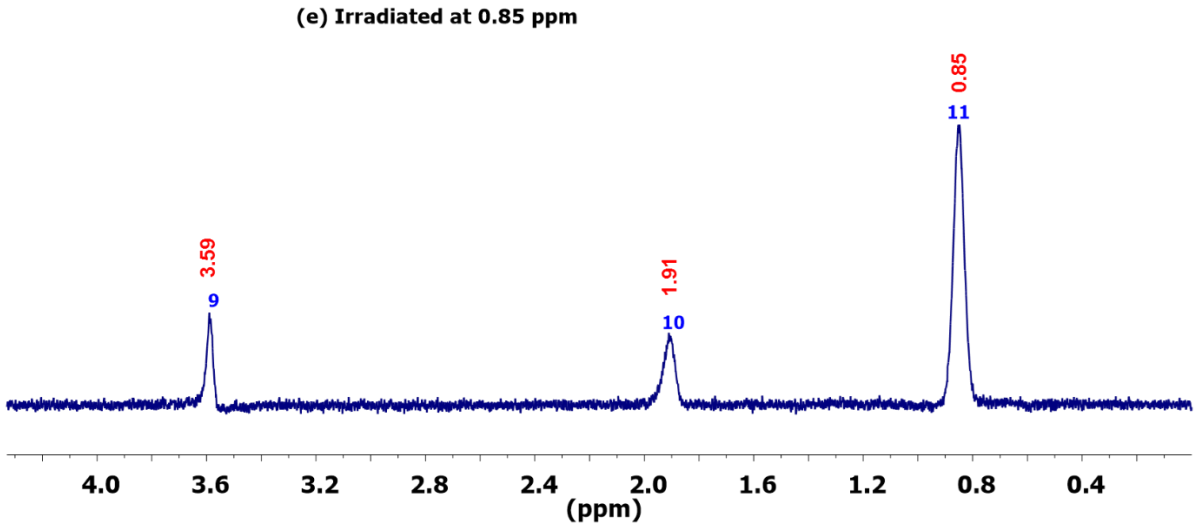

Figure 40 displays the correlation ($^1J_{HC}$) maps for the **Ru—NdL3** complex that corresponds to (a) aliphatic and (b) aromatic atoms. From the correlation maps three correlations present the inverse phase (yellow color), e.g., the H/C at 0.84/11.15, 1.90/27.84 and 3.57/47.98 ppm, figure 32 (a), were in agree with nucleus (at CH_2 propyl chain) noted as 11, 10 and 9 (figure 30 (i)), respectively. The methoxysilyl groups were characterized by the correlation signal in phase (blue color) at 3.57/49.73 ppm as hydrogen 12 (CH_3).

The correlation map (figure 40 (b)) has corroborated the attribution for the nucleus at the thenoyl ring noted as 3, 1 and 2 through the correlations at 9.11/132.11, 7.97/132.11 and 7.53/131.32 ppm, respectively. In addition, the H/C at 8.16/125.49, 7.81/139.62, 7.71/139.46, 7.55/152.91, 7.38/152.40 ppm, 7.28/129.04 and 7.17/128.80 ppm can be ascribed to the bpy ligands noted as 3 (and III), 4, IV, 6, VI, 5 and V, respectively.

Figure 40. $^{1}H\{^{13}C\}$-HSQC NMR spectra of the **Ru—NdL3** complex (MeOD-d_4, 600 MHz): **(a)** aliphatic region; **(b)** aromatic region. The numbering of H and C atoms is given for the complex and present in both spectra.

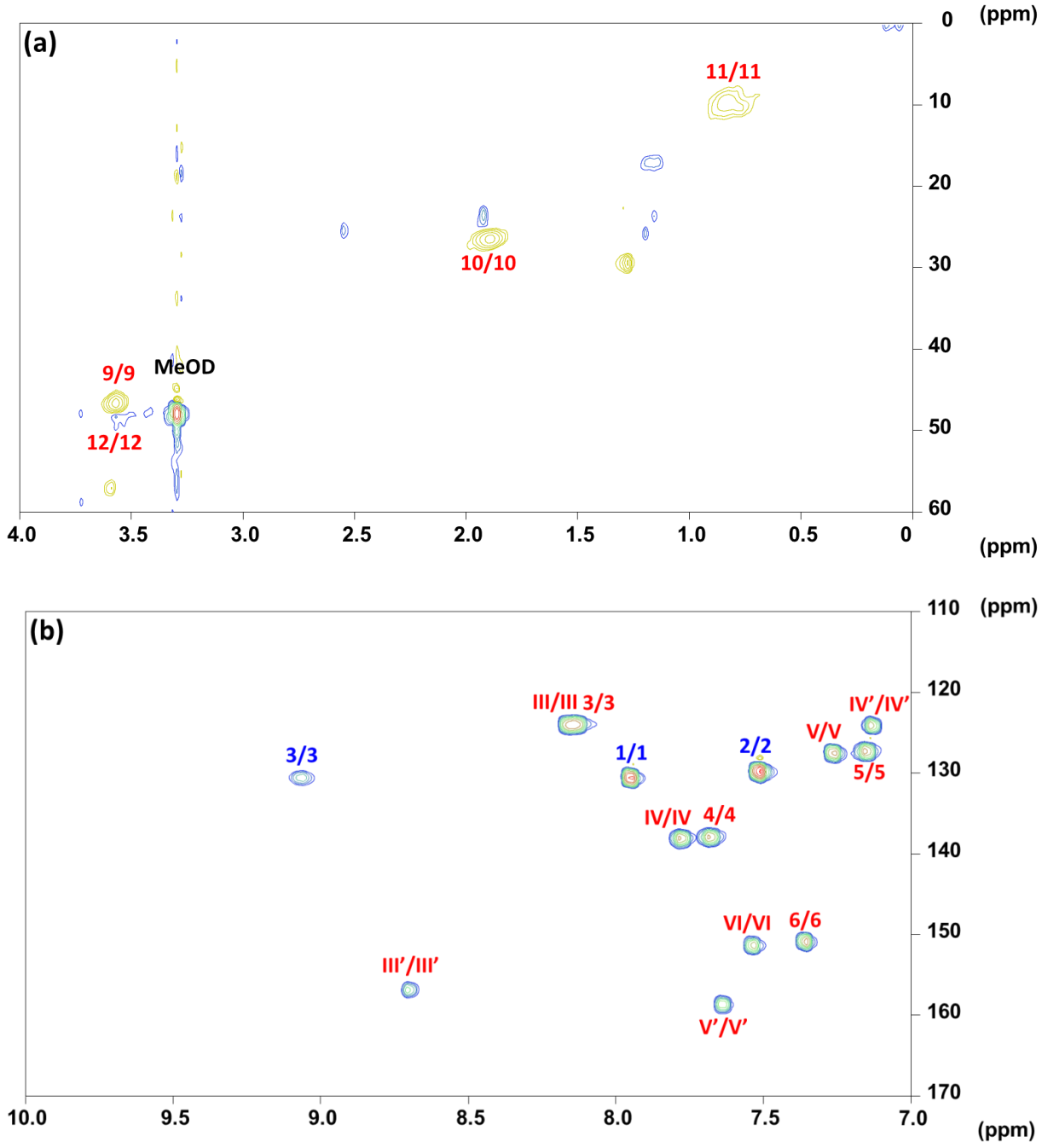

2D Heteronuclear Multiple Bond Correlation,$^{1}H\{^{13}C\}$-HMBC NMR experiment was performed providing the identification for quaternary carbon atoms. As expected, $^{1}H\{^{13}C\}$ HMBC NMR data provides information about H bonded to C long range, which are 2-3 bonds away ($^{2,3}J_{HC}$). The spectrum (figure 41) has showed the long range correlations for hydrogen V´ (7.65 ppm) as H-V´/C-IV´ at 7.65/125.60 ppm, and H-V´/C-I´ 7.65/163.10, assigned to the

quaternary carbon (I'). These correlations are in agreement to TOCSY1D and $^{1}H\{^{13}C\}$-HSQC NMR data, and confirm that at 7.65/160.18 ppm signal as the IV' nuclei.

Figure 41. $^{1}H\{^{13}C\}$-HMBC NMR spectrum of the **Ru—NdL3** complex in the aromatic region (MeOD-d_4, 600 MHz).

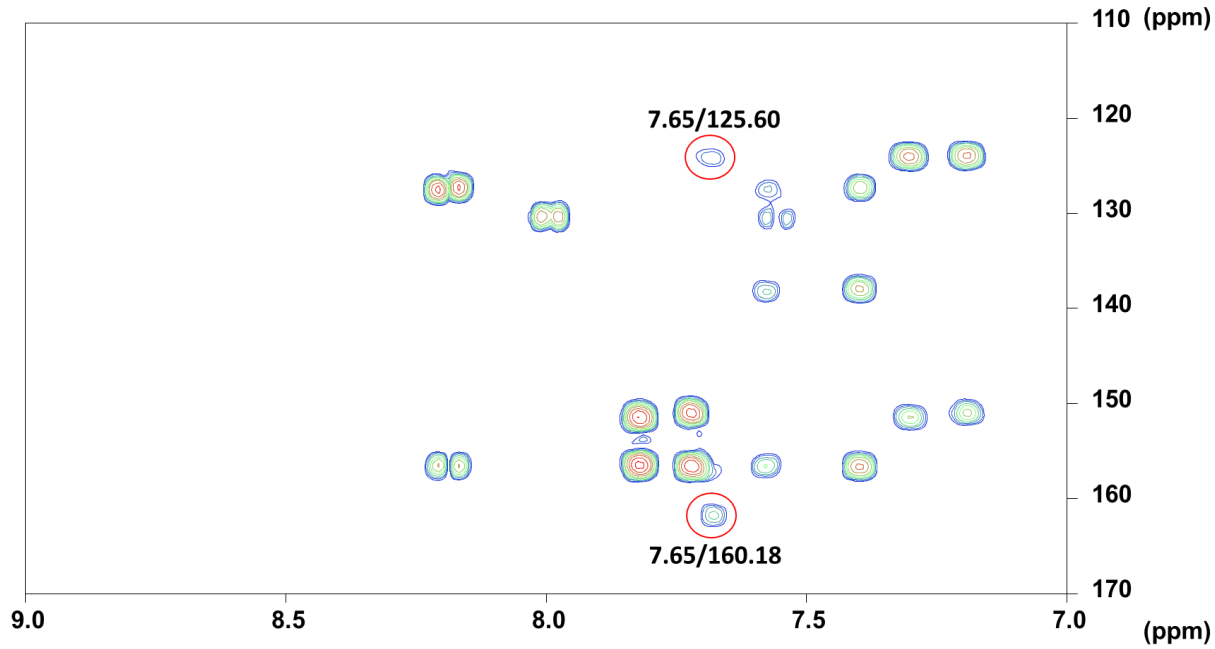

A new **Yb—RuL** complex was prepared by the reaction of **Yb** and **RuL** complexes (1:1) at room temperature in dry and degassed ethanol/dichlorometane.

Figure 42 shows ^{1}H NMR spectrum of the **Yb—RuL** complex. Broadening of signals was observed in the same way observed for the **Ru—NdL3** complex. This observation suggests that the paramagnetic core is present and it may indicate the formation of the binuclear complex.

TOCSY1D, $^{1}H\{^{13}C\}$-HSQC and $^{1}H\{^{13}C\}$-HMBC NMR experiments were performed in order to corroborate with the structural characterization of the **Yb—RuL** complex.

Figure 42. ^{1}H NMR spectrum of the **Yb—RuL** complex (MeOD-d_4, 600 MHz).

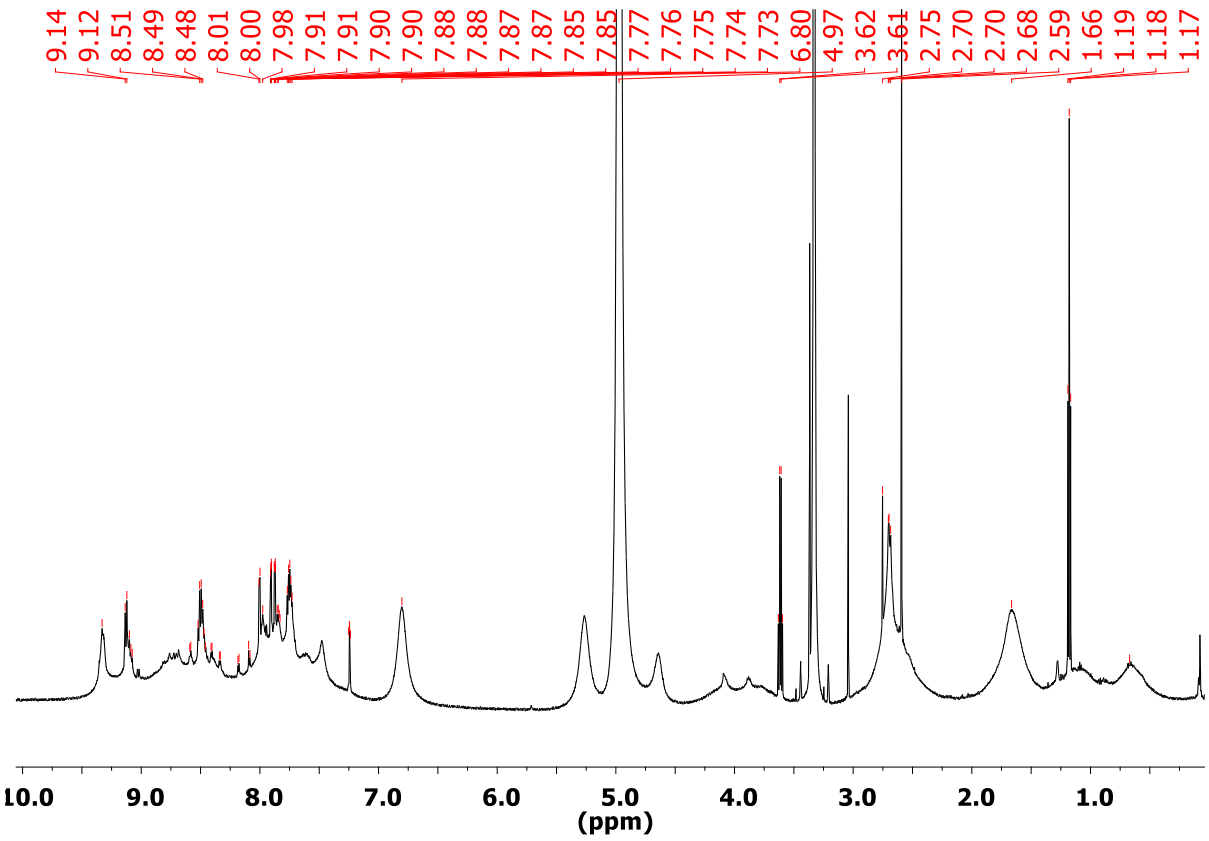

Figure 43 shows the TOCSY1D spectra obtained with different selective irradiation for the **Yb—RuL** complex.

By the selective irradiation at 8.58 ppm (d, J_{H-H}=5.1Hz), figure 43 (a), two signals were observed in the same spin system, at 9.33 ppm (broadening signal) related to the hydrogen III', and at 7.84 ppm (broadening signal) assigned to the hydrogen IV'. The selected signal irradiated (at 8.58 ppm) was in agreement with the hydrogen V', and these protons were attributed to the **bpmd** ligand. In addition, for the irradiation (figure 43 (b)) at 8.18 ppm (d, J_{H-H}=5.4Hz) assigned to hydrogen 6'', it was observed four broad signals in the same spin system, at 9.10, 8.50 and 7.74 ppm, attributed to hydrogens 3'', 4'' and 5'', respectively, present in the bpy ring. The additional hydrogens for the ligand bpy were identified by selective irradiation at 8.01 ppm (d, J_{H-H}=5.2Hz) (assigned to hydrogen VI, figure 43 (c)). It was possible to observe the correlations in the same spin system with broad signals at 9.15, 8.52 and 7.77 ppm as noted to hydrogens III, IV and V, respectively. However, as showed in figure 42, the overlay and broadening of the signals at the range ascribed to the hydrogens in **bpy-Si** ligand made it

hard to identify hydrogen atoms in this system. In other words the TOCSY1D NMR experiment was not conclusive.

Hydrogens atoms (with short $^{1}J_{H\text{-}H}$ coupling) from betadiketonate ligands could be identified. At first, the hydrogen noted 2 (at thenoyl ring) was irradiated at 7.24 ppm (dd, $J_{H\text{-}H}$=4.9 and 4.7Hz, figure 43 (d)), as consequence, two sharp and resolved signals with same spin system at 7.87 ppm (d, $J_{H\text{-}H}$=3.9Hz) and 7.90 ppm (dd, $J_{H\text{-}H}$=3.9Hz), corresponding to the hydrogens 1 and 3 respectively, was observed.

Figure 43. TOCSY1D NMR spectra of the **Yb—RuL** complex (MeOD-d_4, 600 MHz) irradiated at **(a)** 8.58 ppm, **(b)** 8.18 ppm, **(c)** 8.01 ppm, **(d)** 7.24 ppm, **(e)** 2.68 ppm, **(f)** 1.68 ppm and **(g)** 1.18 ppm**.**

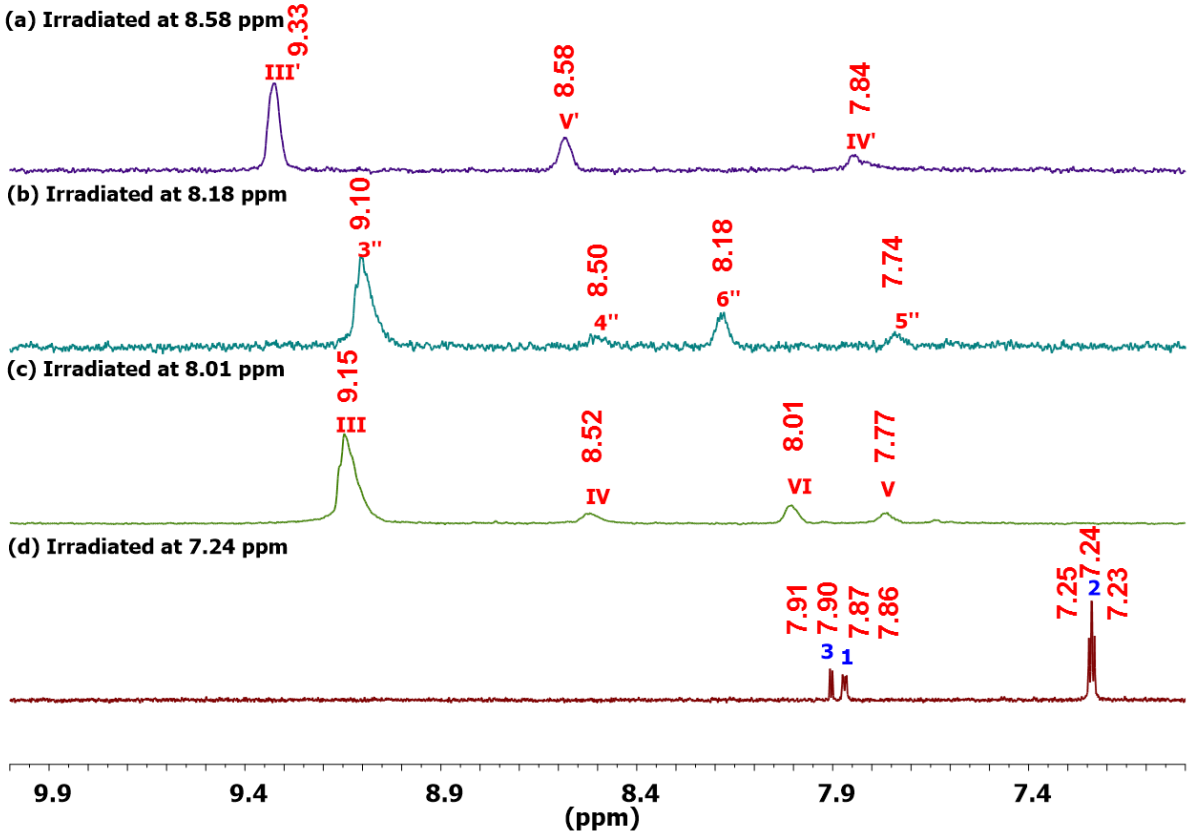

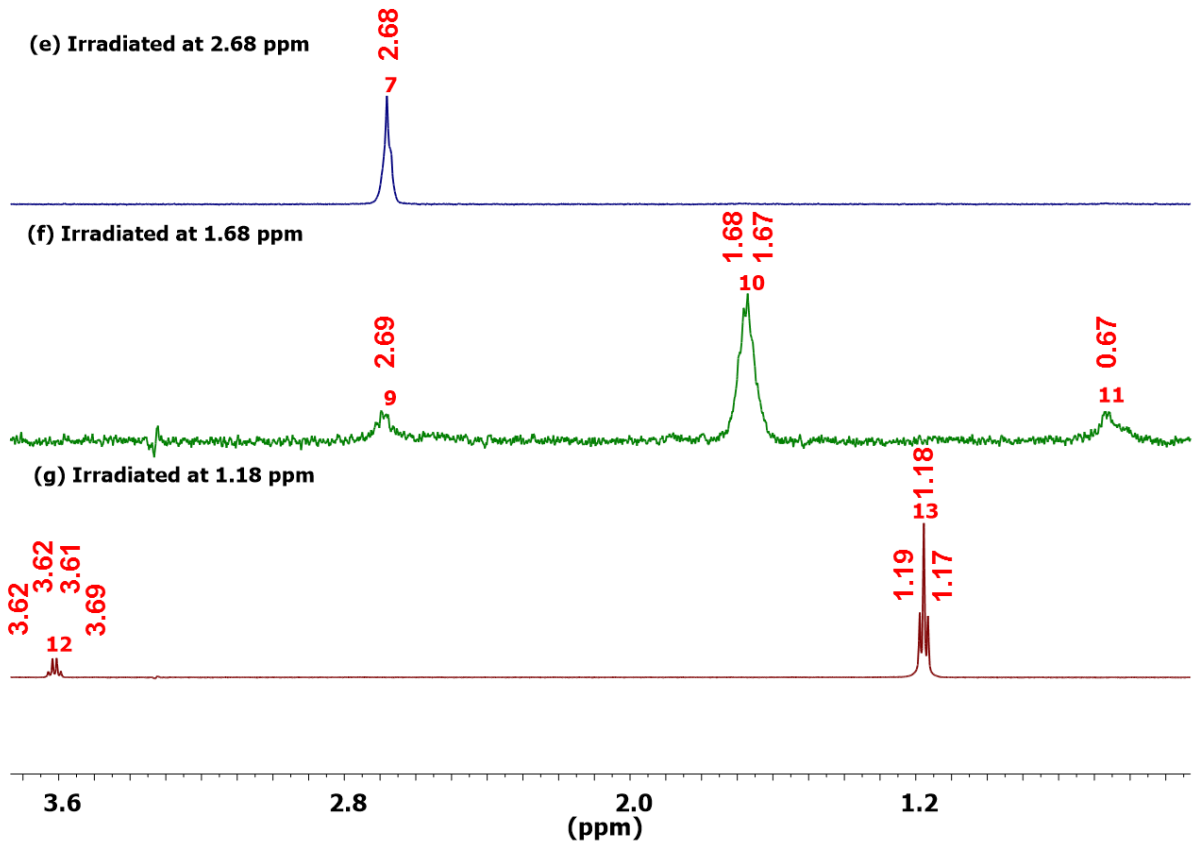

As discussed previously, the identification of the different **bpy** and **bpy-Si** ligands were not possible due to signals overlay. TOCSY1D NMR experiment was performed in the aliphatic range and the data are shown in figure 43 (e-g).

By selective irradiation at 2.68 ppm (broad signal), only the irradiated signal was observed. Therefore, that hydrogen was isolated in the spin system, and there are only quaternary carbons on neighborhood. This hydrogen was attributed to the methyl group (figure 30 (ii)) in the **bpy-Si** ligand.[5, 14] In addition, the hydrogen 10 was selective irradiated at 1.68 ppm (broad signal). Two broad signals in the same spin system were detected at 2.69 ppm and 0.67 ppm, ascribed to hydrogens 9 and 11 of the propyl chain, respectively, as shown in figure 30 (ii). Furthermore, the hydrogen 13 was confirmed by selective irradiation at 1.18 ppm (t, $J_{H\text{-}H}$=7.0Hz). An addition signal in the same spin system was observed at 3.61 ppm (q, $J_{H\text{-}H}$=7.0Hz), which corresponds to the hydrogen 12.

Therefore, these results confirm the presence of ethoxysilyl groups in the **bpy-Si** ligand and, consequently, in the **Yb—RuL** complex.

Hydrogens 9, 10 and 11 (in the propyl chain of the **bpy-Si** ligand) have enhancement relaxation effect due to Yb^{3+} ion paramagnetic; however, this effect was not observed for the hydrogens 12 and 13.

Two-dimensional $^{1}H\{^{13}C\}$-HSQC and $^{1}H\{^{13}C\}$-HMBC NMR experiments were performed to complement the structural elucidation of the **Yb—RuL** complex, as well as the identification of each carbon and hydrogen atoms present in the different chemical environments of hydrogen atoms, e.g. the quaternary carbons.

Figure 44 showed $^{1}H\{^{13}C\}$-HSQC NMR data and the $^{1}J_{HC}$ correlations were divided on aliphatic (figure 44 (a)) and aromatic (figure 44 (b)) regions, and the identification of each H/C was in agree to the labeling at figure 30 (ii). The correlations observed at 0.60/9.61 ppm, 1.62/23.06 ppm and 2.59/47.69 ppm were ascribed to the H/C 11/11, 10/10 and 9/9 respectively. Additionally, the correlation at 2.67/19.95 ppm corresponds to the H/C 7/7 as a methyl group observed in the **bpy-Si** ligand. The correlations at 3.61/56.96 ppm and 1.17/17.07 ppm were ascribed to the 12/12 and 13/13 respectively. These results are consistent with the TOCSY1D NMR data described above and also confirm that **Yb—RuL** complex are available for grafting reactions. The results are in agreement with the $^{1}H\{^{13}C\}$-HMBC NMR data (figures 45 and 46), in which the $J_{H\text{-}C}$ correlations at long range was analysed. Thus, the data set corroborated with the presence of **bpy-Si** ligand with ethoxysilyl groups in the **Yb—RuL** complex.

Figure 44. $^{1}H\{^{13}C\}$-HSQC NMR spectra of the **Yb—RuL** complex (MeOD-d_4, 600 MHz): **(a)** aliphatic region; **(b)** aromatic region. The numbering of H and C atoms is given for the complex and present in both spectra.

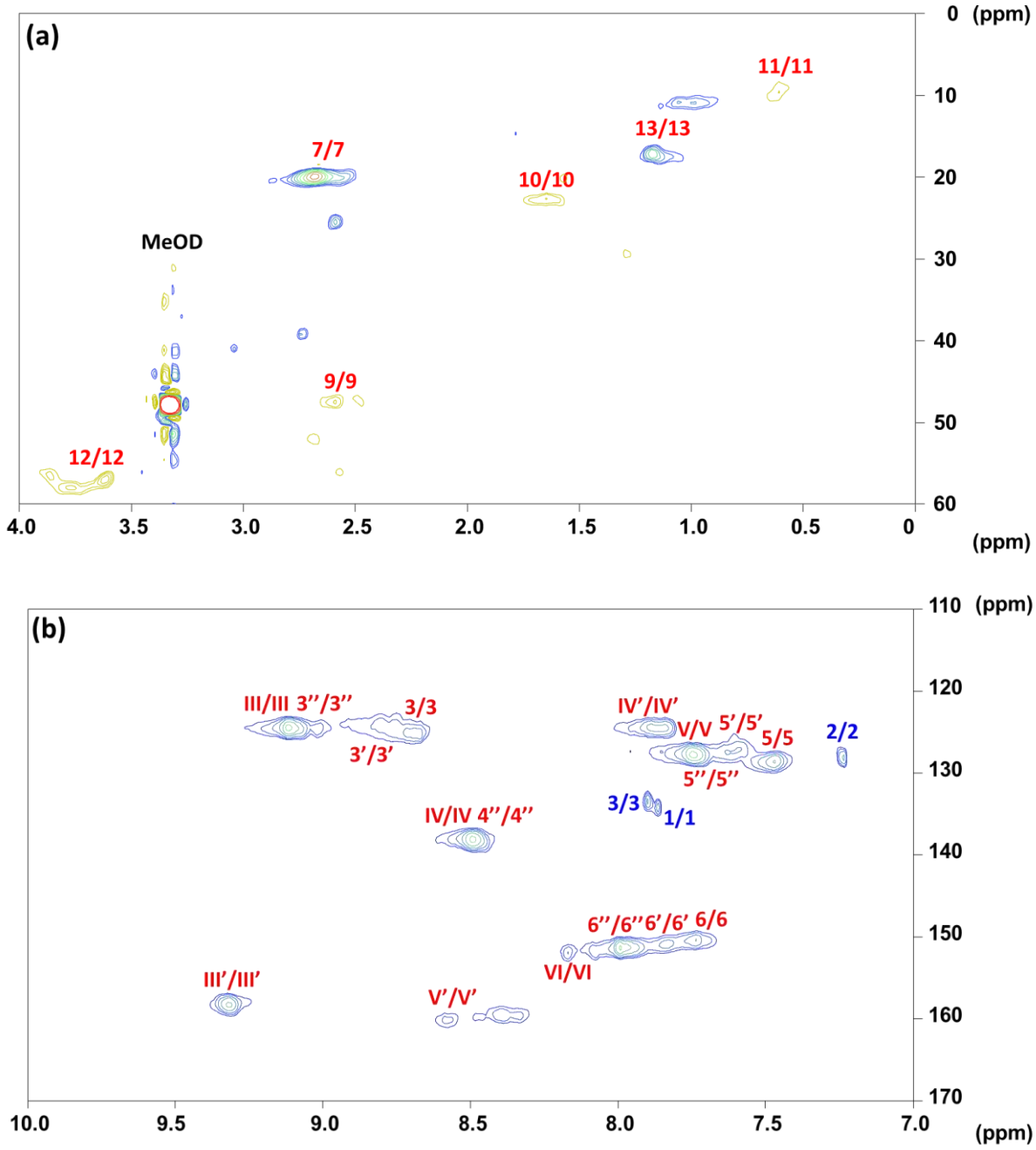

The correlation map for the aromatic region (figure 44 (b)) shows the correlations at 7.24/128.00 ppm, 7.90/133.45 ppm and 7.87/134.15 ppm, corresponding to the 2/2, 3/3 and 1/1 in the thenoyl rings in the betadiketone ligands respectively. At 9.33/158.31 ppm, 8.58/160.15 ppm and 7.86/124.45 ppm, the correlations can be ascribed to the III'/III', V'/V' and IV'/IV' respectively and these were confirmed by $^{1}H\{^{13}C\}$-HMBC NMR data (figures 45 and

46) where it was observed the $J_{H\text{-}C}$ long range correlations between the hydrogen III' and carbons V' and IV' respectively. These correlations are ascribed to the **bpmd** ligand.

Figure 45. $^{1}H\{^{13}C\}$-HMBC NMR spectrum of the **Yb—RuL** complex in the aromatic region (MeOD-d_4, 600 MHz).

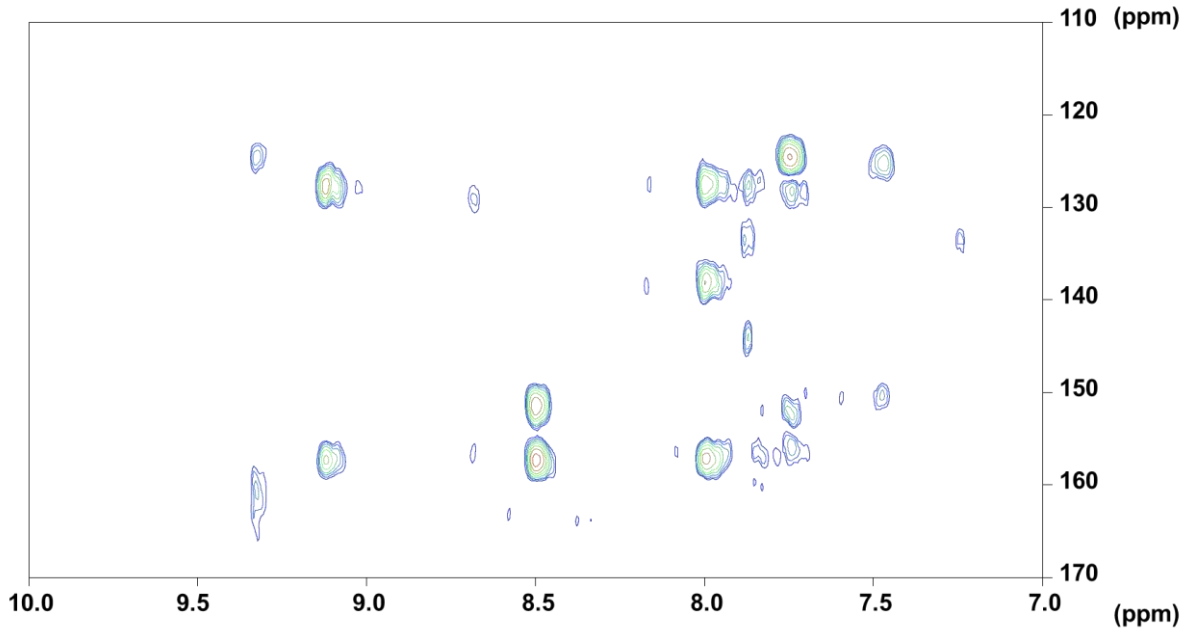

Figure 46. $^{1}H\{^{13}C\}$-HMBC NMR spectrum of the **Yb—RuL** complex (MeOD-d_4, 600 MHz).

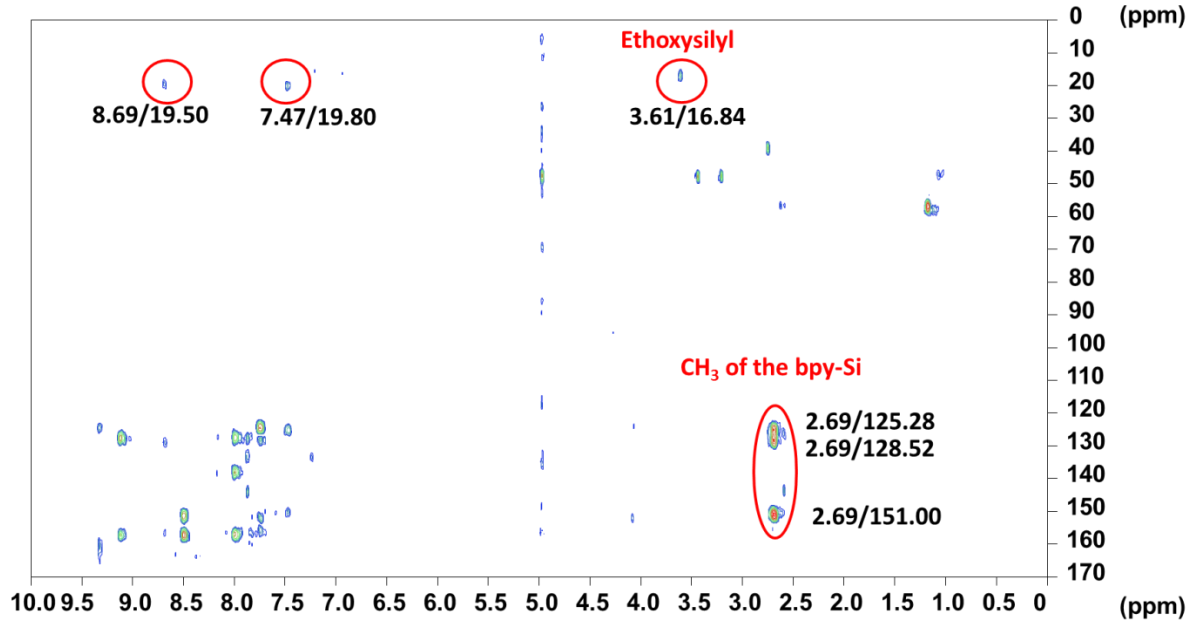

As observed in the TOCSY1D spectra, the signals of **bpy** and **bpy-Si** ligands was overlaid due to the similarity of chemical environments, thus making it difficult to identify the signals

of carbon and hydrogen atoms. However for the **bpy** ligand, the identification could be made by J_{H-C} direct and long range correlation. The correlation observed in the $^{1}H\{^{13}C\}$-HSQC NMR spectrum at 9.15/124.50 ppm, 8.52/138.08 ppm 8.01/151.50 ppm and 7.77/127.58ppm were attributed to the III, IV, VI and V in the ring I of **bpy** respectively. For ring II of the **bpy**, the $^{1}J_{H-C}$ (direct correlation correlation) was observed. At 9.10/124.60 ppm, 8.50/138.18 ppm 8.18/152.00 ppm and 7.74/127.58 ppm, the correlations were attributed to the 3", 4" 6" and 5" respectively. The $^{1}J_{H-C}$ observed was confirmed by $^{1}H\{^{13}C\}$-HMBC NMR spectrum and it was also possible to identify the C-II (157.26 ppm) and the C2" (156.00 ppm) which were observed by J_{H-C} long range correlation with hydrogen atoms III, IV and VI in the ring I and hydrogen atom 5" in the ring II respectively. For the **bpy-Si** ligand, the complete identification was also possible in which we observed that the correlations at 8.68/125.60 ppm, 7.76/150.60 ppm and 7.47/128.70 ppm were attributed to the 3, 6 and 5 respectively.

For the ring of the **bpy-Si** ligand bonded with methyl group, the identification of the carbon and hydrogen atoms was possible by $^{1}H\{^{13}C\}$-HMBC NMR data. The correlation of the J_{H-C} long range (figure 46) and the identification of the correlation for 3', 6' and 5' were observed at 8.70/125.31 ppm, 7.84/151.10 ppm and 7.47/128.38 ppm respectively. Futhermore, correlation of the J_{H-C} long range (figure 46) of hydrogen 12 (3.61 ppm) with H-12/C-13 at 3.61/16.85 ppm are ascribed to the ethoxysilyl groups available in the **Yb—RuL** complex confirming TOCSY1D and $^{1}H\{^{13}C\}$-HSQC experiments.

The results by NMR confirmed that the ethoxysilyl function is present in the **bpy-Si** ligand, and consequently, confirm that the **RuL** complex is available. The correlations attributed to the betadiketones ligands confirmed the successful coordination of **Yb** complex, leading to the **Yb—RuL** complex and the NMR data are consistent with the proposed structure present in figure 30 (ii).

FTIR analyses were performed for all complexes, as described at experimental section (3.1), and those results have supported the proposal structure for each complex and it has corroborated the NMR experiments, elemental analysis and mass spectrometry. An important point is, all reaction process were carried out in anhydrous conditions and it was avoiding the hydrolysis and self-polymerization of metoxysilyl groups, for instance to **NdL3** complex was observed the presence of bands at 1184 ν(Si—O—CH_3), 1060 δ(O—CH_3) and 932 δ(Si—O—C).

These bands (figure 47 (a), green line) were in agreement with NMR experiments already described.

Figure 47. FTIR spectra for the samples (a) **LnL3** (green line), **Ru—LnL3** (blue line), **Ru** (red line) and (b) **Ln** (green line), **Ln—RuL** (blue line), **RuL** (red line), Nd(III) complex at left and Yb(III) at right, all analysis were carried out at KBr pellets.

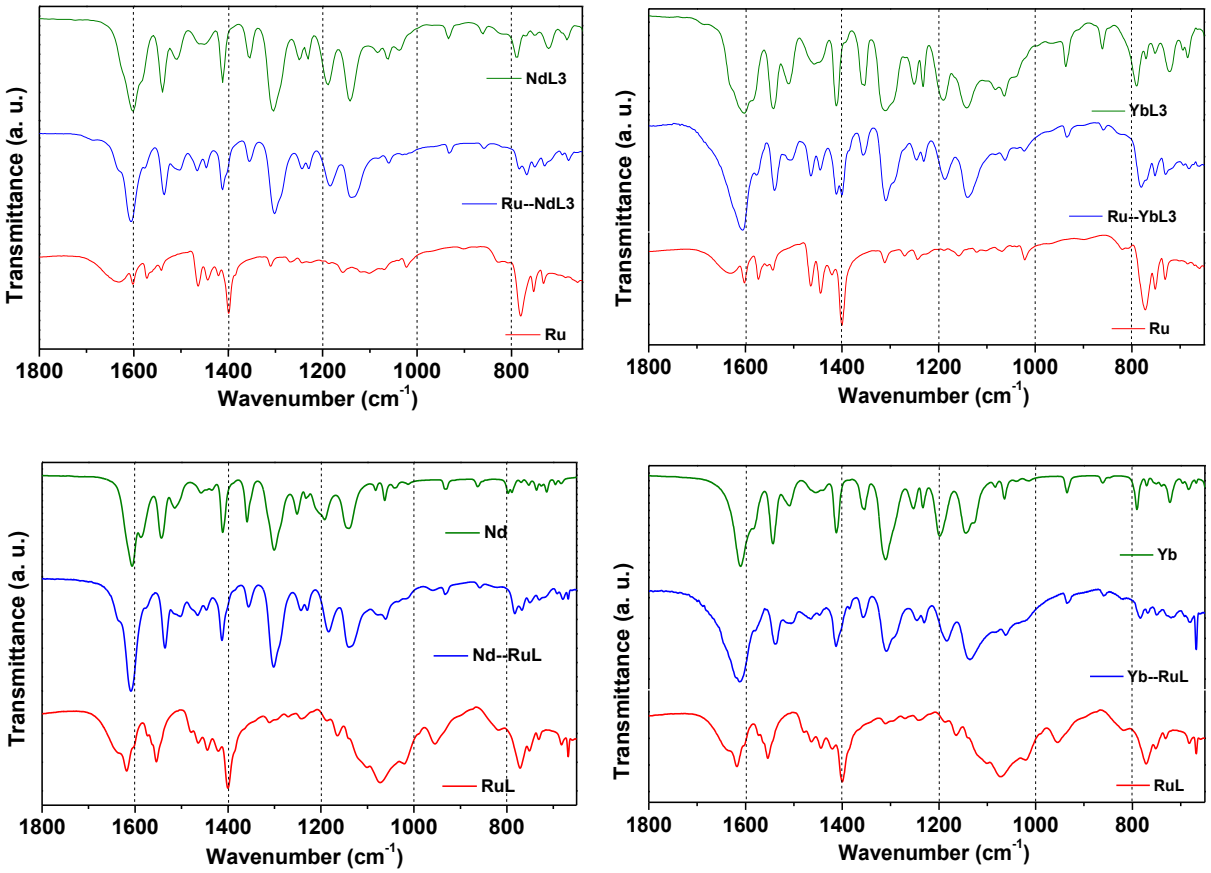

Concerning the **Ru—NdL3** complex (figure 47 (a), blue line), FTIR results show a broad and intense band at 3420 ν_{as}(NH) that may be related with the presence of **Ru** complex. Two bands at 1465 and 1446 cm^{-1} were attributed to ν(C=C) of the **Ru** complex. Additionally, a group of four bands at 784 – 729 cm^{-1} range were assigned as deformation bands δ(CH_{ar}, $CH_{thienyl}$) for **Ru** and **NdL3** complexes. The characteristic stretching vibrations for **NdL3** complex were observed at 1605 ν(C--O); 1535 and 1505 cm^{-1} ν(C--O, C--C) as intense bands. The CF_3 group was characterized by vibration and deformation bands at 1302, 858 and 679 cm^{-1}, respectively. Finally, in agreement with NMR spectra, elemental analysis and mass

spectroscopy experiments, the presence of bands at 1184 ν(Si—O—CH_3), 1060 δ(O—CH_3) and 932 cm^{-1} δ(Si—O—C) have proved the successful synthesis of the heterobimetallic silylated complex. The synthesis methodology has avoided the hydrolysis and sef-polimerisation of the metoxysilyl groups. Additionally, FTIR results obtained for **YbL3** complex (figure 47 (a), green line on the right) were similar to the **NdL3** complex showing bands at 1190 and 1082 cm^{-1} attributed to ν(Si—O—CH_3) and δ(O—CH_3), respectively. These results are in agreement with EA and MS and confirm that methoxysilyl groups are available for grafting reactions. Subsequently, **Ru—YbL3** complex was synthesized similarly to the **Ru—NdL3** complex and FTIR analysis (figure 39 (a), blue line at right) shows a broad and intense band at 3430 ν_{as}(NH) attributed to the **Ru** complex. Bands at 1400 and 1355 cm^{-1} can be attributed to ν(C=C) and ν(C=S $_{thienyl}$), characteristic of **Ru** and **YbL3** complexes, respectively. Characteristic bands at 1185 ν(Si—O—CH_3), 1065 δ(O—CH_3) and 931 δ(Si—O—C) proof that the reaction was performed avoiding the hydrolysis and sef-polimerisation of the metoxysilyl groups. These results can be supported by NMR, EA and MS experiments, with the molecular peak at m/z = 946 [M^{2+}/2].

A new ruthenium silylated complex (**RuL**) was synthesized using the **bpy-Si** ligand (named **L**) according to the method developed by Menu and co-workers (see experimental section (3.1.2)).[1] For this complex, the FTIR analysis has evidenced the presence of non-hydrolyzed ethoxysilyl groups by two bands at 1072 and 955 cm^{-1}, assigned to ν(Si—O—C) and ν(Si—O), respectively. These results were in agreement with NMR spectra, elemental analysis and mass spectrometry (molecular peak at *m/z* = 409.5 [M^{2+}/2]). The **Yb** complex was successfully obtained and characterized was described in the experimental section (3.1.3). At last, the new **Yb—RuL** complex (described in the experimental section (3.1.4)) was carried out and the FTIR results corroborated with the heterobimetallic proposition; bands at 1604 ν(C—O); 1537 and 1506 cm^{-1} ν(C—O, C—C) as ascribed to the **Yb** complex. As well as, the presence of CF_3 group (from **Yb** complex) was shown by the bands at 1305, 858 and 679 cm^{-1}, respectively. Bands at 3432 ν_{as}(NH), 1182 ν(Si—O—CH_3), 1057 δ(O—CH_3) and 930 cm^{-1} δ(Si—O—C) were ascribed to the presence of **RuL** silylated complex. Thus, FTIR results are in agreement with other characterization experiments and confirm the presence of un-reacted ethoxysilyl groups. Additionally, mass spectroscopy confirm too the proposed structure (molecular peak at m/z = 1691 corresponding to [M - Cl]).

Finally, FTIR analysis obtained from **Nd—RuL** complex (figure 47 (b) on the left, blue line) were similar to the **Yb—RuL** complex and shows a broad and intense band at 3430 ν_{as}(NH) attributed to the **RuL** complex. Bands at 1400 and 1355 cm^{-1} can be attributed to ν(C=C) and ν(C=S $_{thienyl}$), characteristic of **RuL** and **Nd** complexes, respectively. Characteristic bands at 1183 ν(Si—O—CH_3), 1057 δ(O—CH_3) and 930 δ(Si—O—C) confirm that the reaction was performed avoiding the hydrolysis and sef-polimerisation of the ethoxysilyl groups. These results can be verified by EA and MS, with the molecular peak at m/z = 1661 [M - Cl].

FTIR results showed several characteristic vibrations and deformations bands attributed to the *d-f* heterobimetallic silylated complexes. However, bands usually ascribed to Ln/Ru–N (or O) vibrations were not be observed by FTIR spectra. On the other hand, a complementary technique FT-RAMAN shown characteristics bands ascribed to Ln—O and Ru—N bonds (figure 48 (a) and (b)).

Figure 48. FT-Raman spectra of (a) **LnL3** (green line), **Ru—LnL3** (blue line), **Ru** (red line) and (b) **Ln** (green line), **Ln—RuL** (blue line), **RuL** (red line).

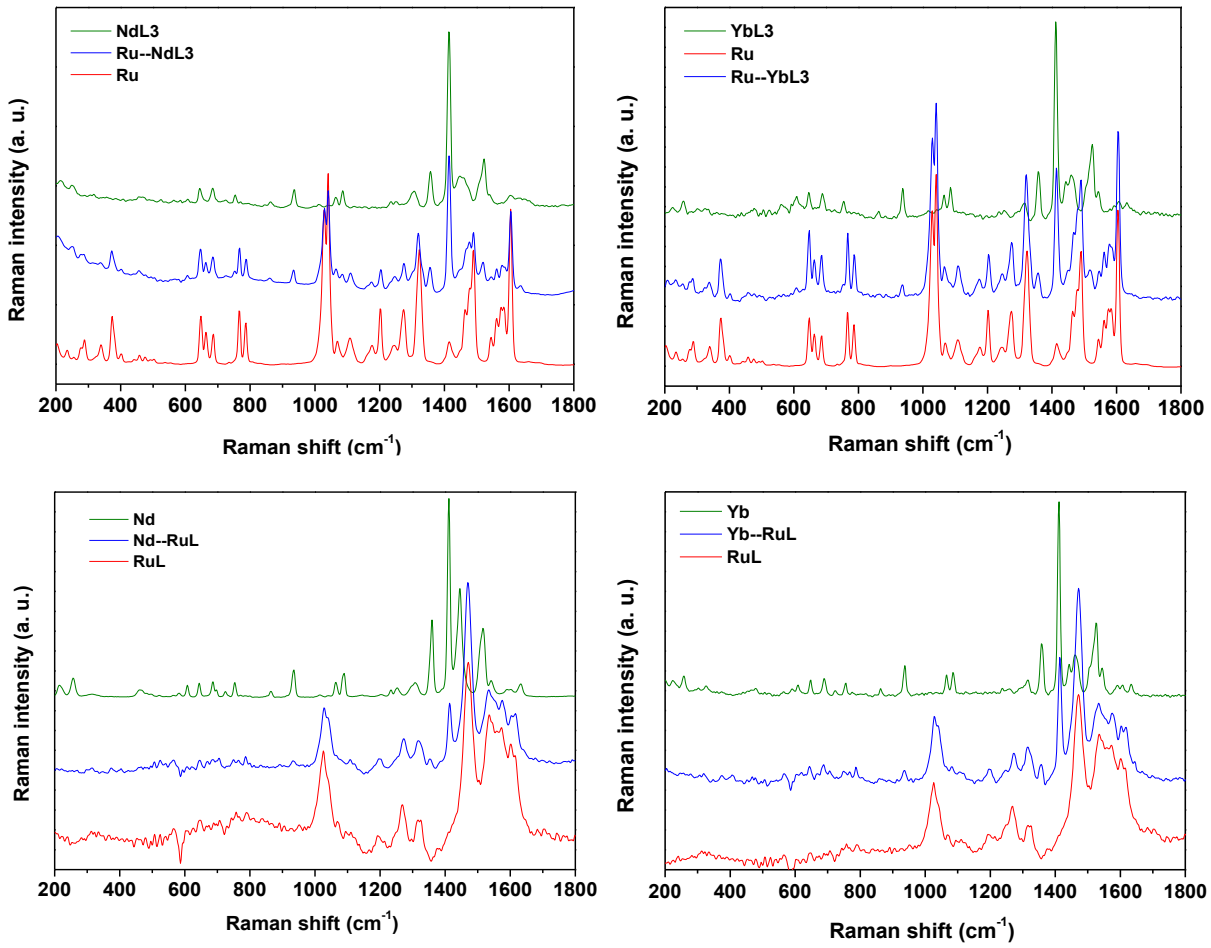

Low intense bands at 210 – 260 cm^{-1} were ascribed to ν(Ln—O), figure 48 ((a), green line) confirming the preparation of the **LnL3** complex.[85, 86]

The Ru^{2+} coordination was confirmed by the bands at 372, 663 and 1030 cm^{-1} ν(Ru—N)[87, 88] (figure 48 (a), red line). The **Ru—LnL3** complex presented the bands observed for the precursors, figure 48 (a), blue line. Bands at 210 – 260 cm^{-1} and 372, 663 and 1030 cm^{-1} were ascribed to the ν(Ln—O) and ν(Ru—N), respectively.[85–88]

FT-RAMAN measurements were also performed to **Ln**, **RuL** and **Ln—RuL** complexes (figure 48 (b)). For the **RuL** (figure 48 (b), red line) and **Ln—RuL** (figure 48 (b), blue line) bands were observed at 1028 cm^{-1}, ascribed to ν(Ru—N).[87, 88] The Ln coordination was supported by the bands at 210 – 260 cm^{-1} ν(Ln—O), figure 48 (b), green line.[85, 86]

Figure 49. Absorption spectra (2,5 x 10^{-5} mol/L, ethanol) of (a) **NdL3** (green line), **Ru—NdL3** (blue line), **Ru** (red line); (b) **YbL3** (green line), **Ru—YbL3** (blue line), **Ru** (red line); (c) **Nd** (green line), **Nd—RuL** (blue line), **RuL** (red line) and (d) **Yb** (green line), **Yb—RuL** (blue line), **RuL** (red line).

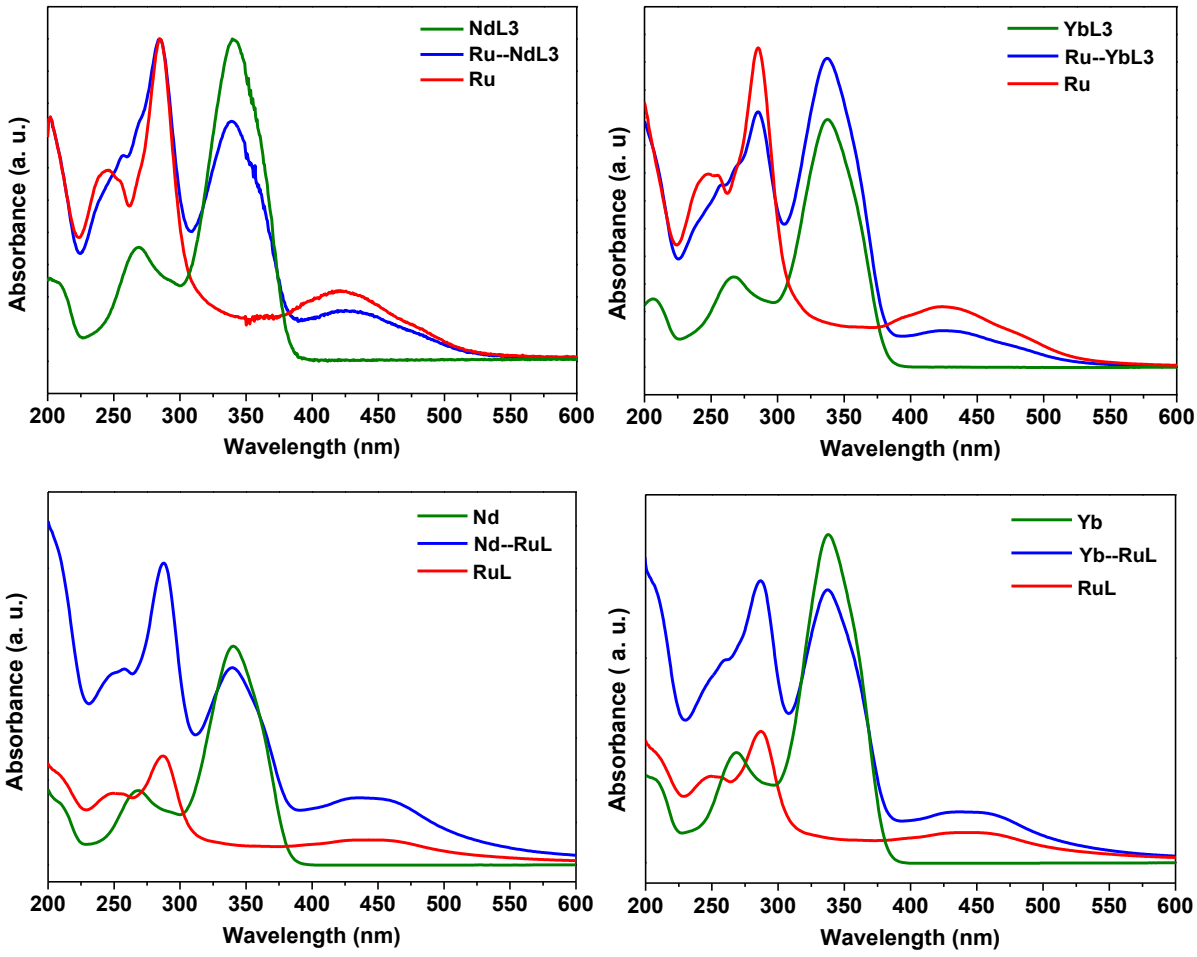

The UV-Vis absorption spectra for **Ru**, **NdL3** and **Ru—NdL3** complexes are shown in figure 49 (a). Figure 49 (a) red line, shows the spectrum obtained for the **Ru** complex. Strong and broad bands are observed at 246 and 424 nm attributed to d→π* ^{1}MLCT (metal-to-ligand charge transfer) transitions: **Ru** to **bpy** and **bpmd** ligands, respectively, and a strong and sharp band at 285 nm attributed to π→π* transitions of **bpy** and **bpmd** ligands.[45] For **NdL3** complex (figure 49 (a), green line), the absorption bands at 268 and 340 nm were assigned to singlet-to-singlet transitions in the **TTA-Si** ligands.[71] The spectrum obtained for **Ru—NdL3** complex (figure 49 (a), blue line) shows the strong and broad absorption bands at 257, 285 and 425 nm, attributed to the π→π* transitions of the ligands coordinated to the ruthenium center and d→π* ^{1}MLCT transitions from the ruthenium center to **bpy** and **bpmd** ligands. The absorption bands at 268 and 339 nm are ascribed to singlet-to-singlet ligands transitions present in the neodymium center.

YbL3 and **Ru—YbL3** were also evaluated by UV-Vis absorption measurements (figure 49 (b), green and blue lines, respectively). The absorption spectra profile is similar to the **Ru—NdL3** complexes, with broad and intense bands regarding to π→π* transitions of the ligands coordinated to the ruthenium center and d→π* ^{1}MLCT transitions from the ruthenium center to **bpy** and **bpmd** ligands (248, 285 and 423 nm). Intense bands at 268 and 340 nm regarding to singlet-to-singlet ligands transitions present in the Yb^{3+} complex.

Thereafter, UV-Vis analysis were carried out for **RuL**, **Nd** and **Nd—RuL** complexes (figure 49 (c)). Concerning the **RuL** complex, the **bpy-Si** was confirmed by bands at 250 and 436 nm, attributed to d→π* ^{1}MLCT transitions from the **Ru(II)** center to **bpy-Si** and **bpmd** ligands (figure 49 (b), red line) and a strong and sharp band at 287 nm attributed to π→π* transitions of **bpy-Si** and **bpmd** ligands. The spectrum obtained for **Nd** complex (figure 49 (c), green line) displays two bands at 267 and 340 nm assigned to singlet-to-singlet transitions in the **TTA** ligands.[71] The spectrum of **Nd—RuL** complex (figure 49 (c), blue line) has displayed strong and broad absorption bands at 260, 287 and 442 nm, characteristic of π→π* transitions of the ligands coordinated to the ruthenium center and d→π* ^{1}MLCT transitions from the ruthenium to **bpy-Si** and **bpmd** ligands. The absorption bands at 258 to 339 nm are assigned to the singlet-to-singlet ligands transitions present in the Nd^{3+} complex.

Figure 49 (d) shows absorption spectra obtained for **Yb** and **Yb—RuL** complexes (figure 49 (d) green and blue line, respectively). **Yb** complex has showed two bands at 267 and 337

nm assigned to singlet-to-singlet transitions in the **TTA** ligands.[71] The spectrum of **Yb—RuL** complex (figure 49 (d), blue line) has displayed strong and broad absorption bands at 260, 287 and 442 nm, characteristic of $\pi \rightarrow \pi^*$ transitions of the ligands coordinated to the ruthenium center and $d \rightarrow \pi^*$ ^{1}MLCT transitions from the ruthenium to **bpy-Si** and **bpmd** ligands. The absorption bands at 271 to 337 nm are assigned to the singlet-to-singlet ligands transitions present in the ytterbium center.

4.4. Luminescent properties of ruthenium(II), ytterbium(III) and neodymium(III) complexes.

Figure 50. Room temperature excitation (on the left, monitoring at $\lambda_{emission}$ = 660 nm) and emission (on the right, excitation at $\lambda_{excitation}$ = 455 nm) spectra of the **RuL1** complex in solid state.

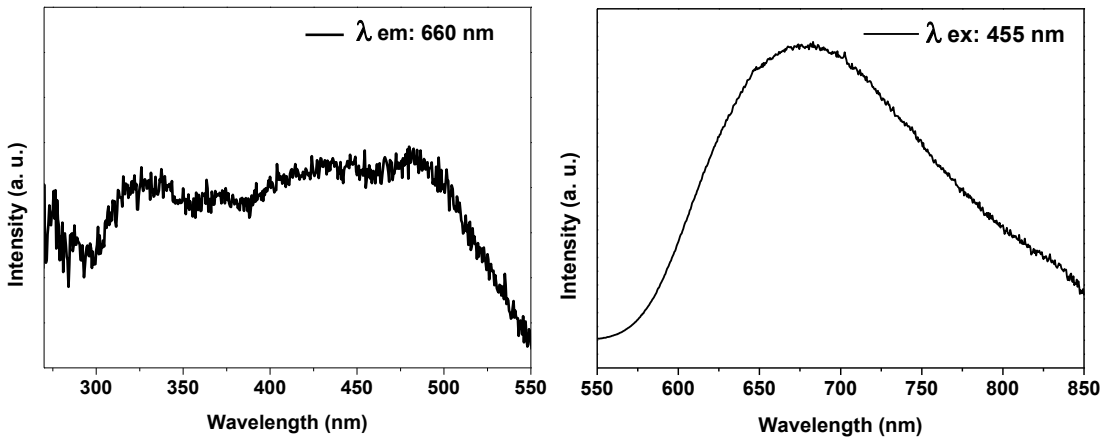

Figure 50 (on the left) shows the excitation spectrum with characteristic bands at 325 and 455 nm relating to transitions centered on the metal, as $\pi_M \rightarrow \sigma^*_M$ and transitions from the singlet of metal-to-ligand charge transfer (^{1}MLCT), as $d \rightarrow \pi^*$, respectively.[74, 89] The characteristic emission band of the **RuL1** complex was observed at 660 nm, as a result of the transition from the triplet MLCT (^{3}MLCT) excited state to the ground state.[74, 89]

Figure 51 shows the luminescence properties of the **Ru** complex. The excitation spectrum was obtained by monitoring the Ru(II) ^{3}MLCT emission to the ground state transition ($\lambda_{emission}$ = 670 nm). Bands up to 400 nm were assigned to transitions centered on ligands ($\pi \rightarrow \pi^*$ transitions) and transitions centered on the metal ($\pi_M \rightarrow \sigma^*_M$ transitions).[45] The band at

475 nm was ascribed to the d→π* ^{1}MLCT (metal-to-ligand charge transfer) transitions, in agreement with the UV-Visible results.

Figure 51. Room temperature excitation (on the left, monitoring at $\lambda_{emission}$ = 670 nm) and emission (on the right, monitoring at $\lambda_{excitation}$ = 475 nm) spectra of the **Ru** complex in solid state.

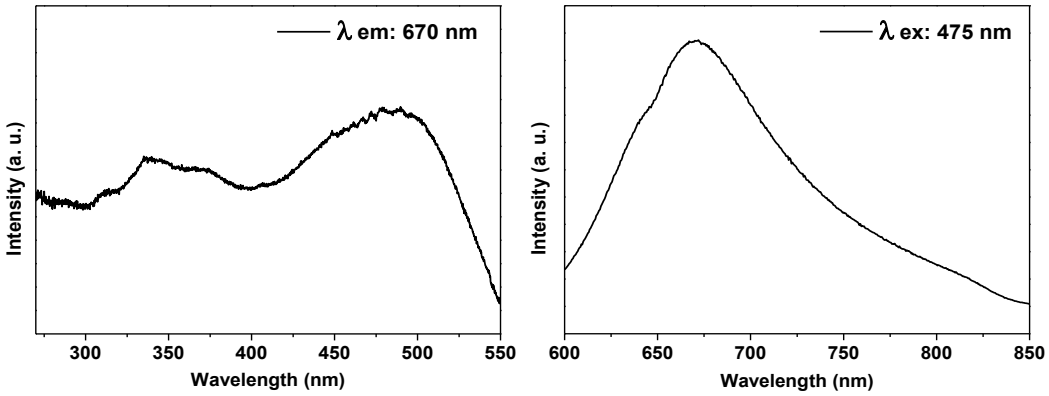

Luminescent measurements were performed for the new **RuL** complex according to the excitation and emission spectra showed in the figure 52. Bands at 282 and 365 nm were assigned to transitions centered on ligands (π→π* transitions) and transitions centered on the metal (π_M→σ^*_M transitions), respectively (figure 52, on the left).[45] The d→π* ^{1}MLCT transition was observed at 465 nm. By monitoring the excitation at 465 nm (figure 52, on the right), the characteristic emission band of the **RuL** complex was at 620 nm, as a result of the transition from the ^{3}MLCT excited state to the ground state.[74, 89]

It is worth to noting that the difference of energy for ^{3}MLCT between the **Ru** and **RuL** precursors complexes may be resulted of different π-donor or π-acceptor behavior by ligands on the complexes, as consequence, the MLCT energy[52] may shifted to red, and that fluctuation will be important for the subsequent obtaining of *d-f* heterobimetallic complexes and efficient energy transfer process.

Figure 53 shows the excitation (on the left) and emission (on the right) spectra from **Nd** complex. The excitation spectrum shows a broad band up to 400 nm ascribed to the singlet-to-singlet transitions in the **TTA** ligands.[71] The bands above 400 nm were attributed to Nd(III) intraconfigurational f-f transitions, observed at 463, 525, 580, 684, 746, 798 and 818 nm.[28, 49] Despite the intensity of the bands are quite similar, the **Nd** complex presents a high absorption cross section of light due to the TTA ligands. In the solid state, the high absorption cross section due to the TTA ligands promotes the saturation emission spectra and the

excitation spectrum was distorted.[71, 90] The emission spectrum (figure 53, on the right) displays two bands at NIR; a sharp band at 1062 nm attributed to $^4F_{3/2} \rightarrow {}^4I_{11/2}$ transition and a low intensity band centered at 1334 nm, ascribed to the $^4F_{3/2} \rightarrow {}^4I_{13/2}$ transition.[28, 45, 49]

Figure 52. Room temperature excitation (on the left, monitoring at $\lambda_{emission}$ = 620 nm) and emission (on the right, monitoring at $\lambda_{excitation}$ = 465 nm) spectra of the **RuL** complex in solid state.

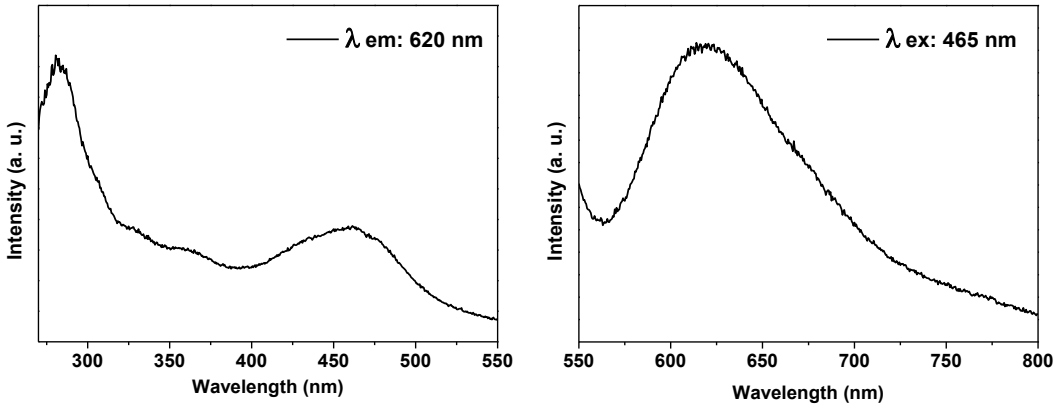

Figure 53. Room temperature excitation (on the left, monitoring at $\lambda_{emission}$ = 1062 nm) and emission (on the right, monitoring at $\lambda_{excitation}$ = 395 nm) spectra of the **Nd** complex in solid state.

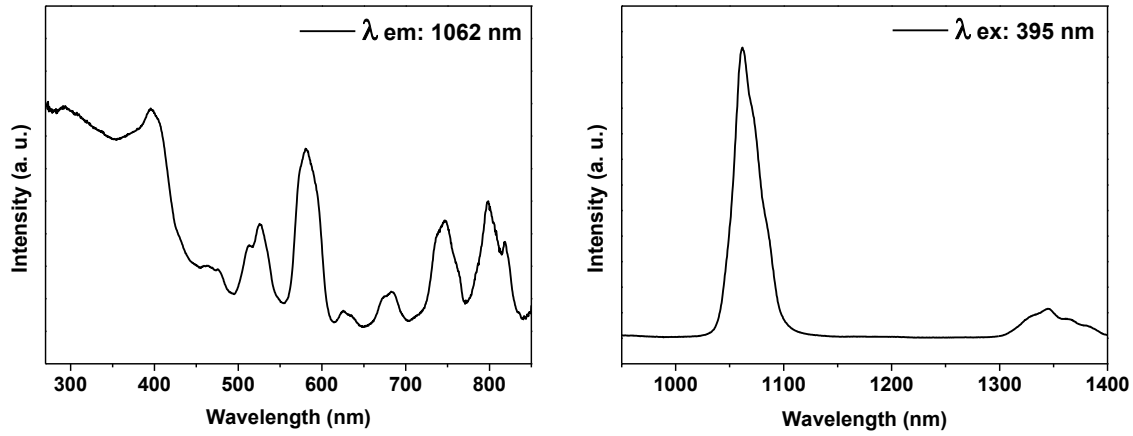

The luminescent properties of **Yb** complex were evaluated and displayed in the figure 54. The excitation spectrum (figure 54, on the left) shows a broad band up to 400 nm quite similar to the **Nd** complex, which was ascribed to the singlet-to-singlet transitions in the **TTA** ligands.[71] By monitoring the excitation at 290, 370 and 395 nm, a broad emission spectra centered at 977 nm with broader components from 1000 to 1050 nm ascribed to the $^2F_{5/2} \rightarrow {}^2F_{7/2}$ transition.[91]

Figure 54. Room temperature excitation (on the left, monitoring at $\lambda_{emission}$ = 977 nm) and emission (on the right, monitoring at $\lambda_{excitation}$ = 395 nm) spectra of the **Yb** complex in solid state.

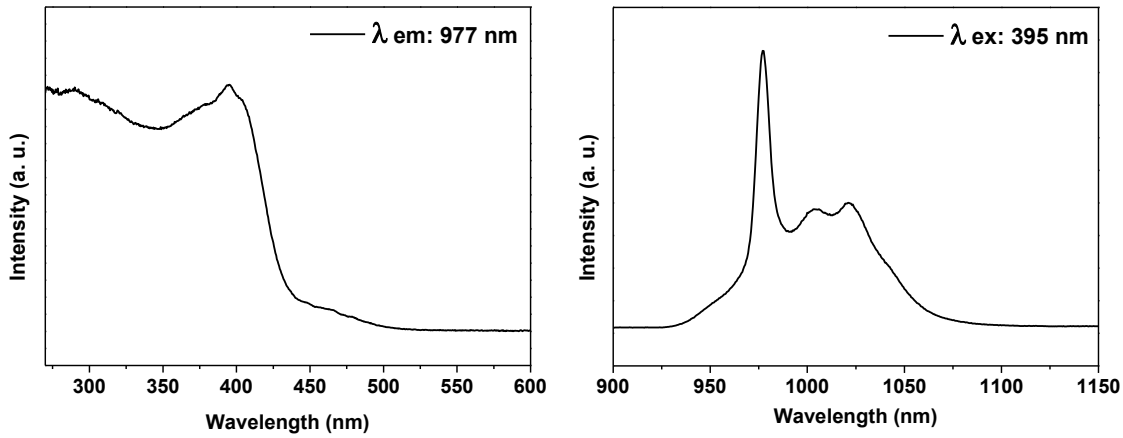

Figure 55 displays the excitation (on the left) and emission (on the right) spectra obtained from **NdL3** complex. Similar to the **Nd** complex, the excitation spectrum shows a broad band up to 400 nm ascribed to the singlet-to-singlet transitions in the **TTA-Si** ligands. [71] Bands above 400 nm were attributed to Nd(III) intraconfigurational f-f transitions.[28, 49] The emission spectrum displays a sharp band at 1063 nm attributed to $^4F_{3/2} \rightarrow {}^4I_{11/2}$ transition and a low intensity band centered at 1335 nm, ascribed to the $^4F_{3/2} \rightarrow {}^4I_{13/2}$ transition.[28, 45, 49]

Figure 55. Room temperature excitation (on the left, monitoring at $\lambda_{emission}$ = 1063 nm) and emission (on the right, monitoring at $\lambda_{excitation}$ = 391 nm) spectra of the **NdL3** complex in solid state.

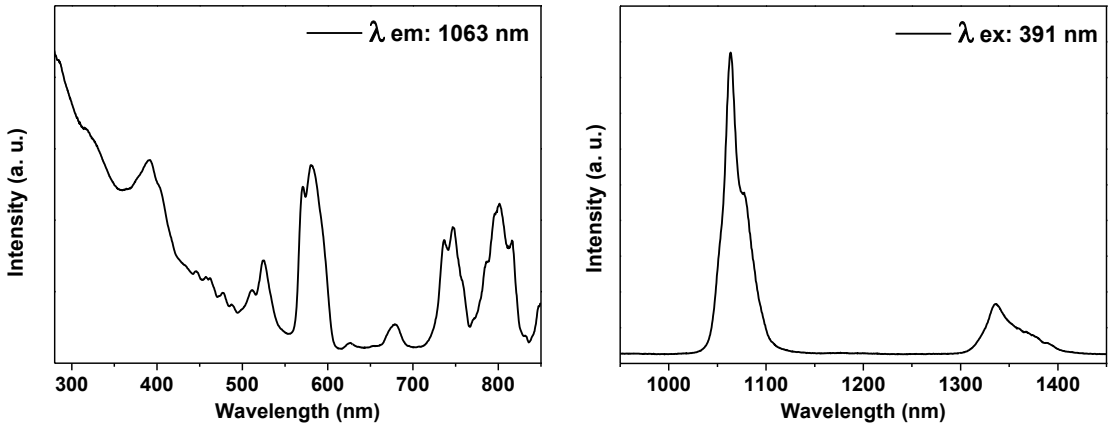

Figure 56 shows the excitation and emission spectra obtained from **YbL3** complex. A broad band up to 400 nm was observed (figure 56, on the left) and ascribed to the singlet-to-singlet transitions in the **TTA-Si** ligands.[71] By monitoring the excitation at 395 nm, a broad emission spectra (figure 56, on the right) was assigned to the $^2F_{5/2} \rightarrow {}^2F_{7/2}$ transition. The splitting of the emission spectrum was not similar to the **Yb** complex. In this case, the **YbL3** complex shows **TTA** ligands modified by alkoxisilyl groups and without water molecules in the first coordination sphere, consequently, the ligand-field effect is different.

Figure 56. Room temperature excitation (on the left, monitoring at $\lambda_{emission}$ = 980 nm) and emission (on the right, monitoring at $\lambda_{excitation}$ = 395 nm) spectra of the **YbL3** complex in solid state.

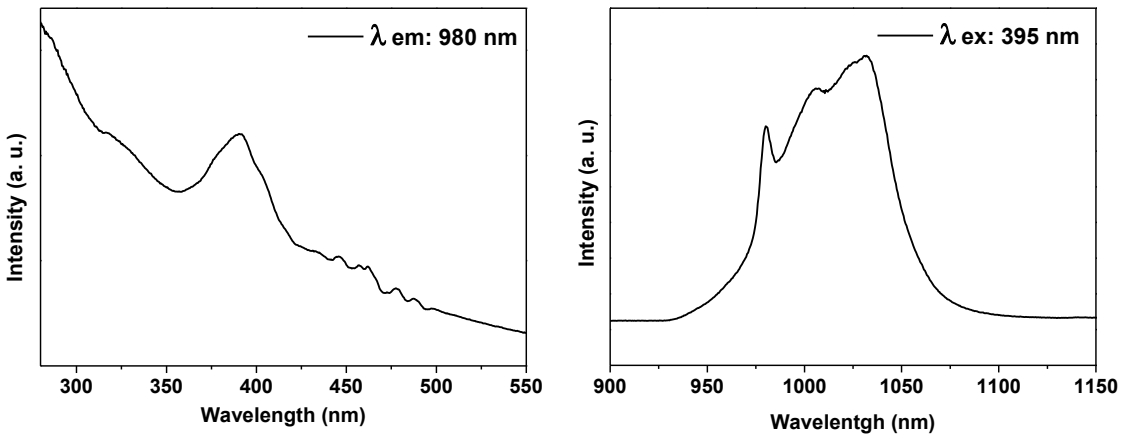

4.5. Photophysical properties of heterobimetallic Ru(II)—Yb/Nd(III) silylated complexes.

Ru^{2+} emission bands were observed at 665 nm (~ 15038 cm^{-1}), 670 (~ 14925 cm^{-1}) and 610 nm (~ 16393 cm^{-1}) for **Ru—NdL3**, **Ru—YbL3** and **Nd—RuL** (**Yb—RuL**), respectively. That difference of energy for ^{3}MLCT between complexes may be resulted of different π-donor or π-acceptor behavior by ligands on the complexes, as consequence, the MLCT energy[46] may shifted to red, and that fluctuation will be important for the best the d-f energy-transfer process. When, these results were comparable with the precursors (**Ru** and **RuL**, figures 51 and 52, respectively), for both heterobimetallic complex the ^{3}MLCT energy had blue shifted; so the structural symmetry of heterobimetallic complexes have more important role than the different π-donor or π-acceptor behavior from ligands. The excitation spectra for **Ru—LnL3** and **Ln—RuL**, by monitoring the Ru(II) ^{3}MLCT emission to the ground state transition, were composed of bands assigned to the d$\rightarrow\pi^*$ ^{1}MLCT (metal-to-ligand charge transfer) transitions or transitions centered on ligands, as $\pi\rightarrow\pi^*$ transitions[45], in agreement with the UV-Visible results.

Figure 57. Room temperature excitation ((a), $\lambda_{emission}$: 665 nm and (c), $\lambda_{emission}$: 1065 nm) and emission ((b), $\lambda_{excitation}$: 450 nm; and (d), $\lambda_{excitation}$: 375, 450 and 801 nm) spectra of the **Ru—NdL3** complex in solid state.

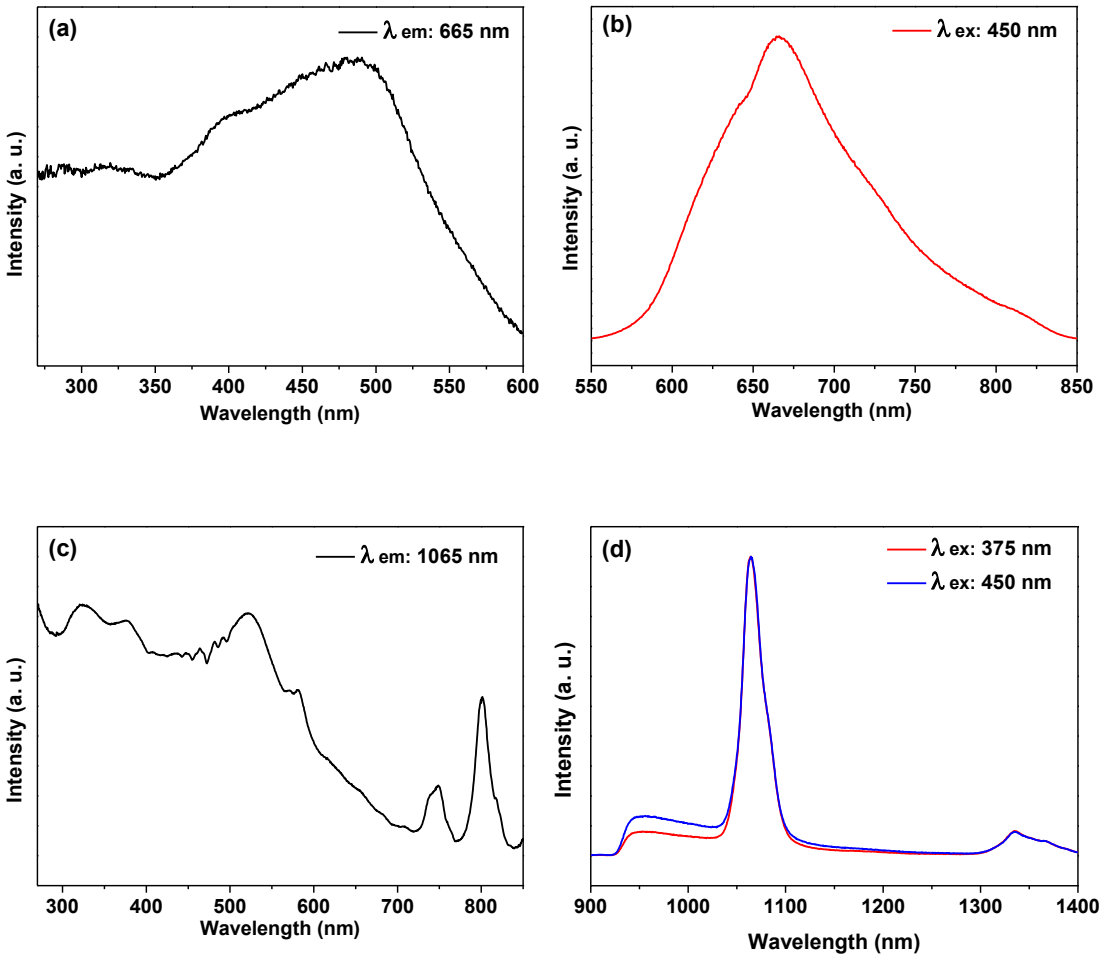

Figure 58. Room temperature excitation ((a), $\lambda_{emission}$: 670 nm and (c), $\lambda_{emission}$: 978 nm) and emission ((b), $\lambda_{excitation}$: 455 nm; and (d), $\lambda_{excitation}$: 370 and 455 nm) spectra of the **Ru—YbL3** complex in solid state.

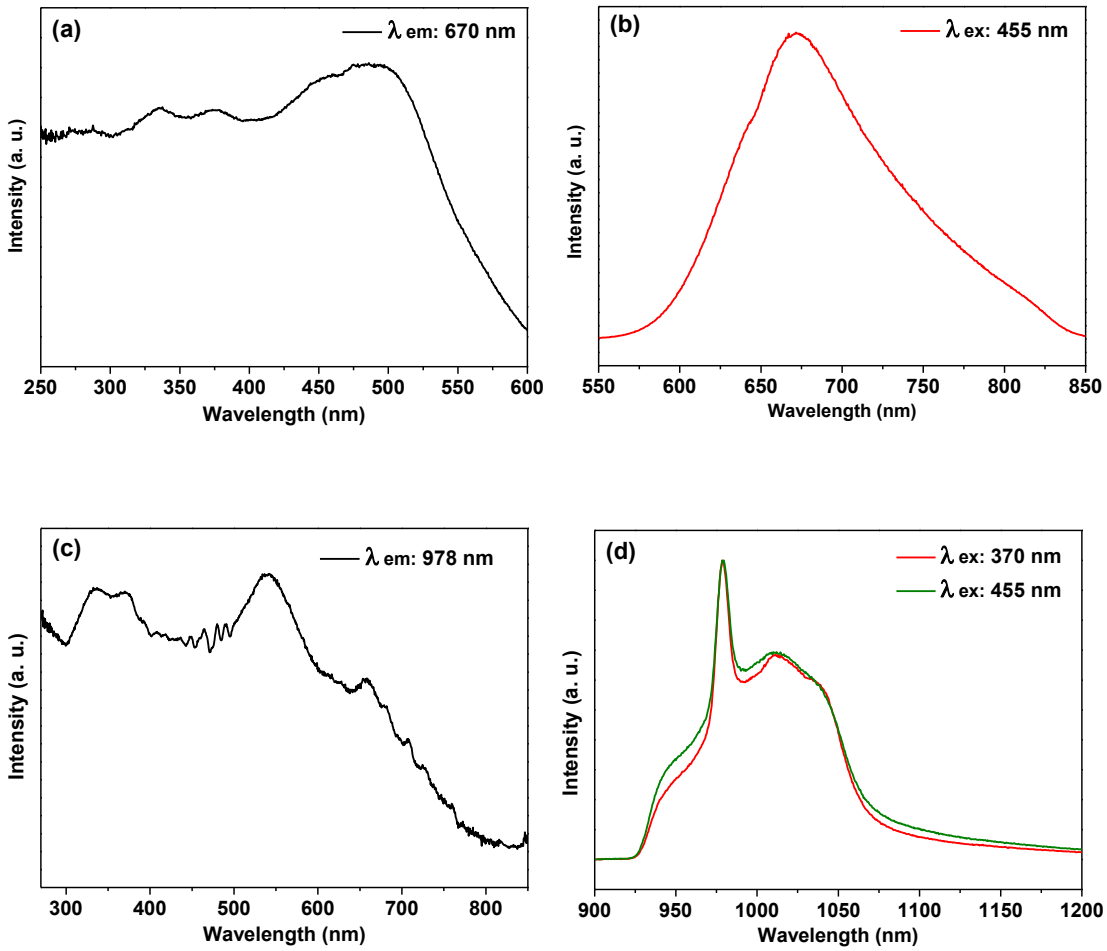

Figure 59. Room temperature excitation ((a), $\lambda_{emission}$: 610 nm and (c), $\lambda_{emission}$: 1063 nm) and emission ((b), $\lambda_{excitation}$: 465 nm; and (d), $\lambda_{excitation}$: 335, 370, 455 and 802 nm) spectra of the **Nd—RuL** complex in solid state.

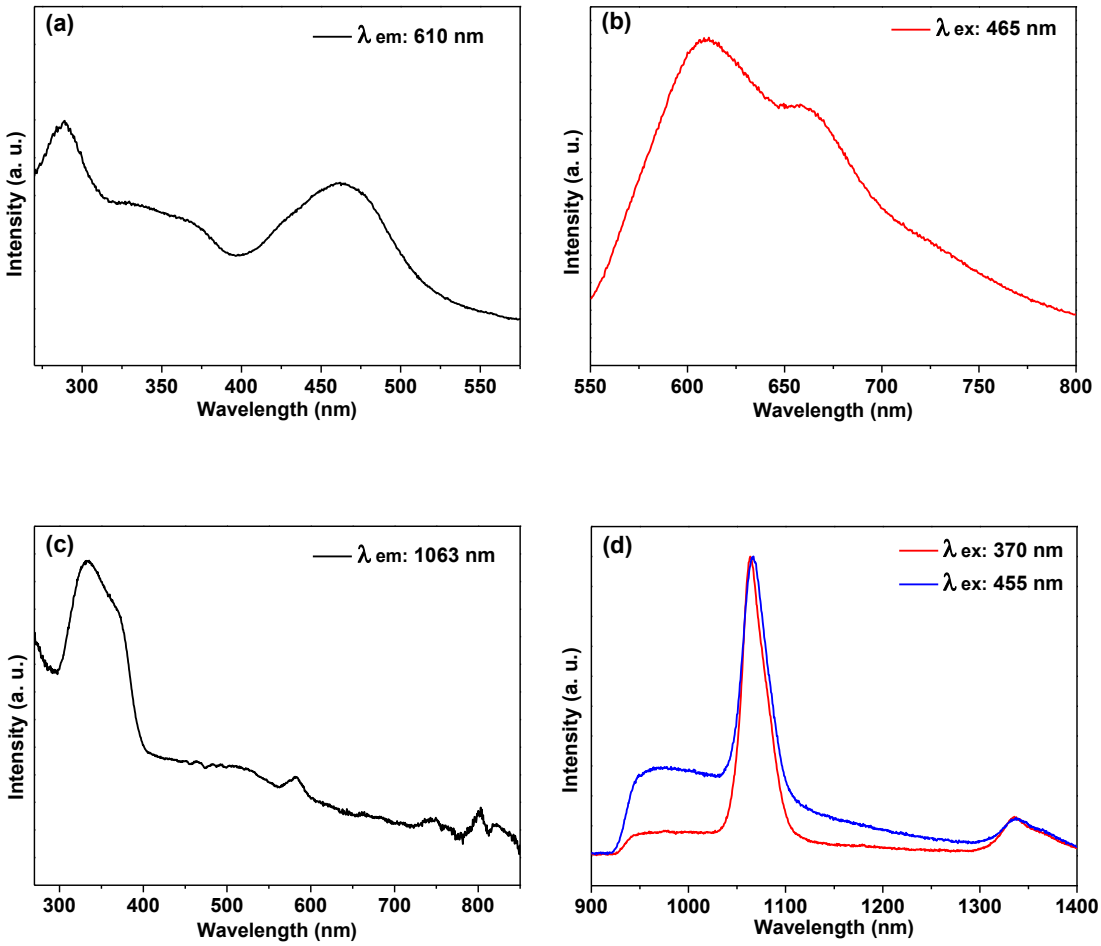

Figure 60. Room temperature excitation ((a), $\lambda_{emission}$: 610 nm and (c), $\lambda_{emission}$: 980 nm) and emission ((b), $\lambda_{excitation}$: 450 nm; and (d), $\lambda_{excitation}$: 370 and 450 nm) spectra of the **Yb—RuL** complex in solid state.

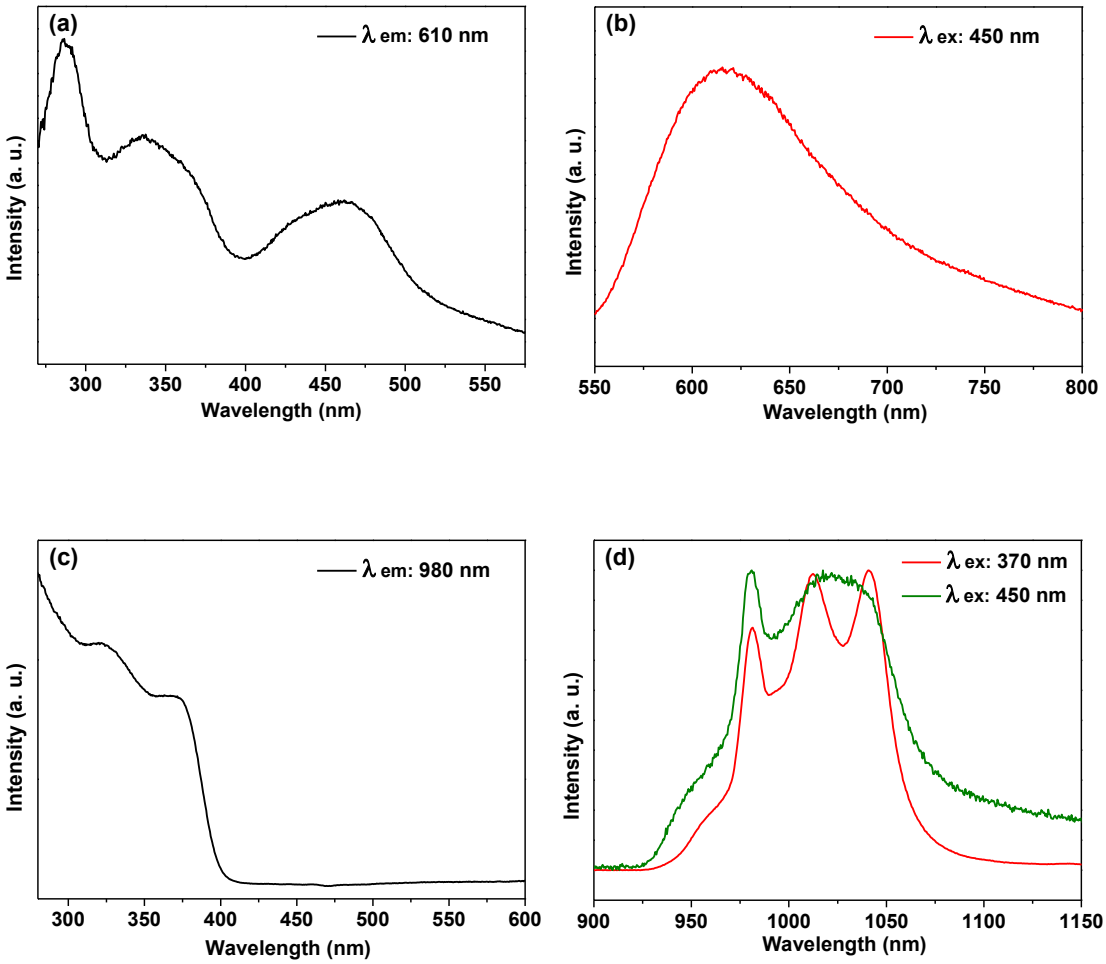

The four studied systems showed sensitized near-infrared emission upon excitation of the Ru(II) antenna, figures 57, 58, 59 and 60 ((c) and (d)). First, for the **Ru—NdL3** (figure 57 (d)), two bands were detected at infrared region; a sharp band at 1065 nm attributed to $^4F_{3/2} \rightarrow {}^4I_{11/2}$ transition and a low intensity band centered at 1334 nm, attributed to the $^4F_{3/2} \rightarrow {}^4I_{13/2}$ transition.[28, 45, 49]

Concerning the **Ru—YbL3** (figure 58 (d)), a broad emission band at 978 nm was ascribed to Yb(III) $^2F_{5/2} \rightarrow {}^2F_{7/2}$ transition.[45, 46, 92] The Nd^{3+} IR emission bands are observed for **Nd—RuL** (figure 59 (d)), In the same way the IR Yb^{3+} emission band was observed for the **Yb—RuL** (figure 60 (d)). It is important emphasize that the evident splitting of the emission spectrum (figure 60 (d)).

The excitation spectra, by monitoring the NIR emission (λ_{em}: 1065 nm to **Ru—NdL3**, λ_{em}: 978 nm to **Ru—YbL3**, λ_{em}: 1063 nm to **Nd—RuL** and λ_{em}: 980 nm to **Yb—RuL**), have shown distinct profile. For the **Ru—NdL3**, three sharp band, ascribed to Nd(III) intraconfigurational f-f transitions, were observed at 581, 746 and 800 nm.[28, 49] The broad band from 270 to 400 nm were assigned to transitions centered at **TTA-Si**, **bpy** and **bpmd** ligands[48, 49, 71, 72]; additionally, at the range from 400 to 600 nm were noted the band to the Ru(II) ^{3}MLCT transition.[45] For the **Ru—YbL3**, a broad band from 270 to 400 nm were assigned to transitions centered at **TTA-Si**, **bpy** and **bpmd** ligands.[48, 49, 71, 72] From 400 to 650 nm were observed the band ascribed to Ru(II) ^{3}MLCT transition.[45] For the **Nd—RuL**, three low intensity bands assigned to to Nd(III) intraconfigurational f-f transitions appear at 581, 746 and 800 nm.[28, 49] A broad intense band centered at 334 nm was ascribed to **TTA**, **bpy-Si** and **bpmd** ligands.[48, 49, 71, 72] The band from 400 to 600 nm was assigned to Ru(II) ^{3}MLCT transition.[45] However, that last transition was not detectable at excitation spectra for **Yb—RuL** complex, even that the infrared emission was carried out by excitation centered on Ru(II) ^{3}MLCT. The spectrum has showed a broad excitation band from 270 to 400 nm assigned to ligands transitions (**TTA**, **bpy-Si** and **bpmd**).[48, 49, 71, 72] A probable pathway of energy transfer (ET) was presented in the figure 61. The proposed energy level diagram suggests that the **RuL** and **Ru** ^{3}MLCT energy are suitable for the sensitization of the Ln^{3+} luminescence. Although the excited state of Yb(III) lies around 10204 cm^{-1} and the **RuL** ^{3}MLCT are at 16129 cm^{-1}, so an energy gap of about 5925 cm^{-1}, the **RuL** excitate state (^{3}MLCT) may be an efficient way on energy transfer process. In this sense, **Yb—RuL** complex showed energy transfer rate of $1.54x10^7$ s^{-1} and ET quantum yield of 73 %. These values are in agreement with the better ET rate observed for the **Nd—RuL** complex, it has shown values of ET rate and quantum yield of $3.04x10^7$ s^{-1} and 84 %, respectively. On the other hand, **Ru** ^{3}MLCT energy level appears at 14925 cm^{-1} whereas Nd(III) ions possess some excited levels higher than 11110 cm^{-1}, with an energy gap of about 3814 cm^{-1} relating to **Ru** ^{3}MLCT energy level. In this case, ET rate and quantum yield of $0.61x10^7$ s^{-1} and 44 %, respectively, were obtained for **Ru—NdL3** complex. The comparable system based on Yb^{3+} ions (**Ru—YbL3** complex) displayed ET rate and quantum yield of $0.34x10^7$ s^{-1} and 30 %, respectively. For all complexes, faster ET rate for Nd(III) than Yb-based heterobimetallic complexes could be explained by Nd(III) presents excited levels with compatibly energy at the **Ru** and **RuL** ^{3}MLCT states with energy gap lower than for Yb(III) ions, in a same system. The

lifetime data, ET rate constant and quantum yield were obtained to support the d-f sensitization according to the table 1. Ruthenium quantum yield obtained from precursors and heterobimetallic complexes were calculated to corroborate lifetime measurements and ET rate constant data.

Table 1. Photophysical properties for MLCT-based visible emission and Ln(III) based NIR.

	MLCT-based emission (Ex: 448 nm)				**MLCT-based emission (Ex: 450 nm)**
	λ / nm	τ / ns	[a] k_{ET} / 10^7 s^{-1}	[b] Φ_{ET} / %	[c] Φ_{Ru} / 10^3
Ru	670	128.1	---	---	1,88
Ru—NdL3	670	72.0	0.61	43.8	1,38
Ru—YbL3	670	89.1	0.34	30.4	---
RuL	620	178.8	---	---	4,76
Nd—RuL	620	27.8	3.04	84.4	---
Yb—RuL	620	47.5	1.54	73.4	3,76

[a] k_{ET} (energy transfer rate constant) = $1/\tau_q - 1/\tau_u$ (τ_q and τ_u refer to the "quenched" and "unquenched" lifetime of Ru^{2+} complexes before and after coordination with Ln^{3+}). [b] Φ_{ET} (energy transfer quantum yield) = $1 - (\tau_q/\tau_u)$. [c] Φ_{Ru} (ruthenium quantum yield).

The quantum yield (ϕ) is the ratio of emitted to absorbed photons. Relative quantum yield (ϕ') were obtained for ruthenium and heterobimetallic complexes in ethanol solution by using $[Ru(bpy)_2bpy\text{-}Si]Cl_2$ as a reference (ϕ= 2.4% in water, λ_{exc} = 450 nm)[73, 84], according to the equation 6.[17]

Where, Abs is the absorbance at the excitation wavelength, Em is emission intensity, and n is the refractive index of the solvent used. Subscripts R and S refer to the reference and the unknown, respectively.

Figure 61. Assumed schematic energy transfer processes from **Ru** and **RuL** complexes (Ru(II)) to **Nd**$^{3+}$ and **Yb**$^{3+}$ (A = Absorption; ISC = Inter-System Cross; P = phosphorescence; ET = Energy Transfer; F = Fluorescence) in the **Ru—LnL3** and **Ln—RuL** complexes.

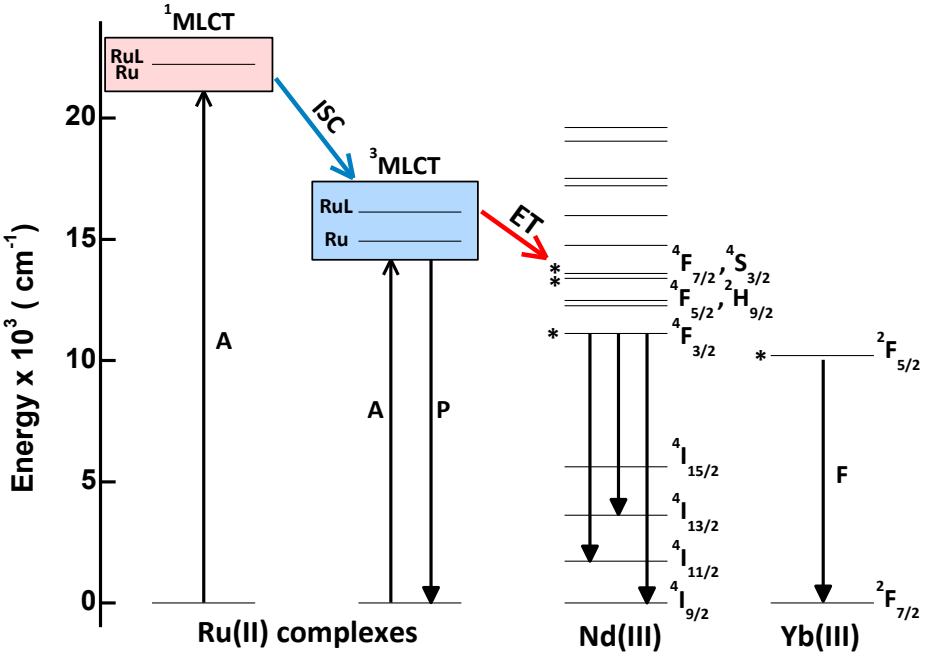

The **Ru** and **RuL** lifetimes were substantially reduced in **Ru—LnL3** and **Ln—RuL** complexes confirming energy transfer processes for all complexes. Beyond that, decreasing of ruthenium quantum yield values for the heterobimetallic complexes confirm the quenching of the luminescence Ru(II) ^{3}MLCT emission and, consequently, the sensitized NIR emission from Ln^{3+} units (table 1).

It is important to emphasize that ET rate and quantum yield data from **Yb—RuL** complex were the greatest results obtained for Yb(III)-based heterobimetallic complexes reported in the literature.[28, 44–46, 93] Although **Yb—RuL** complex showed faster ET rate and higher ET quantum yield than **Ru—NdL3** complex, the similar **Nd—RuL** complex displayed high values of ET rate and quantum yield compared to **Yb—RuL** complex.

In this way, it was demonstrated successfully synthesis and characterization of new *d-f* heterobimetallic (Ru(II)—Nd/Yb(III)) complexes containing organic ligands modified by alkoxysilyl groups. The energy transfer processes were evaluated and confirmed for lifetimes and ruthenium quantum yield data, making **Ru—LnL3** and **Ln—RuL** complexes good

candidates for grafting onto any hydroxylated matrix besides a promising luminescent-emitting probes in the near infrared region.

5 – LUMINESCENT NANOHYBRIDS OBTAINED BY GRAFTING OF RUTHENIUM(II), LANTHANIDE(III) AND *d-f* HETEROBIMETALLIC SILYLATED COMPLEXES

5.1. Characterization of mesoporous silica nanoparticles (MSNs)

Mesoporous silica nanoparticles were synthesized by water/oil microemulsion as described in the experimental section (3.1.5) and then were evaluated by SEM, TEM and STEM measurements. Figure 62 shows a size distribution for the mesoporous silica nanoparticles. The result was obtained by analysis of SEM images (figure 63) by Image J software. The y axis corresponds to the percentage of nanoparticles (number of nanoparticles = 400) and the x axis represents the nanoparticles diameter in nanometers.

Figure 62. Size distribution for the MSNs. Number of nanoparticles = 400. SEM images of MSNs used in size distribution measurements.

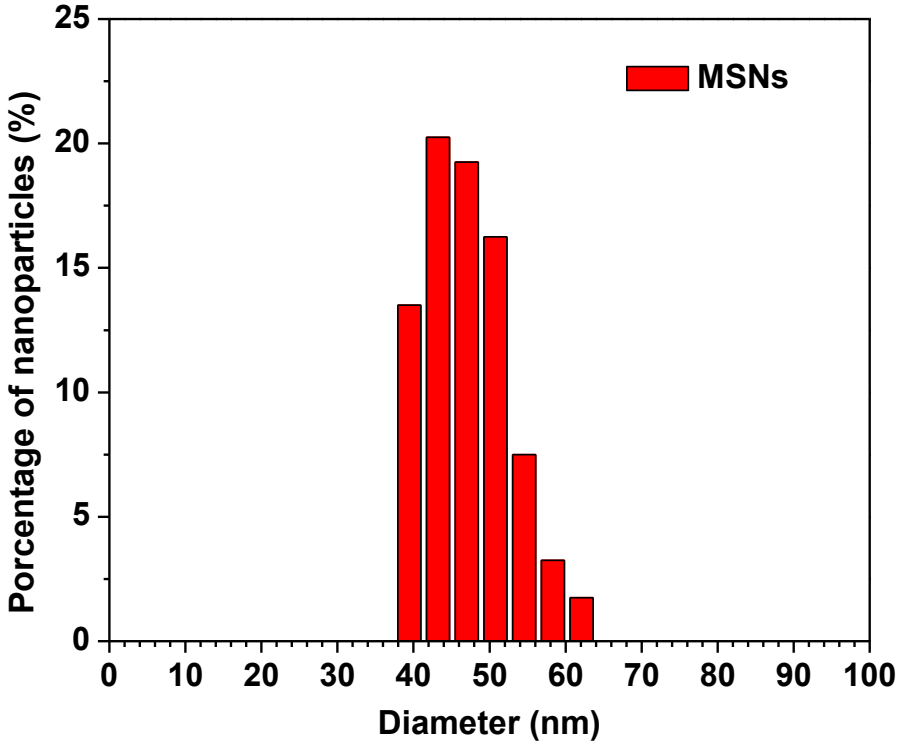

SEM analyses were performed to evaluate the morphology and the particle size. Spherical silica nanoparticles with pores size of 9 ± 3 nm and mean diameter of 47 nm ± 4 nm were obtained from the figure 63. The last two SEM images below (figure 63) showed clearly

the nanopores; these images were carried out by a careful analysis of the samples without conductor film on the samples as metallization or carbon thin film.

Figure 63. SEM images of mesoporous silica nanoparticles (MSNs).

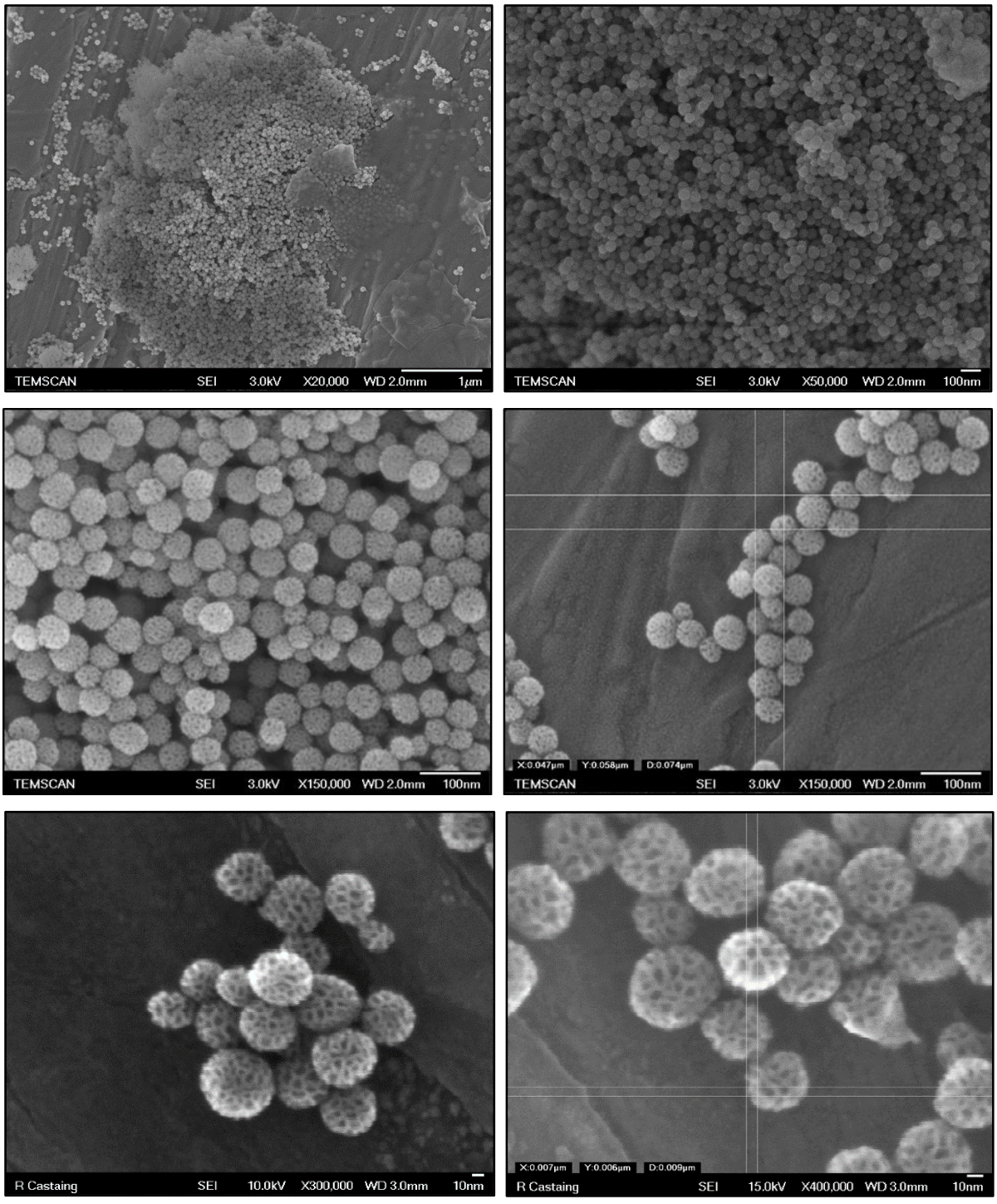

TEM analysis were carried out to confirm the results obtained by SEM analysis and evaluate the porous structure of the nanoparticles. Figure 64 displays TEM images that confirm the nearly monodispersed spherical nanoparticles with pores in the nanometer range. A random distribution of nanopores inside the nanoparticles and on the nanoparticles surface may be observed.[78]

Figure 64. TEM images of mesoporous silica nanoparticles (MSNs).

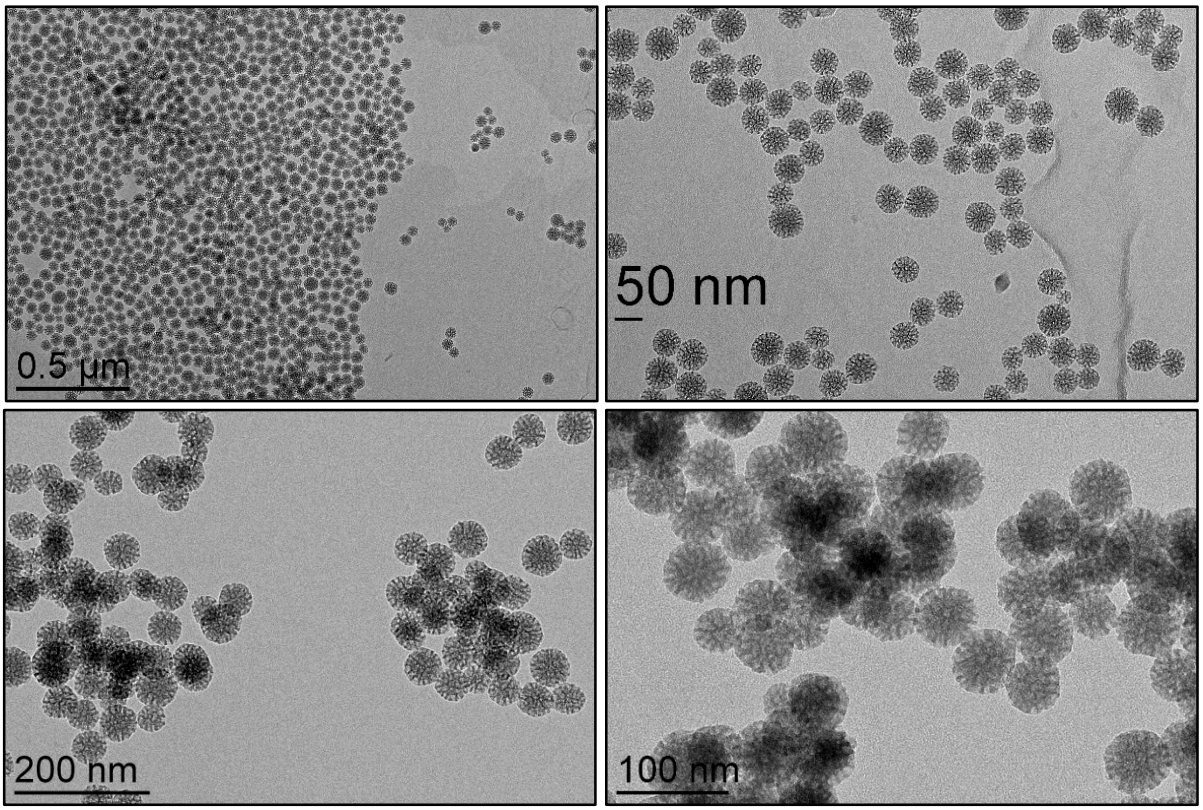

Figure 65 shows on the left bright field images and on the right dark field images obtained from STEM measurements. Spherical mesoporous silica nanoparticles with a random distribution of nanopores were observed corroborating SEM and TEM measurements. From dark field images metallic charges are observed at the surface and inside nanoparticles. Metallic charges were ascribed to the Si atoms presents in the silica network.

Figure 65. STEM images of mesoporous silica nanoparticles (MSNs). On the left: bright field images; on the right: dark field images.

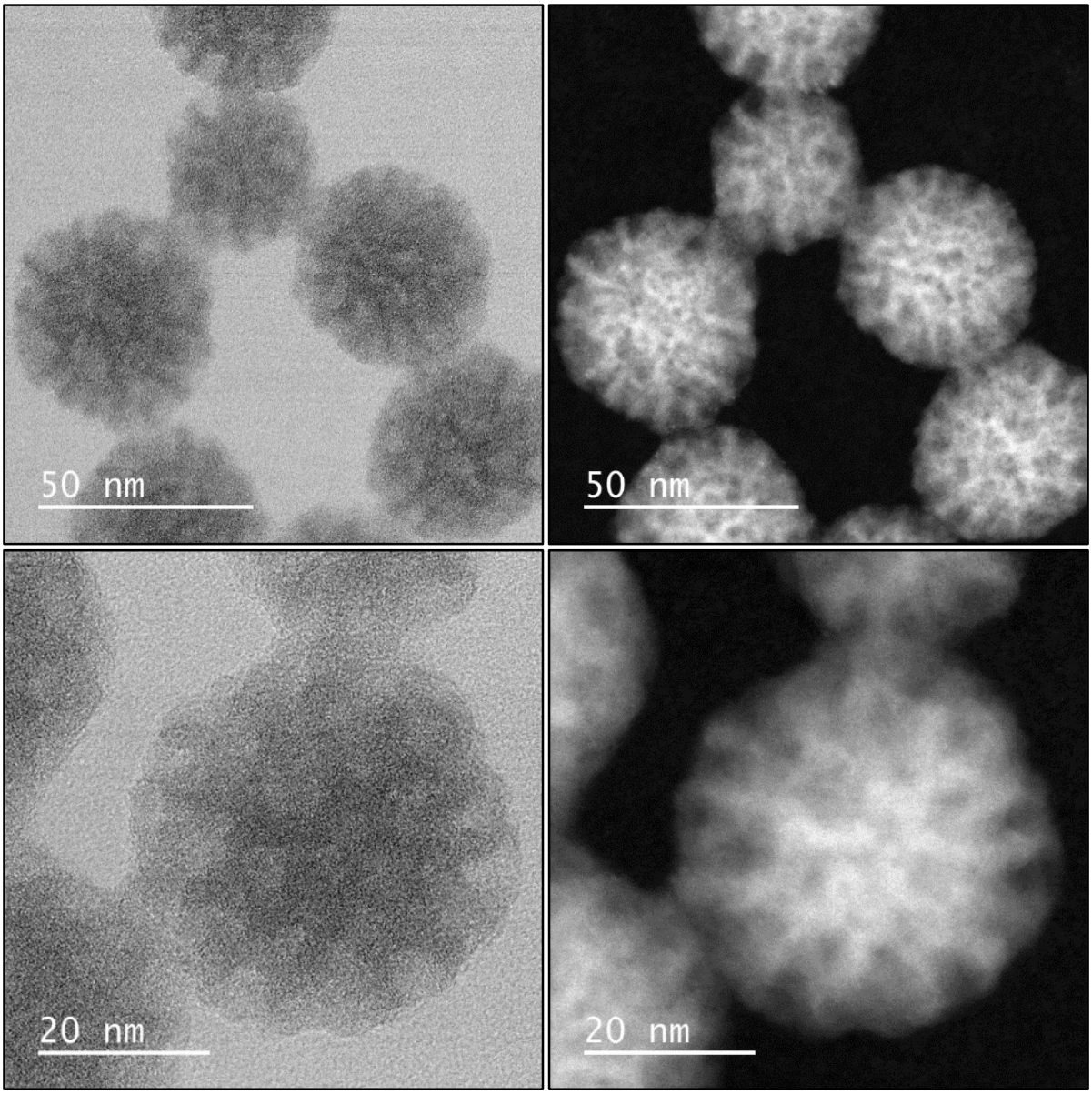

Figure 66. DRIFT spectrum of the MSNs.

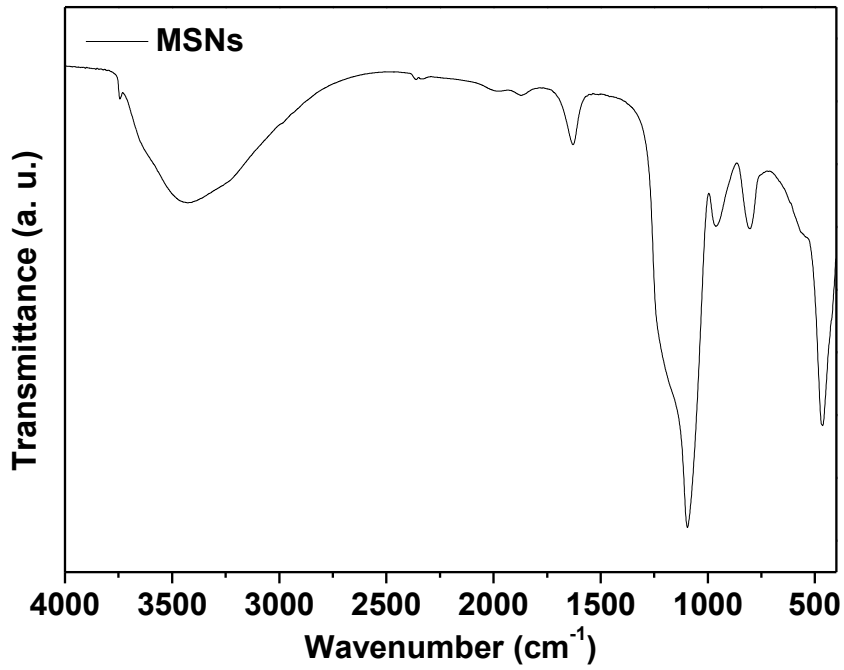

Figure 66 displays characteristic bands of the silica network at 465, 805 and 1095 cm^{-1} corresponding to δ(Si—O—Si), ν_s(Si—O—Si) and ν_{as}(Si—O—Si), respectively. Bands at 961 and 1630 cm^{-1} were ascribed to ν(Si—OH) and δ(OH). These results confirm that silanol groups are available on the surface or inside the pores of the MSNs. The band at 3430 cm^{-1} was attributed to ν(OH) of water molecules.[74, 77, 89]

Thermogravimetric analysis (TGA) results are shown in Figure 67. An endothermic event from 25 to 100 °C corresponding to dehydration with a loss weight of 18.8 % is ascribed to desorption of physisorbed solvent molecules. The mass loss of 6.5% observed from 200 to 990 °C in the MSNs was attributed to structural changes and condensation of pore-surface silanol groups with the corresponding water release.[54, 89]

Figure 67. TGA/DTA curves of the MSNs.

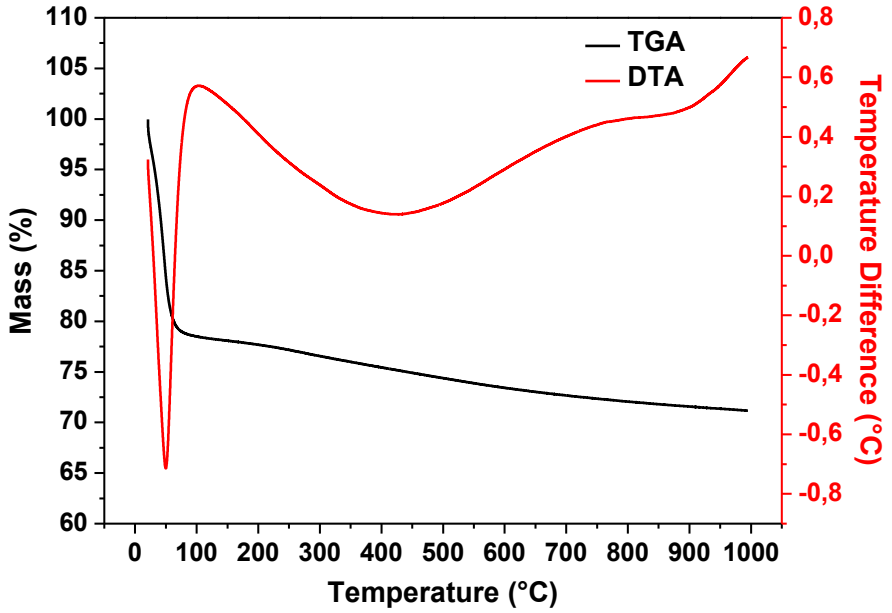

Nitrogen adsorption/desorption isotherms were obtained in order to confirm the pores structure and determine the specific surface area (S_{BET}), total pore volume (V_p) and mean pore size (D_p).

Figure 68. Nitrogen adsorption/desorption isotherms of the MSNs.

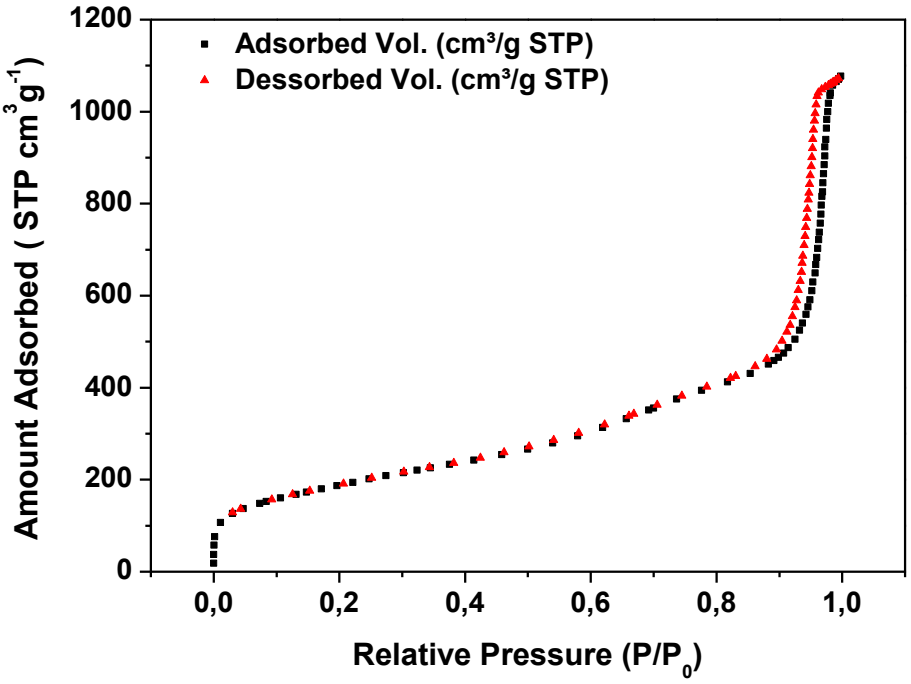

Figure 68 shows Isotherms of MSNs that exhibits a type IV shape, which is characteristic of mesoporous materials.[89, 94] According to IUPAC definition, this adsorption isotherm presents a type 1 hysteresis, and the hysteresis type was consequence mainly by the pores geometry. In this case the pores show cylindrical or polyhedral shape and with open extremity.[94, 95]

Remarkable values of specific surface area (S_{BET} = 675 m^2 g^{-1}) with large pores volume (V_p = 1.55 cm^3 g^{-1}) and average pore size (D_p = 9 nm) were obtained from the isotherms curves of MSNs.

^{29}Si-MAS NMR measurements were performed to identify the Si species in the matrix, and consequently, to determine the percentage of species (Q^n) available for grafting reactions.

Figure 69. ^{29}Si-MAS NMR spectrum (black line) and its respective deconvolution (red line) of the MSNs.

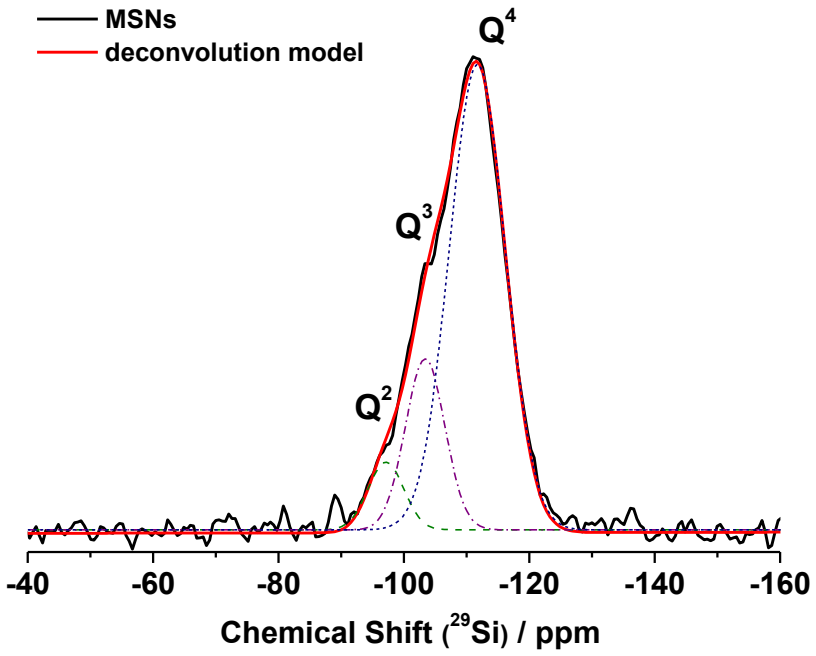

Spectrum deconvolution was carried out to determine the percentage of Q^n species (figure 69). Subsequently, the condensation degree was calculated according to the equation 7.[96]

$$C\% = \frac{[(Q^1 + 2 \times Q^2 + 3 \times Q^3 + 4 \times Q^4) \times 100]}{4} \quad (7)$$

The notation Q^n is used for the Si species, where *n* is the number of siloxane bonds observed at Si atom. The chemical shift ranges were based on the literature values, i.e. -80 to -90 ppm for Q^1 ($Si(OH)_3(OSi)$), -91 to -100 ppm for Q^2 ($Si(OH)_2(OSi)_2$), -101 to -110 for Q^3 ($Si(OH)(OSi)_3$) and -111 to -119 ppm for Q^4 ($Si(OSi)_4$).[96, 97] The chemical shift, percentage of species and the condensation degree of the MSNs are displayed in the table 2.

Table 2. Chemical shift (ppm), percentage of species and condensation degree obtained from deconvolution of ^{29}Si MAS spectrum from MSNs.

Sample	Q^2		Q^3		Q^4		Condensation degree (%)
	δ (ppm)	Area (%)	δ (ppm)	Area (%)	δ (ppm)	Area (%)	
MSNs	-97	7	-103	19	-112	74	91,75

From the spectrum deconvolution (table 2) three Si species were observed Q^2, Q^3 and Q^4 species. The presence of Q^2 (7 %) and Q^3 (19 %) species confirm that silanol groups are available in the MSNs. As expected, these results are in agreement with FTIR, TGA measurements and the high surface area by particle, and showing that 26 % of the Si species correspond to the silanol groups, which are available for grafting reactions.

5.2. Dense silica nanoparticles (Ludox silica AS-40)

Ludox silica sol (AS-40) with 40 % of water (colloidal solution at pH=9) was chosen for comparison purposes with spherical mesoporous silica nanoparticles as matrix for grafting reactions. Menu and co-workers[77, 98] have used a commercial Ludox silica sol as monodisperse nanoparticles and after characterization, the commercial DSNs showed mean diameter of 24 nm and specific surface area of 138 m^2g^{-1}.[77, 98]

The number of silanols groups per nm^2 of silica was calculated from mass loss obtained from TGA analysis and using a S_{BET} from N_2 adsorption/desorption isotherms. Table 3 displays morphological properties of Ludox silica and MSNs.

Table 3. Morphological properties of commercial Ludox silica AS-40 and MSNs.

Nanoparticles	Mean diameter (nm)	Silanol groups per nm^2	Specific surface area ($m^2\ g^{-1}$)
MSNs	47 ± 4	5.8	675 ± 4
SiO_2-Ludox AS-40	24 ± 2	5	138 ± 1

The number of silanol groups was 5 per nm^2 for Ludox silica AS-40 as calculated and described by Menu et al.[77, 98] For MSNs was obtained 5.8 silanol groups per nm^2. Despite the heat treatment performed with MSNs, high values of silanol per nm^2 were achieved. Moreover, the MSNs showed a notable specific surface area (675 $m^2\ g^{-1}$) compared to DSNs (138 $m^2\ g^{-1}$) due to the mesoporosity of the MSNs. Although the MSNs exhibited high surface area, the OH groups are usually more available at the DSNs surface than at the MSNs pores. Thus, both silica matrix shows OH groups available for grafting reactions.

5.3. Synthesis and characterization of silica-based nanohybrids obtained by grafting of silylated ruthenium(II) and lanthanide (III) complexes onto MSNs

The methodology for grafting of ruthenium and lanthanide complexes containing alkoxysilane groups onto mesoporous silica nanoparticles (MSNs) were performed as described by Menu and co-workers.[71–73, 75, 76] These grafting reactions are based on covalent bounds between the complex and silica matrix by hydrolysis and condensation processes of the alkoxysilanes groups onto the silanol groups present in the silica matrix. Figure 70 shows a representation of the grafting reactions of silylated complexes onto MSNs.

Figure 70. Representation of grafting reactions of silylated complexes onto MSNs.

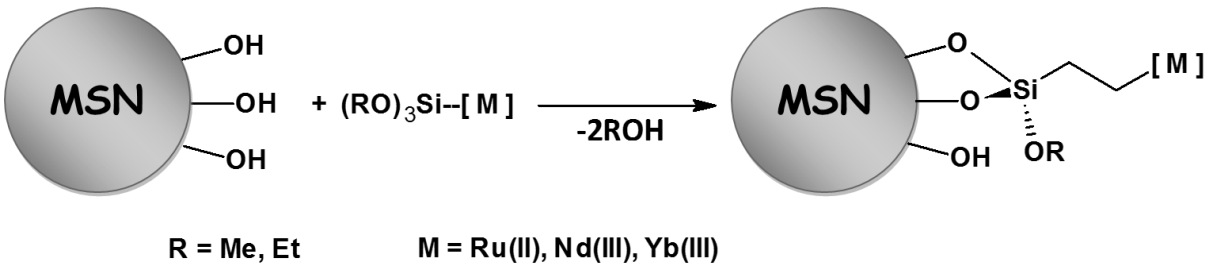

In this way, two types of nanohybrids were obtained. First with just only one grafted complex (**RuL1**, **NdL3** or **YbL3**) and second, with two grafted complexes (**RuL1/NdL3** and **RuL1/YbL3**). The nanohybrids obtained by one complex grafted on MSNs were labeled as **SiO_2-Ru**, **SiO_2-Nd** and **SiO_2-Yb**. The ratios of complexes per gram of MSNs added were 1.10, 0.40 and 0.49 mmol g^{-1} for **SiO_2-Ru**, **SiO_2-Nd** and **SiO_2-Yb**, respectively. The nanohybrids containing two complexes grafted on the MSNs were labeled as **SiO_2-RuNd** and **SiO_2-RuYb**. In both case, the ratios of complexes per gram of MSNs were 0.44 and 0.44 mmol g^{-1} of Ru and Nd/Yb complexes, respectively (to **SiO_2-RuNd** or **SiO_2-RuYb** nanohybrid). The quantity of complexes per gram of silica was kept lower than 1.0 mmol g^{-1} in order to obtain monolayer of the complexes, and to avoid unwanted polymerization reactions as described by Cousinié et al.[98]

5.3.1. Spectroscopic characterization of silica-based nanohybrids obtained by grafting of silylated ruthenium(II) and lanthanide (III) complexes onto MSNs

Diffuse Reflectance Infrared Fourier Transform (DRIFT) measurements were performed to confirm that the complexes were present in the MSNs after grafting reactions. Figure 71 shows DRIFT spectra of MSNs and the obtained nanohybrids.

As already previously discussed, figure 71 (a) displays DRIFT spectrum of pure MSNs and confirm the absence of bands relating to organic residues observed from 1700 to 1300 cm-1. For the nanohybrids, from 1200 to 1700 cm-1 characteristic bands ascribed to the ligands are observed.[71, 73, 77, 84] Bands from 3100 to 2900 cm^{-1} were confirmed for all nanohybrids and ascribed to v(CH) and v(CH_2).[71, 73, 77, 84] Bands attributed to v(C=O) and v(C=C) were observed for SiO_2-Nd, SiO_2-Yb, SiO_2-RuNd, and SiO_2-RuYb nanohybrids.[71, 73, 77, 84] For SiO_2-Ru, SiO_2-RuNd and SiO_2-RuYb nanohybrids, v(C=N), v(C=C) and δ(NH) bands were confirmed and ascribed to the ruthenium complexes grafted onto MSNs.[71, 73, 77, 84] These vibration and deformation bands confirming that SiO_2-RuNd and SiO_2-RuYb nanohybrids present both silylated complexes (ruthenium and lanthanide complexes) onto MSNs. Table 4 displays the bands ascribed to the ligands present in the complexes.

Figure 71. DRIFT spectra of (a) **MSNs** and different nanohybrids: (b) **SiO_2-Ru**, (c) **SiO_2-Nd**, (d) **SiO_2-Yb**, (e) **SiO_2-RuNd** and (f) **SiO_2-RuYb**.

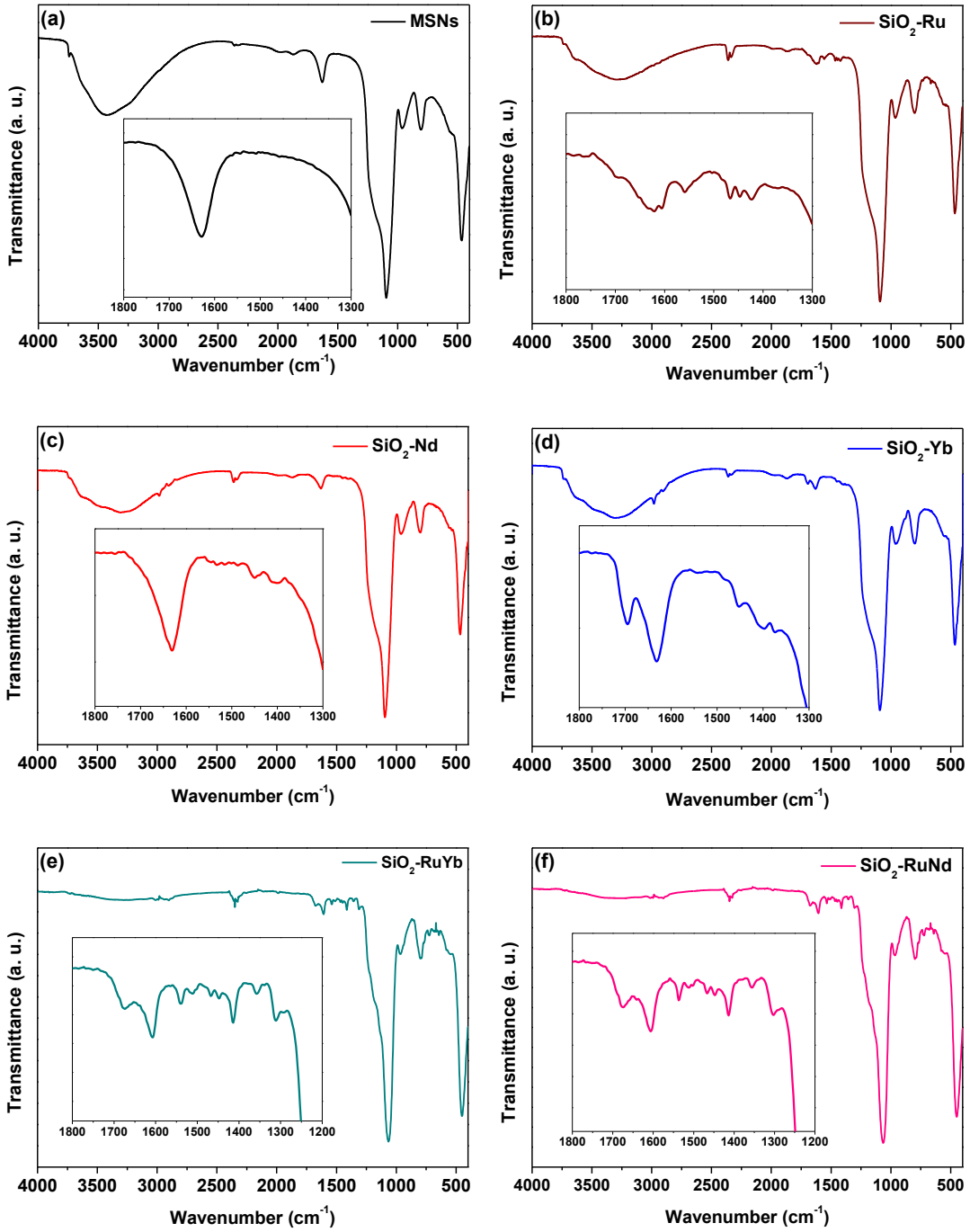

Table 4. DRIFT data for the nanohybrids.

Nanohybrids	DRIFT (cm^{-1})					
	ν_{as} (CH)	ν_{as} (CH_2)	ν_s (C=O)	ν(C=N)	ν(C=C)	δ(NH)
SiO_2-Ru	3083	2982	---	1698, 1620, 1605	1558, 1467	1446, 1422
SiO_2-Nd	---	2982	1531	---	1450, 1406	---
SiO_2-Yb	---	2982	1695, 1539	---	1483, 1454, 1400	---
SiO_2-RuNd	3011	2988	1674	1605, 1536	1510, 1501, 1466	1447, 1414, 1356
SiO_2-RuYb	3013	2987	1675	1540	1512, 1467	1447, 1413, 1356

FT-RAMAN measurements show characteristic bands ascribed to the complexes and also bands relating to Ln—O and Ru—N bonds, not observed in DRIFT spectra. The figure 72 displays FT-RAMAN similar spectra obtained for **SiO_2-RuYb** (figure 72 (a)) and **SiO_2-RuNd** (figure 72 (b)) nanohybrids.

Figure 72. FT-Raman spectra of (a) **YbL3** (green line), **RuL1** (red line) and **SiO_2-RuYb** (blue line); (b) **NdL3** (green line), **RuL1** (red line) and **SiO_2-RuNd** (blue line).

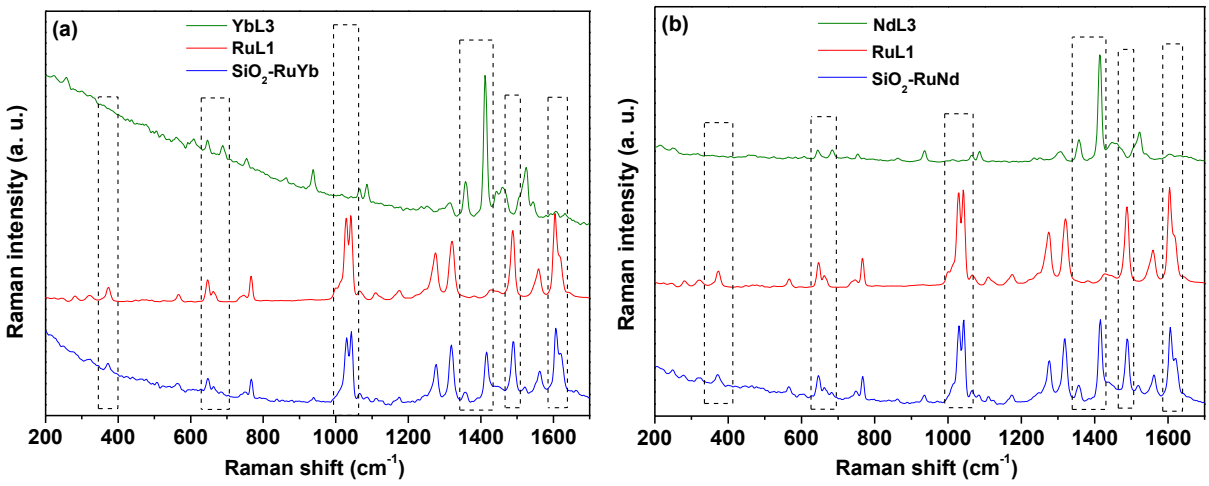

Bands in the 640-685 cm^{-1} region were assigned to ν(Ln—O) and ν(Ru—N) as previously described for the ruthenium and lanthanide silylated complexes (section 3.1) and as shown in both spectra (figure 72, red and green lines, respectively).[15-18] Additionally, at 372 and 1030-1045 cm^{-1} vibration bands attributed to ν(Ru—N) were observed.[17, 18] Bands observed at 1605-1629 cm^{-1} were ascribed to ν(C=N) and at 1490 and 1560 cm^{-1} assigned to ν(C=C) present in the ruthenium silylated complex. Bands relating to lanthanide silylated complexes were found at 1357 and 1415 cm^{-1} corresponding to ν(C=O and C=C).[15, 16] These results corroborate the FTIR analysis confirming the ruthenium and lanthanide silylated complexes are grafted onto MSNs.

The chemical integrity of the complexes grafted onto MSNs was verified by $^{13}C\{^{1}H\}$CP-MAS NMR spectroscopy. Figure 73 (I) shows $^{13}C\{^{1}H\}$CP-MAS spectra for the nanohybrids obtained by grafting of ruthenium and lanthanide complexes. The spectrum ascribed to the **SiO2-Ru** nanohybrids (figure 73 (I, a)) shows signals of carbon atoms of the ruthenium complexes grafted in the silica matrix. Signals at 125, 139, 151 and 157 ppm were attributed to the carbon atoms of the bpy ligands, CIII-CV, CIV, CVI and CII, respectively.[73] The signals ascribed to the carbon atoms of the propyl chain were observed with low intensity at 10 (C11), 22 (C10 and C7), 55 (C9) and 58 (C8) ppm.[73] For the nanohybrids obtained by grafting of silylated lanthanide complexes (**SiO_2-Nd** and **SiO_2-Yb**) the spectra were quite similar. Signals are observed at 47, 26 and 10 ppm ascribed to the carbon atoms of the methoxysilyl groups (propyl chains), C9, C11 and C10, respectively. It is worth noting that the characteristic signals expected from TTA ligands were not observed. The low sensibility in both spectra (figure 73 (I) b and c) can be ascribed to the paramagnetic interactions, compromising the efficiency of the cross-polarization process owing to very short ^{1}H spin-lattice relaxation times in the rotating frame.[68] In this way, for the **SiO_2-RuNd** and **SiO_2-RuYb** nanohybrids (figure 73 (I, d and e)) only signals ascribed to the bpy ligands, ethoxysilyl and methoxysilyl groups, present in the ruthenium and lanthanide complexes could be observed. The spectra were similar for both nanohybrids with signals at 125, 139, 151 and 157 ppm assigned to the carbon atoms of the bpy ligands, CIII-CV, CIV, CVI and CII, respectively, for the ruthenium complexes. Signals at 10, 22, 55 and 58 ppm, C11, C10-C7, C9 and C8, respectively, were attributed to the ethoxysilyl groups present in the ruthenium complexes. The signals at 47, 26 and 10 ppm were ascribed

to the carbon atoms of the methoxysilyl groups, C9, C10 and C11, respectively, present in the lanthanide complexes.

$^{29}Si\{^{1}H\}$CP-MAS NMR measurements were performed to provide information about the silicon atom environment and confirm the results obtained by $^{13}C\{^{1}H\}$CP-MAS NMR.[73] The presence of complexes can be revealed by T^n peaks since these indicate covalent bonding and condensation of the alkoxysilyl groups with the silanol available in the silica matrix. Figure 73 (II, a) shows $^{29}Si\{^{1}H\}$CP-MAS NMR spectrum for **SiO_2-Ru**. Weak peaks are observed for T^2 and T^3 at -58 and -67 ppm, respectively, ascribed to the condensation of ethoxysilyl groups on MSNs. The spectra ascribed to **SiO_2-Nd** and **SiO_2-Yb** (figure 73 (II) b and c) show T^2 and T^3 peaks at -57 and -66 ppm, respectively, for both nanohybrids. The presence of these peaks suggests incomplete condensation of the methoxysilyl groups with the MSNs.

The grafting of ruthenium and lanthanide complexes were evaluated for **SiO_2-RuNd** and **SiO_2-RuYb** nanohybrids according to the figure 73 (II, d and e). In both spectra, strong and well-defined T^2 and T^3 peaks are observed at -59 and -68 ppm. These results corroborate high grafting ratios obtained by EA and confirm the condensation of the ethoxysilyl and methoxysilyl groups present in the complexes with the silanol available in the silica matrix. Table 5 shows the chemical shifts ascribed to T^n peaks and Q^n species obtained by $^{29}Si\{^{1}H\}$CP-MAS NMR measurements for all nanohybrids.

Table 5. T^n and Q^n chemical shifts of the nanohybrids.

Samples	$^{29}Si\{^{1}H\}$CP-MAS NMR				
	T^2 (ppm)	T^3 (ppm)	Q^2 (ppm)	Q^3 (ppm)	Q^4 (ppm)
SiO_2-Ru	-58	-67	-91	-101	-110
SiO_2-Nd	-57	-66	-91	-101	-110
SiO_2-Yb	-57	-66	-91	-101	-110
SiO_2-RuNd	-59	-68	-93	-102	-111
SiO_2-RuYb	-59	-68	-93	-102	-111

In this way, by $^{13}C\{^{1}H\}$CP-MAS NMR and $^{29}Si\{^{1}H\}$CP-MAS NMR spectroscopy allowed the identification of silylated ruthenium and lanthanide complexes grafted onto MSNs for all nanohybrids.

Figure 73. $^{13}C\{^{1}H\}$CP-MAS NMR spectra (**I**) and $^{29}Si\{^{1}H\}$CP-MAS NMR spectra (**II**) of (a) **SiO_2-Ru**, (b) **SiO_2-Nd**, (c) **SiO_2-Yb**, (d) **SiO_2-RuYb** and (e) **SiO_2-RuNd**. *: carbon atoms in residual ethanol groups. **12**: carbon atoms in methoxysilyl groups not grafted. The numbering of carbon atoms is given on the left side with Roman figures for the bipyridine ligands; Arabic numerals for the alkoxysilane groups (methoxysilyl and ethoxysilyl).

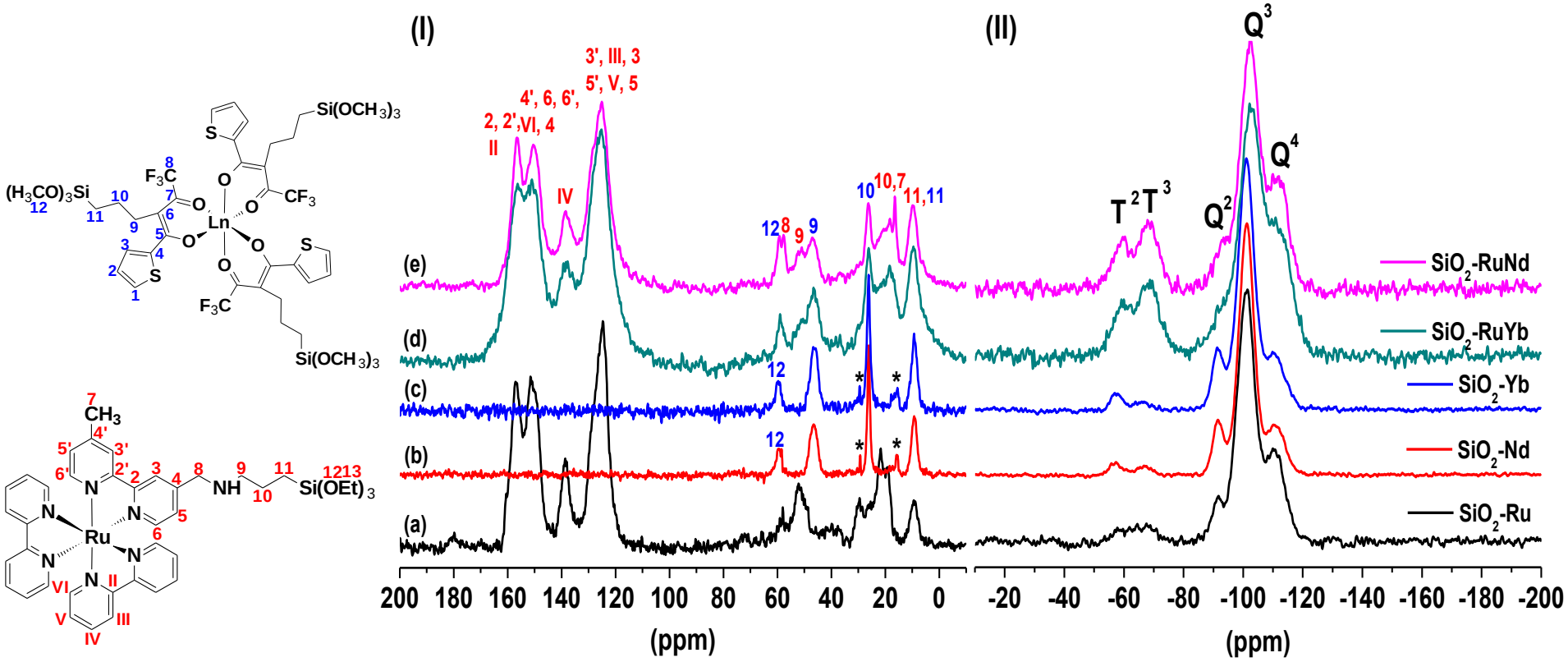

Figure 74 displays SEM images obtained from **MSNs** (a) and the nanohybrids **SiO_2-Ru** (b), **SiO_2-Nd** (c), **SiO_2-Yb** (d), **SiO_2-RuYb** (e) and **SiO_2-RuNd** (f). It is worth emphasizing those FEG-SEM images from MSNs and nanohybrids were obtained without metallization that allows a better viewing of the nanopores. The carbon layer on the samples can cloak the nanopores and prevent to observe if there is something into the pores. Figure 74 (a) displays SEM image of MSNs for comparison with the nanohybrids. In this case, the nanopores are well observed as already previously discussed in the section 5.1.

5.3.2. Microstructural characterization of silica-based nanohybrids obtained by grafting of silylated ruthenium (II) and lanthanide (III) complexes onto MSNs

Figure 74. FEG-SEM images of (a) **MSNs** and different nanohybrids: (b) **SiO_2-Ru**, (c) **SiO_2-Nd**, (d) **SiO_2-Yb**, (e) **SiO_2-RuYb** and (f) **SiO_2-RuNd**.

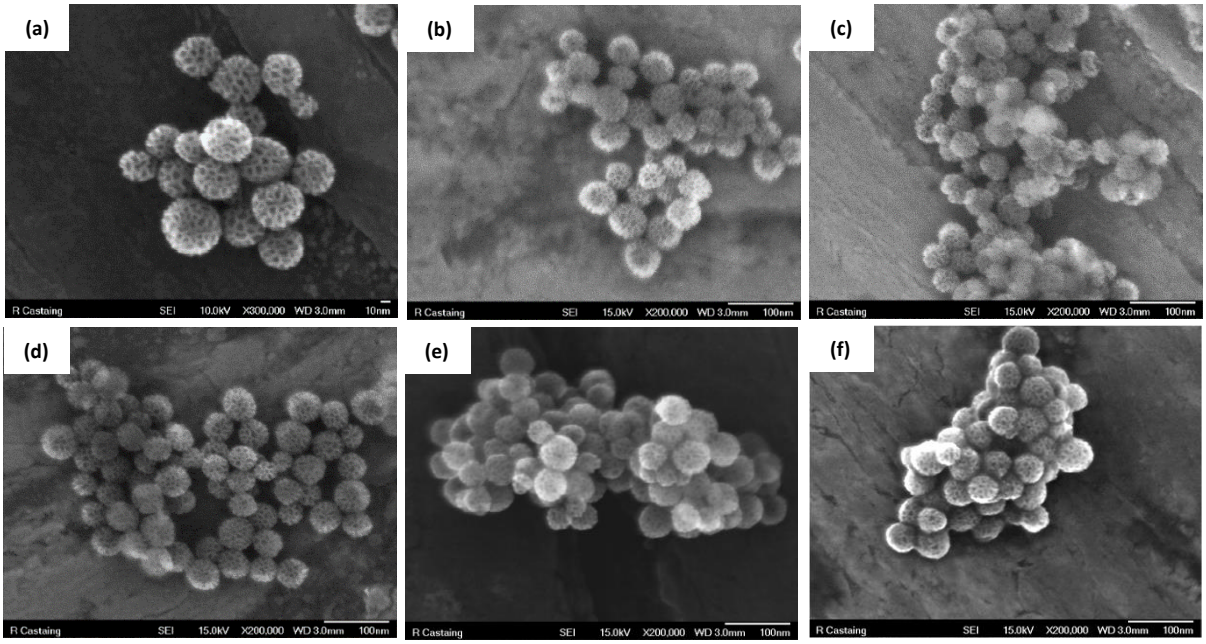

For all nanohybrids (figure 74) the morphology and structure were kept unchanged. These FEG-SEM images were hardly performed due to the presence of organic compounds (ruthenium and lanthanide complexes) onto MSNs in agreement with DRIFT and NMR data presviously described. HR-TEM measurements were carried out to confirm FEG-SEM images evaluating the nanopores structure after grafting of the silylated complexes.

Figure 75 shows HR-TEM images of the MSNs (a) and the nanohybrids **SiO_2-Ru** (b), **SiO_2-Nd** (c), **SiO_2-Yb** (d), **SiO_2-RuYb** (e) and **SiO_2-RuNd** (f). The MSNs (figure 75 (a)) displays a random distribution of the nanopores clearly observed as described in the section 5.1. However, according to the HR-TEM images, all nanohybrids present spherical morphology without changing of the structure besides shows the nanopores filled up that confirm the most of complexes are grafting inside de nanopores. These results corroborate DRIFT, NMR and FEG-SEM analysis showing the presence of the complexes inside de nanopores of the matrix.

Figure 75. HR-TEM images of (a) **MSNs** and different nanohybrids: (b) **SiO_2-Ru**, (c) **SiO_2-Nd**, (d) **SiO_2-Yb**, (e) **SiO_2-RuYb** and (f) **SiO_2-RuNd**.

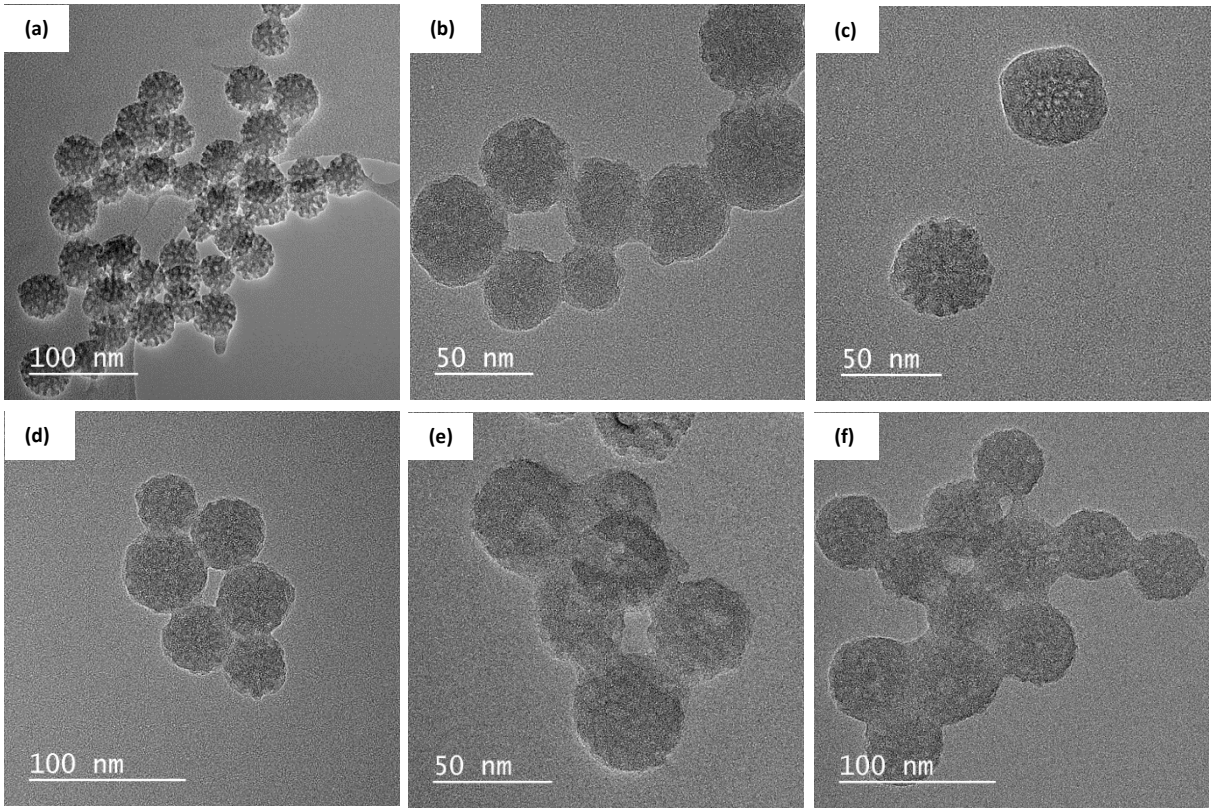

In STEM measurements atoms with high electron density as ruthenium, neodymium and ytterbium can be easly distinguished from Si atoms. The elemental cartographies were obtained by EDX spectroscopy on STEM microscopy, and the obtained results for **SiO_2-Ru**, **SiO_2-Nd** and **SiO_2-Yb** are shown in figures 76-78.

Figure 76. Electron microscope images and elemental cartography of the **SiO_2-Ru**: (a) STEM image, (b) Si cartography, (c) Ru cartography and (d) Si (blue color) and Ru (red color) cartographies.

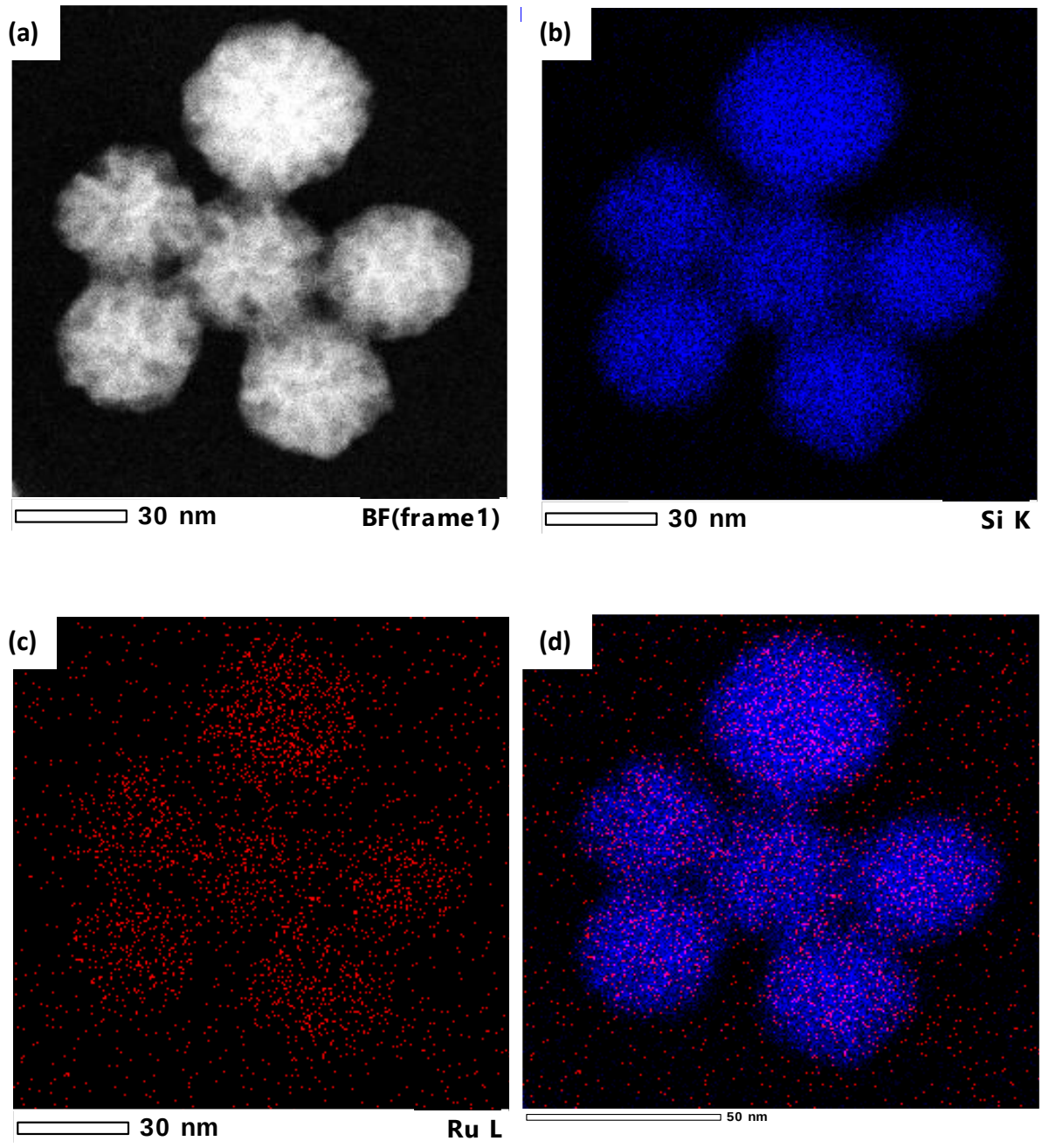

Figure 77. Electron microscope images and elemental cartography of the **SiO_2-Nd**: (a) STEM image, (b) Si cartography, (c) Nd cartography and (d) Si (blue color) and Nd (green color) cartographies.

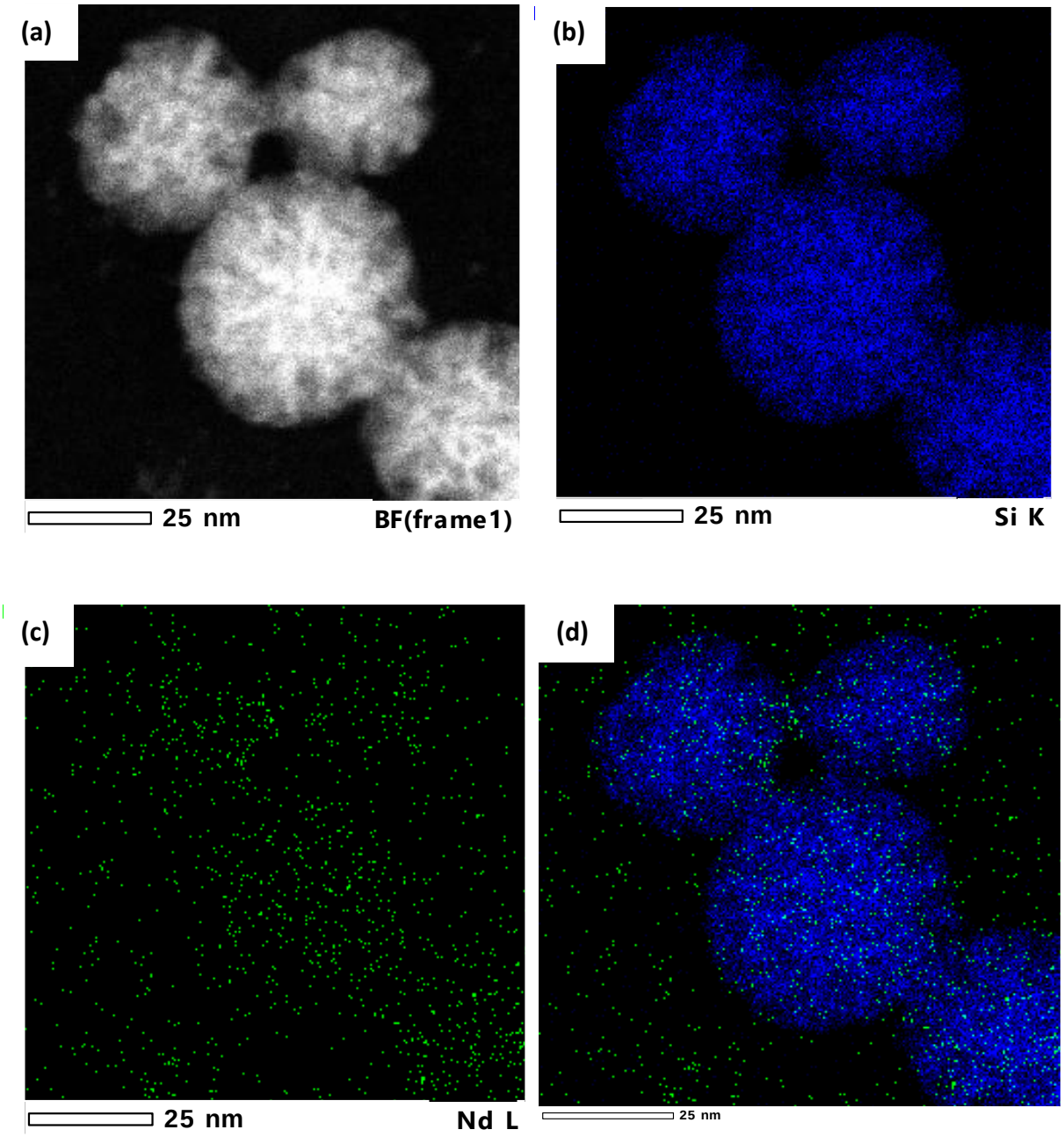

Figure 78. Electron microscope images and elemental cartography of the **SiO_2-Yb**: (a) STEM image, (b) Si cartography, (c) Yb cartography and (d) Si (blue color) and Yb (green color) cartographies.

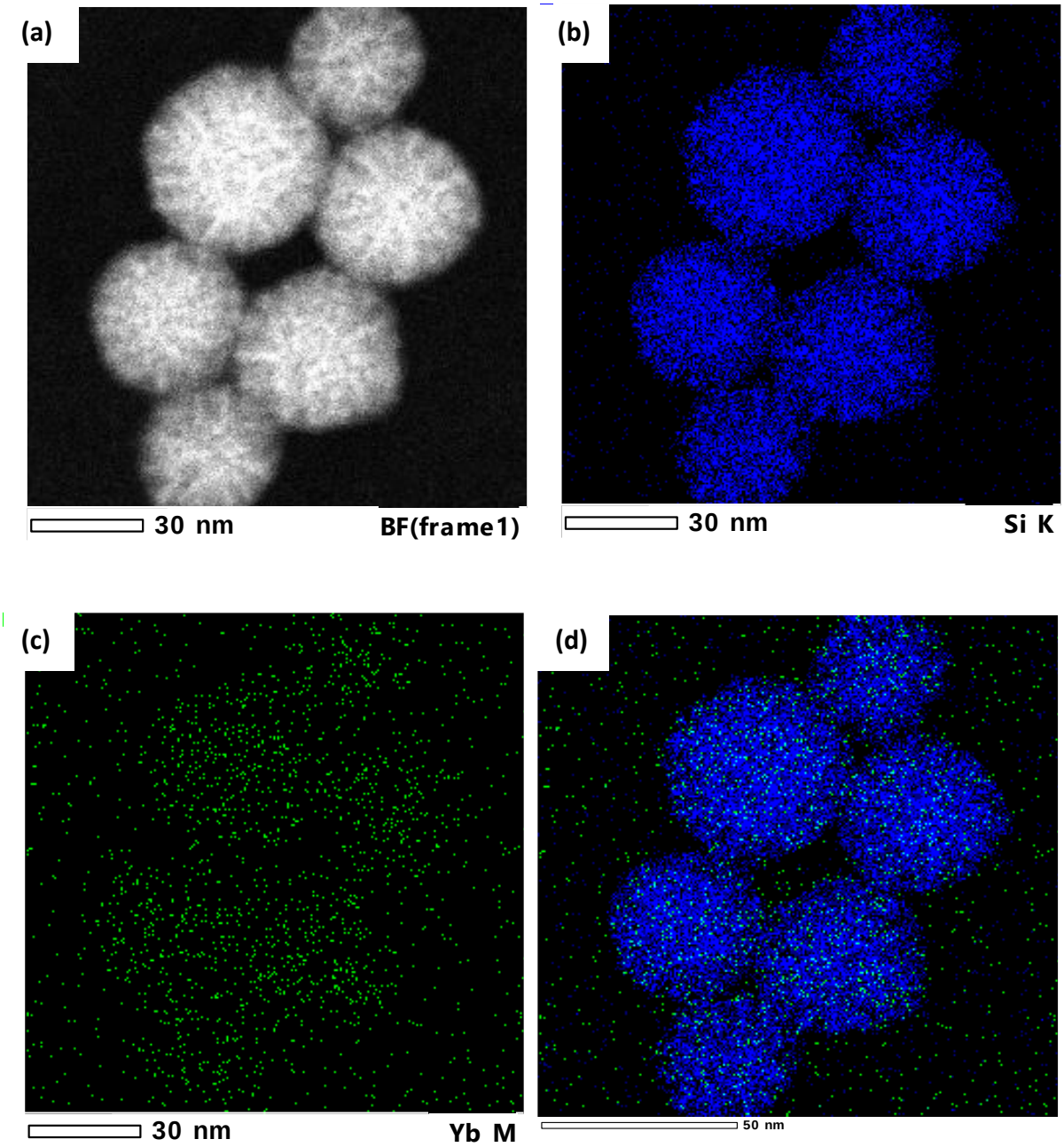

SiO_2-Ru nanohybrid keept the spherical shape. Elemental catography of Si atoms confirm that these elements are homogenously dispersed to form the MSNs. Ru atoms are also detected and its appear homogenously well dispersed inside the nanopores. Yb and Nd were detected and the cartography ensure the homogenity of dispertion confirming silylated complexes to be grafted at the nanopores of the MSNs. Grafting efficiency observed by STEM

are in agreement with the EA data (**SiO_2-Ru:** 0.18 mmol. g^{-1} of silica, **SiO_2-Nd:** 0.08 mmol. g^{-1} of silica, and **SiO_2-Yb:** 0.08 mmol. g^{-1} of silica)

SiO_2-RuYb and **SiO_2-RuNd** nanohybrids displayed higher grafting efficiency higher than the nanohybrids discussed above due to the grafting of two types of complexes onto MSNs. The elemental cartographies and STEM images for **SiO_2-RuYb** and **SiO_2-RuNd** are shown in figures 79 and 80.

Concerning **SiO_2-RuYb** and **SiO_2-RuNd** nanohybrids elemental cartography of Si atoms confirms that these elements are homogenously dispersed to form the MSNs. Ru and Yb atoms appear heterogenously distributed inside and at the surface of the nanopores (figure 79). The higher Yb concentration compared with Ru atoms at the nanoparticles surface is in agreement with the EA data (**SiO_2-RuYb:** 0.11 and 0.15 mmol. g^{-1} of silica using N and S contents for the calculation, respectively). On the other hand concerning **SiO_2-RuNd** Ru and Nd atoms are homogenously dispersed inside the nanopores (figure 80). STEM data confirm grafting efficiency as obtained by EA (**SiO_2-RuNd:** 0.14 and 0.16 mmol. g^{-1} of silica using N and S contents for the calculation, respectively).

Figure 79. Electron microscope images and elemental cartography of the **SiO_2-RuYb**: (a) STEM image, (b) Si cartography, (c) Ru cartography, (d) Yb cartography, (e) Si (blue color), Ru (red color) and Yb (green color) cartographies. (f) STEM image with a line profile of Ru (red line) and Yb (green line) atoms in the selected area (blue line).

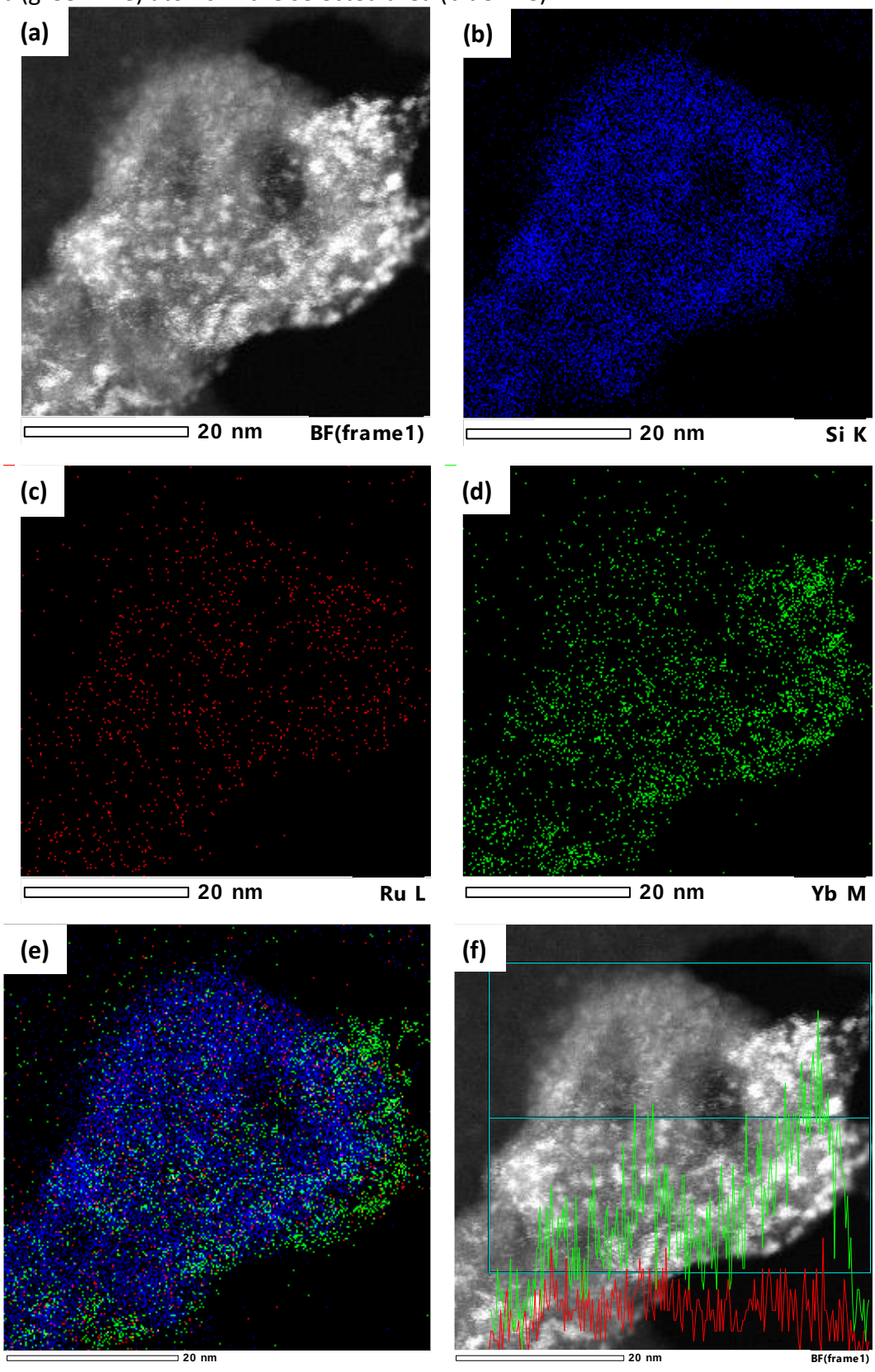

Figure 80. Electron microscope images and elemental cartography of the **SiO_2-RuNd**: (a) STEM image, (b) Si cartography, (c) Ru cartography, (d) Nd cartography and (e) Si (blue color), Ru (red color) and Nd (green color) cartographies. (f) STEM image with a line profile of Ru (red line) and Nd (green line) atoms in the selected area (blue line).

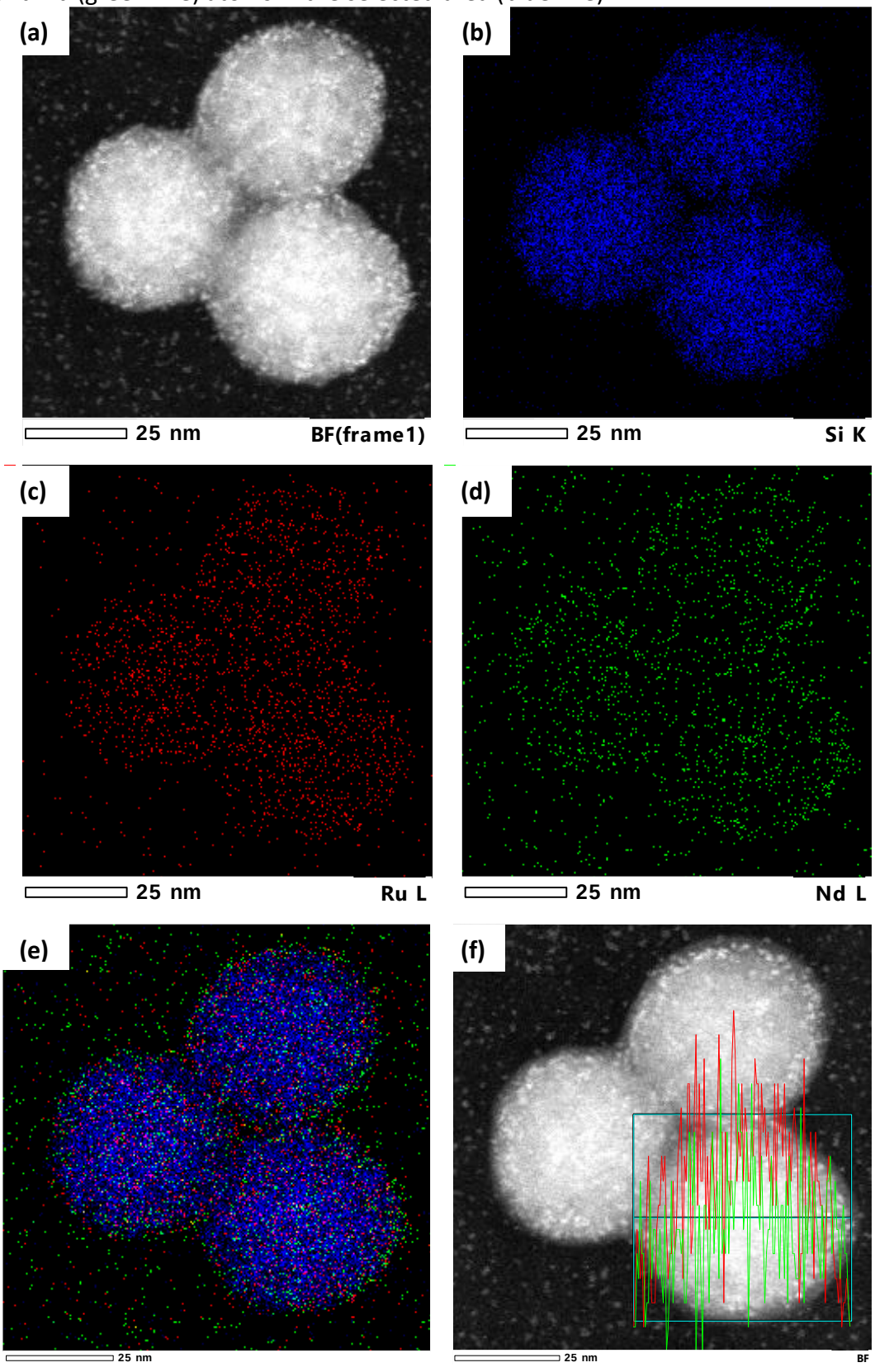

EA results together with STEM data suggest dependence on the nature of alkoxysilane groups used and the grafting efficiency. Additionally, according to Duarte et al.[77], when grafting is lower than 1.0 mmol of complex. g^{-1} of silica polymerization reactions are avoided leading to the formation of a monolayer of complexes on the silica matrix. In this work, the grafting of ruthenium and lanthanide complexes was calculated according to the N and S contents, respectively, as described in the section 3.2.1. The number of binuclear complexes.nm^2 of silica were calculated using grafting efficiency, Avogadro number and specific surface area values of the matrix before grafting of the complexes, according to the equation 8 below:

$$\delta = \frac{R\ x\ 10^{-3}\ x\ 6.023\ x\ 10^{23}}{S_{BET}\ x\ 10^{18}} \quad (8)$$

Table 6 shows grafting efficiencies, R, in mmol of ruthenium and lanthanide complexes.g^{-1} of silica and number of binuclear complexes.nm^2 of silica for the nanohybrids.

Table 6. Grafting efficiencies, in mmol of ruthenium and lanthanide complexes.g^{-1} of silica, and amount of ruthenium and lanthanide complexes.nm^{-2} of silica for the nanohybrids.

Samples	R (mmol.g^{-1} of SiO_2)		Number of complex per nm^2	
	R_{Ru}	R_{Ln}	Ru	Ln
SiO_2-Ru	0.18	---	0.16	---
SiO_2-Nd	---	0.08	---	0.07
SiO_2-Yb	---	0.08	---	0.07
SiO_2-RuYb	0.11	0.15	0.09	0.13
SiO_2-RuNd	0.14	0.16	0.12	0.14

The grafting efficiency using MSNs with 765 $m^2.g^{-1}$ of silica were higher for **SiO_2-Ru**, **SiO_2-RuYb** and **SiO_2-RuNd** than **SiO_2-Nd** and **SiO_2-Yb** nanohybrids. Additionally, 0.07-0.26 complexes per nm^2 were grafted onto MSNs. For **SiO_2-Ru**, **SiO_2-RuYb** and **SiO_2-RuNd** nanohybrids, the number of complexes per nm^2 of silica are in agreement with values obtained by Duarte et al.[77] However, for **SiO_2-Nd** and **SiO_2-Yb** nanohybrids, these results are lower than the expected. Low grafting ratios and complexes per nm^2 of silica for these

nanohybrids can be explained considering unavailability of silanol groups in the matrix or hydrolysis processes of the methoxysilyl groups before grafting reactions.

5.3.3. Photophysical properties of silica-based nanohybrids obtained by grafting of ruthenium(II) and lanthanide(III) silylated complexes

Figure 81 shows the excitation (on the left) and emission (on the right) spectra from the **SiO_2-Ru** nanohybrids.

Figure 81. Room temperature excitation ($\lambda_{emission}$ = 643 nm, on the left) and emission ($\lambda_{excitation}$ = 455 nm, on the right) spectra of the **SiO_2-Ru** nanohybrid in solid state.

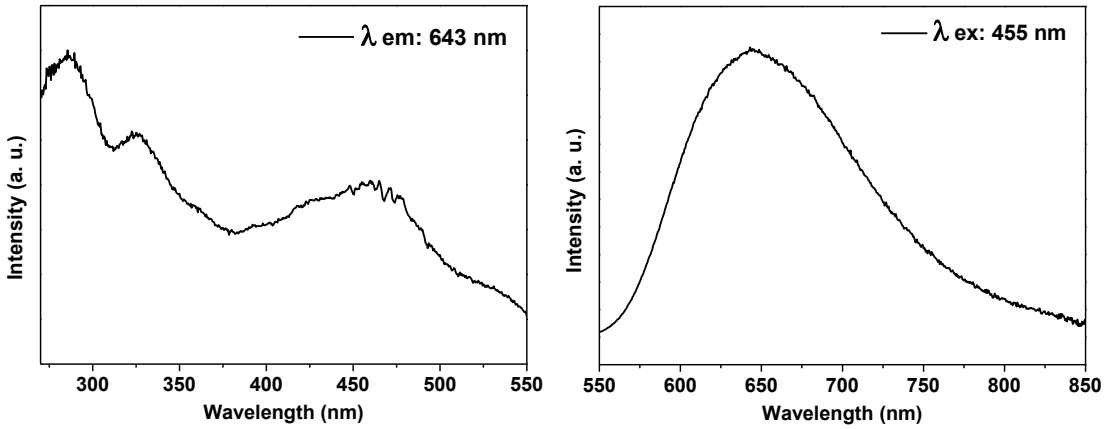

Bands at 285, 325 and 455 nm are observed in the excitation spectrum related to transitions centered on the ligand ($\pi \rightarrow \pi^*$ transitions) on the metal ($\pi_M \rightarrow \sigma^*_M$ transitions) and ^{1}MLCT ($d \rightarrow \pi^*$ transitions), respectively.[74, 89] The characteristic emission band of **SiO_2-Ru** nanohybrid centered at 643 nm was ascribed to the transition from the ^{3}MLCT excited state to the ground state.[74, 89] The blue shift compared to the free **RuL1** complex is related to the rigido- chromism phenomenon[99, 100] due the interaction between the complexes and the silanol groups of the rigid network avoid the spatial reorientation of complex. When the **RuL1** complex was grafted onto the mesoporous surface, the solvent present into the pores was unable to reorient around the excited complex. As a consequence, the Franck-Condon excited state was not completely stabilized, and emission occurred from a higher energy level than free complex.[74]

Luminescent properties of the nanohybrids obtained by grafting of **NdL3** and **YbL3** complexes on the MSNs were evaluated and comparing to the free silylated complexes. Figure

82 displays the excitation (on the left) and emission (on the right) spectra from **SiO_2-Nd** nanohybrids.

Figure 82. Room temperature excitation ($\lambda_{emission}$ = 1063 nm; on the left) and emission ($\lambda_{excitation}$ = 330 nm; on the right) spectra of the **SiO_2-Nd** nanohybrid in solid state.

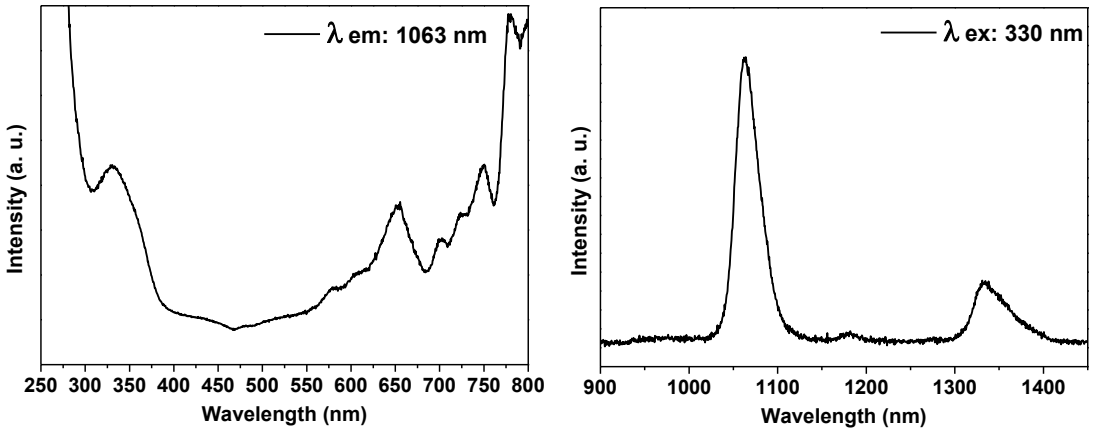

The band observed at 330 nm in the excitation spectrum is assigned to the singlet-to-singlet transitions of the **TTA-Si** ligands.[71] Bands above 400 nm can be attributed to Nd(III) intraconfigurational f-f transitions.[101–103] The emission spectrum shows two bands; a sharp band at 1063 nm attributed to $^4F_{3/2} \rightarrow {}^4I_{11/2}$ transition and a low intensity band centered at 1333 nm, assigned to the $^4F_{3/2} \rightarrow {}^4I_{13/2}$ transition.[101–103] These results corroborate EA, DRIFT, solid NMR and microscopy results confirm the obtained NIR luminescent nanohybrids.

The figure 83 shows the excitation and emission spectra obtained from **SiO_2-Yb** nanohybrids.

Figure 83. Room temperature excitation (on the left; $\lambda_{emission}$ = 981 nm) and emission (on the right; $\lambda_{excitation}$ = 330 and 388 nm; green and red lines, respectively) spectra of the **SiO_2-Yb** nanohybrid in solid state.

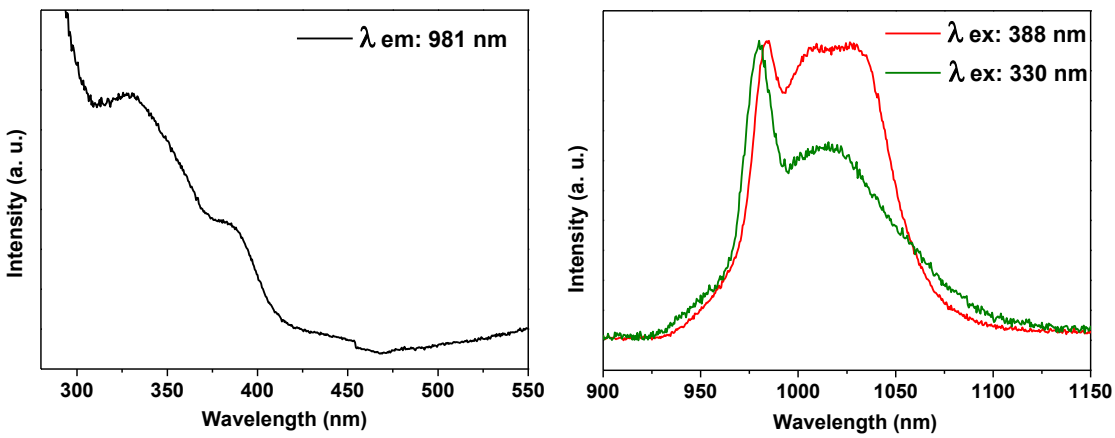

Two bands up to 400 nm are observed in excitation spectrum ascribed to the singlet-to-singlet transitions in the **TTA-Si** ligands.[71] Emission spectra obtained under excitation at 330 and 388 nm present a narrower band at 981 nm with a broader component at around 1025 nm assigned to the Yb^{3+} $^2F_{5/2} \rightarrow {}^2F_{7/2}$ transition.[101–103] Differences observed from the relative intensities between the narrower and the broader component may be related to slightly different site symmetries occupied by Yb^{3+} ions being excited selectively by the two different excitation wavelengths state.[91, 101–103]

Figure 84 shows excitation and emission spectra obtained for **SiO_2-RuNd**. A broad emission band was observed at 610 nm and assigned to the Ru(II) ^{3}MLCT emission[74, 89] in a similar way observed for **SiO_2-Ru** (figure 81). Comparing with free **RuL1** complex the ^{3}MLCT energy was blue shifted as previously described (**SiO_2-Ru** in the figure 81). The excitation spectra obtained by monitoring the Ru(II) ^{3}MLCT emission shows bands ascribed to the $d \rightarrow \pi^*$ ^{1}MLCT transitions, transitions centered on ligands ($\pi \rightarrow \pi^*$ transitions) and transitions centered on the metal ($\pi_M \rightarrow \sigma^*_M$ transitions)[74, 89], in agreement with the free **RuL1** complex.

Two emission bands were detected in the infrared region at 1061.5 nm (attributed to Nd^{3+} $^4F_{3/2} \rightarrow {}^4I_{11/2}$ transition) and at 1333 nm (Nd^{3+} $^4F_{3/2} \rightarrow {}^4I_{13/2}$ transition). The excitation spectrum obtained when monitoring emission at 1061.5 shows Nd^{3+} above 700nm. Two broad bands are observed below 600 nm. Considering the excitation spectrum obtained by monitoring the Ru related visible emission, the sensitization of the Nd^{3+} IR emission is clearly shown here.

Figure 84. Room temperature excitation ((a), $\lambda_{emission}$: 610 nm and (c), $\lambda_{emission}$: 1061.5 nm) and emission ((b), $\lambda_{excitation}$: 455 nm; and (d), $\lambda_{excitation}$: 365 and 455 nm) spectra of the **SiO_2-RuNd** nanohybrid in solid state.

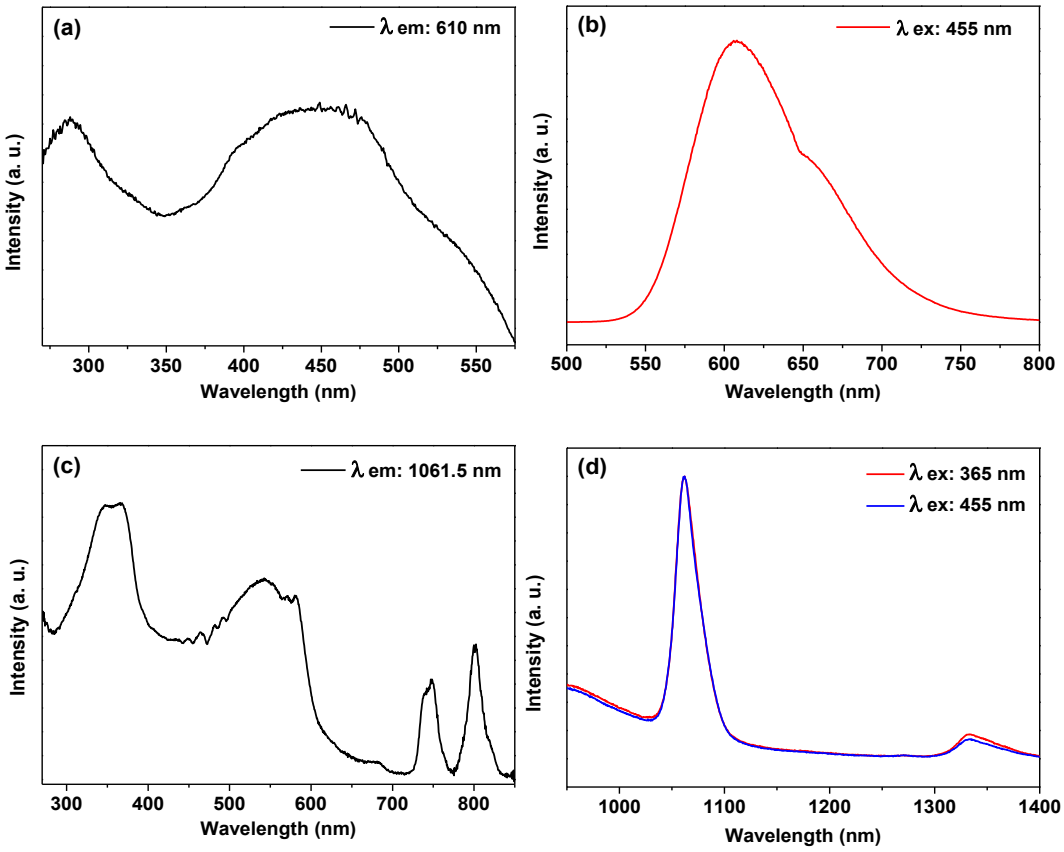

Figure 85 shows results obtained for **SiO_2-RuYb**. The Ru related broad emission band is observed peaking at 610 nm (figure 85 (b)). Excitation spectrum obtained by monitoring the broad emission bands shows the broad bands assigned to the ligands and Ru^{2+} in similar way obtained for the **SiO_2-RuNd**.

The IR emission band peaking at 980 nm with broader components at 1010 and 1030 nm (figure 85 (d)) could be ascribed to the Yb(III) $^2F_{5/2} \rightarrow {}^2F_{7/2}$ transition.[101–103] The excitation spectrum (Figure 85 (c)) shows the broad ligand centered band below 400 nm and the Ru^{2+} related band from 400 to 700 nm. In the same way observed for the **SiO_2-RuNd** nanohybrid, here the Ru^{2+} to Yb^{3+} energy transfer is evidenced.

Figure 85. Room temperature excitation ((a), $\lambda_{emission}$: 610 nm and (c), $\lambda_{emission}$: 980 nm) and emission ((b), $\lambda_{excitation}$: 370 and 455; and (d), $\lambda_{excitation}$: 365 and 475 nm) spectra of the **SiO_2-RuYb** nanohybrid in solid state.

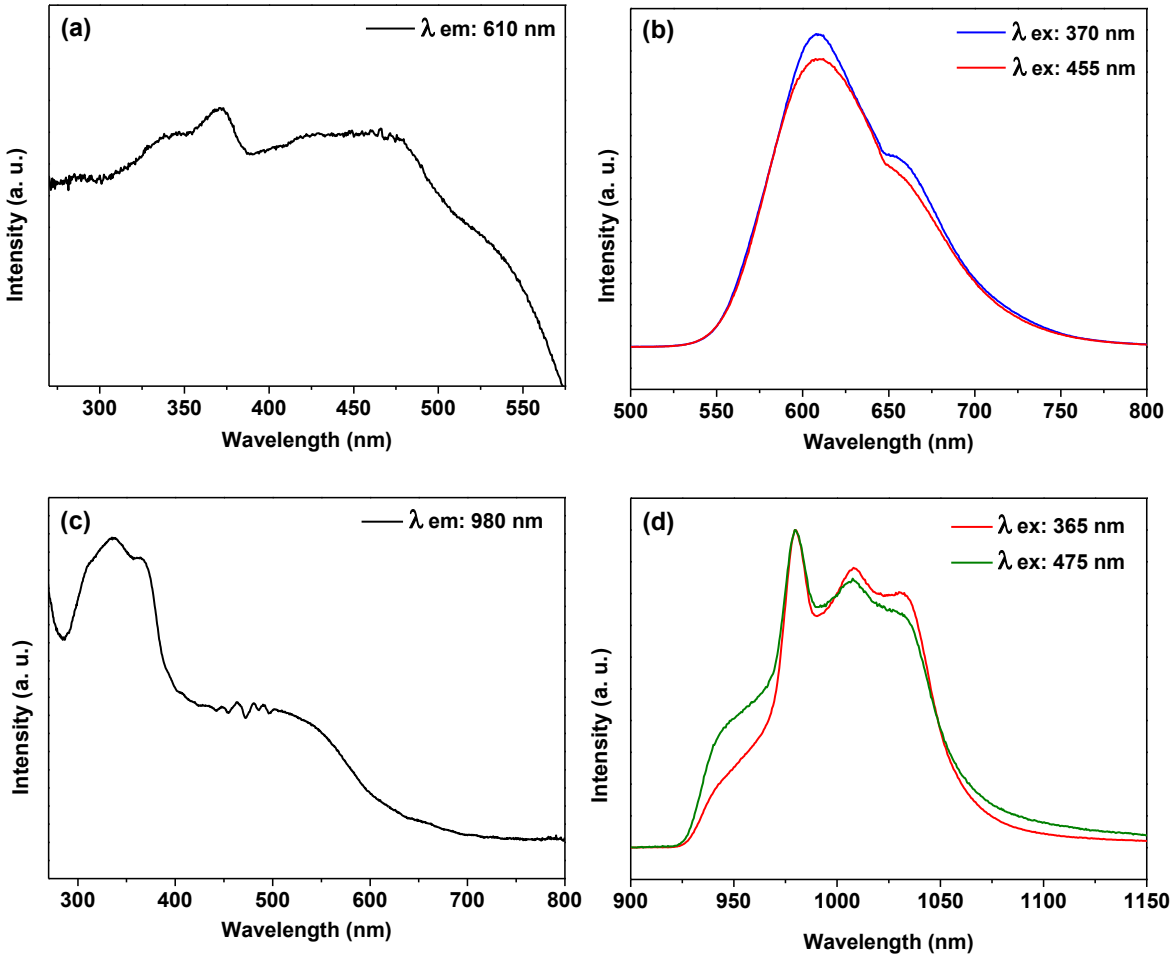

The energy levels diagram presented in figure 86 illustrates the observed energy transfer processes.

Figure 86. Schematic energy transfer processes (Ru(II)) to Nd^{3+} and Yb^{3+} (A = Absorption; ISC = Inter-System Cross; P = phosphorescence; ET = Energy Transfer; F = Fluorescence) in the **SiO_2-Ru**, **SiO_2-RuNd** and **SiO_2-RuYb** nanohybrids.

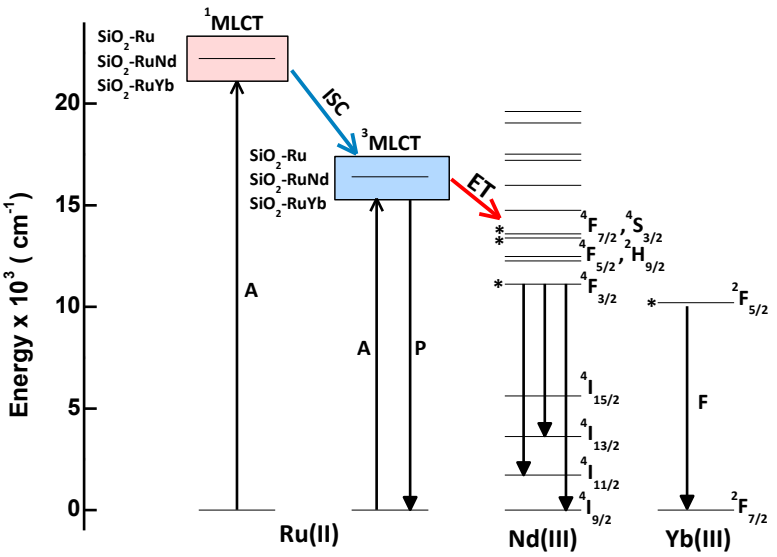

Decay time results observed for the Ru^{2+} MLCT level are presented in table 7. Decreasing decay times in the presence of lanthanide ions put in evidence Ru-Ln energy transfer process.

Energy transfer rate of 0.20×10^7 s^{-1} and ET quantum yield of 40 % could be evaluated for **SiO_2-RuNd.** ET rate of of 0.11×10^7 s^{-1} and quantum yield and 27.5 %, were obtained for **SiO_2-RuYb**. The higher values observed for the Nd(III) hybrid is well explained by the matching of donor and acceptor energy levels as shown in figure 86.

Table 7. Photophysical properties for MLCT-based visible emission and Ln(III) based NIR.

	MLCT-based emission (Ex: 448 nm)			
	λ / nm	τ / ns	[a] k_{ET} / 10^7 s^{-1}	[b] Φ_{ET} / %
SiO_2-Ru	610	344.7	---	---
SiO_2-RuNd	610	206.2	0.20	40.2
SiO_2-RuYb	610	249.8	0.11	27.5

[a] k_{ET} (energy transfer rate constant) = $1/\tau_q - 1/\tau_u$ (τ_q and τ_u refer to the "quenched" and "unquenched" lifetime of Ru^{2+} complexes before and after coordination with Ln^{3+}). [b] Φ_{ET} (energy transfer quantum yield) = $1 - (\tau_q/\tau_u)$.

Therefore, two new luminescent nanohybrids were prepared. The photophysical properties of both nanohybrids were evaluated and energy transfer processes were confirmed for lifetimes data obtained from Ru(II) emission decay and emission/excitation spectra.

5.4. Synthesis and characterization of silica-based nanohybrids obtained by grafting of *d-f* heterobimetallic silylated complexes onto MSNs and Ludox silica AS-40 (DSNs)

The *d-f* heterobimetallic silylated complexes successfully synthesized (section 4.2) were grafted onto mesoporous silica nanoparticles (MSNs) by using the methodology previously described in the section 5.3.

Figure 87 shows a representation of grafting reactions of the **Ru—LnL3** complexes onto MSNs (a) and **Ln—RuL** complexes onto MSNs or DSNs (b).

Figure 87. Representation of grafting reactions of (a) **Ru—LnL3** complex onto MSNs and (b) **Ln—RuL** complexes onto MSNs and DSNs.

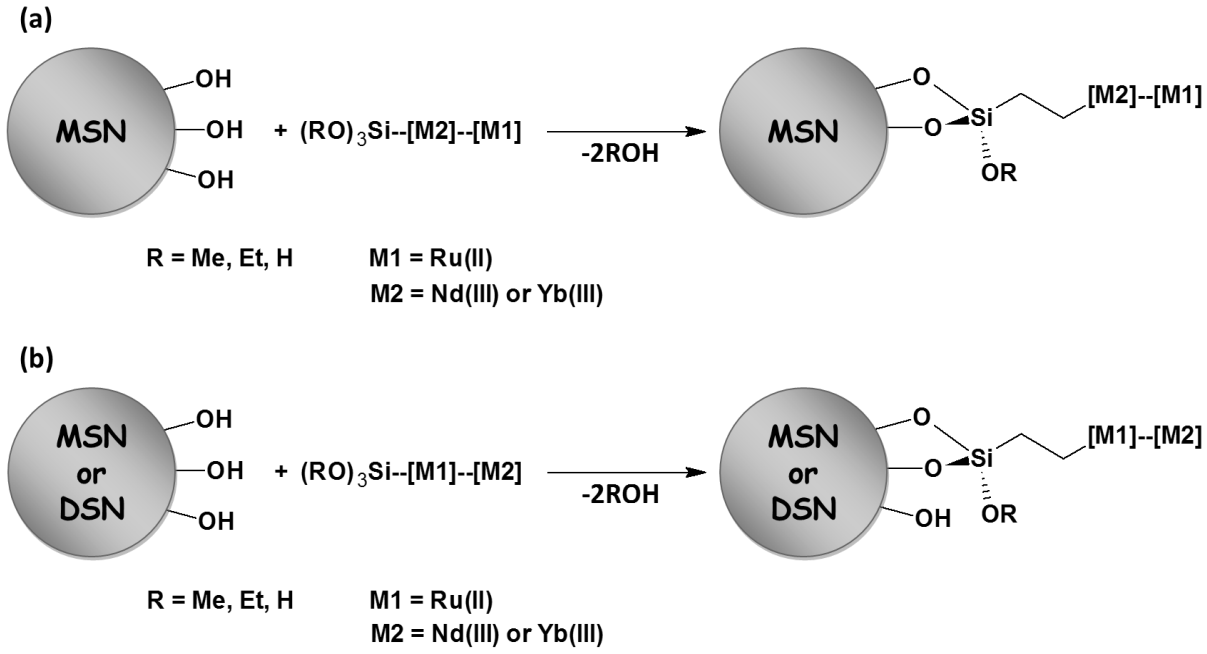

Three luminescent nanohybrids were obtained by grafting of **Ru—YbL3**, **Nd—RuL** and **Yb—RuL** binuclear complexes onto MSNs and one luminescent nanohybrids obtained by grafting of **Yb—RuL** binuclear complex onto DSNs surface (Ludox AS-40). The nanohybrids

from MSNs were labeled **SiO_2-RuYbL3**, **SiO_2-NdRuL** and **SiO_2-YbRuL** and the ratios of complexes per gram of MSNs added were 0.10, 0.12 and 0.14 mmol g^{-1}, respectively. The nanohybrid from DSNs was noted **SiO_2 d-YbRuL** and the ratios of complexes per gram of DSNs added was 0.06 mmol g^{-1}. As already previously discussed, ratios of complexes per gram of silica lower than 1.0 mmol g^{-1} confirm the obtaining of nanohybrids with a monolayer of complexes avoiding polymerization reactions of them on the silica matrix.[77, 98]

5.4.1. Spectroscopic characterization of the silica-based nanohybrids obtained by grafting of *d-f* heterobimetallic silylated complexes onto MSNs and Ludox silica AS-40 (DSNs)

Figure 88 shows DRIFT spectra of (a) **SiO_2-RuYbL3**, (b) **SiO_2-NdRuL**, (c) **SiO_2-YbRuL** and (d) **SiO_2 d-YbRuL** nanohybrids.

Figure 88. DRIFT spectra of (a) **SiO_2-RuYbL3,** (b) **SiO_2-NdRuL**, (c) **SiO_2-YbRuL** and (d) **SiO_2 d-YbRuL** nanohybrids.

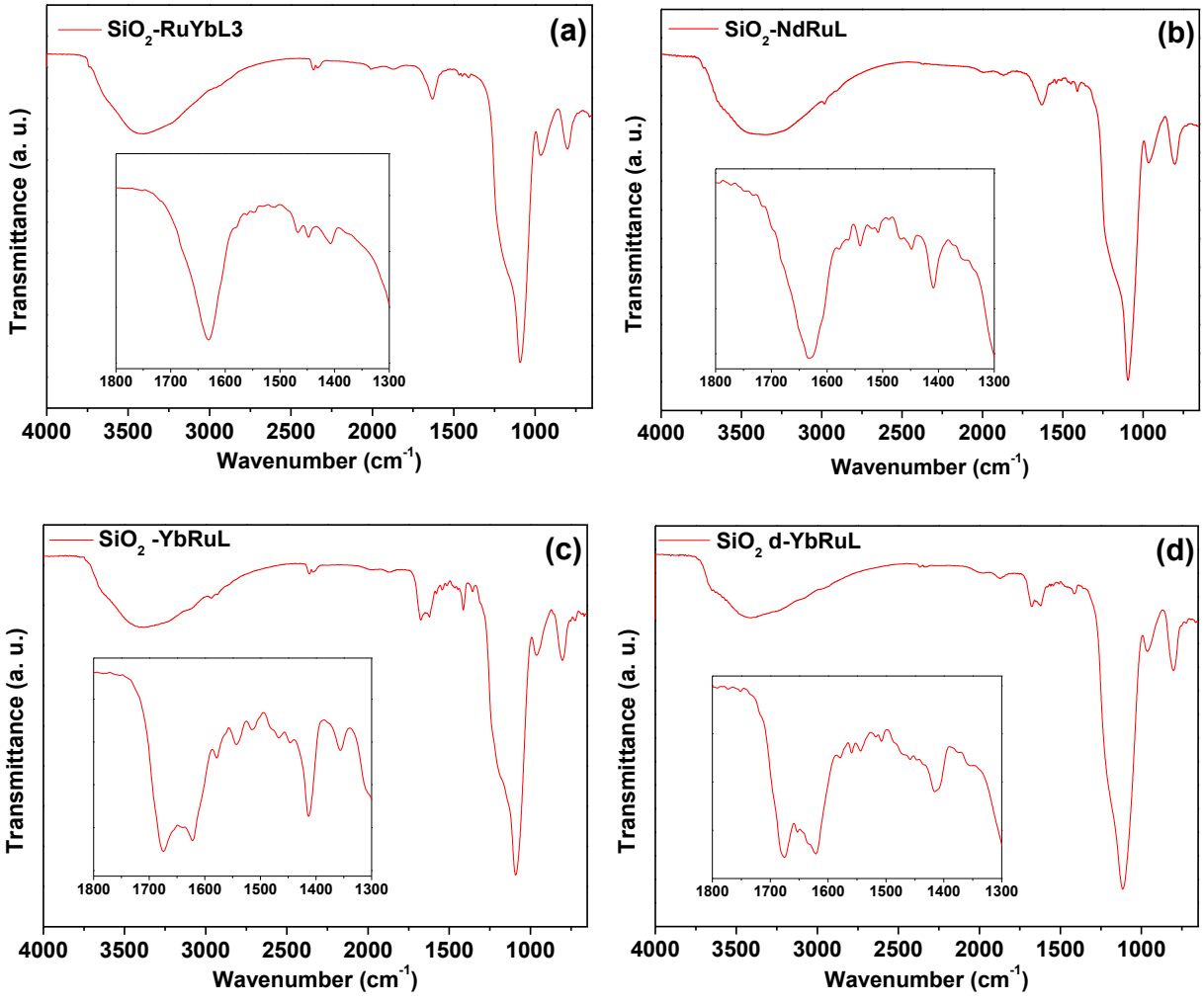

Bands in the 1621 – 1607 cm^{-1} region were attributed to v(C=O, C=C) and from 1468 to 1355 cm^{-1} ascribed to v(C=C, C=S $_{thienyl}$) for all nanohybrids, confirming the presence of complexes in the silica matrix. Table 8 displays the bands ascribed to the ligands present in the complexes.

Table 8. DRIFT data for the nanohybrids.

Nanohybrids	DRIFT (cm^{-1})		
	v(C--O)	**v(C=O, C=C)**	**v(C=C, C=S $_{thienyl}$)**
SiO_2-RuYbL3	---	1579, 1544	1468, 1447, 1407
SiO_2-NdRuL	---	1578, 1540, 1507	1467, 1448, 1408, 1355
SiO_2-YbRuL	1621	1578, 1542, 1512	1467, 1448, 1408, 1355
SiO_2 d-YbRuL	1621	1579, 1558, 1544, 1507	1467, 1412, 1355

FT-RAMAN measurements were also performed. Bands related to Metal—O or Metal—N bonds present in the heterobimetallic complexes could be observed.

Figure 89 displays FT-Raman spectra of the heterobimetallic silylated complexes (blue lines) and their respective nanohybrids (black lines).

Complementary to the DRIFT data, bands in 1617-1606 cm^{-1} and 1580-1470 cm^{-1} region, assigned to v(C=N, C=C), respectively, were observed for all nanohybrids. Bands ascribed to v(C=O, C=C) were found in the 1415 and 1357 cm^{-1} region, characteristic of lanthanide complexes. At 1040 – 1030 cm^{-1} bands were attributed to v(Ru—N), characteristic of ruthenium complexes.[85–88] These results are in agreement with FTIR analysis and confirm that heterobimetallic silylated complexes are grafted onto silica matrix.

Figure 90 (I) shows $^{13}C\{^1H\}$CP-MAS spectra for the nanohybrids obtained by grafting of heterobimetallic complexes. The spectrum obtained from **SiO_2-RuYbL3** (figure 90 (I), a) displays signals referent to the carbon atoms of the **Ru—YbL3** complexes grafted onto MSNs. Signals characteristic of aromatic carbons observed at 126 (CV; V'; 5; III; 3), 139 (CIV), 153 (C4; VI; 6), 157 (CII; 2;) and 163.5 (CIII'; IV') ppm were attributed to the **bpy** and **bpmd** ligands.[73] The contribution of betadiketones ligands present in the **Ru—YbL3** heterobimetallic complex are not observed due to the coordination with ytterbium ions. Paramagnetic interactions from this ytterbium ions compromise the efficiency of the cross-polarization process owing to very short ^1H spin-lattice relaxation times in the rotating frame.[68]

Figure 89. FT-Raman spectra of (a) **Ru—YbL3** (blue line) and **SiO_2-RuYbL3** (black line), (b) **Nd—RuL** (blue line) and **SiO_2-NdRuL** (black line), (c) **Yb—RuL** (blue line) and **SiO_2-YbRuL** (black line) and (d) **Yb—RuL** (blue line) and **SiO_2 d-YbRuL** (black line).

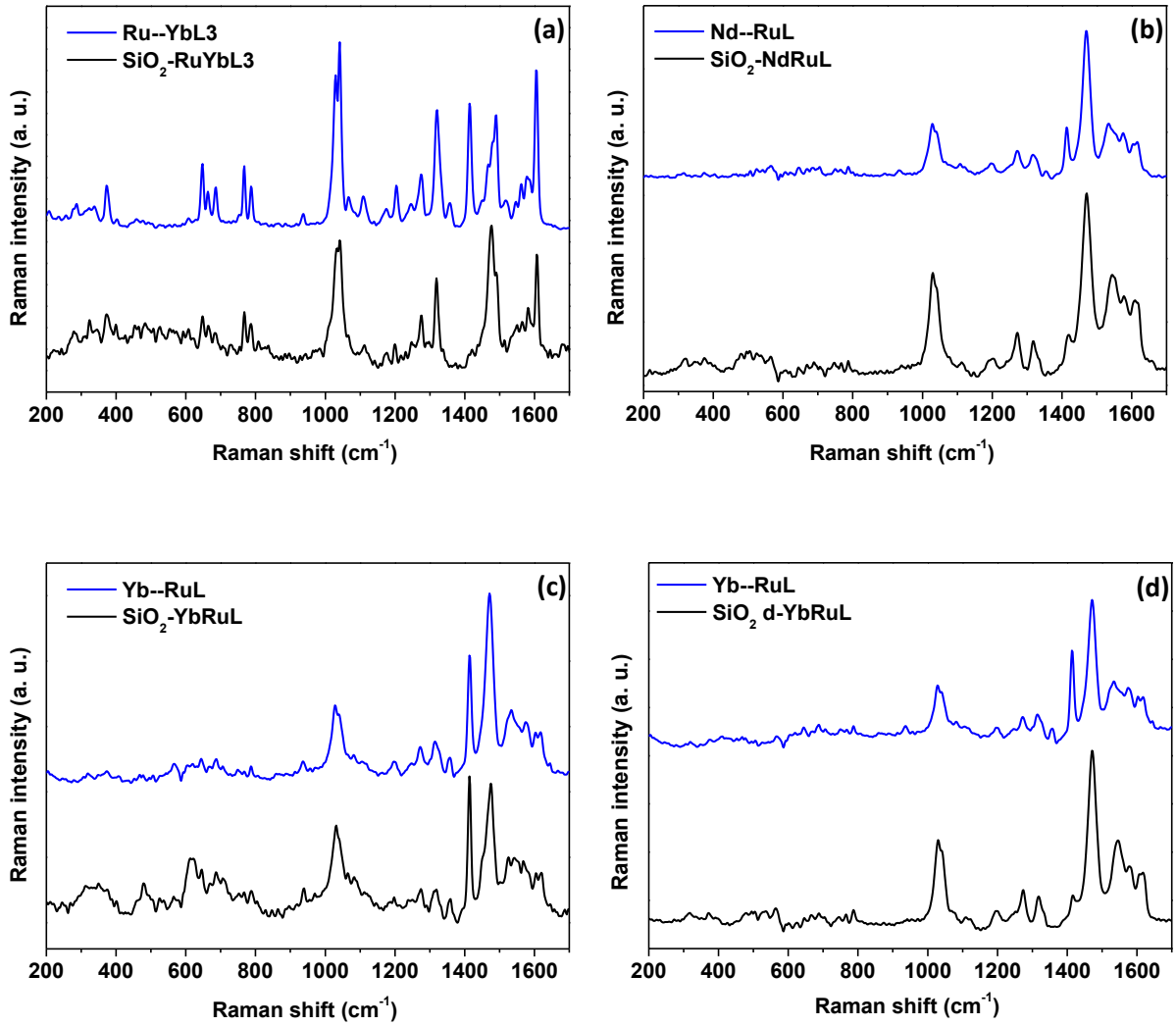

Although the absence of signals relating to betadiketone ligands, carbon atoms ascribed to the propyl chain appear at 10 (C11), 23 (C10) and 46 (C9) ppm. The signal at 72 ppm was not attributed. For the nanohybrids obtained by grafting of **Ln—RuL** complexes (**SiO_2-NdRuL**, **SiO_2-YbRuL and SiO_2 d-YbRuL**) only signals ascribed to the silylated ruthenium complexes were observed. The signals relating to the betadiketone ligands were not detected due to the paramagnetic interactions from neodymium and ytterbium ions. In this way, the spectra present in the figure 90 (I) (b, c and d) were similar showing signals at 162.5 (CIII'; IV'), 157.5 (CII; 2; 2'), 151.5 (C4; 4'; VI; 6; 6'), 138 (CIV) and 125.5 (CV; V'; 5; 5'; III; 3; 3') ppm assigned to the carbon atoms of the bpy and bpmd ligands. Signals at 58 (C8), 51.5 (C9), 21.5

(C10; 7) and 10 (C11) ppm were attributed to the ethoxysilyl groups present in the heterobimetallic complexes. These results are in agreement with DRIFT and FT-RAMAN analysis confirming the chemical integrity of the binuclear complexes.

$^{29}Si\{^{1}H\}$CP-MAS NMR measurements were carried out to confirm the grafting of the binuclear complexes onto the MSNs and DSNs. The covalent bond of the alkoxysilyl groups with the silanol available in the matrix can be confirmed by T^n peaks usually observed from -55 to - 70 ppm. Figure 90 (II, a) displays $^{29}Si\{^{1}H\}$CP-MAS NMR spectrum for **SiO_2-RuUbL3** with T^2 and T^3 peaks observed at -59 and -67 ppm, respectively, that correspond to the successful condensation of methoxysilyl groups with the MSNs. For the **SiO_2-NdRuL** nanohybrids (figure 90 (II), b) T^2 and T^3 peaks observed at -57 and -66 ppm correspond to the condensation of the ethoxysilyl groups with the MSNs. The spectra from **SiO_2-YbRuL** and **SiO_2 d-YbRuL** nanohybrids (figure 90 (II), c and d, respectively) show T^2 and T^3 peaks at -59, -68 and -59, -67 ppm, respectively, attributed to the covalent bond of ethoxysilyl groups onto MSNs and DSNs. Results confirm the condensation of the ethoxysilyl and methoxysilyl groups present in the complexes with the silanol available in the MSNs and DSNs. Table 9 shows the chemical shifts assigned to T^n peaks and Q^n species obtained by $^{29}Si\{^{1}H\}$CP-MAS NMR measurements for all nanohybrids.

Table 9. T^n and Q^n chemical shifts of the nanohybrids.

Samples	$^{29}Si\{^{1}H\}$CP-MAS NMR				
	T^2 (ppm)	T^3 (ppm)	Q^2 (ppm)	Q^3 (ppm)	Q^4 (ppm)
SiO_2-RuYbL3	-59	-67	-94	-103	-111
SiO_2-NdRuL	-59	-68	-94	-103	-111
SiO_2-YbRuL	-59	-68	-93	-103	-111
SiO_2 d-YbRuL	-59	-67	-94	-103	-111

Figure 90. ^{13}C {^{1}H}CP-MAS NMR spectra (**I**) and ^{29}Si {^{1}H}CP-MAS NMR spectra (**II**) of (a)**SiO_2-RuYbL3**, (b)**SiO_2-NdRuL**, (c) **SiO_2-YbRuL** and (d) **SiO_2 d-YbRuL**. *: carbon atoms in residual ethanol groups. *****: signal at 72 ppm was not attributed. **+**: similar to TMS (tretamethylsilane). **M1**: —O—SiR_3. The numbering of carbon atoms is given on the figure 30 with Roman figures for the bpy ligand; Arabic numerals for the bpy-Si and TTA-Si ligands.

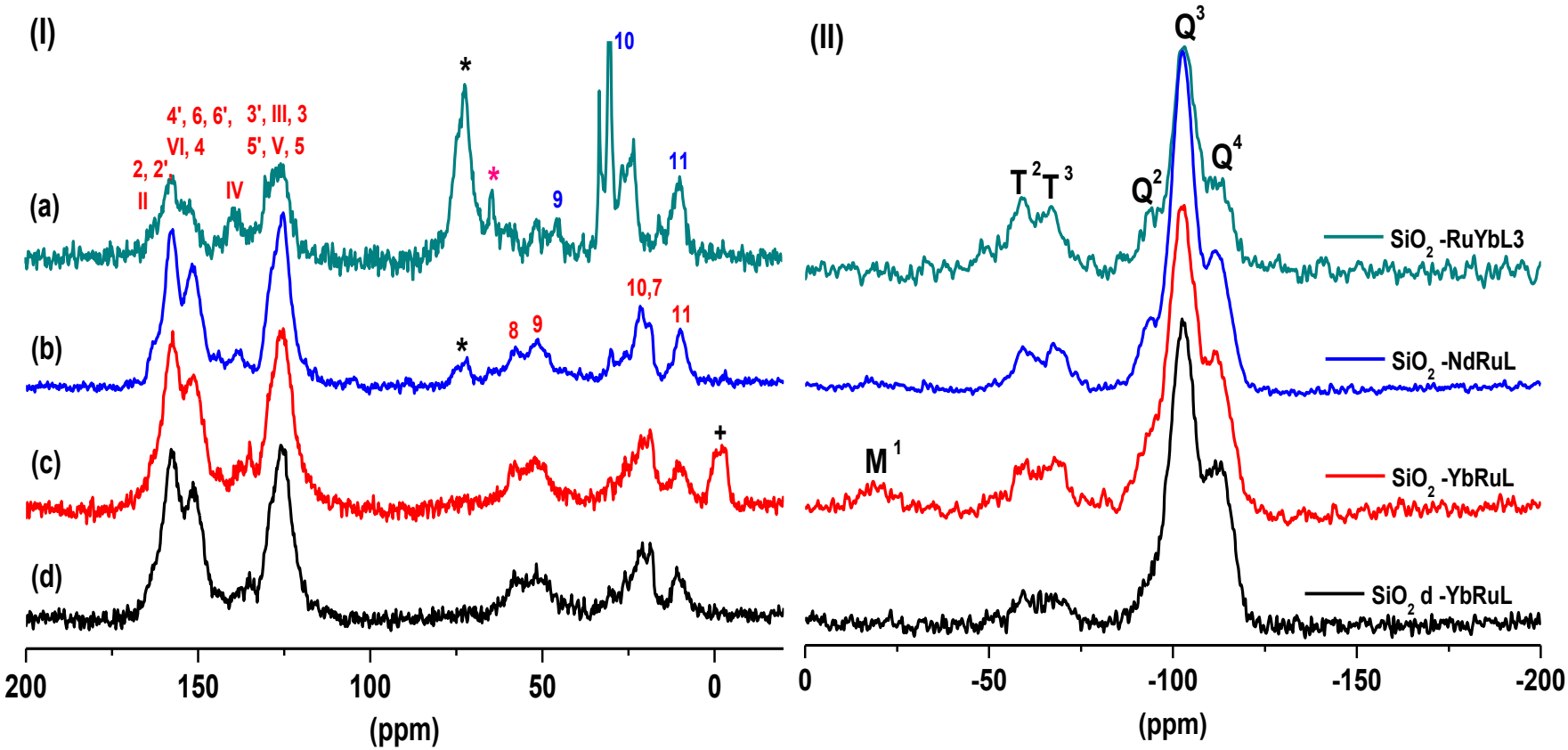

5.4.2. Microstructural characterization of silica-based nanohybrids obtained by grafting of *d-f* heterobimetallic silylated complexes onto MSNs and Ludox silica AS-40 (DSNs).

Figure 91 shows SEM images obtained from (a) **SiO_2-RuYbL3**, (b) **SiO_2-NdRuL**, (c) **SiO_2-YbRuL** and (d) **SiO_2 d-YbRuL** nanohybrids and the morphology of the nanohybrids were observed not to change. However, for **SiO_2-RuYbL3** and **SiO_2-NdRuL** nanohybrids the nanopores were hardly observed due to the presence of the **Ru—YbL3** and **Nd—RuL** complexes grafted, respectively. For **SiO_2-YbRuL** (figure 91, c) was not possible to observe the nanopores because its completely filled up with **Yb—RuL** complex. The **SiO_2 d-YbRuL** nanohybrid (figure 91, d) showed the same morphology of de pure DSNs. It is important noting that FEG-SEM images from all nanohybrids were obtained without metallization. So, the nanopores are not masked and we can affirm that the nanopores are hardly observed due to the presence of heterobimetallic complexes grafted.

Figure 91. FEG-SEM images of (a) **SiO_2-RuYbL3**, (b) **SiO_2-NdRuL**, (c) **SiO_2-YbRuL** and (d) **SiO_2 d-YbRuL** nanohybrids.

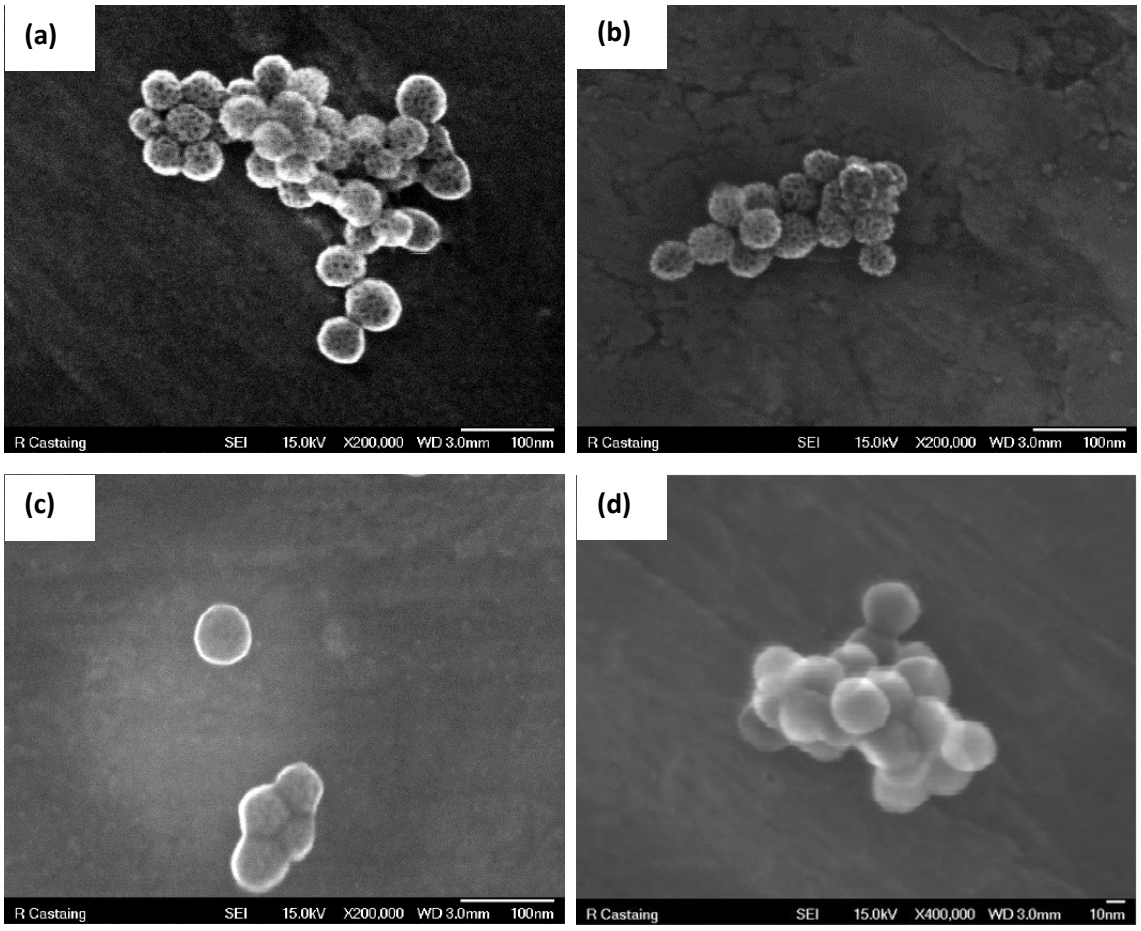

FEG-SEM images corroborate DRIFT, FT-RAMAN and solid NMR analysis showing that the nanohybrids keept the same morphology and the binuclear complexes are grafted inside the nanopores of MSNs and onto DSNs surface. HR-TEM measurements were performed to confirm FEG-SEM images, according to the figure 92.

Figure 92. HR-TEM bright field (above) and dark field (below) images of (a) **SiO_2-RuYbL3**, (b) **SiO_2-NdRuL** and (c) **SiO_2-YbRuL** nanohybrids.

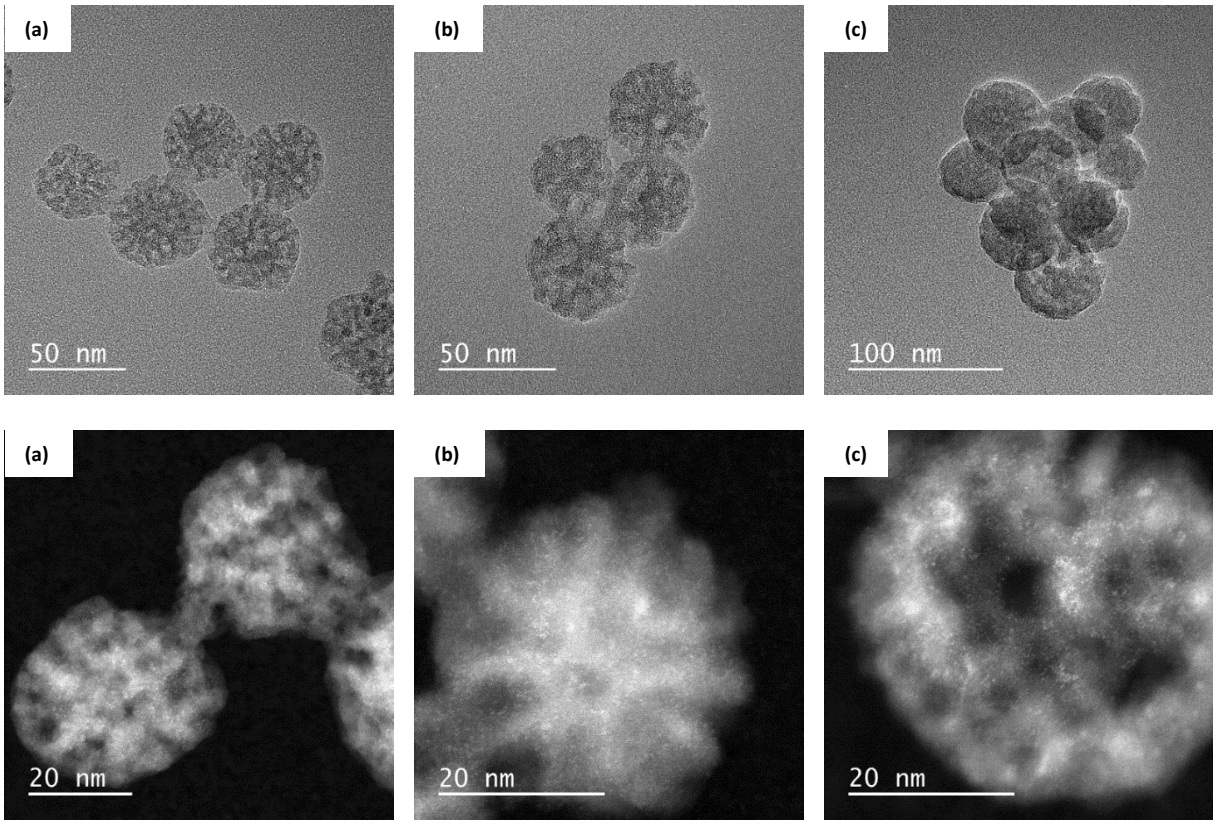

Figure 92 shows HR-TEM bright field and dark field images of (a) **SiO_2-RuYbL3**, (b) **SiO_2-NdRuL** and (c) **SiO_2-YbRuL** nanohybrids. HR-TEM bright field images confirm spherical morphology without changing of the structure for all nanohybrids. Besides that, it was possible to see the nanopores filled up with heterobimetallic complexes. Additionally, from dark field images the observed charges could be ascribed to the ruthenium, neodymium and ytterbium atoms. These results are in agreement with DRIFT, FT-RAMAN, solid NMR and FEG-SEM analysis showing that the heterobimetallic complexes were grafted inside de nanopores of MSNs.

Figure 93 shows STEM images (a and f) and elemental carthographies of the Si (b), Ru (c), Yb (d) atoms and all of them superposed (d) for **SiO_2-RuYbL3** nanohybrid. Figure 93 (a) suggests homogeneous distribution of the metallic atoms onto MSNs and the elemental cartography of Si atoms (figure 93, b) shows a homogenous distribution of them to form the MSNs. Elemental cartographies (figure 93, c and d) of Ru and Yb atoms display both elements well dispersed onto MSNs. Despites elemental cartographies of Si, Ru and Yb atoms superposed (figure 93, e) suggest homogeneous distribution of the Ru and Yb inside the nanopores of the MSNs, low concentrations of Ru and Yb atoms were observed. These results are consistent with the STEM image (figure 93, f) showing the distribution profile with low and similar concentration of both atoms. Grafting efficiencies obtained by EA with 0.06 and 0.03 mmol. g^{-1} of silica for ruthenium and ytterbium complexes, respectively, corroborate STEM data.

Figure 94 (a) shows STEM measurements obtained for **SiO_2-NdRuL**. STEM image suggests high concentration of metallic atoms with homogeneous distribution onto MSNs. Elemental cartography of Ru atoms shows this element well homogeneously dispersed besides high concentration on the MSNs (figure 94 (c)). However, irregular distribution and low concentration of Nd atoms inside de nanopores of the MSNs were detected (figure 94 (d)). Figure 94 (e) displays elemental cartographies of Si, Ru and Nd atoms superposed and confirm higher concentration of Ru than Nd atoms. The figure 94 (f) shows distribution profile of Ru and Nd atoms which clearly confirm higher concentration of Ru than Nd atoms on the surface and inside the MSNs. These results corroborate grafting ratios of 0.17 and 0.05 mmol. g^{-1} of silica for ruthenium and neodymium complexes, respectively, obtained by EA. It is worth pointing out that very distinct grafting ratios for **SiO2-NdRuL** can be assigned to neodymium complexes loss during or after the grafting reactions.

Figure 93. Electron microscope images and elemental cartography of the **SiO_2-RuYbL3**: (a) STEM image, (b) Si cartography, (c) Ru cartography, (d) Yb cartography, (e) Si (blue color), Ru (red color) and Yb (green color) cartographies. (f) STEM image with a line profile of Ru (red line) and Yb (green line) atoms in the selected area (blue line).

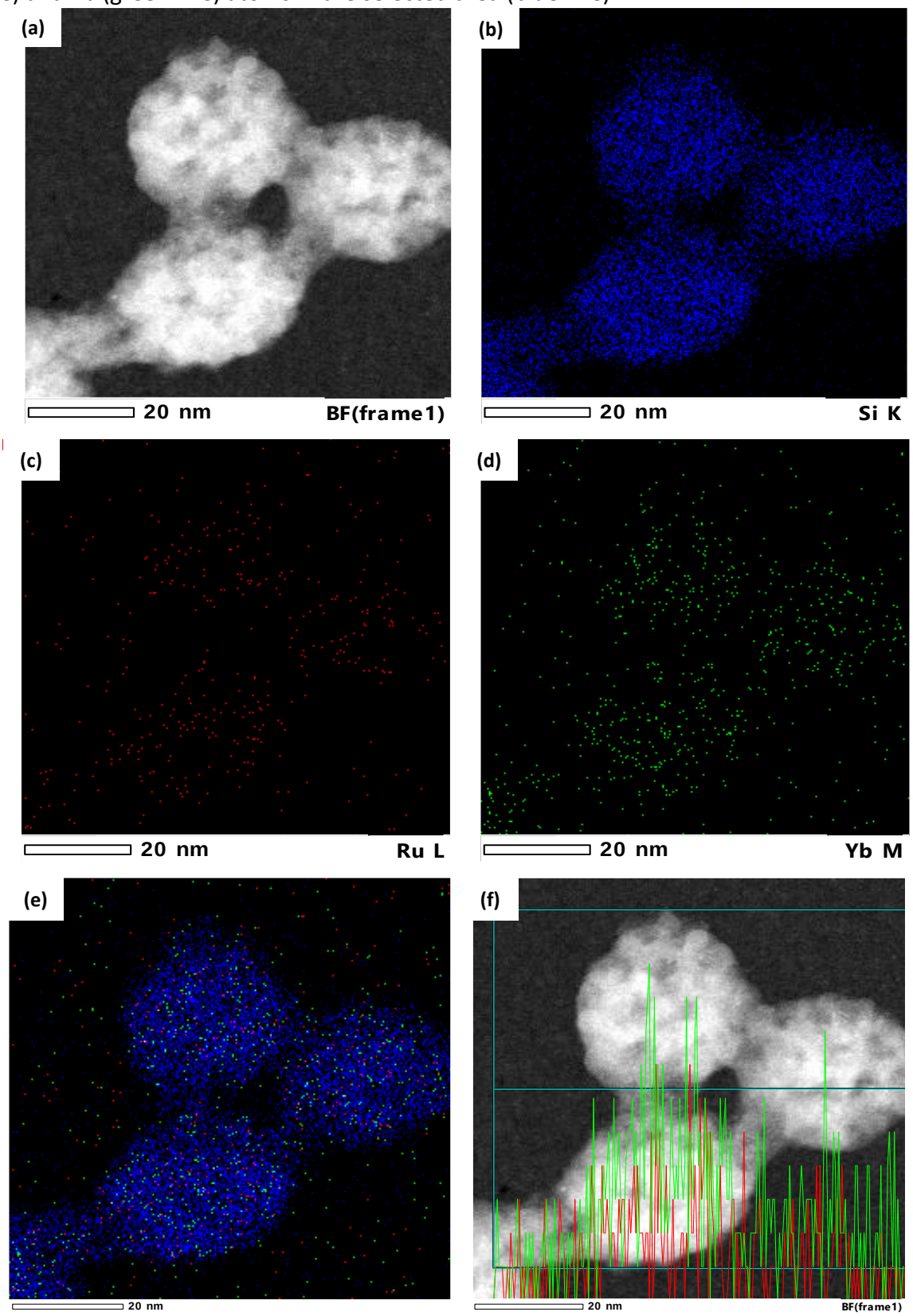

Figure 94. Electron microscope images and elemental cartography of the **SiO_2-NdRuL**: (a) STEM image, (b) Si cartography, (c) Ru cartography, (d) Nd cartography, (e) Si (blue color), Ru (red color) and Nd (green color) cartographies. (f) STEM image with a line profile of Ru (red line) and Nd (green line) atoms in the selected area (blue line).

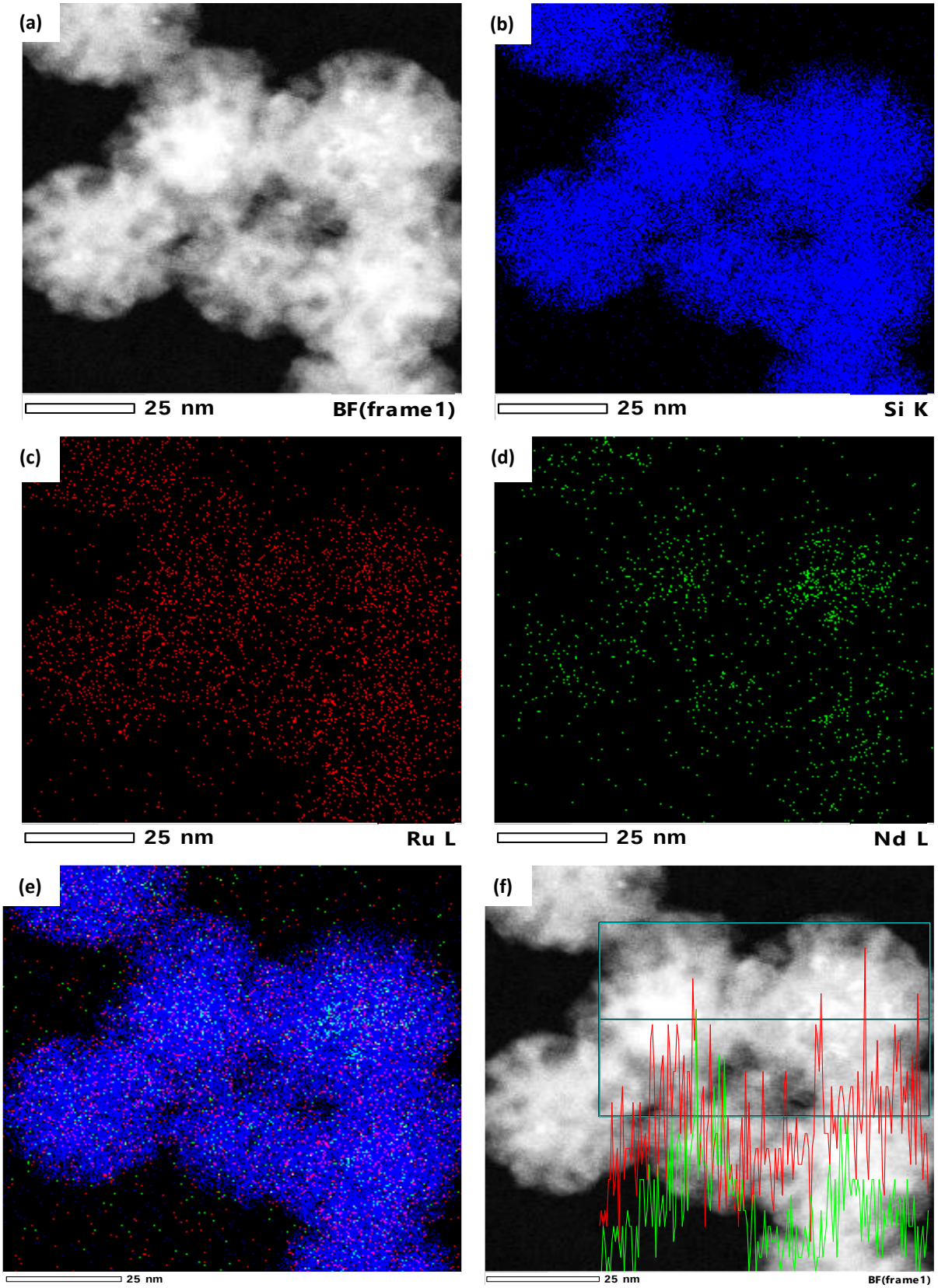

Similarly, concerning **SiO_2-YbRuL** nanohybrid, STEM images (figure 95, a and f) and elemental cartographies of Si (b), Ru (c) and Yb (d) atoms were obtained and evaluated. Figure 95 (a) shows homogeneous distribution with high concentration of metallic atoms onto MSNs. Elemental cartographies of Ru (figure 95 (c)) and Yb (figure 95 (d)) atoms confirm its homogeneously well dispersed inside the nanopores and on the MSNs surface. The elemental cartography obtained by Si, Ru and Yb overlay (figure 95 (e)) corroborate high concentration and homogeneous distribution of Ru and Yb atoms inside the nanopores of MSNs. Figure 95 (f) shows distribution profile of Ru and Yb atoms with similar concentration of them inside the nanopores of the MSNs. These results are in agreement with notable grafting ratios of 0.13 and 0.13 mmol. g^{-1} of silica, for ruthenium and ytterbium complexes, respectively, obtained from EA data.

The nanohybrid obtained by grafting of **Yb—RuL** onto DSNs (**SiO_2 d-YbRuL**) was also characterized by STEM measurements as shown in the figure 96. Figure 96 (a) suggests homogeneous distribution of the metallic atoms onto DSNs and elemental cartography of Si atoms (figure 96 (b)) confirm that morphology and structure of DSNs were keept intact. Elemental cartographies of Ru and Yb atoms (figure 96, c and d, respectively) display both elements well dispersed onto DSNs. Figure 96 (e) shows elemental cartographies of Si, Ru and Yb atoms superposed, suggesting low concentration and homogeneous distribution of Ru and Yb onto DSNs surface. These results are consistent with distribution profile (figure 96 (f)) that shows low and similar concentration of both mettalic atoms. It is worth emphasizing that low grafting rations were obtained due to low ratios of **Yb—RuL** complex (0.06 mmol. g^{-1} of silica) added to the DSNs. So STEM results corroborate grafting ratios of 0.05 and 0.04 mmol. g^{-1} of silica for ruthenium and ytterbium complexes, respectively, obtained by EA.

Figure 95. Electron microscope images and elemental cartography of the **SiO_2-YbRuL**: (a) STEM image, (b) Si cartography, (c) Ru cartography, (d) Yb cartography, (e) Si (blue color), Ru (red color) and Yb (green color) cartographies. (f) STEM image with a line profile of Ru (red line) and Yb (green line) atoms in the selected area (blue line).

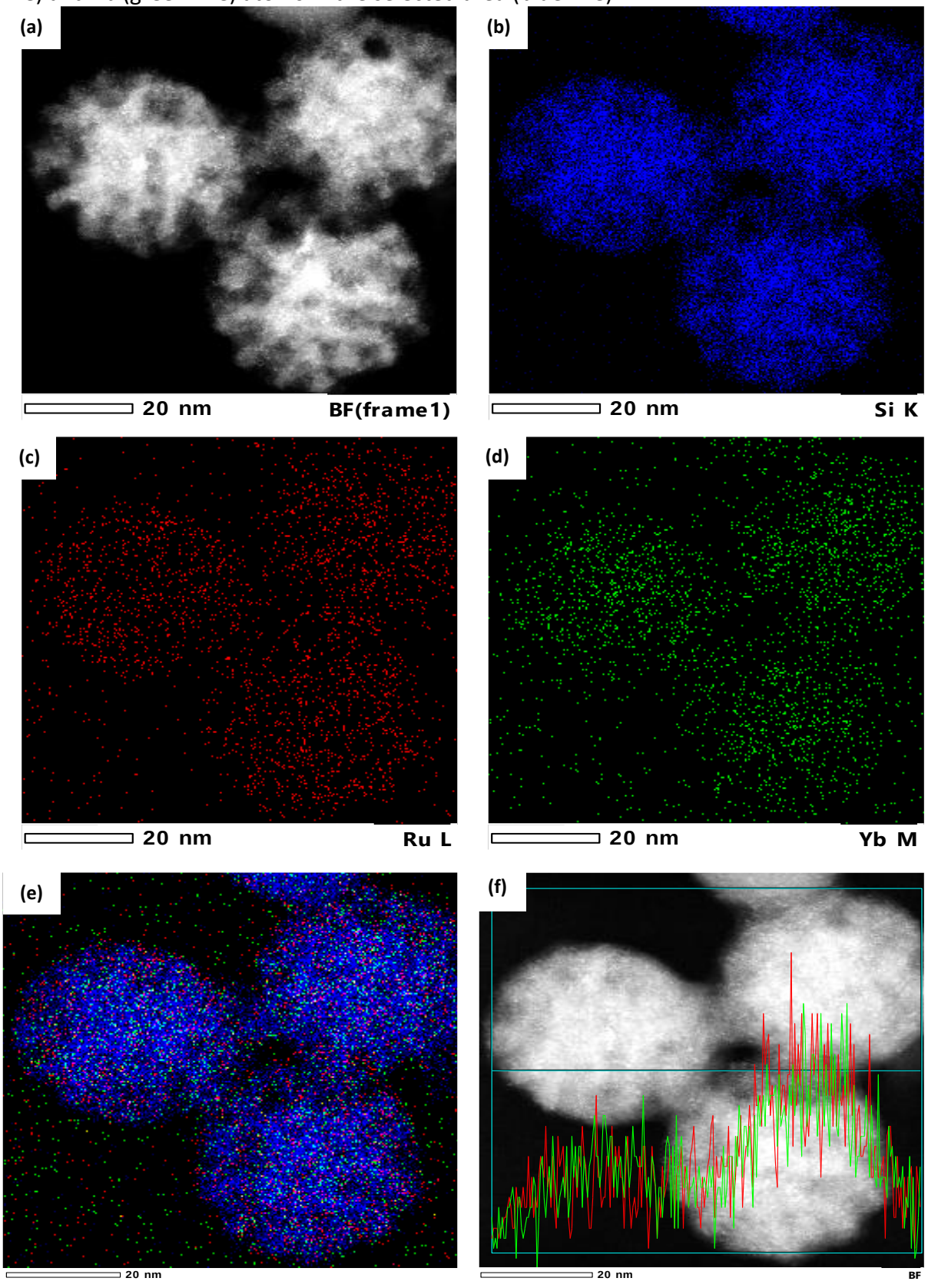

Figure 96. Electron microscope images and elemental cartography of the **SiO_2 d-YbRuL**: (a) STEM image, (b) Si cartography, (c) Ru cartography, (d) Yb cartography, (e) Si (blue color), Ru (red color) and Yb (green color) cartographies. (f) STEM image with a line profile of Ru (red line) and Yb (green line) atoms in the selected area (blue line).

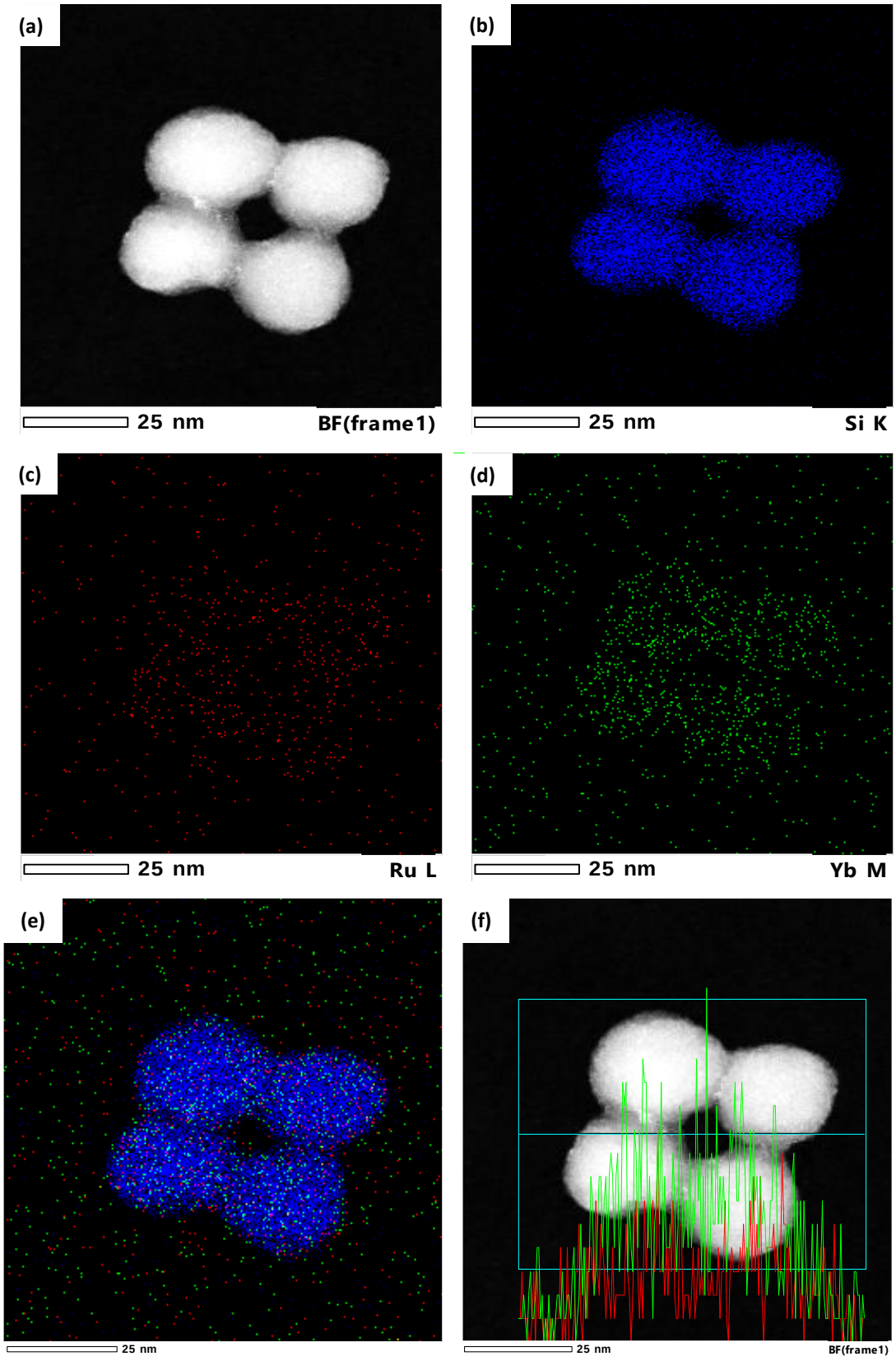

As already discussed, grafting efficiencies lower than 1.0 mmol of complex. g^{-1} of silica confirm that polymerization reactions are avoided, leading to the formation of a monolayer of binuclear complexes onto silica matrix. In this case, grafting efficiency was higher for MSNs than DSNs that can be justified by specific surface area of 765 $m^2.g^{-1}$ for MSNs whereas for DSNs present 138 $m^2.g^{-1}$ of silica.[77]

The grafting efficiencies of the heterobimetallic silylated complexes were calculated according to the N and S contents as previously described (section 3.2.1). Table 10 displays grafting efficiency, R, in mmol of ruthenium and lanthanide complexes.g^{-1} of silica and amount of binuclear complexes.nm^{-2} of silica for the nanohybrids.

Table 10. Grafting efficiencies, in mmol of ruthenium and lanthanide complexes.g^{-1} of silica, and amount of heterobimetallic complexes.nm^{-2} of silica for the nanohybrids.

Samples	R (mmol.g^{-1} of SiO_2)		Number of complex per nm^2	
	R_{Ru}	R_{Ln}	Ru	Ln
SiO_2-RuYbL3	0.06	0.03	0.05	0.03
SiO_2-NdRuL	0.17	0.05	0.15	0.04
SiO_2-YbRuL	0.13	0.13	0.12	0.12
SiO_2 d-YbRuL	0.05	0.04	0.22	0.17

According to table 10, the number of complexes per nm^2 grafted onto MSNs (0.03-0.12) were lower than values obtained from DSNs (0.17-0.22). This difference can be attributed to the silanol groups are more available in DSNs than MSNs. The MSNs were submitted to heat treatment whereas DSNs are used directly for grafting reactions without any treatment.

Specifically, **SiO_2-RuYbL3** nanohybrid presents low grafting ratios and, consequently, low number of complex per nm^2. This can be attributed to the low amount of complexes added for grafting reactions. For **SiO_2-NdRuL** nanohybrid, distinct grafting ratios obtained were ascribed to the loss of neodymium complexes during or after grafting reactions. These results were confirmed by EA and STEM data already discussed. The **SiO_2-YbRuL** and **SiO_2 d-YbRuL** nanohybrids were obtained from grafting of **Yb—RuL** complexes onto MSNs and DSNs,

respectively. High and coherent values of grafting efficiencies (according to the amount of complexes added for grafting) were obtained and confirm remarkable results obtained by STEM and EA measurements.

Although low grafting efficiencies and number of complexes per nm^2 of silica obtained, successful synthesis of different heterobimetallic silylated complexes and, consequently, new four nanohybrids from MSNs and DSNs were prepared e characterized. The luminescent properties of these nanohybrids will be evaluated and relating to their *d-f* heterobimetallic complexes.

5.4.3. Luminescent properties of silica-based nanohybrids obtained by grafting of *d-f* heterobimetallic silylated complexes onto MSNs and Ludox silica AS-40 (DSNs)

By monitoring the luminescence properties of ruthenium in the nanohybrids, figures 97, 98, 99 and 100 ((a) and (b)); the emission levels were determined. In this way, a broad emission band was observed and it can be ascribed to the Ru(II) ^{3}MLCT emission to the ground state.[45] Moreover, the bands were centered at different energies; 664 (~ 15060 cm^{-1}), 614 (~ 16287 cm^{-1}) and 610 nm (~16393 cm^{-1}) for **SiO_2-RuYbL3**, **SiO_2-NdRuL** (**SiO_2 d-YbRuL**) and **SiO_2-YbRuL**, respectively. These differences of energy for ^{3}MLCT are in agreement with the *d-f* heterobimetallic complexes as previously described. The excitation spectra for all nanohybrids by monitoring the Ru(II) ^{3}MLCT emission to the ground state transition shows bands assigned to the d→π* ^{1}MLCT (metal-to-ligand charge transfer) transitions and transitions centered on ligands, as π→π* transitions[45], in agreement with the respective *d-f* heterobimetallic complexes.

By monitoring the NIR emission (λ_{em}: 979 nm to **SiO_2-RuYbL3**, λ_{em}: 1063 nm to **SiO_2-NdRuL**, λ_{em}: 980 nm to **SiO_2-YbRuL** and λ_{em}: 979 nm to **SiO_2 d-YbRuL**), the excitation spectra have shown distinct profile. For the **SiO_2-RuYbL3** (figure 97 (c)) the spectral profile was similar to the **Ru—YbL3** complex with a broad band up to 400 nm assigned to transitions centered at **TTA-Si**, **bpy** and **bpmd** ligands[48, 49, 71, 72] and from 400 to 650 nm the broad band was ascribed to Ru(II) ^{3}MLCT transition.[45] The emission spectra (figure 97 (d)) shows a broad and low intensity band at 979 nm assigned to Yb(III) $^2F_{5/2} \rightarrow {}^2F_{7/2}$ transition. In this case, the low emission intensity can be attributed to the low grafting ratios on the MSN matrix, which is in agreement with EA and STEM data.

Figure 97. Room temperature excitation ((a), $\lambda_{emission}$: 664 nm and (c), $\lambda_{emission}$: 979 nm) and emission ((b), $\lambda_{excitation}$: 455 nm; and (d), $\lambda_{excitation}$: 395 and 455 nm) spectra of the **SiO_2-RuYbL3** nanohybrid in solid state.

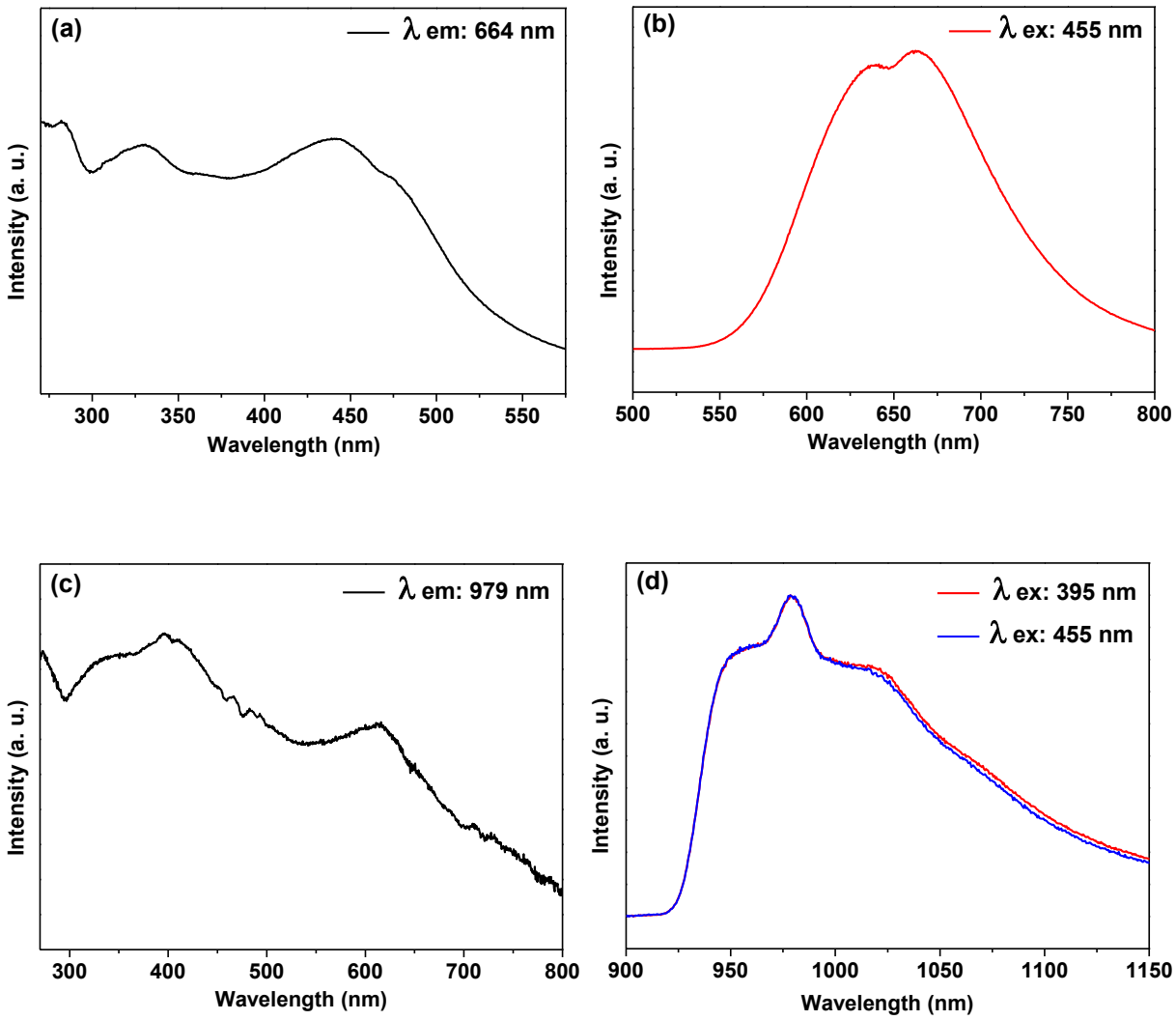

For the **SiO_2-NdRuL** (figure 98 (c)), similar to the **Nd—RuL** complex, the excitation spectrum shows a broad intense band centered at 337 nm ascribed to the ligands (**TTA**, **bpy-Si** and **bpmd** ligands).[48, 49, 71, 72] The broad and low intensity band from 400 to 600 nm was attributed to Ru(II) ^{3}MLCT transition.[45] However, the bands assigned to the Nd(III) intraconfigurational f-f transitions were not observed due to the dilution effect of the d-f binuclear complex in the MSN matrix.[28, 49] The emission spectra (figure 92 (d)) displays a sharp band at 1063 nm ascribed to $^4F_{3/2} \rightarrow {}^4I_{11/2}$ transition and a low intensity band centered at 1334 nm, attributed to the $^4F_{3/2} \rightarrow {}^4I_{13/2}$ transition as already discussed.[28, 45, 49] However, by

monitoring the excitation on the Ru(II) donor (above 400 nm), a low emission intensity of the main transition ($^4F_{3/2} \rightarrow {}^4I_{11/2}$) can be observed. This can be explained by low content of Nd(III) units in the *d-f* binuclear complex that was lost during or after grafting ratios processes, according to EA and STEM data. Despites the great emission intensity obtained by monitoring the excitation at 337 nm, the emission spectra by monitoring on the Ru(II) donor confirm the loss of Nd(III) units in the **SiO_2-NdRuL** nanohybrids.

Figure 98. Room temperature excitation ((a), $\lambda_{emission}$: 614 nm and (c), $\lambda_{emission}$: 1063 nm) and emission ((b), $\lambda_{excitation}$: 455 nm; and (d), $\lambda_{excitation}$: 337 and 455 nm) spectra of the **SiO_2-NdRuL** nanohybrid in solid state.

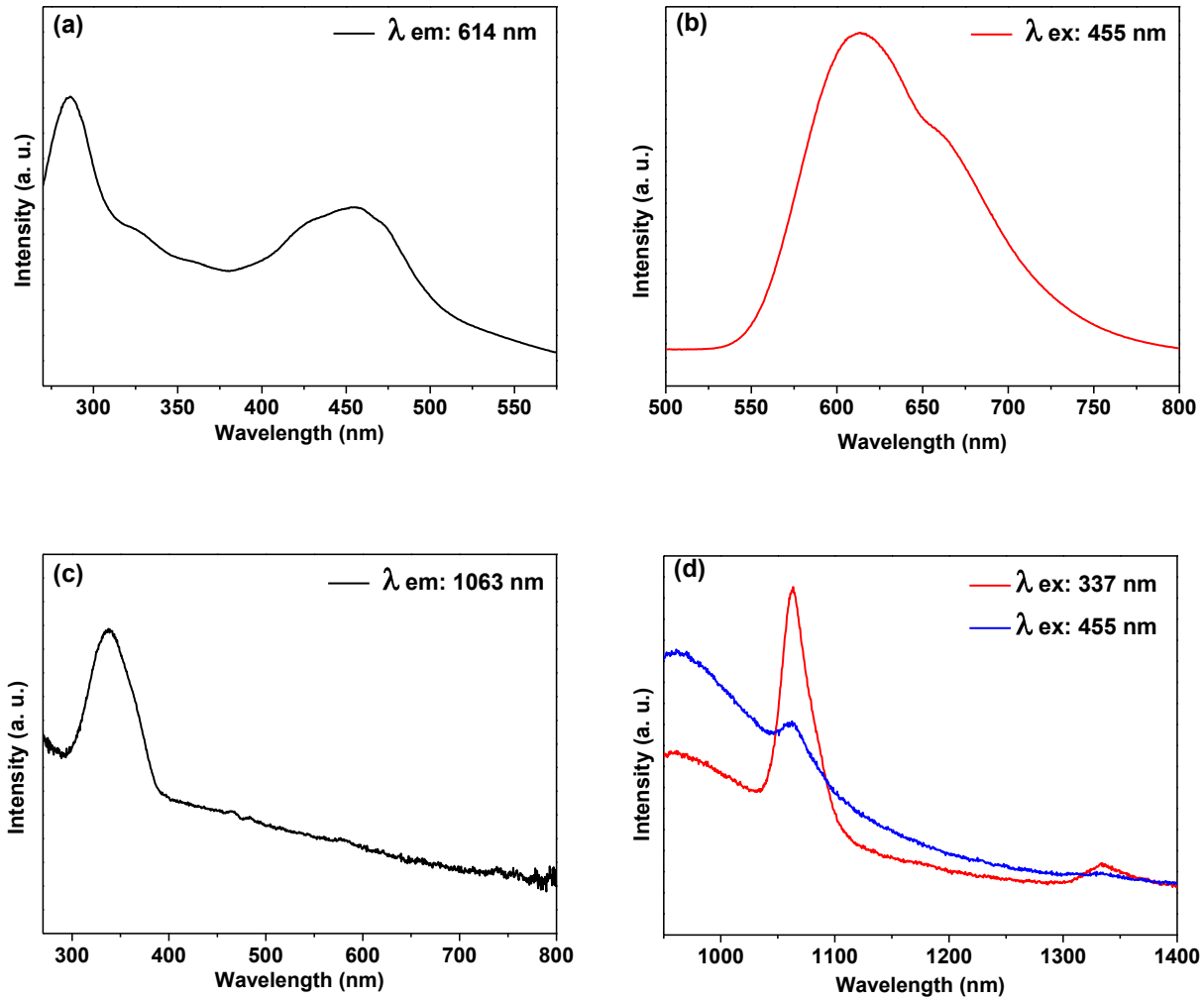

Sequentially, for the **SiO_2-YbRuL** nanohybrids, the excitation spectra (figure 99 (c)) displays a broad excitation band from 270 to 400 nm assigned to ligands transitions (**TTA**, **bpy-Si** and **bpmd**).[48, 49, 71, 72] Although bands above 400 nm in the excitation spectrum of the **Yb—**

RuL3 complex was not detected, in the **SiO_2-YbRuL** nanohybrids a low intensity band ascribed to Ru(II) ^{3}MLCT transitions was detected.[45]

The emission spectra (figure 99 (d)) display similar profiles relating to the free **Yb—RuL** complex. By monitoring the excitation up to 400 nm, the broad emission bands observed at 980 nm were ascribed to Yb(III) $^2F_{5/2} \rightarrow {}^2F_{7/2}$ transitions.[45, 46, 92] When the excitation was monitoring on the Ru(II) ^{1}MLCT transition (above 400 nm), the IR emission spectra was observed as well.[45, 46, 92]

Figure 99. Room temperature excitation ((a), $\lambda_{emission}$: 610 nm and (c), $\lambda_{emission}$: 980 nm) and emission ((b), $\lambda_{excitation}$: 455 nm; and (d), $\lambda_{excitation}$: 377 and 455 nm) spectra of the **SiO_2-YbRuL** nanohybrid in solid state.

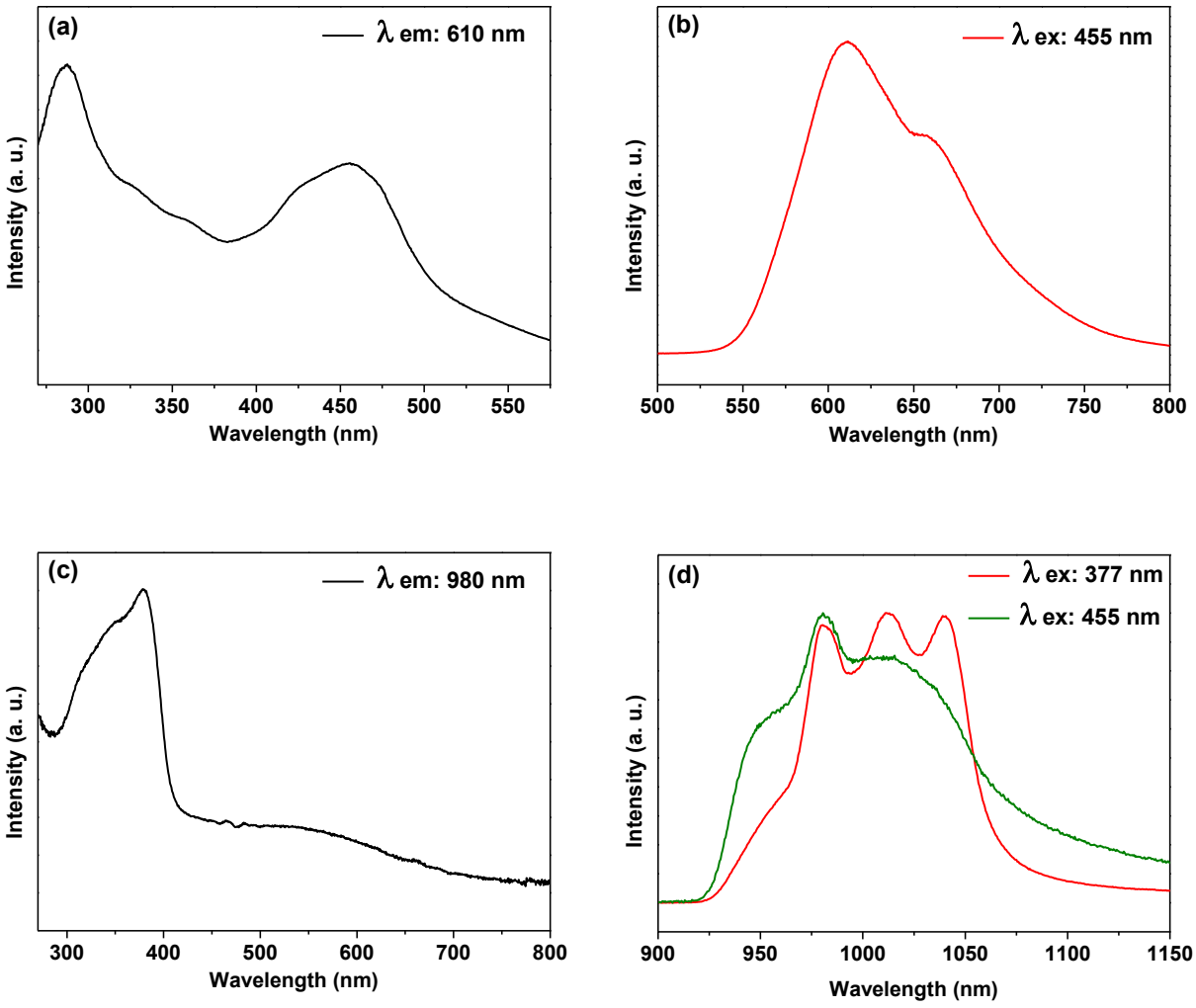

The excitation spectrum (figure 100 (c)) displays a broad band at 345 nm resulting from ligands transitions (**TTA**, **bpy-Si** and **bpmd**)[48, 49, 71, 72] and a low intensity band above 400 nm assigned to the Ru(II) ^{3}MLCT transitions.[45]

Figure 100. Room temperature excitation ((a), $\lambda_{emission}$: 614 nm and (c), $\lambda_{emission}$: 979 nm) and emission ((b), $\lambda_{excitation}$: 455 nm; and (d), $\lambda_{excitation}$: 370 and 455 nm) spectra of the **SiO_2 d-YbRuL** nanohybrid in solid state.

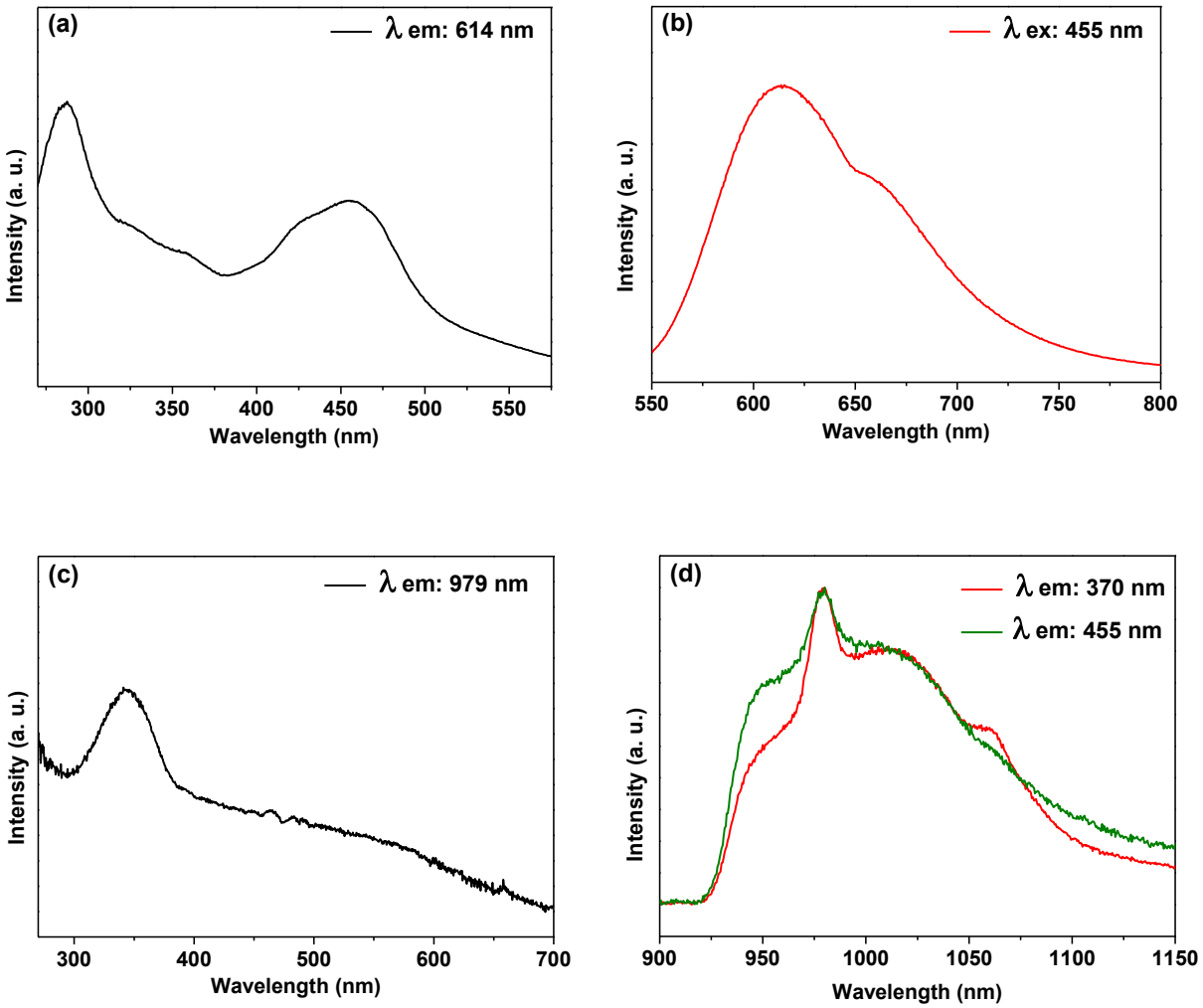

By monitoring the excitation up to 400 nm, the broad emission bands (figure 100 (d)) centered at 979 nm were ascribed to Yb(III) $^2F_{5/2} \rightarrow {}^2F_{7/2}$ transitions.[45, 46, 92] When the excitation was monitored on the Ru(II) ^{1}MLCT transition, the broad band was also observed.[45, 46, 92]

6 – CONCUSION AND PERSPECTIVES

The main goal of this PhD research was to obtain new NIR luminescent systems based on *d-f* energy transfer process for nanoprobes or nanomarkers applications. To achieve this objective new *d-f* heterobimetallic (Ru(II)—Nd/Yb(III)) complexes containing alkoxysilane functional groups were undertaken. The originality of these complexes remains in the presence of silane functional group which allow the chemical modification of any silica matrix.

In this work mesoporous silica nanoparticles were chosen because of their interesting morphologic properties to design the surface chemistry. Grafting of these complexes leaded us to obtain luminescent nanohybrids excitable in the visible light and emitting in the near-IR region. The interest of the NIR emission is that these radiations penetrate human tissue more effectively than UV light. Such nanohybrids have interesting properties sought in many applications of analysis of biological systems.

Preliminary work has consisted in the synthesis of monomers of ruthenium(II), neodymium(III) and ytterbium(III) whether or not the silane group was necessary since two approaches were investigated to obtain clickable dyads: presence of the alkoxisilane group on the ruthenium moiety or on the lanthanide side.

In order to compare the luminescence properties of all the hybrids based on both monomers and heterobimetallic complexes three grafting strategies were implemented. The grafting of the monomers, the grafting of the *d-f* dyads and the grafting of couple of monomers. This later route allows us to highlight the need, or not, to synthesize such *d-f* complex to achieve our objective. Finally, two silica supports with different morphologies were evaluated.

From two ligands bearing trialkoxysilane function; 4-methyl-4'- (n-triethoxysilylpropyl) amine-methyl-2,2'-bipyridine (bpy-Si) and 4,4,4-Trifluoro-2- (3- (trimethoxysilyl) -propyl) - 1- (2-thienyl) -1,3-butanedione (TTA-Si), four new *d-f* heterobimetallic complexes Ru(II)/Ln(III), Ln = Nd^{3+}, Yb^{3+} were isolated and characterized. These complexes have the chemical property to be able to be covalently grafted to any silica-based material, they are excitable by the visible and emit in the IR range. In the resulting series, the **Yb-RuL** complex is one that highlights the most important *d-f* energy transfer with a remarkable energy transfer quantum yield of 73.4%. The objective to isolate *d-f* luminescent complexes with silane function has been reached. With the aim to concentrate the phosphor within a single nanoparticle to obtain more

sensitive sensors and more easily functionalizable/biofunctionnalizable, the preparation of silica based nanohybrids was undertaken. In this way, monodisperse mesoporous silica nanoparticles (47 nm ± 4 nm), which features and appearance of V_{poreux} = 1.55 $cm^3.g^{-1}$; $\varnothing_{pores}$ = 9 nm and specific surface, S_{BET} = 675 $m^2.g^{-1}$, were synthesized using a direct microemulsion system in the presence of structuring agent. A second silica matrix was evaluated, denoted **SiO_2 d**, that is a commercial Ludox type silica, as dense monodisperse nanospheres (24 ± 2 nm) and characterized by a low specific surface area of 138 $m^2.g^{-1}$.

So three types of silica based nanohybrids were undertaken, in all cases the phosphors, monomer or heterobimetallic silylated complexes are covalently bonded to the silica matrix to prevent the release of the phosphor in the further applications. By grafting of the newly-silylated monomers, **RuL1**, **NdL3** and **YbL3**, three hybrids have been isolated: **SiO_2-Ru** and **SiO_2-Nd**, **SiO_2-Yb**. A second type of hybrid was obtained by simultaneous grafting of silylated monomers of ruthenium and lanthanides: **SiO_2-RuNd** and **SiO_2-RuYb**. Finally the grafting of the three new *d-f* heterobimetallic complexes Ru(II)/Ln(III) gave rise to **SiO_2-RuYbL3**; **SiO_2-NdRuL**; **SiO_2-YbRuL** **SiO_2d-YbRuL** nanohybrids. Thus nine new luminescent nanohybrids, whose size varies depending on the silica matrix used (25 or 50 nm) were fully characterized. They highlight grafting efficiencies in the range 0.05 and 0.18 mmol of complex per gram of support. Such grafting efficiencies allow us to consider further chemical functionalization of these nanoobjects.

The study of photophysical properties were then performed by recording of the excitation and emission spectra in the solid state for each sample, free complexes and nanohybrids at room temperature. The excitation spectra obtained in the case of the monomers highlight the characteristic transitions assigned to the various organic ligands (bpy, bpy-Si, bpmd, TTA-Si) while the emission spectra exhibit a luminescence in the visible for the ruthenium complex and in the IR range for the neodymium and ytterbium monomers. The analysis of the corresponding functionalized nanoparticles shows very similar spectra to those of the free complex confirming the presence of the different complexes at the silica surface.

The grafting of couple of monomers Ru/Nd, or Ru/Yb giving **SiO_2-RuNd** and **SiO_2-RuYb** respectively shows surprisingly that an energy transfer is possible between the two *d-f* metal centers when they are intimately confined in mesoporous silica. Significant quantum yield for energy transfer (Φ_{ET}) were determined (27 and 40% for **SiO_2-RuYb** and **SiO_2-RuNd**). This result requires to be further exploited to really understand the involved mechanism. Nevertheless

higher quantum yield for energy transfer could be reached by involving heterobimetallic complexes. Since it is clear from the study of the photophysical properties of the heterobimetallic based nanohybrids that it is possible, by our approach, to get excitable probes emitting in the visible and in the IR with consistent quantum yields for energy transfer (Φ_{ET}). The significant Φ_{ET} values obtained, between 30 and 84%, have to be remark towards the described literature. This work has also shown that the choice of the silica matrix remains an important parameter to consider, mesoporous silica appearing as a better choice to maintain the photophysical properties, the explanation being a better protection of the phosphor by the porous matrix and the higher values of grafting efficiencies obtained for **SiO_2-YbRuL** than **SiO_2 d -YbRuL** nanohybrids.

Perspectives

Based on the photoluminescence properties of the monomers and heterobimetallic complexes besides the silica nanohybrids, we can suggest the following steps as future work proposals:

- Evaluate the photophysical properties of the *d-f* heterobimetallic silylated complexes and the respectives nanohybrids using two-photon excitation;
- Choose the best luminescent nanohybrids such as **SiO_2-RuNd**, **SiO_2-RuYb** and **SiO_2-YbRuL** and then evaluate their viability in cellular media (cytotoxicity assays);
- Evaluate their potential as nanoprobes or nanomarkers in a biological systems using confocal microscopy with single or two-photons excitation to achieve the 3D location.

REFERENCES

1 SOUSA FILHO, P. C. de; SERRA, O. A. Rare earths in Brazil: historical aspects, prodution, and perspectives. **Quim. Nova**, v. 37, n. 4, p. 377-383, 2014.

2 BUNZLI, J.-C. G.; PIGUET, C. Taking advantage of luminescent lanthanide ions. **Chem. Soc. Rev.**, v. 34, n. 12, p. 1048-1077, 2005.

3 BÜNZLI, J.-C. G. On the design of highly luminescent lanthanide complexes. **Coord. Chem. Rev.**, v. 293/294, p. 19-47, 2015.

4 CARLOS, L. D.; FERREIRA, R. A. S.; BERMUDEZ, V. de Z.; RIBEIRO, S. J. L. Lanthanide-containing light-emitting organic-inorganic hybrids: a bet on the future. **Adv. Mater.**, v. 21, n. 5, p. 509-534, 2009.

5 BETTENCOURT-DIAS, A.; BARBER, P. S.; VISWANATHAN, S. Aromatic N-donor ligands as chelators and sensitizers of lanthanide ion emission. **Coord. Chem. Rev.**, v. 273/274, p. 165-200, 2014.

6 ELISEEVA, S. V.; BÜNZLI, J.-C. G. Lanthanide luminescence for functional materials and bio-sciences. **Chem. Soc. Rev.**, v. 39, n. 1, p. 189-227, 2010.

7 BÜNZLI, J.-C. G.; ELISEEVA, S. V. Lanthanide NIR luminescence for telecommunications, bioanalyses and solar energy conversion. **J. Rare Earths**, v. 28, n. 6, p. 824-842, 2010.

8 ZHU, Z.; SONG, B.; YUAN, J.; YANG, C. Enabling the triplet of tetraphenylethene to sensitize the excited state of europium(III) for protein detection and time-resolved luminescence imaging. **Adv. Sci.**, 2016. doi: 10.1002/advs.201600146.

9 ZHOU, L.; JIANG, Y.; CUI, R.; LI, Y.; ZHAO, X.; DENG, R.; ZHANG, H. Efficient red organic electroluminescent devices based on trivalent europium complex obtained by designing the device structure with stepwise energy levels. **J. Lumin.**, v. 170, p. 692-696, 2016.

10 XIMENDES, E. C.; SANTOS, W. Q.; ROCHA, U.; KAGOLA, U. K.; SANZ-RODRÍGUEZ, F.; FERNÁNDEZ, N.; GOUVEIA NETO, A. D. S.; BRAVO, D.; DOMINGO, A. M.; ROSAL, B. del; BRITES, C. D. S.; CARLOS, L. D.; JAQUE, D.; JACINTO, C. Unveiling in vivo subcutaneous thermal dynamics by infrared luminescent nanothermometers. **Nano Lett.**, v. 16, n. 3, p. 1695-1703, 2016.

11 LI, G. S.; ZHANG, C. M.; ZHU, P. F.; JIANG, C.; SONG, P.; ZHU, K. Broadband near-infrared emission in Pr^{3+}-Er^{3+} codoped phosphate glasses for optical amplifiers. **Ceram. Int.**, v. 42, n. 4, p. 5558-5561, 2016.

12 MANZANI, D.; FERRARI, J. L.; POLACHINI, F. C.; MESSADDEQ, Y.; RIBEIRO, S. J. L. 1.5 μm and visible up-conversion emissions in Er^{3+}/Yb^{3+} co-doped tellurite glasses and optical fibers for photonic applications. **J. Mater. Chem.**, v. 22, n. 32, p. 16540-16545, 2012.

13 CHEN, F.-F.; CHEN, Z.-Q.; BIAN, Z.-Q.; HUANG, C.-H. Sensitized luminescence from

lanthanides in d–f bimetallic complexes. **Coord. Chem. Rev.**, v. 254, n. 9/10, p. 991-1010, 2010.

14 BÜNZLI, J.-C. G. Lanthanide light for biology and medical diagnosis. **J. Lumin.**, v. 170, p. 866-878, 2016.

15 MALTA, O. L.; BRITO, H. F.; MENEZES, J. F. S.; SILVA, F. R. G. E.; ALVES, S.; FARIAS, F. S.; ANDRADE, A. V. M. de. Spectroscopic properties of a new light-converting device Eu(thenoyltrifluoroacetonate)$_3$ $_2$(dibenzyl sulfoxide). A theoretical analysis based on structural data obtained from a sparkle model. **J. Lumin.**, v. 75, n. 3, p. 255-268, 1997.

16 BINNEMANS, K. Lanthanide-based luminescent hybrid materials. **Chem. Rev.**, v. 109, n. 9, p. 4283-4374, 2009.

17 ISHIDA, H.; TOBITA, S.; HASEGAWA, Y.; KATOH, R.; NOZAKI, K. Recent advances in instrumentation for absolute emission quantum yield measurements. **Coord. Chem. Rev.**, v. 254, n. 21/22, p. 2449-2458, 2010.

18 SHAVALEEV, N. M.; POPE, S. J. A.; BELL, Z. R.; FAULKNER, S.; WARD, M. D. Visible-light sensitisation of near-infrared luminescence from Yb(III), Nd(III) and Er(III) complexes of 3,6-bis(2-pyridyl)tetrazine. **Dalton Trans.**, n. 5, p. 808-814, 2003.

19 BOTELHO, M. B. S.; GÁLVEZ-LÓPEZ, M. D.; DE COLA, L.; ALBUQUERQUE, R. Q.; CAMARGO, A. S. S. de. Towards the design of highly luminescent europium(III) complexes. **Eur. J. Inorg. Chem.**, v. 2013, n. 29, p. 5064-5070, 2013.

20 XIAO, Y.; ZHANG, R.; YE, Z.; DAI, Z.; AN, H.; YUAN, J. Lanthanide complex-based luminescent probes for highly sensitive time-gated luminescence detection of hypochlorous acid. **Anal. Chem.**, v. 84, n. 24, p. 10785-10792, 2012.

21 WANG, X.; CHANG, H.; XIE, J.; ZHAO, B.; LIU, B.; XU, S.; PEI, W.; REN, N.; HUANG, L.; HUANG, W. Recent developments in lanthanide-based luminescent probes. **Coord. Chem. Rev.**, v. 273/274, p. 201-212, 2014.

22 ANDREIADIS, E. S.; GAUTHIER, N.; IMBERT, D.; DEMADRILLE, R.; PEAUT, J.; MAZZANTI, M. Lanthanide complexes based on β-diketonates and a tetradentate chromophore highly luminescent as powders and in polymers. **Inorg. Chem.**, v. 52, p. 14382-14390, 2013.

23 LIMA, N. B. D.; SILVA, A. I. S.; GERSON, P. C.; GONÇALVES, S. M. C.; SIMAS, A. M. Faster synthesis of beta-diketonate ternary europium complexes: elapsed times & reaction yields. **PLoS One**, v. 10, n. 12, 2015. doi: 10.1371/journal.pone 0143998.

24 SÁ, G. F. de; MALTA, O. L.; DONEGÁ, C. de M.; SIMAS, A. M.; LONGO, R. L.; SANTA-CRUZ, P. A.; SILVA JUNIOR, E. F. da. Spectroscopic properties and design of highly luminescent lanthanide coordination complexes. **Coord. Chem. Rev.**, v. 196, n. 1, p. 165-195, 2000.

25 WARD, M. D. Transition-metal sensitised near-infrared luminescence from lanthanides in d–f heteronuclear arrays. **Coord. Chem. Rev.**, v. 251, n. 13/14, p. 1663-1677, 2007.

26 AHMED, Z.; IFTIKHAR, K. Sensitization of visible and NIR emitting lanthanide(III) ions in

noncentrosymmetric complexes of hexafluoroacetylacetone and unsubstituted monodentate pyrazole. **J. Phys. Chem. A**, v. 117, n. 44, p. 11183-11201, 2013.

27 WOODWARD, A. W.; FRAZER, A.; MORALES, A. R.; YU, J.; MOORE, A. F.; CAMPIGLIA, A. D.; JUCOV, E. V.; TIMOFEEVA, T. V.; BELFIELD, K. D. Two-photon sensitized visible and near-IR luminescence of lanthanide complexes using a fluorene-based donor-π-acceptor diketonate. **Dalton Trans.**, v. 43, n. 44, p. 16626-16639, 2014.

28 LAZARIDES, T.; SYKES, D.; FAULKNER, S.; BARBIERI, A.; WARD, M. D. On the mechanism of d-f energy transfer in RuII/LnIII and OsII/LnIII Dyads: Dexter-type energy transfer over a distance of 20 Å. **Chem. - Eur. J.**, v. 14, n. 30, p. 9389-9399, 2008.

29 LAZARIDES, T.; TART, N. M.; SYKES, D.; FAULKNER, S.; BARBIERI, A.; WARD, M. D. $[Ru(bipy)_3]^{2+}$ and $[Os(bipy)_3]^{2+}$ chromophores as sensitisers for near-infrared luminescence from Yb(III) and Nd(III) in d/f dyads: contributions from Förster, Dexter, and redox-based energy-transfer mechanisms. **Dalton Trans.**, n. 20, p. 3971-3979, 2009.

30 SHAVALEEV, N. M.; MOORCRAFT, L. P.; POPE, S. J. A.; BELL, Z. R.; FAULKNER, S.; WARD, M. D. Sensitized near-infrared emission from complexes of YbIII, NdIII and ErIII by energy-transfer from covalently attached PtII-based antenna units. **Chem. - Eur. J.**, v. 9, n. 21, p. 5283-5291, 2003.

31 SHI, G.-X.; FENG, W.-X.; ZOU, D.; LÜ, X.-Q.; ZHANG, Z.; ZHANG, Y.; FAN, D.-D.; ZHAO, S.-S.; WONG, W.-K.; JONES, R. A. Hetero-binuclear near-infrared (NIR) luminescent ZnLn (Ln = Nd, Yb or Er) complexes self-assembled from the benzimidazole-based ligand. **Inorg. Chem. Commun.**, v. 22, n. 3, p. 126-130, 2012.

32 ZOU, D.; FENG, W.; SHI, G.; LÜ, X.; ZHANG, Z.; ZHANG, Y.; LIU, H.; FAN, D.; WONG, W.-K.; JONES, R. A. Hetero-binuclear near-infrared (NIR) luminescent Zn–Nd complexes self-assembled from the benzimidazole-based ligands. **Spectrochim. Acta Part A**, v. 98, p. 359-366, 2012.

33 LI, L.; ZHANG, S.; XU, L.; CHEN, Z.-N.; LUO, J. Highly sensitized near-infrared luminescence in Ir–Ln heteronuclear coordination polymers via light-harvesting antenna of Ir(III) unit. **J. Mater. Chem. C**, v. 2, n. 9, p. 1698-1703, 2014.

34 CHEN, F.-F.; WEI, H.; BIAN, Z.; LIU, Z.; MA, E.; CHEN, Z.; HUANG, C. Sensitized near-infrared emission from Ir III-Ln III (Ln = Nd, Yb, Er) bimetallic complexes with a (NΛO)(NΛO) bridging ligand. **Organometallics**, v. 33, n. 13, p. 3275-3282, 2014.

35 JANA, A.; BAGGALEY, E.; AMOROSO, A.; WARD, M. D. A new ligand skeleton for imaging applications with d–f complexes: combined lifetime imaging and high relaxivity in an Ir/Gd dyad. **Chem. Commun.**, v. 51, n. 42, p. 8833-8836, 2015.

36 BAGGALEY, E.; CAO, D.-K.; SYKES, D.; BOTCHWAY, S. W.; WEINSTEIN, J. A.; WARD, M. D. Combined two-photon excitation and d→f energy transfer in a water-soluble Ir III /Eu III dyad: two luminescence components from one molecule for cellular imaging. **Chem. - Eur. J.**, v. 20, n. 29, p. 8898-8903, 2014.

37 SYKES, D.; CANKUT, A. J.; ALI, N. M.; STEPHENSON, A.; SPALL, S. J. P.; PARKER, S. C.; WEINSTEIN, J. A.; WARD, M. D. Sensitisation of Eu(III)- and Tb(III)-based luminescence by Ir(III) units in Ir/lanthanide dyads: evidence for parallel energy-transfer and electron-transfer based mechanisms. **Dalton Trans.**, v. 43, n. 17, p. 6414-6428, 2014.

38 JANA, A.; CROWSTON, B. J.; SHEWRING, J. R.; McKENZIE, L. K.; BRYANT, H. E.; BOTCHWAY, S. W.; WARD, A. D.; AMOROSO, A. J.; BAGGALEY, E.; WARD, M. D. Heteronuclear Ir(III)–Ln(III) luminescent complexes: small-molecule probes for dual modal imaging and oxygen sensing. **Inorg. Chem.**, v. 55, n. 11, p. 5623-5633, 2016.

39 CAMPAGNA, S.; PUNTORIERO, F.; NASTASI, F.; BERGAMINI, G.; BALZANI, V. Photochemistry and phophysics of coordinations compounds: ruthenium. In: BALZANI, V.; Campagna, S. (Ed.). **Photochemistry and photophysics of coordination compounds I**. Berlin: Springer, 2007. p. 117-214. (Topics in current chemistry, v. 280).

40 CHEN, Y.; GUAN, R.; ZHANG, C.; HUANG, J.; JI, L.; CHAO, H. Two-photon luminescent metal complexes for bioimaging and cancer phototherapy. **Coord. Chem. Rev.**, v. 310, p. 16-40, 2016.

41 XU, W.; ZUO, J.; WANG, L.; JI, L.; CHAO, H. Dinuclear ruthenium(II) polypyridyl complexes as single and two-photon luminescence cellular imaging probes. **Chem. Commun.**, v. 50, n. 17, p. 2123-2025, 2014.

42 BAGGALEY, E.; GILL, M. R.; GREEN, N. H.; TURTON, D.; SAZANOVICH, I. V.; BOTCHWAY, S. W.; SMYTHE, C.; HAYCOCK, J. W.; WEINSTEIN, J. A.; THOMAS, J. A. Dinuclear ruthenium(II) complexes as two-photon, time-resolved emission microscopy probes for cellular DNA. **Angew. Chem. Int. Ed.**, v. 53, n. 13, p. 3367-3371, 2014.

43 GREENOUGH, S. E.; HORBURY, M. D.; SMITH, N. A.; SADLER, P. J.; PATERSON, M. J.; STAVROS, V. G. Excited-state dynamics of a two-photon-activatable ruthenium prodrug. **ChemPhysChem**, v. 17, n. 2, p. 221-224, 2016.

44 WEI, Q.-H.; LEI, Y.-F.; XU, W.-R.; XIE, J.-M.; CHEN, G.-N. Ru(II) sensitized lanthanide luminescence: synthesis, photophysical properties, and near-infrared luminescent determination of alpha-fetal protein (AFP). **Dalton Trans.**, v. 41, n. 36, p. 11219-11225, 2012.

45 ZHANG, L.-Y.; HOU, Y.-J.; PAN, M.; CHEN, L.; ZHU, Y.-X.; YIN, S.-Y.; SHAO, G.; SU, C.-Y. Near-infrared (NIR) emitting Nd/Yb(III) complexes sensitized by MLCT states of Ru(II)/Ir(III) metalloligands in the visible light region. **Dalton Trans.**, v. 44, n. 34, p. 15212-15219, 2015.

46 SINGARAVADIVEL, S.; BABU, E.; VELAYUDHAM, M.; LU, K.-L.; RAJAGOPAL, S. Sensitized near-infrared luminescence of NdIII, YbIII and ErIII complexes by energy transfer from a ruthenium antenna. **J. Organomet. Chem.**, v. 738, n. 6, p. 49-54, 2013.

47 SHAVALEEV, N. M.; ACCORSI, G.; VIRGILI, D.; BELL, Z. R.; LAZARIDES, T.; CALOGERO, G.; ARMAROLI, N.; WARD, M. D. Syntheses and crystal structures of dinuclear complexes containing d-block and f-block luminophores. sensitization of NIR luminescence from Yb(III), Nd(III), and Er(III) centers by energy transfer from Re(I)− and Pt(II)−bipyrimidine metal centers. **Inorg. Chem.**, v. 44, n. 1, p. 61-72, 2005.

48 FRATINI, A.; RICHARDS, G.; LARDER, E.; SWAVEY, S. Neodymium, gadolinium, and terbium complexes containing hexafluoroacetylacetonate and 2,2‘-bipyrimidine: structural and spectroscopic characterization. **Inorg. Chem.**, v. 47, n. 3, p. 1030-1036, 2008.

49 ZUCCHI, G.; MAURY, O.; THUÉRY, P.; EPHRITIKHINE, M. Structural diversity in neodymium bipyrimidine compounds with near infrared luminescence: from mono- and binuclear complexes to metal-organic frameworks. **Inorg. Chem.**, v. 47, n. 22, p. 10398-10406, 2008.

50 ZUCCHI, G.; MAURY, O.; THUÉRY, P.; GUMY, F.; BÜNZLI, J.-C. G.; EPHRITIKHINE, M. 2,2’-Bipyrimidine as efficient sensitizer of the solid-state luminescence of lanthanide and uranyl ions from visible to near-infrared. **Chem. - A Eur. J.**, v. 15, n. 38, p. 9686-9696, 2009.

51 WARD, M. D. Mechanisms of sensitization of lanthanide(III)-based luminescence in transition metal/lanthanide and anthracene/lanthanide dyads. **Coord. Chem. Rev.**, v. 254, n. 21/22, p. 2634-2642, 2010.

52 LAZARIDES, T.; ADAMS, H.; SYKES, D.; FAULKNER, S.; CALOGERO, G.; WARD, M. D. Heteronuclear bipyrimidine-bridged Ru–Ln and Os–Ln dyads: low-energy ^{3}MLCT states as energy-donors to Yb(III) and Nd(III). **Dalton Trans.**, v. 2, n. 5, p. 691-698, 2008.

53 FAULKNER, S.; NATRAJAN, L. S.; PERRY, W. S.; SYKES, D. Sensitised luminescence in lanthanide containing arrays and d-f hybrids. **Dalton Trans.**, n. 20, p. 3890-3899, 2009.

54 ROCHA, L. A.; CAIUT, J. M. A.; MESSADDEQ, Y.; RIBEIRO, S. J. L.; MARTINES, M. A. U.; FREIRIA, J. do C.; DEXPERT-GHYS, J.; VERELST, M. Non-leachable highly luminescent ordered mesoporous SiO_2 spherical particles. **Nanotechnology**, v. 21, n. 15, 2010. doi:10.1088/0957-4484/21/15/155603.

55 ROCHA, L. A.; FREIRIA, J. do C.; CAIUT, J. M. A.; RIBEIRO, S. J. L.; MESSADDEQ, Y.; VERELST, M.; DEXPERT-GHYS, J. Luminescence properties of Eu-complex formations into ordered mesoporous silica particles obtained by the spray pyrolysis process. **Nanotechnology**, v. 26, n. 33, 2015. doi:10.1088/0957-4484/26/33/335604.

56 BOTELHO, M. B. S.; QUEIROZ, T. B. de; ECKERT, H.; CAMARGO, A. S. S. de. Efficient luminescent materials based on the incorporation of a Eu(III)tris-(bipyridine-carboxylate) complex in mesoporous hybrid silicate hosts. **J. Lumin.**, v. 170, p. 619-626, 2016.

57 FADEEL, B.; GARCIA-BENNETT, A. E. Better safe than sorry: understanding the toxicological properties of inorganic nanoparticles manufactured for biomedical applications. **Adv. Drug Deliv. Rev.**, v. 62, n. 3, p. 362-374, 2010.

58 LI, Z.; BARNES, J. C.; BOSOY, A.; STODDART, J. F.; ZINK, J. I. Mesoporous silica nanoparticles in biomedical applications. **Chem. Soc. Rev.**, v. 41, n. 7, p. 2590-2605, 2012.

59 LU, J.; LIONG, M.; LI, Z.; ZINK, J. I.; TAMANOI, F. Biocompatibility, biodistribution, and drug-delivery efficiency of mesoporous silica nanoparticles for cancer therapy in animals. **Small**, v. 6, n. 16, p. 1794-1805, 2010.

60 COTÍ, K. K.; BELOWICH, M. E.; LIONG, M.; AMBROGIO, M. W.; LAU, Y. A.; KHATIB, H. A.; ZINK, J. I.; KHASHAB, N. M.; STODDART, J. F. Mechanised nanoparticles for drug delivery. **Nanoscale**, v. 1, n. 1, p. 16-39, 2009.

61 CROISSANT, J. G.; PICARD, S.; AGGAD, D.; KLAUSEN, M.; JIMENEZ, C. M.; MAYNADIER, M.; MONGIN, O.; CLERMONT, G.; GENIN, E.; CATTOËN, X.; MAN, M. W. C.; RAEHM, L.; GARCIA, M.; GARY-BOBO, M.; BLANCHARD-DESCE, M.; DURAND, J.-O. Fluorescent periodic mesoporous organosilica nanoparticles dual-functionalized via click chemistry for two-photon photodynamic therapy in cells. **J. Mater. Chem. B**, v. 4, n. 33, p. 5567-5574, 2016.

62 NAKAHARA, Y.; TATSUMI, Y.; AKIMOTO, I.; OSAKI, S.; DOI, M.; KIMURA, K. Fluorescent silica nanoparticles modified chemically with terbium complexes as potential bioimaging probes: their fluorescence and colloidal properties in water. **New J. Chem.**, v. 39, n. 2, p. 1452-1458, 2015.

63 ZHANG, H.; LEI, B.; DONG, H.; LIU, Y.; ZHENG, M.; XIAO, Y. Temperature and oxygen sensing properties of Ru(II) covalently-grafted sol–gel derived ormosil hybrid materials. **J. Nanosci. Nanotechnol.**, v. 16, n. 4, p. 4023-4028, 2016.

64 OLIVEIRA, E. de; NERI, C. R.; SERRA, O. A.; PRADO, A. G. S. Antenna effect in highly luminescent Eu^{3+} anchored in hexagonal mesoporous silica. **Chem. Mater.**, v. 19, n. 22, p. 5437-5442, 2007.

65 SUN, L.; ZHANG, H.; PENG, C.; YU, J.; MENG, Q.; FU, L.-S.; LIU, F.-Y.; GUO, X.-M. Covalent linking of near-infrared luminescent ternary lanthanide (Er^{3+}, Nd^{3+}, Yb^{3+}) complexes on functionalized mesoporous MCM-41 and SBA-15. **J. Phys. Chem. B**, v. 110, n. 14, p. 7249-7258, 2006.

66 RAJ, D. B. A.; BIJU, S.; REDDY, M. L. P. Highly luminescent europium(III) complexes containing organosilyl 4,4,5,5,5-pentafluoro-1-(naphthalen-2-yl)pentane-1,3-dionate ligands grafted on silica nanoparticles. **J. Mater. Chem.**, v. 19, n. 42, p. 7976-7983, 2009.

67 DIVYA, V.; BIJU, S.; VARMA, R. L.; REDDY, M. L. P. Highly efficient visible light sensitized red emission from europium tris[1-(4-biphenoyl)-3-(2-fluoroyl)propanedione](1,10-phenanthroline) complex grafted on silica nanoparticles. **J. Mater. Chem.**, v. 20, n. 25, p. 5220-5227, 2010.

68 ILIBI, M.; QUEIROZ, T. B. de; REN, J.; DE COLA, L.; CAMARGO, A. S. S. de; ECKERT, H. Luminescent hybrid materials based on covalent attachment of Eu(III)-tris(bipyridinedicarboxylate) in the mesoporous silica host MCM-41. **Dalton Trans.**, v. 43, n. 22, p. 8318-8330, 2014.

69 LECHEVALLIER, S.; JORGE, J.; SILVEIRA, R. M.; RATEL-RAMOND, N.; NEUMEYER, D.; MENU, M.-J.; GRESSIER, M.; MARÇAL, A. L.; ROCHA, A. L.; MARTINES, M. A. U.; MAGDELEINE, E.; DEXPERT-GHYS, J.; VERELST, M. Luminescence properties of mesoporous silica nanoparticles encapsulating different europium complexes: application for biolabelling. **J. Nanomater.**, v. 2013, 2013. doi: 10.1155/2013/918369.

70 COUSINIÉ, S.; GRESSIER, M.; ALPHONSE, P.; MENU, M.-J. Silica-based nanohybrids containing dipyridine, urethan, or urea derivatives. **Chem. Mater.**, v. 19, n. 26, p. 6492-6503, 2007.

71 DUARTE, A. P.; GRESSIER, M.; MENU, M.-J.; DEXPERT-GHYS, J.; CAIUT, J. M. A.; RIBEIRO, S. J. L. Structural and luminescence properties of silica-based hybrids containing new silylated-diketonato europium(III) complex. **J. Phys. Chem. C**, v. 116, n. 1, p. 505-515, 2012.

72 COUSINIÉ, S.; MAULINE, L.; GRESSIER, M.; KANDIBANDA, S. R.; DATAS, L.; REBER, C.; MENU, M.-J. Bulk or surface grafted silylated Ru(II) complexes on silica as luminescent nanomaterials. **New J. Chem.**, v. 36, n. 6, p. 1355-1367, 2012.

73 MAULINE, L.; GRESSIER, M.; ROQUES, C.; HAMMER, P.; RIBEIRO, S. J. L.; CAIUT, J. M. A.; MENU, M.-J. Bifunctional silica nanoparticles for the exploration of biofilms of *Pseudomonas aeruginosa*. **Biofouling**, v. 29, n. 7, p. 775-788, 2013.

74 SÁBIO, R. M.; GRESSIER, M.; CAIUT, J. M. A.; MENU, M.-J.; RIBEIRO, S. J. L. Luminescent multifunctional hybrids obtained by grafting of ruthenium complexes on mesoporous silica. **Mater. Lett.**, v. 174, p. 1-5, 2016.

75 COUSINIÉ, S.; GRESSIER, M.; REBER, C.; DEXPERT-GHYS, J.; MENU, M.-J. Europium (III) complexes containing organosilyldipyridine ligands grafted on silica nanoparticles. **Langmuir**, v. 24, n. 12, p. 6208-6214, 2008.

76 DUARTE, A. P.; MAULINE, L.; GRESSIER, M.; DEXPERT-GHYS, J.; ROQUES, C.; CAIUT, J. M. A.; DEFFUNE, E.; MAIA, D. C. G.; CARLOS, I. Z.; FERREIRA, A. A. P.; RIBEIRO, S. J. L.; MENU, M.-J. Organosilylated complex [Eu(TTA)$_3$(Bpy-Si)]: a bifunctional moiety for the engeneering of luminescent silica-based nanoparticles for bioimaging. **Langmuir**, v. 29, n. 19, p. 5878-5888, 2013.

77 DUARTE, A. P. **Híbridos luminescentes à base de sílica e complexos de európio**: ferramenta para análise em meio biológico. 2012. 203 f. Tese (Doutorado em Química) - Instituto de Química, Universidade Estadual Paulista, Araraquara, 2012.

78 NANDIYANTO, A. B. D.; KIM, S. G.; ISKANDAR, F.; OKUYAMA, K. Synthesis of spherical mesoporous silica nanoparticles with nanometer-size controllable pores and outer diameters. **Micropor. Mesopor. Mater.**, v. 120, n. 3, p. 447-453, 2009.

79 MASSIOT, D.; FAYON, F.; CAPRON, M.; KING, I.; LE CALVÉ, S.; ALONSO, B.; DURAND, J.-O.; BUJOLI, B.; GAN, Z.; HOATSON, G. Modelling one- and two-dimensional solid-state NMR spectra. **Magn. Reson. Chem.**, v. 40, n. 1, p. 70-76, 2002.

80 PALMER, A. G.; CAVANAGH, J.; WRIGHT, P. E.; RANCE, M. Sensitivity improvement in proton-detected two-dimensional heteronuclear correlation NMR spectroscopy. **J. Magn. Reson.**, v. 93, n. 1, p. 151-170, 1991.

81 CORSI, D. M.; PLATAS-IGLESIAS, C.; VAN BEKKUM, H.; PETERS, J. A. Determination of paramagnetic lanthanide(III) concentrations from bulk magnetic susceptibility shifts in NMR spectra. **Magn. Reson. Chem.**, v. 39, n. 11, p. 723-726, 2001.

82 KARIMI S.; HELM, L. Water exchange on [Ln(DO3A)(H_2O)$_2$] and [Ln(DTTA–Me)(H_2O)$_2$]$^-$ studied by variable temperature, pressure, and magnetic field NMR. **Inorg. Chem.**, v. 55, n. 9, p. 4555-4563, 2016.

83 PINTACUDA, G.; JOHN, M.; SU, X. C.; OTTING, G. NMR structure determination of protein-ligand complexes by lanthanide labelling. **Acc. Chem. Res.**, v. 40, n. 3, p. 206-212, 2007.

84 MAULINE, L. **Elaboration de nanoparticules de silice bifonctionnelles outils innovants pour l'exploration de biofilms a *Pseudomonas Aeruginosa***. 2012. 200 f. Thèse (Doctorat en Chimie) - Institut Carnot CIRIMAT, Université de Toulouse III - Paul Sabatier, Toulouse, 2012.

85 TSARYUK, V.; ZOLIN, V.; LEGENDZIEWICZ, J.; SZOSTAK, R.; SOKOLNICKI, J. Effect of ligand radicals on vibrational IR, Raman and vibronic spectra of europium b-diketonates. **Spectrochim. Acta - Part A**, v. 61, n. 1/2, p. 185-191, 2005.

86 TRIKHA, A. K.; KUMAR, A.; KAUR, S. Complexes of LnIII theonyltrifluoroacetylacetonates with 1-phenylpiperazine: (synthesis and characterisation). **J. Fluor. Chem.**, v. 78, n. 2, p. 109-112, 1996.

87 SILVERSTEIN, D. W.; MILOJEVICH, C. B.; CAMDEN, J. P.; JENSEN, L. Investigation of linear and nonlinear Raman scattering for isotopologues of Ru(bpy)$_3^{2+}$. **J. Phys. Chem. C**, v. 117, n. 40, p. 20855-20866, 2013.

88 KOKOŠKOVÁ, M.; PROCHÁZKA, M.; ŠLOUFOVÁ, I.; VLČKOVÁ, B. SERRS spectra and Excitation profiles of Ru(II) polypyridine complexes attached to Ag nanoparticle aggregates: structural, electronic, and resonance damping effects of chemisorption. **J. Phys. Chem. C**, v. 117, n. 2, p. 1044-1052, 2013.

89 SÁBIO, R. M. **Ancoragem de complexos de rutênio com ligantes siliados em sílica mesoporosa obtida via pirólise de spray**. 2012. 124 f. Dissertação (Mestrado em Química) - Instituto de Química, Universidade Estadual Paulista, Araraquara, 2012.

90 BLASSE, G.; MEIJERINK, A.; DONEGÁ, C. de M. Vibronic rare earth spectroscopy: results and pitfalls. **J. Alloys Compd.**, v. 225, n. 1/2, p. 24-27, 1995.

91 NOREL, L.; DI PIAZZA, E.; FENG, M.; VACHER, A.; HE, X.; ROISNEL, T.; MAURY, O.; RIGAUT, S. Lanthanide sensitization with ruthenium carbon-rich complexes and redox commutation of near-IR luminescence. **Organometallics**, v. 33, n. 18, p. 4824-4835, 2014.

92 MARTÍN-RAMOS, P.; SILVA, P. S. P. da; LAVÍN, V.; MARTÍN, I. R.; LAHOZ, F.; CHAMORRO-POSADA, P.; SILVA, M. R.; MARTÍN-GIL, J. Structure and NIR-luminescence of ytterbium(III) beta-diketonate complexes with 5-nitro-1,10-phenanthroline ancillary ligand: assessment of chain length and fluorination impact. **Dalton. Trans.**, v. 42, n. 37, p. 13516-13526, 2013.

93 POPE, S. J. A.; COE, B. J.; FAULKNER, S.; LAYE, R. H. Metal-to-ligand charge-transfer sensitisation of near-infrared emitting lanthanides in trimetallic arrays M2Ln (M=Ru, Re or Os; Ln=Nd, Er or Yb). **Dalton Trans.**, n. 8, p. 1482-1490, 2005.

94 OLIVEIRA, V. de M. **Estudo da porosidade de pelotas de minério de ferro para altos-fornos através de adsorção física**. 2010. 86 f. Dissertação (Mestrado em Engenharia Metalurgica e de Minas) - Escola de Engenharia, Universidade Federal de Minas Gerais, Minas Gerais, 2010.

95 PORTELLA, J. A. **Características estruturais de géis de sílica preparados a partir da sonohidrólise do tetraetilortosilicato com adições de álcool polivinílico**. 2008. 55 f. Dissertação (Mestrado em Física) - Instituto de Geociências e Ciências Exatas, Universidade Estadual Paulista, Rio Claro, 2008.

96 CHEN, L. F.; NOREÑA, L. E.; NAVARRETE, J.; WANG, J. A. Improvement of surface acidity and structural regularity of Zr-modified mesoporous MCM-41. **Mater. Chem. Phys.**, v. 97, n. 2, p. 236-242, 2006.

97 MÉNDEZ-VIVAR, J.; MENDOZA-SERNA, R.; VALDEZ-CASTRO, L. Control of the polymerization process of multicomponent (Si, Ti, Zr) sols using chelating agents. **J. Non. Cryst. Solids**, v. 288, n. 1, p. 200-209, 2001.

98 COUSINIE, S. **Nanoluminophores inorganiques greffage de complexes de ruthénium(II) et d'europium(III) sur nanoparticules de silice**. 2007. 169 f. Thèse (Doctorat en Chimie Moléculaire) - Institut Carnot CIRIMAT, Université de Toulouse III - Paul Sabatier, Toulouse, 2007.

99 INNOCENZI, P.; KOZUKA, H.; YOKO, T. Fluorescence properties of the $Ru(bpy)_3^{2+}$ complex incorporated in sol−gel-derived silica coating films. **J. Phys. Chem. B**, v. 101, n. 13, p. 2285-2291, 1997.

100 MATSUI, K.; MOMOSE, F. Luminescence properties of tris(2,2'-bipyridine)ruthenium(II) in sol−gel systems of SiO_2. **Chem. Mater.**, v. 9, n. 11, p. 2588-2591, 1997.

101 SUN, L.-N.; ZHANG, H.-J.; MENG, Q.-G.; LIU, F.-Y.; FU, L.-S.; PENG, C.-Y.; YU, J.-B.; ZHENG, G.-L.; WANG, S.-B. Near-infrared luminescent hybrid materials doped with lanthanide (Ln) complexes (Ln = Nd, Yb) and their possible laser application. **J. Phys. Chem. B**, v. 109, n. 13, p. 6174-6182, 2005.

102 FENG, J.; SONG, S.-Y.; DENG, R.-P.; FAN, W.-Q.; ZHANG, H.-J. Novel multifunctional nanocomposites: magnetic mesoporous silica nanospheres covalently bonded with near-infrared luminescent lanthanide complexes. **Langmuir**, v. 26, n. 5, p. 3596-3600, 2010.

103 LIU, Y.; SUN, L.; LIU, J.; PENG, Y.-X.; GE, X.; SHI, L.; HUANG, W. Multicolor (Vis-NIR) mesoporous silica nanospheres linked with lanthanide complexes using 2-(5-bromothiophen)imidazo[4,5-f][1,10]phenanthroline for in vitro bioimaging. **Dalton Trans.**, v. 44, n. 1, p. 237-246, 2015.

RÉSUMÉ DE THÈSE

SOMMAIRE

1. Introduction

Le groupe d'éléments « terres rares » comprend les métaux lanthanides (éléments ayant un nombre atomique entre Z = 57, le lanthane, et Z = 71, le lutétium), et le scandium (Z = 21) et l'yttrium (Z = 39). Les lanthanides possèdent des propriétés chimiques et physiques similaires avec notamment un état trivalent Ln(III) ([Xe] $4f^n$, n = 0-14) stable.[1-3] Les sous couches électroniques saturées $5s^2$ et $5p^6$ protègent la couche $4f^n$ interne, en conséquence les électrons 4f sont peu affectés par l'environnement chimique lorsque l'ion est introduit dans un champ de ligands. Ainsi, l'émission caractéristique constituée des raies fines et la longue durée de vie des états excités sont observés du domaine du visible à l'infrarouge selon le lanthanide choisi.[1-3] Les matériaux à base de lanthanides ont été largement utilisés en tant que OLEDs, capteurs analytiques, mais aussi comme sondes pour immunoessais et bioimagerie.[3-7] Par exemple, l'émission des ions Eu^{3+} dans le rouge est appropriée pour la détection biologique et l'électroluminescence organique.[8, 9] Les ions Nd^{3+} et Yb^{3+}, émettant dans l'infrarouge (900 à 1400 nm) sont de bons candidats pour l'imagerie in-vivo, les systèmes laser et les nanothermomètres luminescents.[7, 10] L'ion Pr^{3+} et l'ion Er^{3+} qui émettent respectivement à 1300 et 1500 nm ont été utilisés particulièrement dans les amplificateurs optiques pour les réseaux à fibres optiques.[7, 11-13]

Bien qu'il y ait un certain nombre de niveaux d'énergie disponibles pour les transitions *f-f* des ions lanthanides, la faible valeur du coefficient d'extinction molaire (ε <10 M) rend l'excitation directe dans les niveaux 4f de lanthanides inefficace, ces ions nécessitent donc d'être excités via un effet d'antenne.[4, 14] On peut remédier à ce problème en utilisant des chromophores organiques. Ces ligands présentent une forte absorption dans la région UV ($\varepsilon \sim 10^6$ M) laquelle peut sensibiliser les lanthanides via un processus de transfert d'énergie.[4, 14] La figure 1 montre un schéma représentatif du mécanisme de transfert d'énergie entre les ligands organiques et aux ions lanthanides.

Figure 1. Schéma représentatif de l'effet d'antenne du ligand organique pour l'ion lanthanide(III). Abréviations : A = absorption ; F = fluorescence ; P = phosphorescence ; CIS = croisement intersystème; TE = transfert d'énergie; S = singlet; T = triplet. Les flèches pleines indiquent les transitions radiatives ; les flèches en pointillé indiquent les transitions non radiatives.[4, 13, 15, 16]

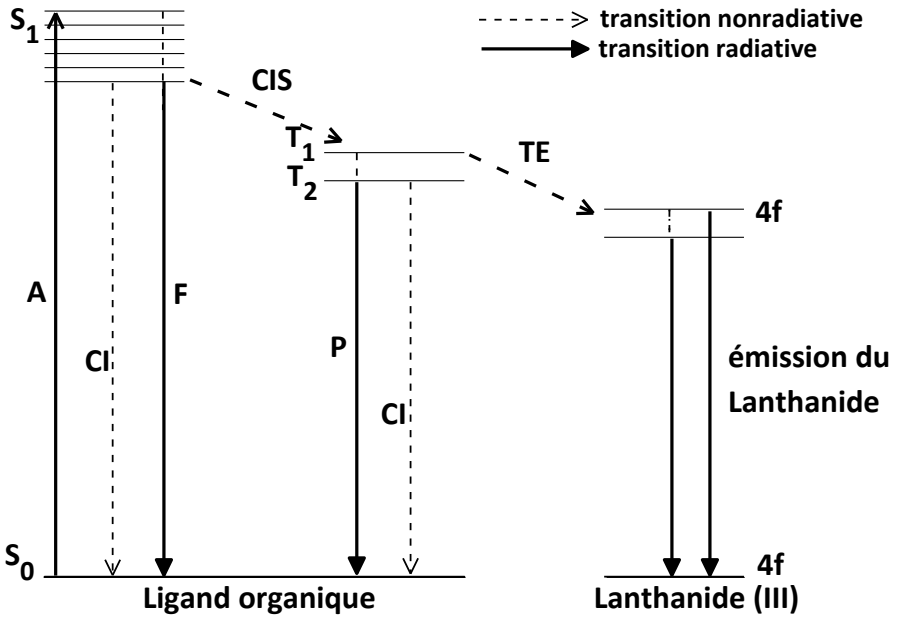

Après irradiation dans l'UV les ligands organiques sont excités à un niveau vibrationnel du premier état singulet excité (S0→S1). La molécule peut être désactivée par conversion interne (CI) du niveau d'énergie excité à un niveau d'énergie plus bas, par exemple due à l'interaction avec des molécules de solvant. L'état singlet excité S1 peut être désactivé de façon radiative vers l'état fondamental par un phénomène de fluorescence (S1→S0) ou bien il peut être désactivé de façon non radiative via le croisement intersystème (CIS) de l'état singlet (S1) à un état triplet (T1 et T2). L'état triplet (T1 et T2) peut être désactivé de façon radiative par phosphorescence moléculaire (P). Le transfert d'énergie (TE, transition non radiative) à partir de l'état triplet du ligand vers aux ions lanthanides (état excité *4f*) traduit l'«effet d'antenne".[4, 13, 15, 16] Après cette excitation indirecte (TE), l'ion lanthanide peut alors être désactivé par une transition radiative vers un état *4f* plus bas par photoluminescence ou être désactivé par des processus non radiatifs. [4, 13, 15, 16]

De ce cadre, le rendement quantique de luminescence (ϕ) est un paramètre important pour l'évaluation de l'efficacité du processus d'émission dans les composés luminescents, par exemple, les complexes luminescents. Le rendement quantique est défini tel que le rapport entre le nombre de photons émis et le nombre de photons absorbés selon l'équation 1.[15, 17]

$$\Phi = \frac{nombre\ de\ photon\ émis}{nombre\ de\ photon\ absorbés} \quad (1)$$

Une méthode pour déterminer le rendement quantique de luminescence consiste à déterminer le rendement quantique relatif (ϕ'). Dans ce cas, le rendement quantique de l'échantillon inconnu est comparé à celui de la référence, en solution, selon l'équation 2.[15, 17]

$$\Phi' = \left(\frac{Abs_R}{Abs_E}\right)\left(\frac{Em_E}{Em_R}\right)\left(\frac{n_E}{n_R}\right)^2 \Phi_R \quad (2)$$

Où Abs est l'absorbance à la longueur d'onde d'excitation, Em est l'intensité d'émission, et n est l'indice de réfraction du solvant utilisé. R et S se réfèrent à la référence et l'échantillon inconnu, respectivement.[15, 17]

L'écart d'énergie entre l'état excité du ligand et celui de l'ion lanthanide détermine si un transfert d'énergie efficace a lieu. Pour un transfert d'énergie efficace, l'état triplet le plus bas du sensibilisateur doit être supérieure de 1 000 à 2 000 cm^{-1} à l'état excité le plus bas (état d'émission) de l'ion lanthanide.[13, 18] De cette manière, plusieurs ligands organiques ont été utilisés pour l'obtention des complexes de lanthanide luminescents activés par effet d'antenne.[5, 15, 21] Parmi les différents ligands organiques utilisés, les ligands β-dicétonates présentent des coefficients d'extinction molaires intéressants ($\varepsilon \sim 10^6$ M) et conduisent à des complexes dont les constantes de stabilité sont également élevées avec d'excellentes propriétés de luminescence. De plus, la synthèse de complexes de lanthanides en utilisant ces chromophores est maintenant bien maitrisée.[16]

Malgré le grand nombre de complexes β-dicétonates de lanthanides décrits[15, 16, 24], très peu émettent dans le proche l'IR. Ceci peut être expliqué par le fait que les lanthanides émettant dans l'IR présentent un état excité plus bas que celui des complexes de lanthanides émettant dans le visible. Ils nécessitent donc des ligands organiques ayant un état excité

suffisamment bas pour les sensibiliser ($^4F_{3/2}$ pour le Nd^{3+}, 11 257 cm^{-1}; $^2I_{13/2}$ pour le Er^{3+}, 6 536 cm^{-1} et $^2F_{5/2}$ pour le Yb^{3+}, 10 400 cm^{-1}), selon la représentation du diagramme des niveaux d'énergie *f-f* donné figure 2.[13, 25]

Figure 2. Représentation du diagramme des niveaux d'énergie *f-f* du Nd(III), de l'Er(III), de l'Yb(III), jusqu'à 20.000 cm^{-1}. Les niveaux d'énergie à partir desquels provient la luminescence dans l'IR sont marqués en gras, et les principales émissions dans l'IR sont montrées en utilisant des flèches descendantes. Adapté de[25].

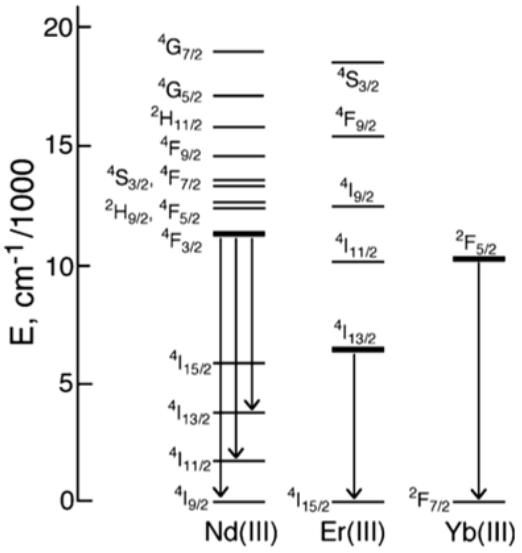

Néanmoins, les ions Nd^{3+} et Yb^{3+} émettant dans l'IR sont rarement utilisés dans la détection analytique ou les imunoessais.

Les complexes de lanthanide émettant dans le visible (tel que Eu^{3+} et Tb^{3+}) sont largement utilisés dans la détection analytique ou les imunoessais en raison de leur forte émission. Cependant, la plupart de ces complexes nécessite une excitation dans le domaine du l'UV, ce qui peut endommager les systèmes biologiques. Les résidus aromatiques de protéines et de l'ADN absorbent aussi en compétition avec les chromophores. De plus les tissus biologiques ne sont pas transparents à la lumière visible.[13, 14] En effet, trois fenêtres d'intérêt biologique (BW) sont décrites sur figure 3 ou sont reportés le spectre d'absorption de la peau (ligne grise), la contribution de la diffusion de la lumière (ligne bleue en pointillés), les longueurs d'onde d'émission de quelques ions de lanthanide(III) et le domaine de la lumière visible.[13, 14] La première est située entre 0,65 à 1,0 μm (BW1), la second va de 1,0 à 1.3 μm (BW2) et la troisième se situe de 1,5 à 1,8 μm (BW3).

Figure 3. Spectre d'absorption de la peau humaine (ligne grise) avec la contribution de diffusion de la lumière (ligne bleue en pointillés), la définition des fenêtres biologiques, et des longueurs d'onde d'émission de certains ions lanthanides(III).[14]

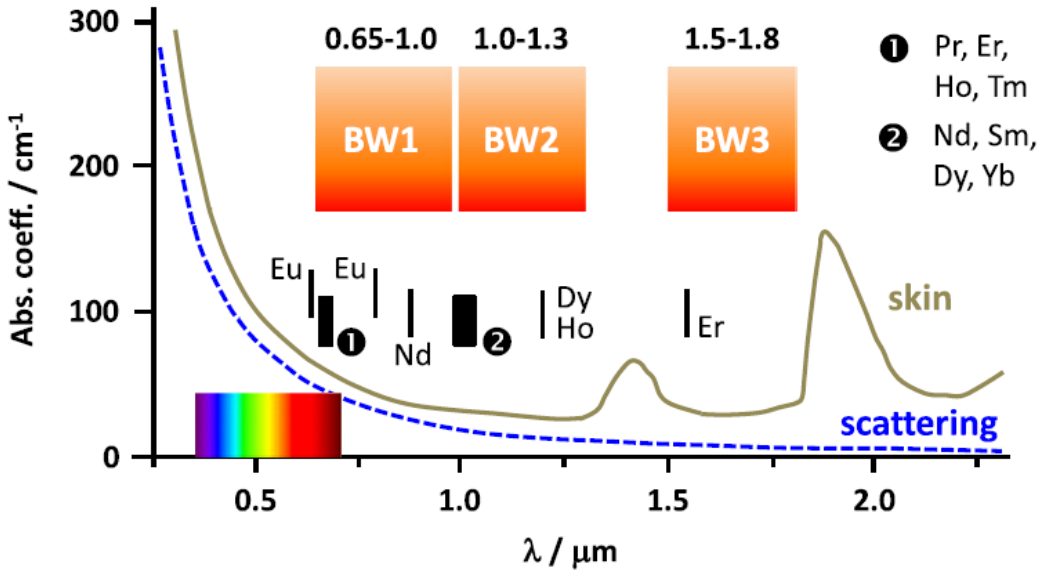

Une des stratégies pour remédier à ces problèmes (absorption de l'UV par les ligands organiques et les molécules biologiques, faible transparence de la peau dans la région visible et diffusion de la lumière) consiste à utiliser des chromophores du bloc *d*, excitables dans le visible, en tant que groupe antenne pour sensibiliser la luminescence de l'état excités *f-f* de basse énergie de lanthanides émettant dans le proche IR.[13, 28, 29] Dans ce cadre plusieurs métaux de transition tels que Ru(II), Os(II), Fe(II), Pt(II), Au(I), Pd(II), Re(I), Cr(III), Co(III), Zn(II) et Ir(III) ont été utilisés pour synthétiser des complexes hétérométalliques avec des ions lanthanide.[13, 25] Notamment, le Ru(II), l'Os(II), le Re(I) et l'Ir(III) sont les métaux plus utilisés pour sensibiliser les ions lanthanides émettant dans l'IR grâce à forte absorption de la lumière dans la région du visible par l'état excité ^{3}TCML (Transfert de Charge Métal-Ligand). Ces chromophores du bloc *d* agissent comme d'excellents donneurs d'énergie gracé à leur état excité ^{3}TCML suffisamment bas, bien situé pour un transfert d'énergie efficace vers les Ln^{3+} (Pr^{3+}, Nd^{3+}, Er^{3+} and Yb^{3+}) émettant dans l'IR. Ainsi la synthèse de complexes hétérobimétalliques *d-f* basés sur des chromophores du bloc *d* et les lanthanides émettant dans l'IR s'est fortement développée et a trouvé un fort intérêt ces dernières années, de par leurs nombreuses possibilités d'application en bioanalyses non-invasives et bioimagerie.[13]

Nous verrons dans le paragraphe suivant qu'il existe quelques complexes heterobimétalliques *d-f* permettant de répondre à ce cahier des charges cependant leur utilisation en tant que nanosondes n'a à ce jour pas été envisagée. En effet l'intérêt de concentrer le luminophore au sein d'une matrice telle que la silice, qui joue également un rôle de protection est maintenant admis et nécessaire à l'obtention de nouveaux outils d'analyse des milieux biologiques. Cela nécessite l'utilisation de luminophores convenablement fonctionnalisés capable d'être greffés de façon covalente au support. Sur la base des travaux de recherche réalisés au CIRIMAT, l'Université Toulouse 3 en collaboration avec le Laboratoire des Matériaux Photoniques de l'UNESP à Araraquara, il a été proposé d'explorer la possibilité d'obtenir des nanosondes à base de silice comportant un complexe hétérobimétallique *d-f* émettant dans le proche infrarouge. C'est l'objectif principal de ce travail de thèse.

Ce mémoire est constitué des 4 parties, une première partie présente le contexte bibliographique. Il détaille l'intérêt des complexes de Ru(II) à ligands bipyridiniques en tant que sensibilisateur pour les Ln(III) émettant dans l'IR et fait le point sur les complexes luminescents silylés ainsi que sur les nanohybrides correspondants à base de silice décrits.

Les objectifs du travail sont ensuite précisés. Un chapitre expérimental récapitule toutes les synthèses des complexes et des nanohybrides ainsi que leurs caractérisations principales. Ce chapitre n'est pas inclus dans le résumé en français. Les résultats et discussions sont présentés en deux grands chapitres. Tout d'abord sont décrits les synthèses et caractérisation des complexes monomères précurseurs et des complexes hétérobimétalliques *d-f* silylés. Enfin dans un dernier chapitre le greffage de ces nouveaux complexes, précurseurs et hétérobimétallique *d-f* silylés, sur la matrice de silice mésoporeuse est présenté ainsi que la caractérisation physico-chimique des différents nanohybrides obtenus avec notamment la caractérisation de leurs propriétés photophysiques.

2. Contexte bibliographique

2.1. Complexes de Ru(II) en tant que sensibilisateur pour les Ln(III) émettant dans l'IR

Les complexes polypyridine de Ru(II) ont été étudiés en raison de propriétés photochimie et photophysique uniques.[39] $[Ru(bpy)_3]^{2+}$ possède une forte et large bande d'absorption dans la région visible (jusqu'à 500 nm) et un bas état triplet (E_T = 17 400 cm^{-1}) qui

permettent de sensibiliser les ions lanthanides émettant dans l'IR de façon efficace. Des plus l'état excité de transfert de charge métal-ligand (TCML) (bandes d'absorption dans le visible) est accessible par la technique biphoton.[39, 40] La figure 4 présente quelques exemples de complexes monomères de Ru(II) et bimétalliques Ru(II)—Ru(II) qui peuvent être excités par absorption de deux photons.

Figure 4. Structure chimique de certains complexes monomères de Ru(II) et bimétalliques Ru(II)—Ru(II) excitables par l'absorption de deux photon.[40-42]

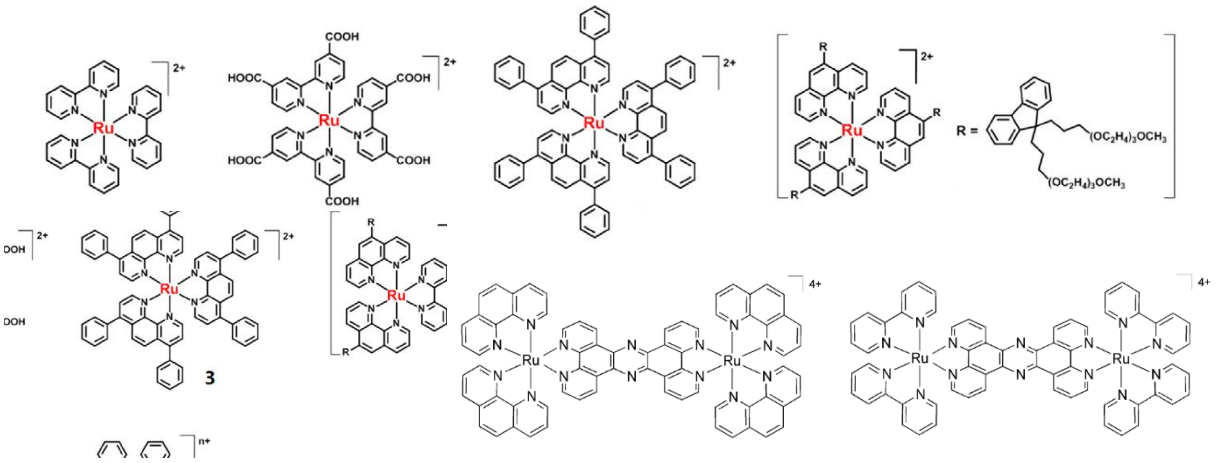

Alternativement, des efforts ont été réalisés pour modifier les ligands 2-2'-bipyridine (bpy) pour permettre une coordination plus efficace avec des ions lanthanides. Dans cette optique, des ligands pontants ont été utilisés pour obtenir des complexes hétérobimétalliques Ru(II)—Ln(III) et ainsi avoir la possibilité de transfert d'électron et d'énergie efficaces. Quelques exemples représentatifs de complexes hétérobimétalliques *d-f* (Ru-Ln) sont décrits dans la figure 5.

Lazarides et al.[28] ont étudiés les processus de transfert d'énergie (EnT) Ru(II)-Ln(III) à partir du chromophores $[M(bpy)_3]^{2+}$ (M = Ru, Os) vers les ions Ln(III) possédant des état f-f de basse d'énergie (Ln = Yb, Nd, Er). Les complexes bimétalliques *d-f* obtenus en utilisant des ligands pontants saturés ($-CH_2CH_2-$) et des ligands pontant insaturés et conjugués (*p*-C_6H_4 et *p*-$(C_6H_4)_2$). Ils démontrent que le mécanisme dominant était un mécanisme de type-Dexter ce qui implique le couplage électronique via les orbitales du ligand pontant. Le processus de transfert d'énergie est aussi plus rapide dans le cas des ligands pontants conjugués par rapport au ligand aliphatique. L'effet de la distance a été également évaluée par le système Ru→Nd

en utilisant les diffèrent ligands pontant conjugués. Dans le plus cas de la plus longue distance ([Ru(*p*-C_6H_4)$_2$—Nd)]) le transfert d'énergie est le moins efficace).

La figure 5. Exemples représentatifs de complexes hétérobimétalliques *d-f* (Ru—Ln) mettant en œuvre des ligands pontants décrits dans la littérature.[13, 22, 28, 29]

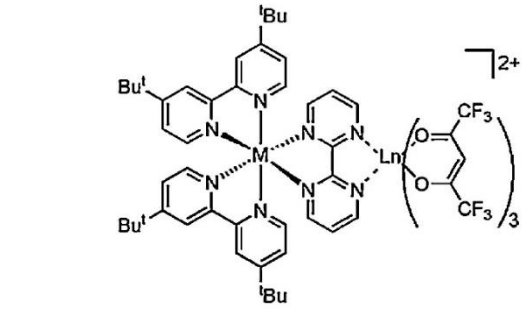

Ln = Nd, Yb, Pr

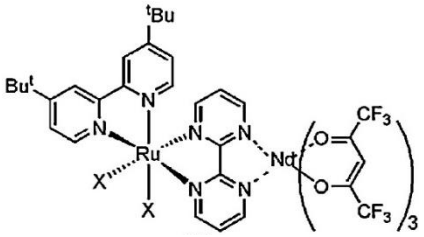

X = Cl or NCS
Ln = Nd, Yb, Pr

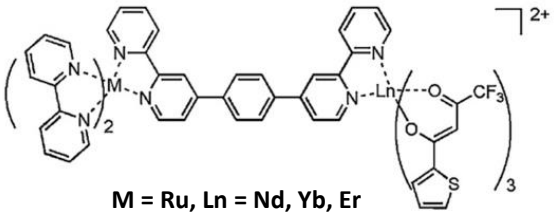

M = Ru, Ln = Nd, Yb, Er

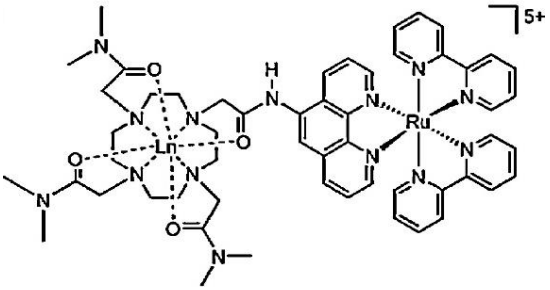

Ln = Nd, Yb

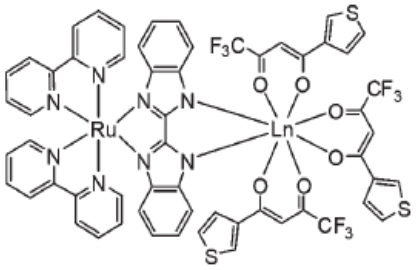

Ln = Nd, Yb, Gd

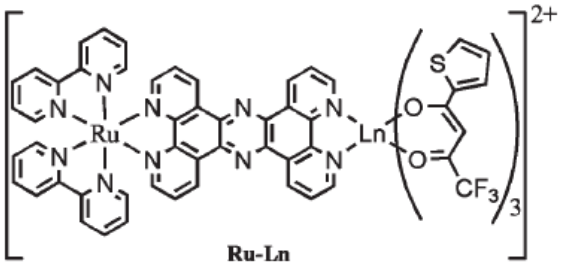

Ln = Nd, Yb, Er, Pr, Gd

La 2,2'-bipyrimidine (bpmd) est un des ligands pontants classiquement utilisés pour synthétiser des complexes hétérobimétalliques. Cet hétérocycle planaire peut coordonner facilement deux centres métalliques à travers quatre atomes d'azote afin de maintenir la distance métal—métal très courte idéal pour un canal efficace pour le transfert d'électron et d'énergie à partir de chromophores du bloc d (dans la région visible) vers les lanthanides.[47-51] Les complexes bimétalliques Ru—Ln utilisant la bpmd comme ligand pontant ont été développés par Lazarides et al.[52] Les complexes précurseurs [Ru(^{t}Bu$_2$bpy)(bpmd)X$_2$] (X = Cl,

NCS) et $[M(^tBu_2bpy)_2(bpmd)][PF_6]_2$ (M = Ru, Os) ont été synthétisés et puis connectés au {Ln(dicétonate)$_3$} (Ln = Pr, Nd, Yb or Gd) via la 2,2'-bipyrimidine (bpmd). Ces chromophores du bloc d ont montré des états excités ^{1}TCML et ^{3}TCML de basse énergie par rapport aux analogues contenant la bipyridine. Pour le complexes hétérobimétalliques $[Ru(^tBu_2bpy)_2(\mu\text{-bpmd})Ln(diketonate)_3][PF_6]_2$ le niveau d'énergie de l'état ^{3}TCML (13 500 cm^{-1}) a permis un transfert d'énergie efficace vers l'Yb(III) et le Nd(III), confirmant la sensibilisation de la luminescence dans l'IR.

Le transfert d'énergie à partir de ligands organiques a été bien discuté[4] dans la bibliographie. Dans le cas des complexes hétérobimétalliques où le donneur et accepteur sont reliés par des ligands pontant conjugués, un couplage électronique à longue distance donneur-accepteur peut se produire par le processus de super-échange indirect *via* les orbitales du ligand pontant qui peut se produire sur des distances importantes plus longues.[28, 53]

Pour confirmer les processus de transfert d'énergie dans les complexes hétérobimétalliques *d-f*, la durée de vie de luminescence de l'émission du ^{3}TCML a été déterminée et utilisée ensuite pour quantifier le taux de transfert d'énergie selon l'équation 3.[28, 53]

$$k_{ET} = 1/\tau_q - 1/\tau_u \quad (3)$$

Où k_{ET} est le taux de transfert d'énergie et τ_q and τ_u sont les durées de vie en présence d'un agent d'extinction ("quenching") (complexe de Ru(II) après la coordination avec le Ln^{3+}) et la durée de vie sans agent d'extinction ("unquenched") (complexe de Ru(II) avant la coordination avec le Ln^{3+}). Le rendement quantique du transfert d'énergie (Φ_{ET}) peut être calculé selon l'équation 4.

$$\Phi_{ET} = 1 - \tau_q/\tau_u \quad (4)$$

Les taux de transfert d'énergie ont été utilisés pour établir le mécanisme de transfert d'énergie en solution dans des systèmes rigides où la séparation entre le chromophore et les lanthanides (r) est bien défini.[53] Ainsi le rendement quantique de transfert d'énergie (Φ_{ET}) a été calculé pour déterminer l'efficacité du transfert d'énergie du chromophore Ru(II) vers le Ln(III) émettant dans l'IR.

2.2. Complexes Luminescent Silylés et les Nanohybrides à Base de Silice

Bien que la bibliographie décrive quelques exemples de complexes hétérobimétalliques *d-f* (Ru-Ln), leur utilisation en tant que nanosondes ou nanomarqueurs est rarement discutée. Les faibles stabilité et solubilité dans l'eau et aussi la luminescence relativement faible peuvent en être les principales raisons.[44] Rocha et al.[54, 55] ont proposé un moyen de remédier à ces problèmes en utilisant des particules sphériques de silice mésoporeuse pour encapsuler des complexes métalliques tel que $Eu(fod)_3$ (fod = 6,6,7,7, 8,8,8-heptafluoro-2,2-diméthyl-3,5-octanedionate) dans des canaux mésoporeux. Les excellentes propriétés de luminescence de ces hybrides à base de silice et les succès dans le processus d'encapsulation permettent à ces hybrides d'être mis en œuvre dans le domaine de LEDs (Light Emitting Diodes) émetteurs dans le rouge.

Parce que la silice est biocompatible, abondante et facilement fonctionnalisable, c'est un matériau de choix utilisé dans de très nombreuses applications en tant que support notamment dans le domaine de l'analyse. De plus sa versatilité au niveau de sa morphologie (porosité, surface spécifique, taille des particules primaires, taille des agrégats…) justifie l'ampleur des travaux menés sur cette matrice.[57-59] En particulier, les nanoparticules de silice mésoporeuses (MSNs) présentent des caractéristiques très intéressantes pour l'application comme nanosondes ou nanomarqueurs dans le domaine de l'analyse des milieux biologiques. En effet il est possible de contrôler la taille, même submicronique, et la morphologie (creuse, dense) des nanoparticules de silice. De même la surface spécifique et la porosité restent modulables en plus de la possibilité d'en modifier chimiquement la surface.[54, 58, 59] En général, le chargement des médicaments, de colorants organiques et de complexes luminescents à l'intérieur des pores de MSNs permet d'éviter les processus de dégradation, de désactivation ou encore la libération prématurée d'espèce active.[54, 58, 59] Ainsi, les MSNs peuvent être utilisés en tant que véhicules pour la libération de drogues, en tant que nanosondes luminescentes ou nanomarquers cellulaires. Il est également possible d'envisager le greffage de photocatalyseurs, ou de molécules actives pour la thérapie photodynamique, parmi autres.[54, 57-61]

Afin d'explorer le potentiel des complexes *d-f* hétérobimétalliques en tant que sondes, une alternative a été trouvée avec l'utilisation de ligands organiques à fonction alkoxysilane pour préparer de nouveaux complexes métalliques également fonctionnalisés par le

groupement hydrolysable $Si(OR)_3$. Cette stratégie permet de greffer, par un lien covalent à la matrice de silice, des complexes de façon homogène en évitant les processus de lixiviation et apportant de la stabilité au luminophore comme cela a été montré dans les travaux de Cousinià[70, 72, 75], Mauline[72, 73] et Duarte[71, 76] au CIRIMAT. Des ligands silylés bidentés dérivés de la bipyridine (bpy-Si) et du ligand dicétonate (TTA-Si)[53, 54] ont été décrits et ont permis l'obtention de complexes de ruthénium(II)[55-57] et d'europium(III)[54, 58, 59] comportant la fonction alkoxysilane apte à l'ancrage à la matrice de la silice. Certains exemples représentatifs sont présentés dans la figure 6.

Figure 6. Ligands silylés bidentés (bpy-Si, TTA-Si) et complexes de ruthénium(II) et d'europium (III).[70-76]

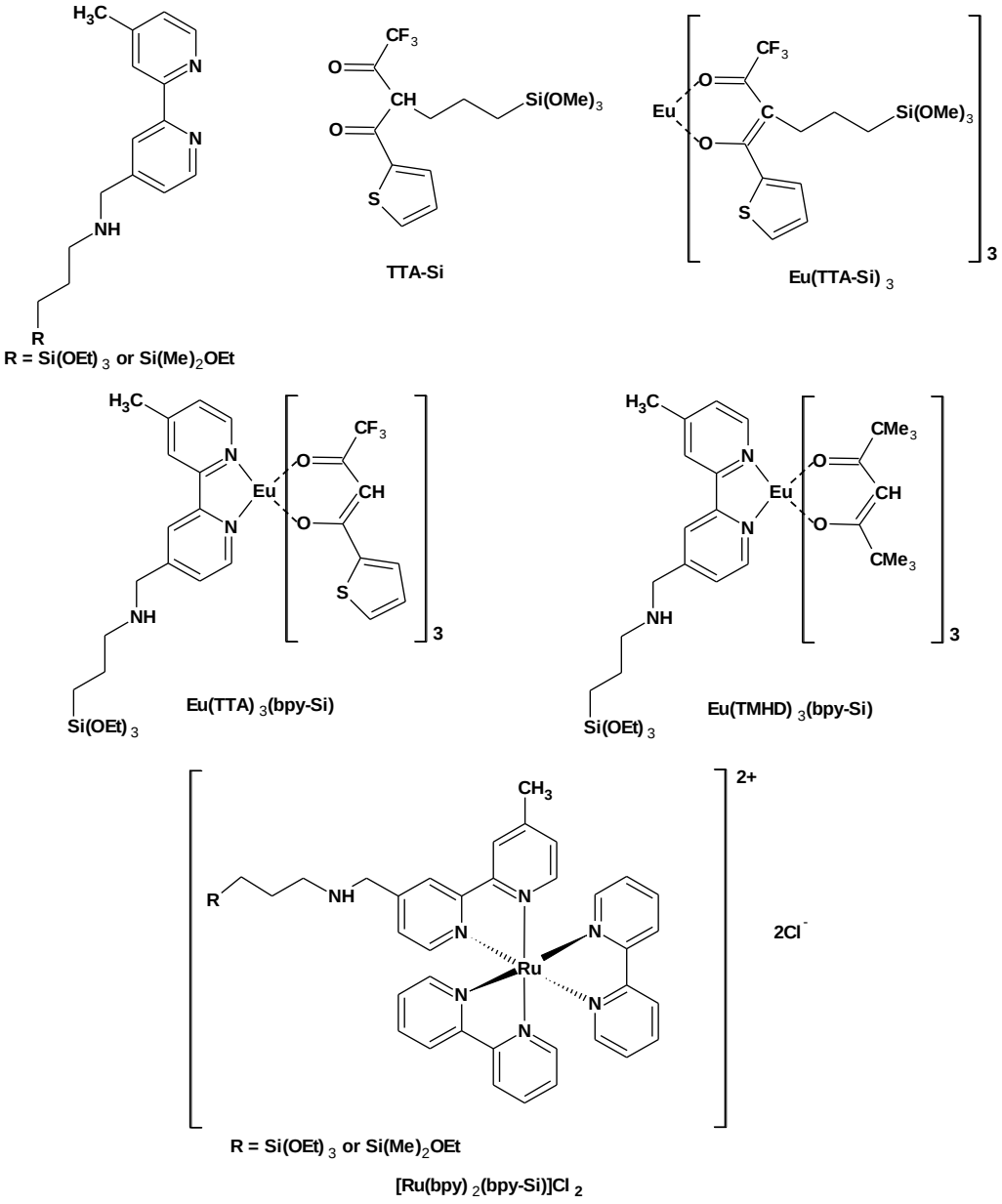

Duarte et al.[71, 76] ont décrit la synthèse du ligand β-dicétonate modifié par un groupe triméthoxysilane (TTA-Si) et dans la suite, un complexe d'europium silylé très luminescent [Eu(TTA-Si)$_3$] a été obtenu. Le complexe avec la fonction silane a été greffé sur la matrice de silice en utilisant deux approches. D'abord, l'incorporation de ce complexe au cœur des nanoparticules de silice par la méthode de synthèse mettant en œuvre une microémulsion inverse (W/O) et la deuxième approche a consisté à greffer le complexe dans les pores de nanoparticules de silice mésoporeuse. Des taux de greffage significatifs compris entre 0.3 et 0.6 mmol.g^{-1} sont obtenus dans les deux cas. Parmi les complexes synthètisés, le complexe silylé [Eu(TTA)$_3$(bpy-Si)] fortement luminescent est intéressant puisque comportant dans sa sphère de coordination à la fois un ligand bipyridine modifié par un groupe éthoxysilane (bpy-Si) et le ligand TTA. Ces nanohybrides luminescents ont été employés en tant que nanomarqueurs pour l'imagerie sélective de bactéries *Escherichia coli*.[76]

Des complexes de Ru(II) silylé ont aussi été décrits par Cousinié et al. puis par Mauline et al.[72, 73] avec notamment l'obtention du complexe silylé [Ru(bpy)$_2$(bpy-Si)]Cl$_2$. Ce complexe a ensuité été incorporé par microémulsion inverse au cœur de nanoparticules de silice et également greffé à la surface de nanoparticules de silice dense type Ludox. Les nanohybrides luminescents bifonctionnels sont décrits comme d'interessant outils pour étudier les systèmes biologiques complexes tels que les biofilms de *Pseudomonas aeruginosa*.[73] de par la possibilité de modifier chimiquement la surface des particules de silice pour en modifier les propriétés de surface (charge, hydrophilicité/hydrophobicité, groupement fonctionnels...). Ces résultats nous ont encouragé à développer des complexes hétérobimétalliques silylés *via* l'utilisation de ce type précurseurs monomères silylés.

Dans cette optique nous avons proposé la synthèse de nouveaux complexes hétérobimétalliques *d-f* possédant des ligands à fonction trialkoxysilane. Ces ligands silylés ont été synthétisés donnant accès à de nouveaux complexes monomères de ruthénium(II) [Ru(bpy)$_2$(bpmd)]Cl$_2$ (**Ru**), [Ru(bpy)(bpy-Si)(bpmd)]Cl$_2$ (**RuL**), de lanthanide(III) [Ln(TTA-Si)$_3$] (**LnL3**). Dans la suite, quatre complexes hétérobimétalliques *d-f* silylés ont été obtenus ; deux comportant la fonction silane sur la partie lanthanide (notés **Ru—LnL3**) et deux comportant cette fonctionnalité sur la complexe de ruthénium (notés **Ln—RuL**). Ces complexes ont été entièrement caractérisées et leurs propriétés photophysiques ont été évalués et discutées par rapport à l'efficacité du processus de transfert d'énergie du chromophore Ru(II) vers le lanthanide émettant dans l'IR. Le greffage de ces complexes hétérométalliques a été ensuite

entrepris sur deux types de matrice : des nanoparticules de silice mésoporeuse et dense. Les propriétés photophysiques, particulièrement la luminescence, associées à la morphologie de ces nanohybrides et à leur stabilité suggèrent que ces hybrides à base de silice et de complexes hétérobimétalliques *d-f* sont de bons candidats comme outils d'analyse des milieux biologiques émettant dans l'IR.

3. Objectifs

L'objectif général de cette thèse est l'élaboration de nouveaux systèmes luminescents dans l'IR à base de silice et complexes hétérobimétalliques *d-f* en tant que nanosondes ou nanomarqueurs en vue d'application pour l'analyse de milieux biologiques.

Objectifs spécifiques

- Préparer, caractériser et étudier les propriétés luminescentes de complexes monomères, de ruthénium (II), de néodyme (III) et d'ytterbium (III) comportant une fonction trialkoxysilane.

- Préparer, caractériser et étudier les propriétés photophysiques de complexes hétérobimétalliques *d-f* (Ru(II)—Nd/Yb(III)) comportant une fonction trialkoxysilane.

- Préparer et caractériser des nanoparticules de silice mésoporeuses par la méthode de microémulsion directe.

- Explorer la voie d'élaboration de nanohybrides à base de silice et de complexes à fonction alkoxysilane:

  - Greffage des complexes monomères de ruthénium(II), de néodyme(III) et d'ytterbium(III) silylés sur de nanoparticules de silice mésoporeuses
  - Greffage simultané des deux types de complexes monomères silylés, ruthénium(II) et lanthanides(III) sur de nanoparticules de silice mésoporeures

- Greffage des complexes hétérobimétalliques *d-f* silylés sur deux types de nanoparticules de silice (mésoporeuse ou dense).

- Etudier les propriétés photophysiques des nanohybrides luminescents obtenus dans cette thèse.

4. Complexes monomères précurseurs et complexes hétérobimétalliques *d-f* silylés

4.1. Caractérisation de complexes hétérobimétalliques *d-f* silylés

En premier lieu, nous avons synthétisé deux ligands organiques possédant une fonction trialkoxysilane; le 4-méthyl-4'-(N-triéthoxysilylpropyl)amine-méthyl- 2,2'-bipyridine (**bpy-Si**) et le 4,4,4-trifluoro-2-(3-(triméthoxysilyl)-propyl)-1-(2-thienyl)-1,3-butanedione (**TTA-Si**) selon la méthodologie décrite par Menu et al.[70, 72] Ensuite de nouveaux complexes monomères à ligand silylé ou non ont été synthétisés avec de bons rendements: le $[Ru(bpy)_2(bpmd)]Cl_2$ (**Ru**, 85%), le $[Ru(bpy)(bpy\text{-}Si)(bpmd)]Cl_2$ (**RuL**, 80%) et le $[Ln(TTA\text{-}Si)_3]$ (**LnL3**) où **Ln = Nd^{3+}, Yb^{3+}**. Ainsi après avoir isolé et entièrement caractérisés ces complexes précurseurs, nous avons synthétisé les complexes hétérobimétalliques *d-f* silylés. Les voies de synthèse mises en œuvre pour l'obtention des complexes dimères sont présentées sur la figure 7. La voie (i) permet d'accéder aux complexes dimères portant la fonction silane sur le lanthanide en faisant réagir en proportion équivalente (1:1) le complexe **Ru** avec le monomère silylé **LnL3** dont les rendements sont respectivement 55 % et 55 % pour **Ru—NdL3** et **Ru—YbL3**. Dans les mêmes conditions de stœchiométrie, la voie (ii) permet d'accéder aux complexes dimères portant la fonction silane sur le fragment ruthénium en faisant réagir **RuL** avec $Ln(TTA)_3$ déja décrits dans la bibliographie. Les rendements sont dans ce cas respectivement 55 % et 55 % pour **Nd—RuL** et **Yb—RuL**. Les structures proposées à partir des données de caractérisation physico-chimiques pour les différents complexes isolés dans ce travail sont présentées sur la figure 7.

Figure 7. Voies de synthèse et structures proposées pour les complexes hétérobimétalliques silylés **Ru—LnL3** (i) and **Ln—RuL** (ii), (Ln = Nd^{3+}, Yb^{3+}).

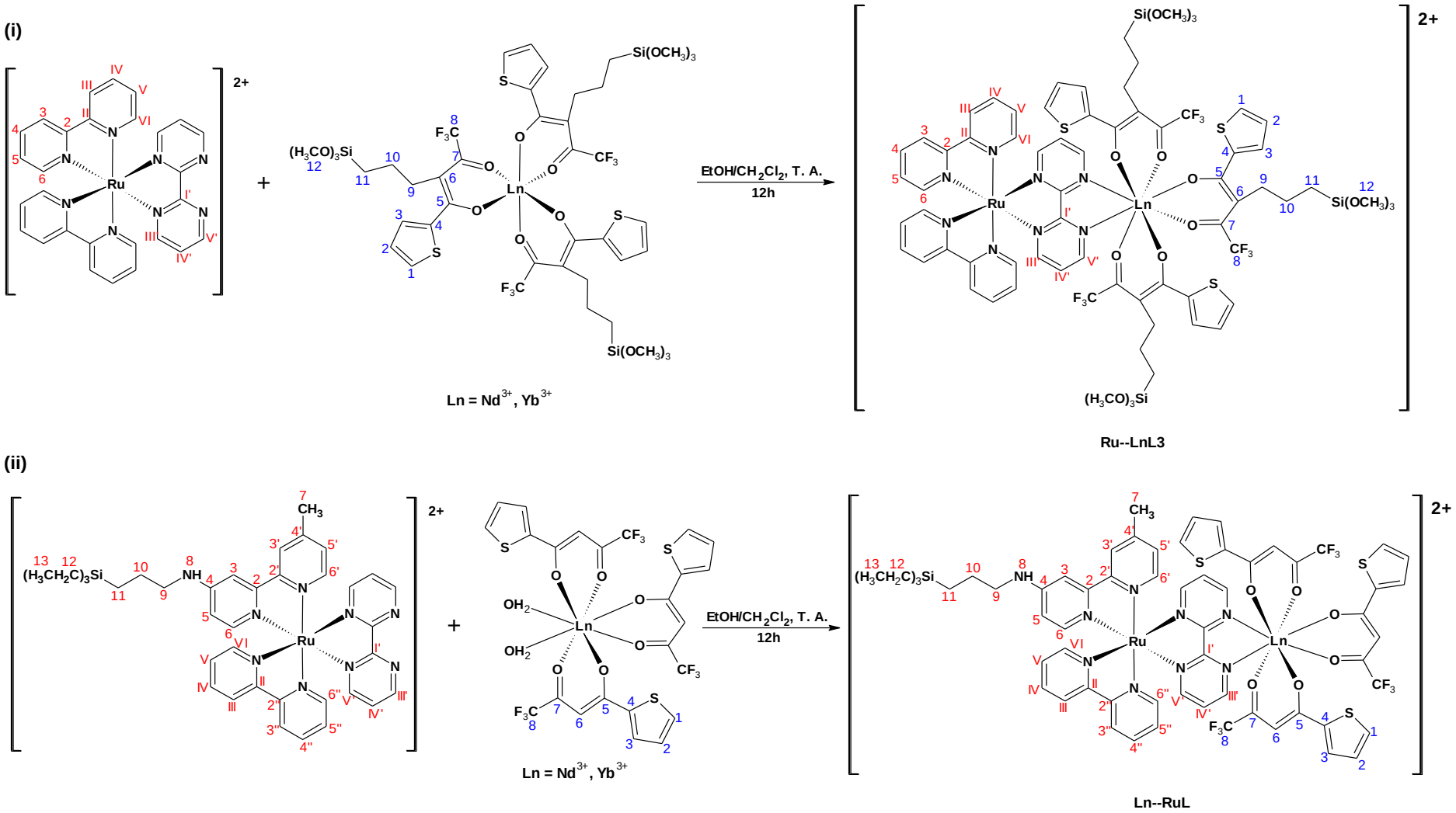

Les structures de complexes silylés, monomères et dimères, ont été confirmées par RMN en solution et à l'état solide, spectroscopie infrarouge, UV/Visible, FT-Raman, spectrométrie de masse et analyse élémentaire. Les complexes précurseurs monomères **RuL** (80 % de rendement) et **Ru** (85 % de rendement) ont été caractérisés par mesures de CP MAS du ^{13}C et RMN du ^{1}H (liquide), respectivement. L'utilisation de différentes séquence RMN a permis d'identifier sans ambiguïté la structure des complexes notamment en présence de ligands bipyridine et bipyrimidine. Les mesures de RMN 1D (TOCSY 1D; figure 32, page 107) et 2D (HSQC et HMBC; figures 33 et 34, pages 108 et 109, respectivement) montrent distinctement les signaux attribués aux ligands bpy et bpmd, ce qui nous permet de confirmer la structure du complexe proposé. De façon similaire, le complexe **NdL3** a été caractérisé par différentes séquences RMN du proton (figure 35, page 110), TOCSY 1D (figure 36, pages 111 et 112) HSQC (figure 37, page 113), les résultats indiquent la présence des signaux caractéristiques de la partie aromatique du ligand TTA ainsi que la présence de la chaine propyl et du groupe méthoxysilane et ce malgré la présence du noyau paramagnétique (Nd^{3+}). L'effet du Nd^{3+} a été bien observé dans les spectres, particulièrement en RMN du proton, par l'élargissement de signaux et également le déplacement chimique par rapport le ligand **TTA-Si** non complexé.

Le complexe hétérobimétallique **Ru—Nd3** a été caractérisé par RMN du liquide. Le RMN du ^{1}H montre plusieurs signaux plutôt mélangés ce qui confirme la présence du noyau paramagnétique (Nd^{3+}). Si par RMN du proton il n'a pas été possible de distinguer et d'attribuer les signaux des différents ligands, des mesures de TOCSY 1D (figure 39, pages 115 et 116), HSQC (figure 40, page 117) et HMBC (figure 41, page 118) ont été réalisées et ont permis d'identifier les signaux attribués aux ligands bpy, bpmd et bpy-Si.

Les spectroscopies infrarouge et FT-Raman (figures 47 et 48, pages 126 et 129, respectivement) ont confirmés la présence des différentes fonctions notamment la fonction alkoxysilane par la présence de bandes de vibration caractéristiques. Particulièrement, les bandes $\nu(Si—O—CH_3)$, $\delta(O—CH_3)$ et $\delta(Si—O—C)$ observées par infrarouge confirment que les synthèses ont été effectuées en évitant l'hydrolyse et la polymérisation des groupes alkoxysilanes présent dans les complexes. Les mesures de FT-Raman ont confirmés la coordination des ligands par la présence des bandes vibration Ln—O et Ru—N des complexes.

Le spectre d'absorption dans la région UV-visible des complexes, mesurés en solution dans l'éthanol, sont présentés dans la figure 49 (page 130). Les bandes d'absorption du **Ru**,

LnL3 et **Ru—Ln3** ont été superposés sur cette figure 49 (a et b) pour comparaison. Les bandes à environ 246 et 424 nm ont été attribuées à la transition ^{1}TCML (d→π*, caractéristiques du **Ru** vers les ligands bpy et bpmd), et la bande autour de 285 nm est attribuée aux transitions π→π* des ligands bpy et bpmd.[19] Les bandes des complexes **LnL3** observées à environ 268 et 340 nm ont été attribuées aux transitions singulet-à-singulet des ligands **TTA-Si**.[4] Toutes ces bandes sont retrouvées dans les spectres d'absorption des complexes **Ru—LnL3**. De façon similaire, les bandes d'absorption de complexes **RuL**, **Ln** et **Ln—RuL** ont été superposés et dans la suite présentés sur la figure 49 (c et d) pour comparaison. Les absorptions à de 250 et 436 nm ont été attribuées à la transition ^{1}TCML (d→π*, caractéristiques du **Ru** vers les ligands bpy, bpy-Si et bpmd), et la bande à 287 nm est attribuée aux transitions π→π* des ligands bpy, bpy-Si et bpmd.[19] Les bandes d'absorption des complexes **Ln** observées à 258 et 339 nm ont été attribuées aux transitions singulet-à-singulet des ligands **TTA**.[4] Tous ces bandes sont également retrouvées dans les spectres d'absorption des complexes **Ln—RuL**, ce qui corrobore l'obtention de ces complexes hétérobimétalliques.

4.2. Propriétés photophysiques de complexes hétérobimétalliques Ru(II)—Nd/Yb(III) silylés

Après avoir isolé et entièrement caractérisé les complexes hétérobimétalliques *d-f* silylés, leur propriétés photophysiques ont été évaluées par les mesures de luminescence et de durée de vie à l'état solide.

Dans ce cadre, lorsque l'excitation est faite sur le chromophore Ru(II), l'émission dans l'IR est observée dans les quatre systèmes hétérobimétaliques *d-f* selon les figures 57-60 (pages 138-141) indiquant un transfert d'énergie dont le mécanisme probable est proposé figure 61 (page 144).

La durée de vie de complexes précurseurs **Ru** et **RuL** et des complexes hétérobimétalliques **Ru—LnL3** et **Ln—RuL** ont été mesurées pour confirmer le phénomène de transfert d'énergie et permettre de calculer les taux de transfert d'énergie (k_{ET}) et les rendements quantiques de transfert d'énergie (Φ_{ET}). Ainsi, lorsque nous avons mesurés les durées de vie de complexes, une réduction des valeurs de durées de vie pour les complexes hétérobimétalliques est observée par rapport aux durées de vie de leur précurseur de Ru(II). Ce résultat nous confirme le processus de transfert d'énergie dans ces complexes permettant ainsi d'atteindre l'objectif visé par cette thèse.

Pour le complexe **Yb—RuL,** k_{ET} de 1.54x10^7 s^{-1} et Φ_{ET} de 73 % a été obtenu. Ces valeurs sont en accord avec les meilleurs résultats de transfert d'énergie observé par le complexe **Nd—RuL** selon le k_{ET} de 3.04x10^7 s^{-1} et and Φ_{ET} de 84 %. Le complexe **Ru—NdL3** a presenté le k_{ET} de 0.61x10^7 s^{-1} et Φ_{ET} de 44 %. Le système équivalent basé sur l'ion Yb^{3+} (**Ru—YbL3**) a montré de k_{ET} de 0.34x10^7 s^{-1} et Φ_{ET} de 30 %. Pour les quatre systèmes, le taux de transfert d'énergie a été plus rapide pour les complexes hétérométalliques impliquant le Nd(III) qu'avec l'Yb(III). Ce transfert plus rapide peut être justifié par des niveaux des états excites du Nd(III) plus compatibles en énergie avec les états ^{3}TCML de complexes **Ru** et **RuL** par comparaison au niveau d'état excité du Yb(III), dans un même système. Le taux de transfert d'énergie et le rendement quantique obtenus pour le complexe **Yb—RuL** est, à notre connaissance, la meilleure valeur reportée dans la littérature.[18, 22, 26, 31, 32] Bien que le complexe **Yb—RuL** montre un taux de transfert d'énergie k_{ET} plus rapide et un rendement Φ_{ET} plus haut que le complexe **Ru—NdL3**, le complexe similaire (**Nd—RuL**) montre de valeurs de k_{ET} et Φ_{ET} plus élevé par rapport le complexe **Yb—RuL**.

En conclusion de cette partie, nous avons présentés les synthèses et caractérisations de quatre nouveaux complexes hétérobimétalliques *d-f* (Ru(II)—Nd/Yb(III)) possédant de ligands organiques modifiés par de groupes alkoxysilanes. Le processus de transfert d'énergie a été évalué et également confirmé par les mesures de durées de vie et de rendement quantique. Ces résultats suggèrent que de par leur structure et propriétés photophysiques, les complexes **Ru—LnL3** et **Ln—RuL** sont de bons candidats pour envisager la réaction de greffage sur des matrices hydroxylés pour accéder à de nouvelles nanosondes ou nanomarqueurs exitables dans le visible et émettant dans l'IR.

5. Nanohybrides luminescents à base de silice et de complexes hétérobimétalliques *d-f*

- *Matrices de silice utilisées (MSNs et DSNs)*

La silice, SiO_2, est un matériau de choix pour élaborer à façon des nano-objets multifonctionnels. En effet il est possible de concentrer le luminophore au cœur de la particule tout en le protégeant des perturbations externes susceptibles d'inhiber le processus de luminescence, de modifier la surface des nanoparticules de silice via une fonctionnalisation

par voie chimique pour rendre ces hybrides biocompatibles voire biospécifiques donc adaptés à l'analyse des milieux biologiques.

Nous avons choisi d'utiliser deux supports qui se différencient à plusieurs niveaux, ceci pour montrer que la méthodologie de greffage peut être adaptée quelque que soit la silice. Ceci nous permettra également, l'étude des propriétés de luminescence des hybrides, de préciser les avantages et inconvénients de chacun de ces supports.

Dans cette optique, nous avons synthétisés de nanoparticules de silice mésoporeuses (notées *MSNs)* par la méthode de microémulsion directe selon le protocole décrit par Nandiyanto et al.[78] Certaines réactions de greffage ont été réalisées en utilisant des nanoparticules de silice dense (notées *DSNs)* de type Ludox (AS-40) commerciale.

La morphologie des nanoparticules mésoporeuses a été caractérisée par microscopie à balayage et à transmission, figures 63, 64 et 65 (pages 150-152), respectivement. Le pourcentage de sites silanol a été obtenu par des mesures quantitatives de analyse thermogravimétrique (figure 67, page 154) et par RMN du solide (figure 69, page 156). Les nanoparticules *MSNs* d'environ 47 nm de diamètre présentent une surface spécifique élevée (S_{BET} = 675 $m^2.g^{-1}$, figure 68, page 155) avec une taille de pores de $ø_p$ = 9 nm, figure 68, page 155. L'ensemble de ces propriétés, morphologiques notamment, sont très intéressantes pour l'objectif visé qui est d'en modifier chimiquement la surface.

5.1. Greffage et caractérisation des complexes précurseurs monomères et hétérobimétallique *d-f* silylés sur la matrice de silice mésoporeuse

- *Greffage de complexes monomères silylés sur la MSNs*

La réaction de greffage consiste à réaliser l'hydrolyse et la condensation d'un groupe alkoxysilanes sur un site silanol de la silice de façon à créer une liaison covalente entre le complexe et la matrice de silice. Ces réactions ont été réalisées selon la méthodologie décrite par Menu et al.[71-73, 75, 76] Les quantités de complexes introduits et aussi greffés sont inférieurs à 1 mmol g^{-1} de silice pour minimiser la possibilité de greffage d'oligomères.

La morphologie des nanoparticules n'est pas modifiée par la réaction de greffage comme observé en microscopie électronique à balayage (figure 74, page 166) et transmission (figure 75, page 158). Ainsi le greffage des complexes monomères, de ruthénium ou de lanthanides ont conduit à l'obtention des hybrides: **SiO_2-Ru**; **SiO_2-Nd** et **SiO_2-Yb**; le greffage

simultané des deux types de complexes monomères silylés, ruthénium et lanthanides conduit aux hybrides: **SiO_2-RuNd** et **SiO_2-RuYb**. Les caractérisations par spectroscopies Raman (figure 72, page 162), DRIFT (figure 71, page 160) et RMN du solide (figure 73, page 165) ont confirmé l'intégralité de complexes greffés sur le MSNs. Les taux de greffages ont été calculés à partir des analyses élémentaires. Les taux obtenus compris entre 0,08 et 0,18 mmol de complexes par gramme de support sont en accord avec les taux de greffage décrits dans la bibliographie.

Des mesures de microscopie en transmission et à balayage (STEM) ont été réalisées pour identifier et distinguer les atomes tels que le ruthénium, le néodyme, l'ytterbium et le silicium. Les cartographies des éléments ont été obtenues par spectroscopie EDX (figures 76-80, pages 168-173). Malgré le faible taux de greffage que possèdent les nanohybrides **SiO_2-Nd** et **SiO_2-Yb**, la cartographie indique que les éléments métalliques sont répartis de façon homogène dans les particules de silice.

- *Nanohybrides à base de silice et de complexes hétérobimétalliques d-f silylés*

Les réactions de greffages ont été effectuées sur les deux types de matrices : nanoparticules de silice mésoporeuses *MSNs* et la nanoparticule de silice danse type Ludox *DSNs*, selon la méthodologie décrite figure 87 (page 183). Comme dans le cas précédent, les quantités de complexes introduites et greffées sont inférieures à 1 mmol de complexe par g de silice pour minimiser la possibilité de greffage d'oligomères. Ainsi 4 hybrides ont été obtenus par greffage de complexes hétérobimétalliques *d-f* : **SiO_2-RuYbL3**; de **SiO_2-NdRuL** et **SiO_2-YbRuL** sur MSN, et **SiO_2 d-YbRuL** sur silice dense *DSNs*. Les résultats obtenus par microscopies (MEB et MET, figures 91 et 92, pages 190 et 191, respectivement) montrent que la morphologie des nanoparticules (MSNs et DSNs) sont conservées. De plus, il est possible d'observer que les pores la silice mésoporeuse sont en partie bouchés par la présence de densité électronique possiblement attribuée aux charges métalliques (ruthénium et lanthanide) des complexes (figure 92, page 191). Les mesures de FT-Raman (figure 89, page 186), DRIFT (figure 88, page 184) et RMN du solide (figure 90, page 189) ont confirmé l'intégralité de complexes greffés sur les deux matrices. Les taux de greffages ont été calculés à partir des données d'analyse élémentaire, ils sont compris entre 0,03 et 0,17 mmol de complexes par gramme de support.

Les analyses STEM des nanohybrides **SiO_2-RuYbL3**, **SiO_2-YbRuL** et **SiO_2 d-YbRuL** ont montrées que les éléments ruthénium et ytterbium sont distribués de façon homogène dans

le réseau de silice. Ces résultats corroborent les données d'analyse élémentaire (AE). Dans le cas du nanohybride **SiO_2-NdRuL** il est noté une distribution hétérogène des éléments ruthénium et néodyme, la quantité de ruthénium étant plus élevée que celle du néodyme comme cela avait été observé en AE. Dans ce cas il semble que le complexe se détériore lors de la réaction de greffage, éliminant le fragment néodyme. Par la suite seuls les nanohybrides **SiO_2-YbRuL** et **SiO_2 d-YbRuL** seront discutés pour leurs propriétés de luminescence.

5.3. Caractérisation photophysiques des nanohybrides

- *Propriétés photophysiques de nanohybrides à base de silice obtenues par greffage de complexes de ruthénium(II) et de lanthanide(III) silylés*

Nous avons préparés cinq nanohybrides à base de complexes monomères de ruthénium et de lanthanides (Ln = Nd^{3+}, Yb^{3+}). Les propriétés de luminescence ont été évaluées pour les échantillons **SiO_2-Ru**, **SiO_2-Nd** et **SiO_2-Yb**. Les spectres d'émission de ces nanohybrides (figures 81-83, pages 176, 177) sont superposés aux spectres des complexes silylés libres (figures 50, 53 et 54, pages 132, 134 et 135, respectivement). Le spectre d'émission de l'hybride **SiO_2-Ru** montre un déplacement vers basse énergie par rapport le complexe libre qui peut-être due à l'interaction du complexes avec les hydroxyles de surface de la matrice. Les mesures de durée de vie pour l'échantillon **SiO_2-Ru** conduisent à une valeur de 344 ns, valeur qui sera utilisée pour les calculs de processus de transfert d'énergie.

En ce qui concerne les deux autres nanohybrides, **SiO_2-RuNd** et **SiO_2-RuYb**, obtenus par greffage simultané des complexes monomères silylés, **RuL1**/**NdL3** et **RuL1**/**YbL3**, respectivement, l'évaluation des propriétés photophysiques a permis d'évaluer si la proximité de ces complexes lorsqu'ils sont confinés dans les pores est suffisante pour permettre une situation favorable à un transfert d'énergie et observer l'émission dans l'infrarouge du lanthanide. Les propriétés photophysiques pour ces nanohybrides ont été évaluées. Les spectres d'émission et d'excitation (figures 84 et 85, pages 179 et 180) confirment l'existence d'un transfert d'énergie. Lorsque l'excitation est faite sur la bande ^{1}TCML nous pouvons observer la sensibilisation de l'émission des ions Nd^{3+} et Yb^{3+} dans l'IR. Les mesures de durées de vie indiquent des valeurs de 206 et 250 ns (tableau 7, page 182) pour les nanohybrides, **SiO_2-RuNd** et **SiO_2-RuYb**, respectivement. Les calculs de transfert d'énergie montrent le k_{ET} de 0.20 x 10^7 (Φ_{ET} = 40 %) et 0.11x10^7 s^{-1} (Φ_{ET} = 27.5 %), pour le **SiO_2-RuNd** et le **SiO_2-RuYb**,

respectivement. Ce résultat est très intéressant et tout à fait inattendu. Cela met en évidence que dans ces nanohybrides où les deux complexes de ruthénium et de lanthanides totalement indépendants lors de la réaction de greffage, se retrouvent dans le réseau de silice, au moins en petite quantité, suffisamment proche pour permettre un transfert d'énergie. La faible valeur de Φ_{ET} pour ces deux nanohybrides vient aussi de la faible probabilité d'avoir les deux complexes orientés favorablement pour ce transfert d'énergie.

- *Propriétés photophysiques de nanohybrides à base de silice obtenues par greffage de complexes hétérobimétalliques d-f silylés sur le MSNs et la Ludox AS-40 (DSNs).*

Les profils des spectres d'émission des quatre nanohybrides à base de complexes hétérobimétalliques *d-f* sont rassemblés figures 97-100, pages 202-206) sont comparables aux spectres de complexes silylés libre (figures 57-60, pages 138-141). L'utilisation des deux matrices de silice pour le greffage du complexe **Yb—RuL**, a permis de mettre en évidence des différences concernant les spectres d'émission attribuées aux nanohybrides. L'hybride **SiO_2d-YbRuL** montre une faible intensité d'émission par rapport l'hybride **SiO_2-YbRuL**. Ce dernier possède une forte émission dans l'IR lorsque nous avons fixés l'excitation sur la bande ^{1}TCML du ruthénium(II). Dans ce dernier cas, le complexe **Yb—RuL** peut être confinés dans les pores et, par conséquence, éviter les perturbations externes tels que processus de solvatation, susceptibles d'inhiber l'émission du complexe dans l'IR. Ce résultat très important met en évidence l'avantage d'utiliser la silice mésoporeuse tel que support inorganique pour l'obtention de nanohybrides luminescents.

Ces propriétés photophysiques, particulièrement la luminescence, associées à la morphologie de ces hybrides et à leur stabilité suggèrent que ces nanohybrides sont de bons candidats comme nanosondes ou nanomarqueurs des systèmes biologiques émettant dans l'IR.

6. Conclusion

Dans ce travail de thèse, nous avons choisi de synthétiser de nouveaux complexes hétérobimétalliques *d-f* (Ru(II)—Nd/Yb(III)) comportant au moins un groupement fonctionnel alcoxysilane dans le but d'obtenir, apres greffage sur des matrices de silice, des nanohybrides luminescents, excitable dans le visible et emettant dans l'IR, domaine d'emission recherché dans de nombreuses applications d'analyses des systèmes biologiques puisqu'il correspond à la transparence des tissus biologiques. Un travail préalable de synthèse de nouveaux complexes monomères de ruthénium(II) et de lanthanides(III) comportant ou pas le groupement silane a donc été necessaire.

Plusieurs stratégies de greffage ont été mis en œuvre d'une part pour connaitre les propriétés de luminescence des hybrides à base de monomères de façon à les comparer ensuite aux propriétés des hybrides hétérobimétalliques, d'autre part pour mettre en évidence la nécessité, ou pas, de synthétiser de tels complexes *d-f* pour atteindre l'objectif visé. Enfin deux supports de silice présentant des morphologies différentes ont été évalués.

A partir de deux ligands possédant une fonction trialkoxysilane ; le 4-méthyl-4'-(n-triéthoxysilylpropyl)amine-méthyl- 2,2'-bipyridine (**bpy-Si**) et le 4,4,4-Trifluoro-2-(3-(triméthoxysilyl)-propyl)-1-(2-thienyl)-1,3-butanedione (**TTA-Si**), quatre nouveaux complexes hétérobimétalliques *d-f* Ru(II)/Ln(III) , Ln = Nd^{3+}, Yb^{3+} ont été isolés et caractérisés. Ces complexes possèdent la propriété chimique de pouvoir être greffer de façon covalente à n'importe quel matériau à base de silice, ils sont excitables dans le visible et émettent dans le domaine IR. Dans la série obtenue, le complexe Yb-RuL est celui qui met en évidence le transfert d'énergie le plus important avec un rendement quantique de transfert d'énergie remarquable de 73.4%. L'objectif d'isoler des complexes *d-f* à fonction silane luminescents dans l'IR a donc été atteint.

Dans l'idée de concentrer le luminophore au sein d'une même nanoparticule pour obtenir des sondes plus sensibles et plus facilement fonctionnalisables, voire biofonctionnalisables, il a été entrepris de préparer des nanohybrides a base de silice. Pour cela des particules de silice mésoporeuses monodisperses (47 nm ± 4 nm), dont les caratéristiques, V_{poreux} = 1.55 $cm^3.g^{-1}$; $\varnothing_{pores}$ = 9 nm et de surface spécifique, S_{BET} = 675 $m^2.g^{-1}$, ont été synthétisées en utilisant un système de microémulsion directe en présence d'agent porogène. Elles possèdent des caractéristiques morphologiques très intéressantes pour l'obtention d'hybride par greffage. Des nanoparticules de silice commerciales, se différentiant

par une absence de porosite, ont également été mis en œuvre à des fins comparatives. La silice, notée **SiO_2d**, est une silice de type Ludox, nanosphères denses de 24 ± 2 nm, très monodisperses de surface spécifique 138 $m^2 .g^{-1}$.

Ainsi la synthèse de trois types de nanohybrides à base de silice a été entreprise. Dans tous les cas les luminophores, complexes métalliques silylés monomères ou hétérobimétalliques, sont liés de façon covalente à la matrice silicique pour éviter tout relargage du luminophore lors des applications ultérieures envisagées.

Par greffage des nouveaux complexes monomères silylés, **RuL1**, **NdL3** et **YbL3**, trois hybrides ont été isolés et caractérisés: **SiO_2-Ru**, de **SiO_2-Nd** et **SiO_2-Yb**. Un deuxième type d'hybride a été obtenu par greffage simultané des complexes monomères silylés de ruthénium et et de lanthanide: **SiO_2-RuNd** et **SiO_2-RuYb**. Enfin le greffage des quatres nouveaux complexes hétérobimétallique *d-f* silylés ont conduits à l'obtention des hybrides : **SiO_2-RuYbL3** ; **SiO_2-NdRuL** ; **SiO_2-YbRuL** et **SiO_2 d-YbRuL**. Ainsi neuf nouveaux nanohybrides à base de silice et de complexes métalliques, dont la taille varie selon la matrice de silice utilisée, 25 ou 50 nm) ont été préparés et caractérisés. Ils mettent en évidence des taux de greffage compris entre 0,05 et 0,18 mmol de complexes par gramme de support. De tels taux de greffage permettent d'envisager une fonctionnalisation chimique ultérieure de ces nanoobjets.

L'étude des propriétés photophysiques a été ensuite réalisée avec l'enregistrement des spectres d'excitation et d'émission à l'état solide pour chacun des échantillons, complexes libres et nanohybrides, à température ambiante. Les spectres d'excitation obtenus dans le cas des complexes monomères mettent en évidence les transitions caractéristiques attribuées aux divers ligands organiques (bpy, bpmd, TTA) tandis que les spectres d'émission présentent une luminescence dans le visible pour les complexes de ruthénium et dans l'IR pour les complexes de néodyme et ytterbium. L'analyse des nanoparticules fonctionnalisées montre des spectres très proches de ceux des complexes libres confirmant la présence des différents complexes à la surface de la silice.

Le greffage des deux complexes monomères donnant respectivement **SiO_2-RuNd** et **SiO_2-RuYb** met en évidence qu'un transfert d'énergie est possible entre les deux centres métalliques Ru et Ln quand ils sont introduits sous forme de monomère. En effet des rendements quantiques de transfert d'énergie (Φ_{ET}) significatifs, (27 et 40 % respectivement

pour **SiO_2-RuYb** et **SiO_2-RuNd**) ont été déterminé. Ce résultat mérite d'être encore exploité pour en comprendre réellement le mécanisme.

Enfin il ressort de l'étude des propriétés photophysiques des hybrides à base de complexes hétérobimétalliques qu'il est possible, par notre approche, d'obtenir des sondes excitables dans le visible et émettant dans l'IR avec des rendements quantiques de transfert d'énergie (Φ_{ET}) significatifs compris entre 30 et 84 %. De plus le choix de la matrice de silice semble un paramètre important à considérer, la silice mésoporeuse apparaissant comme un choix plus judicieux pour maintenir les propriétés photophysiques, l'explication proposée étant une meilleure protection du luminophore.

Perspectives

Sur la base des propriétés de photoluminescence de ces complexes monomères et hétérobimétalliques et des nanohybrides à base de silice, nous pouvons suggérer les étapes suivantes comme des propositions de travail futur :

- Evaluer les propriétés photophysiques des complexes hétérobimétalliques *d-f* silylés et des nanohybrides correspondant en utilisant l'excitation bi-photons;
- Choisir les meilleurs nanossystèmes luminescents tels que **SiO_2-RuNd**, **SiO_2-RuYb** and **SiO_2-YbRuL** et puis évaluer ces nanohybrides dans les milieux cellulaires (essais de cytotoxicité);
- Evaluer leurs potentialités en tant que sondes ou marqueurs dans un système biologique en utilisant notamment la microscopie confocale avec excitation mono ou bi-photon pour accéder à la localisation 3D.

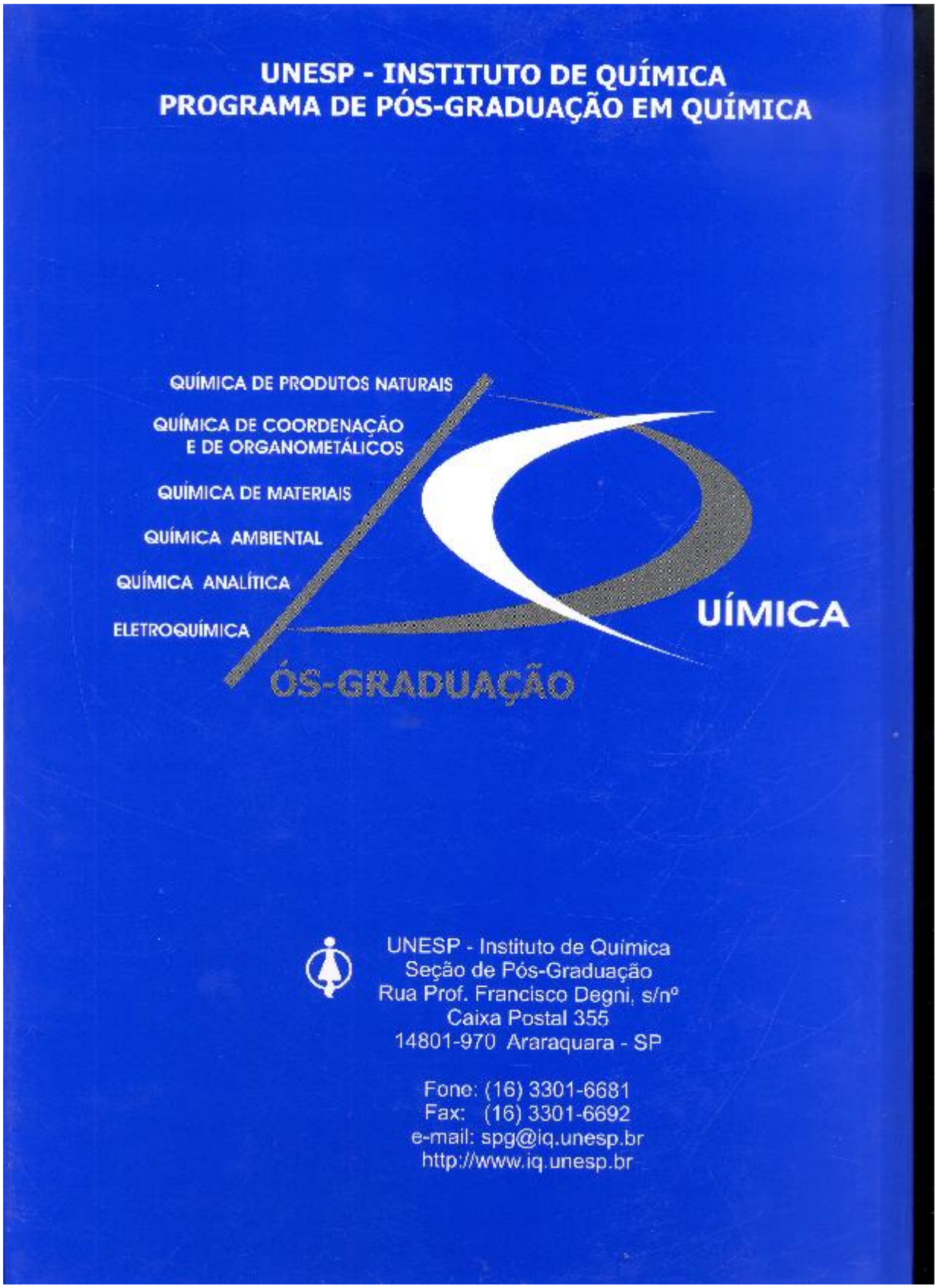
UNESP - INSTITUTO DE QUÍMICA
PROGRAMA DE PÓS-GRADUAÇÃO EM QUÍMICA
QUÍMICA DE PRODUTOS NATURAIS
QUÍMICA DE COORDENAÇÃO
E DE ORGANOMETÁLICOS
QUÍMICA DE MATERIAIS
QUÍMICA AMBIENTAL
QUÍMICA ANALÍTICA
ELETROQUÍMICA
UÍMICA
ÓS-GRADUAÇÃO
UNESP - Instituto de Química
Seção de Pós-Graduação
Rua Prof. Francisco Degni, s/nº
Caixa Postal 355
14801-970 Araraquara - SP
Fone: (16) 3301-6681
Fax: (16) 3301-6692
e-mail: spg@iq.unesp.br
http://www.iq.unesp.br